Haemodynamic Alterations After Percutaneous Valve Implantation

Jacob Andrew Salmonsmith

Submitted in accordance with the requirements for the degree of

Doctor of Philosophy

Department of Mechanical Engineering

UCL

I, Jacob Andrew Salmonsmith, confirm that the work presented in this thesis is my own. Where information has been derived from other sources, I confirm that this has been indicated in the work.

This work was funded by the British Heart Foundation, Grant number **FS/14/39/30874**

Abstract

Many patients who suffer from aortic valve dysfunction are too weak to be eligible for valve replacement via surgery, due to co-morbidities and old age. Transcatheter aortic valve (TAV) implantation has been developed as an alternative to surgery, enabling replacement of the dysfunctional valve percutaneously. However, the inability to remove the native leaflets leads to the bioprosthetic being held in place inside a pseudo-cylindrical structure. The passive nature of heart valves means the surrounding fluid environment's dynamics are critical in producing optimum performance, and would ideally be returned to the healthy, physiological state. The association of TAVs with thrombotic events, such as strokes, has not yet been fully explained.

A pulse duplicator and particle image velocimetry were used to model and characterise the flow fields of a healthy, physiological aortic root and valve, which was then compared to those resulting from a number of typical post-surgical outcomes, identifying the fluid mechanisms promoted by the root geometry to optimise the ejection and closing phases of the cardiac cycle, and revealing the importance of an optimal integration of valve and root architecture, and characterising common post-surgical environments.

The same techniques were then used to examine the flow dynamics of the region following TAV implantation, revealing the effect of TAV alignment with its hosts' commissures, and how the presence of native leaflets, commonly omitted from *in vitro* TAV testing, affect the valve performance. Slow and stagnant flow was observed within the sinuses due to the native leaflets, whilst global valve performance was broadly unaffected, and omission of the native leaflets resulted in improved haemodynamic performance.

A model of coronary arteries was incorporated into the benchtop simulation, revealing increase of flow in the upper coronary sinuses, but flow at the base of all sinuses remained very slow following TAV implantation. The elucidation of this stagnation, associated with thrombotic events, provides an explanation for the increased levels of thrombotic-associated pathologies following TAV implantation.

Impact Statement

The research in this thesis provides a link between the hydrodynamics of the aortic root following TAV implantation and the thrombotic events reported in medical follow-up examinations and morbidity reports. Improvements to each generation of TAVs since their first use on patients in 2002 have increased the life duration and quality to their recipients, and this has been achieved by critical examination of existing designs to inform and improve the following devices, reducing the para-valvular leakage and enabling redeployment during the implantation procedure. By showing that the continued presence of the native leaflets following TAV implantation produces flow alterations that tend towards the thrombogenic, design steps in the next generation of TAV devices can be taken to remove or mitigate this feature, reducing the likelihood of thrombosis and improving the outlook for patients post-TAV implantation.

The demonstration of the need for accurate modelling of the geometrical arrangement of the valve and root when simulating aortic root flow has also been shown. The scientific community has yet found consensus on the vortical structure surrounding the systolic flow of blood from the aortic valve, and some of the characterisations have been reproduced in this thesis by placing the valve in over-sized roots or in a sub-annular position. This information has been disseminated in both written form, via articles in the Journal of Biomechanics and the Journal of Cardiovascular Engineering Technology and a book chapter in 'Transcatheter Aortic Valve Implantation: Clinical, Interventional, and Surgical Perspectives', and aurally, via a presentation at the 4th European Society for Vascular Surgery Spring Meeting 2016.

There are also numerous *in vitro* reports on the performance of TAV devices that neglect to include a representation of the native leaflets, affecting both the global and local flow properties of the region, particularly within the modelled sinuses of Valsalva. This has been submitted for publication in the Journal of Cardiovascular Research, and has been presented at the British Cardiovascular Society Conference 2017, and the UCL Institute of Healthcare Engineering Autumn Research Symposium 2018.

The modelling of coronary arteries is of importance to a study of the sinuses in the aortic root region, and this thesis has demonstrated a method of including a representation of these within a benchtop model.

Acknowledgements

I would like to sincerely thank my principal supervisor, Prof Gaetano Burriesci, for his support and guidance throughout this PhD process, right from the suggestion of the topic and to apply for the funding during a catch-up a short time after he had supervised me through my MSc project at UCL. His advice, patience, guidance, and equanimity ("you can't have dinner without making some crumbs") have been essential in my completion of this research, and his ever-genial nature has made conversations both within and without scientific discourses extremely enjoyable. I can only apologise for my complete lack of Italian language skills, despite his best efforts to inculcate a *cultura italiana*, whether it be by attitude, population, or cuisine.

Speaking of which, I must also thank my secondary supervisor, Dr Andrea Ducci, for his help and advice, and for his support throughout the various processes of the programme. And I promise, sorting out the Spurs-Inter tickets wasn't some sort of revenge for a past slight.

I'm grateful to everyone in the Cardiovascular Engineering Lab past and present, but in particular Tobias, with whom I figured out the majority of the rig operation; Riccardo, with whom I researched and published my first paper, and swapped an introduction to the wonders of cricket for a tour of Venice; and Anna Maria, whose work has been so closely associated with mine over the past 4 years.

A special thanks to Andrew, Ryan, and Paul for the many lunches we shared together, the ridiculous conversations, and the numerous badly played games of bar billiards. An additional thanks to Andrew for the many conversations we had about how to approach our research, even if he does think watching sport is just as interesting as a calculator producing random numbers.

Thanks also to everyone in Mechanical Engineering who make the department what it is, whether it be the office staff in 4.04 making the wheels turn, the workshop crew producing components from envelope-back drawings, or any of the numerous academics who happily discuss research.

Thanks to the British Heart Foundation for funding this work, without which I wouldn't have been able to even consider undertaking the programme.

Finally, but most importantly, my unending gratitude to my family and friends for their support and excellent company, especially my parents, who have always encouraged and supported me to follow my heart, and my wife Lauren, who is where it took me.

Contents

List of Figures

List of Tables

Nomenclature

Abbreviations

2D	Two-Dimensional
3D	Three-Dimensional
AV	Aortic Valve
bpm	Beats Per Minute
CA	Coronary Artery
CAD	Computer Aided Design
CCD	Charge-Coupled Device
CO	Cardiac Output
ECG	Electrocardiogram
EOA	Effective Orifice Area
EU	European Union
GA	Gluteraldehyde
GOA	Geometric Orifice Area
IVC	IsoVolumetric Contraction
IVR	IsoVolumetric Relaxation
KI	Potassium Iodide
LCA	Left Coronary Artery
LVOT	Left Ventricular Outflow Tract
MRI	Magnetic Resonance Imaging
NCA	Non-Coronary Artery
PET	Polyethylene Terephthalate
PIV	Particle Image Velocimetry
PTFE	Polytetrafluoethylene
PVL	Paravalvular Leakage
RBC	Red Blood Cell
RCA	Right Coronary Artery
RI	Refractive Index
RSS	Reynolds Shear Stress
SAV	Surgical Aortic Valve
SCLT	Sub-Clinical Leaflet Thrombosis
SoV	Sinuses of Valsalva

SS	Shear Stress
STJ	SinoTubular Junction
TAV	Transcatheter Aortic Valve
US	United States of America
ViV	Valve-in-Valve
WSS	Wall Shear Stress

Symbols

A	Area
α	Upstream leaflet angle
D	Diameter
C_f	Calibration factor
$E_f,\ E_c,\ E_l$	Energy loss during forward flow/valve closure/leakage
$E_L,\ E_H$	Young's modulus during elastic/collagen phase
h_p	Downstream projection
k	μm to pixel ratio
k_f	Conversion factor
L	Displacement
μ	Dynamic viscosity
n	Refractive Index
n_{spot}	Interrogation spot size
P	Pressure
ΔP	Systolic Transvalvular Pressure Drop
φ	Downstream leaflet angle
Q	Flow rate
q_v	Flowmeter flow rate
$q_{v_{RMS}}$	Root mean square of flow rate
ρ	Density
t	Time
ΔT	Image pair time gap
τ_s	Response time
V	Volume
v	Velocity
x_f	Fast flow width

1 Introduction

1.1 Background

The most frequent heart valve disease in the western world is aortic stenosis, a pathology of the leaflets of the aortic valve which drastically reduces its functionality, significantly affecting the life quality of the patient, and is strongly linked with high morbidity and mortality[1–3]. Due to its association with elderly patients[4,5], occurrence of aortic stenosis is expected to increase in the next 20 years alongside the world's ageing population[2,3]. The progression of most cases of aortic stenosis cannot be reversed or prevented via pharmacological treatments[6], and when the stenosis is judged to be too severe for the patient's well-being, the native valve requires replacement[7].

Prosthetic devices have been developed and surgically implanted over the last 70 years, in order to restore valve function to the patient. Mechanical prosthetics, typically utilising hinged rigid leaflets[8], display high levels of durability, but require lifelong anti-coagulation therapy due to the thrombogenicity of the materials and fluid flow patterns[9]. Bioprosthetic aortic valves, often constructed from porcine or bovine pericardium in a trileaflet arrangement mimicking the native aortic valve, can also be surgically implanted, more closely maintaining the natural blood flow of the heart and reducing the necessity of anti-coagulant therapy[8].

However, due to the debilitating effects of aortic stenosis and other co-morbidities, up to third of patients requiring valve replacement are ineligible for surgery[10,11]. A novel percutaneous treatment has been developed, wherein a Transcatheter Aortic Valve (TAV) can be delivered to the aortic region without the need for surgery, reducing the associated risks of surgery and length of hospital stays[12], with the devices anchored in place by expansion of a supporting frame onto the leaflets of the native valve. These benefits are offset by the reported increased incidence of pathologies associated with thrombosis, such as strokes and silent ischemic events, when compared with surgical bioprosthetics, and it is crucial to understand and minimise these problems to improve the efficacy of TAVs[13–16]. Non-physiological haemodynamics, such as stagnation and high shear stress, have been identified as a major cause of platelet activation and thrombus formation[17], and ischemic lesions have been previously linked to thrombus formation in the irregular zone around the TAV frame[16]. Identification of the hemodynamic alterations caused by TAV

implantation is critical in reducing their occurrence and resultant pathological effects.

1.2 Overall Aims

In order to identify the changes to the haemodynamics of the aortic root region caused by TAV implantation, it is first necessary to identify the fluid dynamics of the healthy native physiological condition, upon which there have been many studies in the literature but no consensus, particularly in regards to the systolic vortical patterns downstream of the aortic valve[18,19,28–35,20–27]. Newly refined methods of flow visualisation can clarify these valve dynamics, and subsequent analysis of the flows associated with mechanical-, surgical bioprosthetic-, and transcatheter-aortic valves can then be compared to the characteristics of the physiological flow, revealing the alterations caused by each non-native device. For this thesis, these investigations were *in vitro* experiments, using a hydromechanical pulse duplicator to impose physiological pressures and flow rates upon the blood analogue fluid flowing through various prosthetic devices within mock aortic roots, with simultaneous image acquisition for Particle Image Velocimetry (PIV) analysis, enabling instantaneous velocity fields of a cross-section of the fluid flow to be derived.

To ensure proper testing conditions, some preliminary tests needed to be undertaken. Uniaxial tests measuring the stress-strain response of the biological tissues used in the bioprosthetic Surgical Aortic Valves (SAV) were required, to ascertain whether their stiffness changed after exposure to the chemicals used in typical testing fluids, and are presented in the appendices. Hydrodynamic and PIV analysis of the valve size and position within the mock aortic roots was necessary to reveal their effect upon the fluid dynamics of the test, explaining some of the inconsistencies of flow characterisations in the literature. Once these testing procedures were confirmed, the fluid dynamics of the physiological-, mechanical-, and surgical bioprosthetic-aortic valve environments were identified and contrasted, to reveal the characteristic changes caused by surgical intervention. Finally, the fluid flow alterations caused by implantation of a TAV were investigated and characterised, taking into account the variation of the device's rotational alignment with the native commissures and the effect of coronary flow.

1.3 Thesis Outline

The remainder of this thesis is structured as follows: the following chapter focuses on reviewing the relevant literature to present the current understanding of the fluid dynamics within the healthy native aortic root, the most pertinent pathologies that can affect the region, and the prosthetics that have been used to replace a diseased aortic valve and the fluid dynamics that result. Chapter 3 explains the materials and methods used to investigate and characterise these fluid dynamics, describing the hydro-mechanical pulse duplicator and PIV equipment used to simulate and analyse the flows generated within mock aortic regions, designed to recreate both a healthy native aortic root region as well as a range of post-valve replacement environments. This is followed by descriptions of the valves, roots, and blood analogue testing fluids used for these recreations.

The three experimental chapters examining the global and local fluid flow of the aortic root region follow, with Chapter 4 establishing the flow characterisation of the healthy native aortic root, and contrasting this description with the acquired flow fields from typical post-surgical aortic valve-root configurations, both bioprosthetic and mechanical. This chapter demonstrates how changes to the geometry of the root and/or valve, often as a result of surgical valve implantation, can result in distinct alterations to the vortical patterns during the forward flow of blood through the valve, impacting the efficiency of the heart. Chapter 5 determines the fluid dynamic alterations due to implanting a TAV rather than a surgical valve, including the effect of non-alignment of the TAV with its host valve commissures, which results in little change to the haemodynamics performance of the valve, but affects sinus washout and vortical patterns downstream of the TAV. Chapter 5 also examined the impact of modelling the native leaflets during the *in vitro* TAV assessment, the exclusion of which can give a false indication of higher valve performance than would be expected physiologically. Chapter 6 investigates the same aortic root region after TAV implantation, but with the inclusion of modelling coronary artery flow, examining whether these additional outlets of flow affect the dynamics within the root, particularly in the chambers surrounding the valve. It was found that the upper sinus flow of the coronary sinuses featured more

washout and structured flow than the non-coronary equivalent, but that the lower sinus flow remained slow in all cases, indicating a risk of thrombosis. Chapter 7 then draws together the presented work, discussing the main findings of the work, and providing recommendations for future investigations.
Finally, the appendices contain a full description of the uniaxial testing carried out to determine the stiffness of porcine and bovine pericardial tissue before and after prolonged exposure to typical *in vitro* testing fluids, undertaken to ensure that the dynamic response of the bioprosthetic valves at the end of testing was the same as at the beginning of testing. Further PIV images from Chapters 4-6 follow, placed in the appendices to improve the clarity and succinctness of the presented reports in the main body of the thesis.

2 Literature Review

2.1 The Aortic Root

2.1.1 The Heart

The function of the cardiovascular system is to supply oxygen, hormones and nutritious substances to the tissues of the body and, for some species, to regulate body temperature and pH[2]. The heart pumps blood through the circulatory system of the body via ventricles which provide this blood with the momentum to circulate around the body and return to the heart, and a series of valves to ensure that this blood flow is unidirectional[2,36], with a cross-sectional schematic illustrated in Figure 2-1. For a healthy human, the heart beats on average 60-80 times a minute, with each heartbeat being made up of muscular contraction (known as the systolic phase, or systole) and muscular relaxation (known as the diastolic phase, or diastole) of the ventricles and atria. These contractions are induced by electrical stimulation which is paced by a node in the right atrium known as the sino-atrial node[36,37], and these electrical signals can be detected via an electrocardiogram (ECG), with a typical resultant waveform displayed in Figure 2-2.

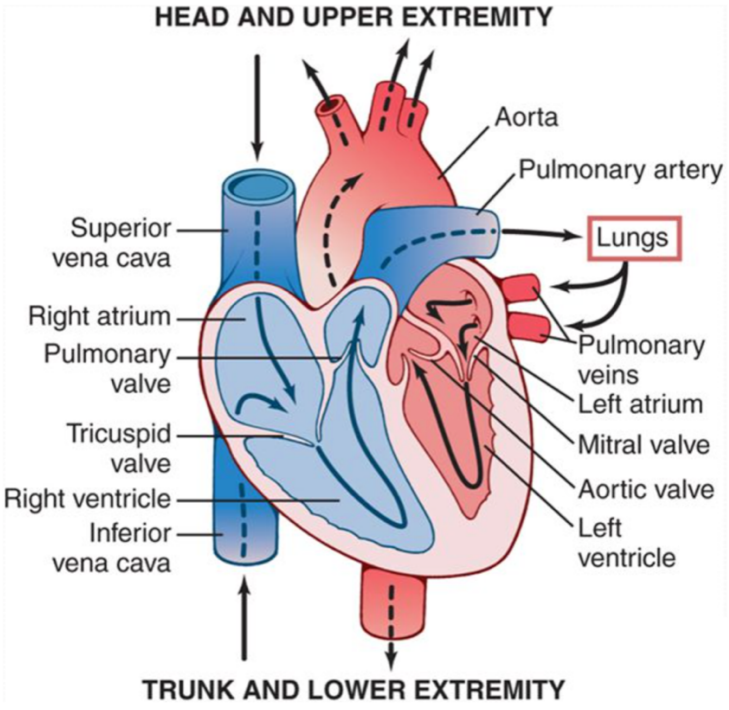

Figure 2-1: schematic of the heart, with indication of local blood flow direction. Oxygenated blood in the left side of the heart is illustrated with red shading, and deoxygenated blood in the right side of the heart with blue[38]

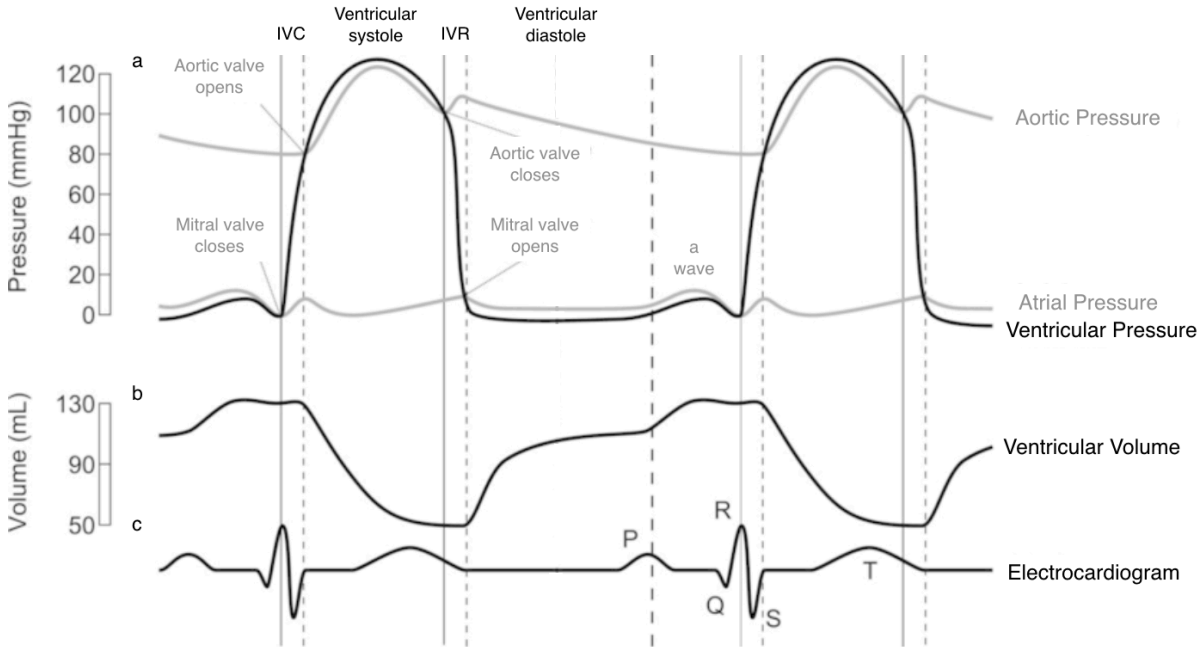

Figure 2-2: Left Side Cardiac Cycle. (a) variations of pressure in the aorta, left ventricle, left atrium; (b) variation of left ventricular volume; (c) an electrocardiogram for a typical cycle of the left side of the heart[39]

The heart is comparted into two halves, with deoxygenated blood returning from the body into the right atrium, from where it is pumped into the right ventricle which in turn pushes the blood towards the lungs, as illustrated in Figure 2-1. The oxygenated blood then returns from the lungs into the left atrium, is pumped into the left ventricle, from where the blood is impelled to the rest of the body via the left ventricle[2,36].

For the left side of the heart, blood is delivered to the atria throughout the cardiac cycle. Pressure and volume variations in the left side of the heart through a typical cardiac cycle are shown in Figure 2-2. During ventricular diastole, the pressure in the ventricle is lower than the pressure of the associated atrium, and as such the mitral valve, connecting the two, is open, whilst the downstream valve of the ventricle, the aortic valve, is shut during this period, as the pressure in the aorta is higher than that in the ventricle[2,37]. This allows filling of the ventricle with blood from its atrium throughout diastole, initially passively, but when atrial systole occurs towards the end of ventricular diastole, commencing at ECG signal ‘P’ and throughout the ‘a wave’ illustrated in Figure 2-2, the contraction of the atrial muscle wall pushes an extra, small amount of blood into the ventricle[2,37]. As the ventricle contracts, the pressure rises, and when it rises above the atrial pressure (shutting the mitral valve) but

remains below the aortic pressure, neither the mitral nor the aortic valve are open, as the ventricle experiences isovolumetric contraction (IVC), and the pressure continues to rise whilst the volume remains constant[2,36,37]. Once the ventricular pressure rises above the aortic pressure, typically around 80 mmHg, the aortic valve opens, and an ejection phase commences, known as ventricular systole[2]. After a period of ejection, the myocardial contraction reverts and the ventricular muscle starts to relax, leading to the pressure in the aorta becoming greater than in the ventricle, resulting in the aortic valve shutting, preventing backflow of blood. As the atrial pressure is still lower than the ventricular pressure, the mitral valve remains shut, resulting in isovolumetric relaxation (IVR) as the pressure continues to drop in the ventricle and the volume remains constant. When the pressure eventually drops beneath that of the atrium due to both IVR and atrial filling, the mitral valve opens, filling of the ventricle commences, and the cycle starts over again[2,37].

A typical human heart rate is around 70 bpm at rest, resulting in a cycle length of ~850 ms, with the ejection period lasting ~330 ms[36,40].

2.1.2 Anatomy of the Aortic Root

The aortic root, illustrated in Figure 2-3, consists of:

- the aortic annulus, the transition between the left ventricle and the aortic root;
- the aortic valve
- the sinuses of Valsalva (SoV), bulges of the aortic tract, each bulge aligned with an aortic valve leaflet, and two of these dilations each house a coronary ostium;
- the sinotubular junction (STJ), where the transversal cross-section of the aortic lumen becomes approximately circular, indicating the transition between the dilations of the SoV and the tubular ascending aorta and the downstream end of the aortic root, and also the furthest downstream point of the attachment of the aortic valve leaflets[41–44]

Due to pressure changes and the compliance of the root walls, the dimensions of the aortic valve and root vary throughout the cardiac cycle[27,45].

Measurements of the diameters of the aortic root region show notable variability across different sources in the literature, as shown in Table 2-1,

which may be due to a combination of anatomic variability and the difficulty of ascertaining the dimensions of a pressurised, fluid filled architecture once removed from its dynamic environment[46,47].

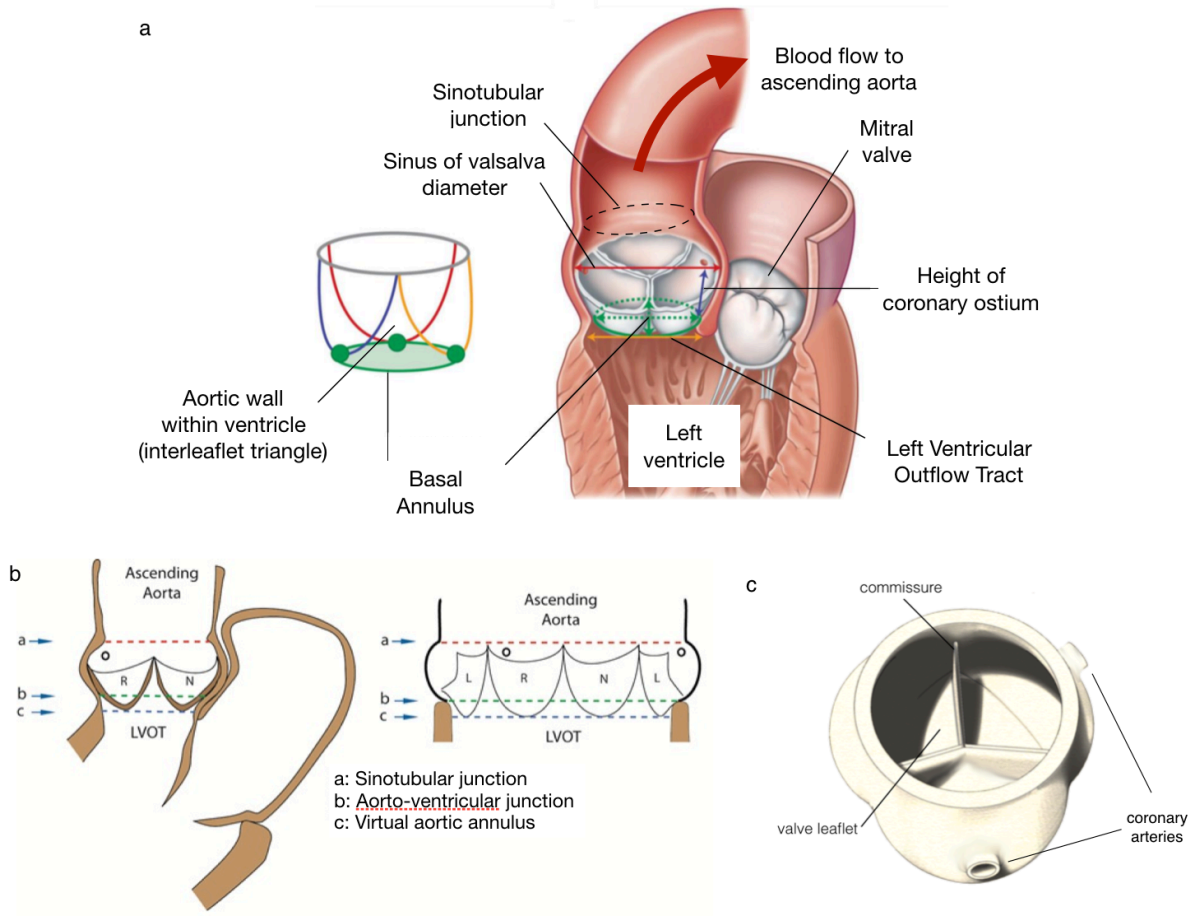

Figure 2-3: The aortic root. (a) cross-section of the aortic root and schematic of the aortic valve, adapted from Gripari 2014[48]; (b) cross-section of the aortic root showing the leaflets[49]; (c) 3D modelled of the aortic root

Some reports state that when normalised against the annulus, the dimensions of the aortic root are proportional for men and women[47], although other investigations report that this changes with age[46]. The diameters of the annulus, the sinuses of Valsalva, and the STJ all increase in relation to body surface area after the age of 20[50]. Some works in the literature indicate that this increase occurs at a similar rate for both sexes[47] but other reports state the rate of annulus diameter increase with age is higher for men[46].

It should be stressed that the diameter of the aortic annulus can be identified as different parts of the aortic root anatomy, and the annulus referred to by surgeons is usually the 'crown-like structure demarcated by the hinges of the leaflets', as described in Figure 2-4[51]. Future reference to the aortic annulus diameter will be in relation to the basal attachment virtual ring as described by

Piazza *et al.*[51] unless noted. In between the annulus and the semi lunar attachment of the valve leaflets are located the interleaflet triangles, as illustrated in Figure 2-3(a), composed of fibrous tissue, and separating the leaflets from each other[52]. Two of these triangles have thickened basal connections to the annulus, one housing the bundle of His, essential in the correct conduction of electrical signals required to control the beating of the heart, and the other connecting the aortic and mitral annuli[51,53].

Anatomy	D_{ab} *(mm)*		$\frac{D_{ab}}{D_{an}}$	
	Vriz[47]	Davis[46]	Vriz	Davis
Annulus	21.0 ± 2.2	23.9 ± 5.3	1.00 ± 0.10	1.00 ± 0.22
Sinuses of Valsalva	31.8 ± 3.7	31.9 ± 7.6	1.51 ± 0.18	1.33 ± 0.32
Sinotubular Junction	26.9 ± 3.7	24.4 ± 6.2	1.28 ± 0.18	1.02 ± 0.26
Ascending Aorta	29.1± 4.3	26.0 ± 7.3	1.39 ± 0.20	1.09 ± 0.31

Table 2-1: Average diameters of aortic root anatomy for men of mass 76.7 ± 12.6 kg, presented both as an absolute value (D_{ab}, mm) and a dimensionless value relative to the annulus diameter (D_{an}). The annulus for both investigations was defined as the basal annulus as described by Piazza et al.[51]

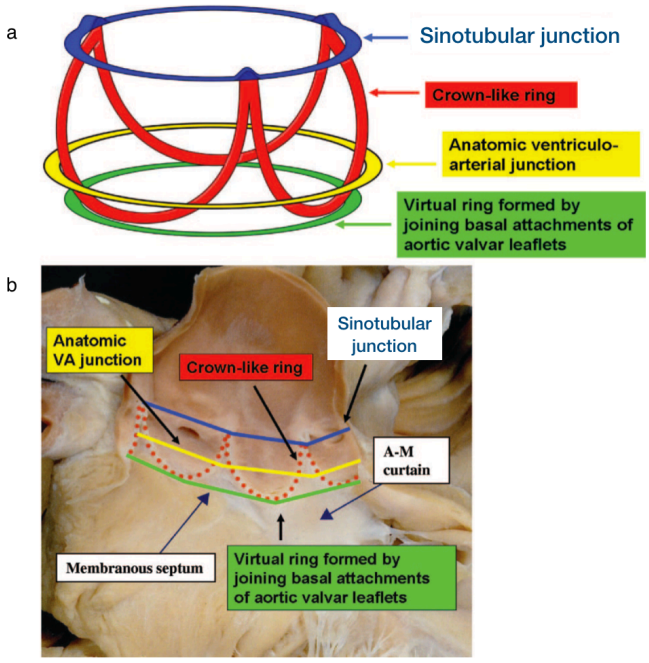

Figure 2-4: Circular rings within the aortic valve. (a) the leaflets are suspended from the commissures in a crown-like arrangement, containing 3 distinct circular rings, one each at the STJ, the ventriculoarterial join, and the virtual ring formed by the basal attachment of the valve leaflets; (b) the rings and crown-like arrangement shown on an explanted aortic root with the valve removed

2.1.2.1 Aortic Valve

The main function of any of the heart valves is passively ensuring that the flow of blood is uni-directional with minimal back flow into the chamber it has just flown from[2,36]. The aortic valve normally comprises of three crescent shaped leaflets, attached both to the aortic annulus, and to the aortic root in three separate regions, with the downstream leaflet cusps coapting during diastole to prevent backflow of blood, as illustrated in Figure 2-5(a). The regions where the leaflet conjugations run parallel, distally upstream towards the ascending aorta, are called the commissures[44]. Despite 84 % of case studies having a difference in leaflet size greater than 5 % within the same aortic valve[50], these size difference between leaflets are thought to be insignificant[44]. Due to congenital disease, between 1 and 2 % of natural aortic valves are not tricuspid, but are instead bicuspid valves, which are associated with increased valvular dysfunction and pathological issues in later life, such as aortic valve stenosis[34], which will be discussed in more detail in Section 2.2.1.

For a normal sized adult, the main body of the valve leaflets is about 0.1 mm thick[37], and consists of three types of tissue, as illustrated in Figure 2-5(b-d). A load bearing collagen-based layer on the aorta side called fibrosa is dominant in the mechanical response under high strain conditions, and a supplementary, elastin-based layer on the ventricular side called ventricularis that is effective in low strain conditions[54–57]. Separating these two tissues is a third, known as spongiosa, allowing the other two predominant layers to deform more easily relative to each other[56,58]. The whole leaflet is covered with a layer of endothelial cells similar to that coating the arterial walls[37,52]. This heterogenicity enables the leaflet to undergo large deformations during fluid-solid interactions[55]. The orientation of the ventricularis fibres results in a compliance that is three times higher in the radial than the circumferential direction[56]. Each leaflet has a coaptation region along its free edge, where the leaflets join together during closure, preventing back flow into the ventricle during diastole. These leaflets meet at a central nodule, known as a nodule of Arantius, halfway along the free margin, identified as a lunule[44,52].

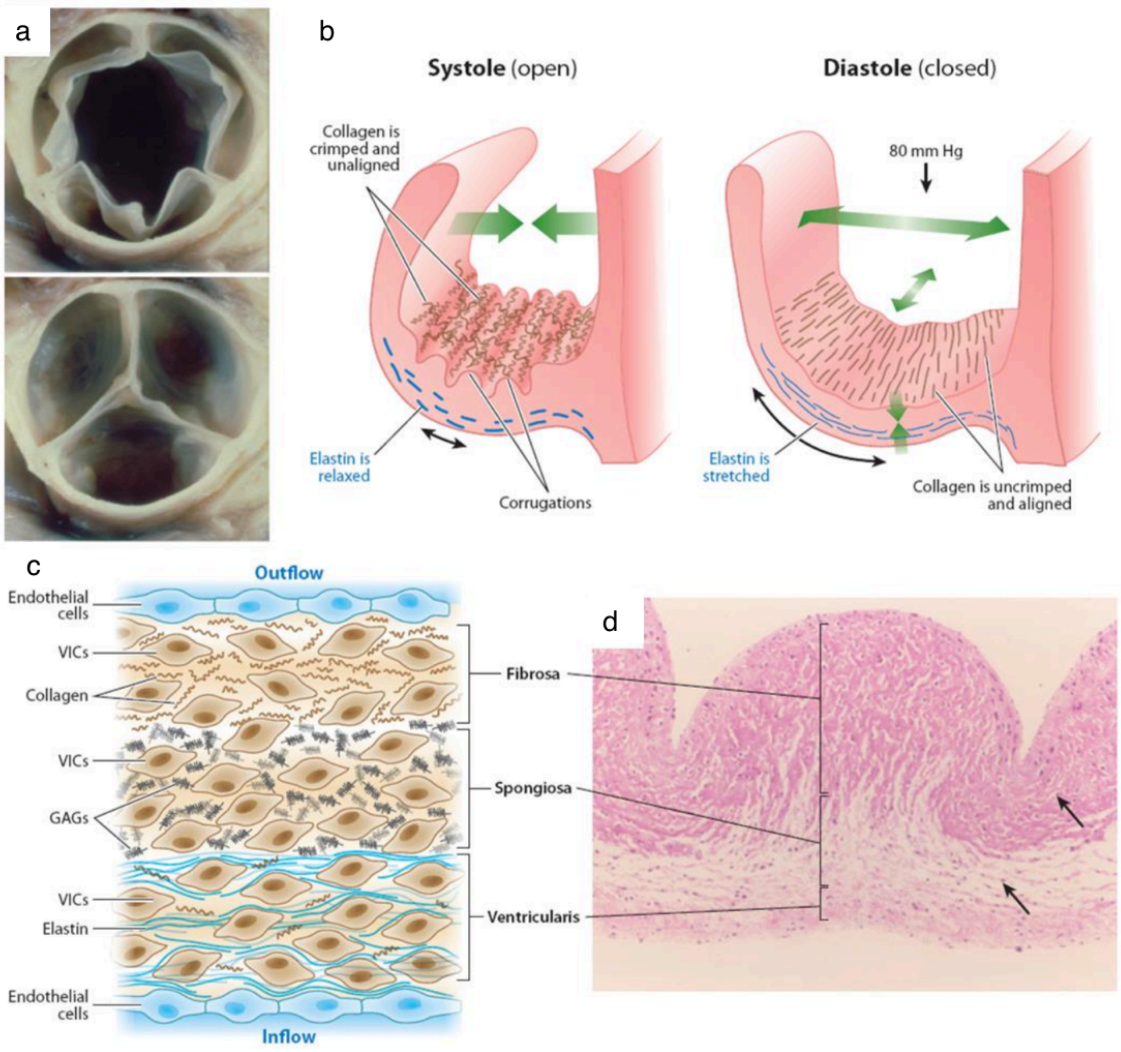

Figure 2-5: Aortic valve tissue structure. (a) systolic (top) and diastolic (bottom) transversal view of aortic valve; (b) schematic cross-section of leaflet cusp illustrating elastin and collagen in systole and diastole; (c) schematic of cellular and extracellular matrix architecture of leaflet, illustrating the ventricularis, spongiosa and fibrosa content; (d) low magnification photomicrograph of cusp cross-section during systole, with the outflow surface at the top. Image adapted from Schoen[57]

The angles of the up- and down-stream edges of the leaflets during diastole are typically within a range of 17 – 28 ° and 31 ° - 37 ° respectively in relation to the basal annulus, as illustrated in Figure 2-6, both of which change to a range of 89 – 99 ° in systole[45]. Leaflet angles of both the bottom and free edges change throughout the cycle, with the bottom edge angle, and the free edge angle varying between (with respect to the STJ) throughout diastole[45].

The shape of the orifice formed by the leaflet cusps during peak systole is not fully agreed upon in the literature, with some investigations reporting that the free leaflet edges form a triangular shaped orifice through which blood flows[59–61], whilst others describe a circular shape that tends towards a stellate outflow at lower blood flow or increased leaflet stiffness[29,62,63].

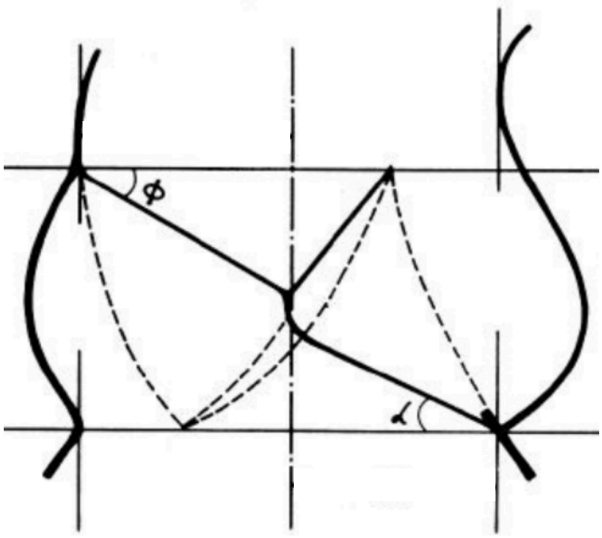

Figure 2-6: Up- (denoted by α) and down-stream (denoted by ϕ) leaflet edge angles of the aortic valve, as reported by Thubrikar et al. [45]

2.1.2.2 Aortic Tract and Sinuses of Valsalva

The SoV comprise of the bulges of the lumen downstream of the aortic valve forming three cavities, each positioned between a pair of valve leaflet commissures, as illustrated in Figure 2-3. The geometric proportions of the sinuses of Valsalva were initially considered as hemispherical[64], but this assumption was soon revised by Swanson and Clark[27], and more recently by Reul *et al.*[65], who studied the transverse and sagittal plane views of the sinuses in depth. The SoV fulfil a number of functions that promote improved cardiac health and efficiency, including: reduction of valve cusp wear, both via improved stress distribution[28] and prevention of cusp-wall impact[66]; promotion of superior haemodynamics within the root during systole[19,67]; modulation of the transvalvular pressure gradient[68]; increased opening of the aortic valve, especially at cardiac outputs above 5 l/min[68]; more efficient closure of the valve during diastole[37,40,67,69].

2.1.2.3 Coronary Arteries

The heart requires oxygenated blood to be supplied to its muscle tissue, and this requirement is fulfilled by the coronary arteries (CA)[40]. The left CA (LCA) and right CA (RCA) originate in two of the SoV as indicated in Figure 2-3(c) and are typically positioned just upstream of the STJ, although this position varies, and the CAs may be closer towards the basal annulus of the aortic valve or above the STJ[42,70]. Optimal CA flow relies upon the haemodynamics of the

aortic root[71,72], and the left CA is responsible for the blood supply of 75 % of the cardiac tissue, including the left ventricle[40].

If taken as a uniform diameter, typical CAs for a healthy adult male have a cross-sectional area of 4.8 mm^2 [73] after an initial ostium diameter of 4.1 ± 0.9 mm for the LCA and 2.8 ± 0.9 mm for the RCA[74].

2.1.3 Dynamics of the Healthy Aortic Root

Due to the cardiac cycle previously discussed in Section 2.1.1, there are four distinct stages that the aortic valve passes through – opening, open, closing, and closed. During valve opening, it is essential that the valve offers minimal resistance to the forward flow of blood, and that the leaflets reconfigure to provide the largest possible orifice area to conserve the optimum amount of pressure and energy within the forward flow[75]. At this point of the cycle, the majority of the valve resistance is related to the energy required to reverse the leaflet curvature of the shut configuration, as can be seen in Figure 2-5(a), and lowering the pressure difference required across the valve leaflets to achieve this results in reduced energy losses and lower levels of stress and strain across the leaflets[75].

Once the valve is fully open, the largest possible geometric orifice area (GOA) is desirable, in order to utilise as much of the aortic lumen as possible, again reducing energy losses. The GOA is defined as the smallest transversal section encompassed within the open leaflets at peak systolic pressure, but this is not directly related to the systolic performance of the valve. The effective dimension of the forward flow also depends on the contraction of the jet downstream of the GOA due to fluid flow through a constriction (i.e. from the ventricle through the aortic valve), the leaflet profile, and the size and position of the vortical structures found at the side of the central jet flow. As a result, a more indicative quantification of valve performance is the Effective Orifice Area (EOA), corresponding to the downstream point of the central jet flow's maximum contraction[76,77]. The EOA is inversely proportional to the pressure drop across the aortic valve and directly proportional to the systolic flow rate, and its measurement is fully discussed in Section 3.2.2.2. The pressure drop across the valve, and hence the fluid energy losses, may also be increased by the

presence of turbulence associated with non-physiological random blood velocity fluctuations[78].

There is agreement that the valve closes due to a combination of reverse transvalvular pressure, as the ventricular pressure begins to decrease, and the action of vortices in the SoV, the latter of which are reported to guide the shape of the leaflets during forward flow and valve closure[18]. The regurgitant volume of blood passing back into the ventricle and loss of energy during forward flow is reduced by the synergy of these two mechanisms working together. In a reflection of efficient valve opening, the stress experienced by the leaflet tissue and energy loss of the flow can both be reduced by diminishing the resistance of the leaflet when changing configuration from open to closed, due to the need to reverse the leaflet curvature. Once the valve has completed closing, a cause of reduction in valve performance may result from intravalvular leakage of blood though the closed valve back into the ventricle, typically due to incomplete coaptation of the free edges of the leaflet cusps[79], referred to as valvular incompetency.

In summary, the energy lost through valve dysfunction is associated with transvalvular pressure loss, related to the EOA, when the valve is open, and with regurgitation when the valve is closing or closed[80].

2.1.3.1 Characteristics of Blood

2.1.3.1.1 Rheology

Blood is a two-phased suspension of formed elements, primarily comprised of red blood cells (RBCs, deformable and non-spherical formed elements which transport and deliver oxygen and carbon dioxide), within plasma, an aqueous solution of organic proteins, molecules and salts[37,40]. These constituent parts are a major factor in the non-Newtonian nature of blood, and as a result the viscosity of blood varies with shear, temperature, RBC concentration (known as the haematocrit) and aggregation, as described in Figure 2-7, amongst other factors[37,40]. Blood viscosity tends towards 3.5 - 4.0 cP at a shear > 100 s^{-1} and a temperature of 37 °C, which is normally reached by the relatively fast flow of blood as it exits the aortic valve[81]. RBCs undergo reversible aggregation in low flow or static conditions, causing an increase in blood viscosity and a decrease in blood fluidity as these aggregations, known as rouleaux, form in the blood

stream, although a subsequent increase in the local shear forces may disperse these rouleaux[37,82]. Healthy endothelium, the cells lining the interior surface of blood vessels, senses and responds to the shear stress levels of the neighbouring blood, contributing towards maintaining the alignment and functionality of the endothelial cells[83]. RBCs do not usually interact with endothelial cells, but there are reports that RBCs may be incorporated into blood clots known as thrombi, detailed in Section 2.1.3.1.3, via activated endothelial cells and/or exposed sub-endothelial tissue[84]. Areas of abnormal Wall Shear Stress (WSS), more likely in the presence of flow altering rouleaux or thrombi, have been shown to predispose to atherosclerosis (the hardening of endothelium via the formation of plaques), plaque rupture, and vascular remodelling[85]. Endothelial cell damage is also associated with turbulence (chaotic velocity fluctuations) in the blood flow[85,86].

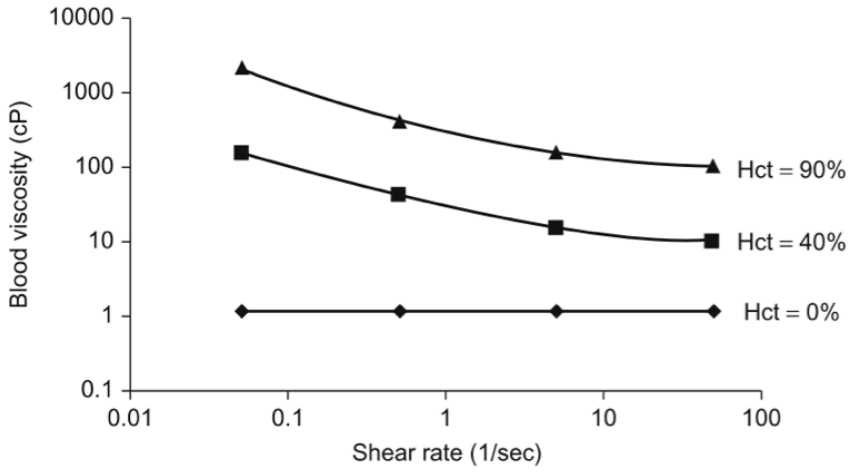

Figure 2-7: Variation of blood viscosity with haematocrit and shear rate[40]

2.1.3.1.2 Haemolysis

RBCs can be physically or chemically forced into rupturing and releasing their contents into the surrounding blood, and this destruction of the RBC is known as 'haemolysis'[83]. This may occur due to medical conditions such as the presence of specific bacteria, parasites, or auto-immune disorders, but is also strongly associated with the flow dynamics of the blood[87], with the presence of turbulence and the shear experienced by the blood flow both related to haemolysis[37]. The levels of shear rate and shear stress vary greatly within each cardiac cycle, and haemolysis is promoted at both non-physiologically high and low shear rates[33,88]. It is not yet agreed upon in the literature what the upper threshold for haemolysis is, measured *in* vitro to range from 150 – 520 N/m^2, or

whether turbulent viscous shear stress (related to the viscous dissipation of turbulent energy) or Reynolds shear stress (derived from the effect of convective acceleration upon the mean velocity profile) is more appropriate as a threshold identifying when haemolysis is likely to occur, but it is agreed that exposure of blood to a higher shear rate for a longer period of time will result in a greater level of haemolysis[37,89,90].

2.1.3.1.3 Thrombosis

Haemolysis raises the platelet activation levels of the blood[88,89], wherein platelets, another component of blood comprising of fragments of cytoplasm, change in shape and adhere to one another to form a plug[37]. Once this platelet plug is established, a fibrin mesh is produced over the formation, trapping white and/or red blood cells to harden the plug, known as a 'thrombus'[37]. Although this mechanism is vital in stopping bleeding in the case of ruptured endothelium, it may also lead to a myriad of pathological issues for the body, such as stroke or myocardial infarction, when the thrombus blocks the supply of blood to the brain or heart respectively[37]. Activated platelets, also associated with the formation of rouleaux, have been identified as the primary cells working via haemostasis and thrombosis to cause cardioembolism[87,91], and there is a growing opinion that the primary clinical problem associated with prosthetic heart valves is thrombosis, as opposed to haemolysis[86].

Thrombosis is described at a functional level by 3 platelet functions – adhesion, activation, and aggregation[83]. Adhesion is triggered when a thrombogenic surface, including most artificial surfaces, the subendothelial layers of blood vessels and fibrous plaques, is exposed to blood, and platelet membrane adheres to the uncovered surface[83]. The amount and type of non-native material the blood is in contact with strongly affects the degree of adhesion[92]. Activation occurs due to haemolysis, as previously discussed, but also at low to moderate shear rates, identified at shear stresses below 0.4 N/m^2 via *in vitro* and *in silico* studies, as platelets form thrombi in sizes inversely proportional to the shear forces of the local environment[82,88,92,93]. Incoming platelets may also be activated by passing through a cloud of thrombin that exudes from the clot[83], and turbulence of blood flow is associated with thrombosis[85]. The final function, aggregation, is caused by the release of fibrin causing the platelets to coagulate

and trap red and/or white blood cells within the mass. Exposure of tissue factor due to lumen injury or plaque rupture accelerates this process[83], and coagulability of the blood depends upon haematocrit and protein levels[92]. Virchow's triad translate these functions into pathophysiological mechanisms, describing 3 broad categories of factors that contribute to thrombosis – interrupted blood flow (resulting in stagnation or turbulence of blood), hypercoagulability (due to alterations to the biological constitution of blood), and endothelial injury/dysfunction (such as exposure to the sub-endothelium or foreign materials)[84].

As RBC aggregation promotes thrombogenicity, the importance of local blood rheology is evident in the maintenance of a healthy cardiovascular system[84]. The risk of thrombosis is decreased if a region is regularly washed out, with an RBC residence time below 10 s, determined *in vitro*, significantly reducing the chance of cell aggregation and blood flow speeds higher than 0.05 m/s associated with a drastic reduction in persistent stagnation[83,92]. Vortices shed from the valve leaflets during systole, discussed in more detail in Section 2.1.3.2, have an associated washout effect, reducing the extended residence of activated platelets within the SoV[92]. As thrombi grow, the chance of portions breaking away from the initial site increases, and their downstream migration may block cardiovascular vessels as the lumen bifurcates and narrows, starving areas of the body of oxygen and other nutrients, with potentially fatal consequences such as stroke or myocardial infarction[36]. Thrombi that remain attached to the valve leaflets have been linked to reduced leaflet motion, resulting in sub-optimal valve performance and increased flow separation[94].

2.1.3.2 Fluid Dynamics of the Healthy Aortic Root

The interaction between the leaflets and the structural/fluid dynamics that establish within the aortic root directly controls the correct operating function of the native healthy aortic valve[66,95,96]. An essentially radial flow causes the valve leaflets to open, moving from the coapted position towards the SoV, from where the flow follows the root wall and realigns with the root axis around the level of the STJ[97]. This results in the leaflets promptly assuming an open configuration, as the leaflets are pushed into the sinuses until they take a near circular orifice shape[55], as shown previously in Figure 2-5(a). A central jet flow with an almost

flat velocity profile enters the aortic root, with peak blood velocity measured *in* vivo to range from 1.1 to 1.7 m/s, accompanied by minimal regurgitant flow back into the ventricle during systole[55,98].

Due to the viscoelastic properties of the aorta, the pressure profile in the aortic root is shifted with a few milliseconds lag with respect to the pressure profile in the ventricle. This causes a backward flow pressure gradient to act upon the blood in the sinus, stabilising the leaflets to prevent over-extension, and aiding in valve closure[37,40]. It is worth noting that the root compliance and the shape of the sinuses of Valsalva both augment the GOA and modulate the transvalvular pressure gradient[68].

Healthy aortic root regions experience an average WSS of 13.3 N/m^2 at peak systole, ascertained via *in silico* investigation, with an increase in WSS towards the leaflet tips[79]. Oscillating shear stress at a magnitude lower than that experienced physiologically is associated with regions prone to atherosclerosis, resulting in a far more aggressive and proliferative phenotype[93]. As well as being associated with endothelial and blood damage and thrombosis as previously discussed, high levels of turbulence in blood flow leads to increased energy losses, as energy is dissipated in the turbulent fluctuations of the flow[99]. As the majority of aortic valve diseases occur on the downstream (i.e. aortic) side of the valve, this may be linked to the more unstable flow conditions and shear rates that are present, in contrast to the comparably more uniform and regular upstream ventricular flow[100]. Abnormal viscous shear stresses at the root lumen as a result of altered velocity gradients may change gene expressions, leading to endothelial remodelling and alterations of root geometry[101].

2.1.3.2.1 Fluid Dynamics of the Sinuses of Valsalva

The presence of vortices within the SoV during systole was first hypothesised and sketched out by da Vinci in the 15th Century[59], but the mechanism of formation and vortical dynamics throughout the cycle have not yet found consensus. Two mechanisms of vortical generation in the sinuses have been identified, depending on whether the angle that the leaflets form with the annulus basal ring is acute or obtuse, as illustrated in Figure 2-8 (a) i and ii[102]. When this angle < 90 °, the shear generated at the interface of the sinus and

forward flow leads to the induction of a vortex without any of the central jet entering the chamber, whilst if the angle ≥ 90 °, part of the forward flow detaches and recirculates into the chamber[102].

The propagation of this initial vortex and the generation of additional sinus vortices within the same systolic cycle also have not yet found consensus within the literature. Bellhouse & Bellhouse reported that the initial positive vortex generated by the forward flow of blood, with positive direction as defined in Figure 2-8(b), expands during systole, so that it dominates the late systolic flow and initiates valve closure, before dissipating away during diastole[18]. Subsequent studies have agreed with this mechanism, whether *in vitro*[18–21], *in vivo*[22–26], or numerical[27–31]. However, recent works based on *in vitro* testing using more advanced imaging techniques have identified more complex fluid flow phenomena, where the initial positive vortex generated during valve opening migrates away from the sinus cavity towards and beyond the STJ, and/or is replaced or accompanied by a negative vortex of lower strength, which remains in the sinus until valve closure, as illustrated in Figure 2-8 (c-f) [32–35],which has also been numerically identified[103].

Vortical presence in the sinuses in late systole and early diastole promotes washout of the blood, preventing stagnation at the base of the sinuses that could result in thrombosis and associated pathologies[29,30,104–106]. The location and size of these vortices affects the pressure within the sinuses, with optimal position aiding coronary flow and pressure gradient[30]. Equal distribution of vortical strength across the three sinuses helps prevent sudden early closure of the valve [19,100], and although axial pressure alone is sufficient to close the valve at the end of systole[55,100], the vortical behaviour around the physiological aortic valve can enhance swift and efficient closure[30,100]. The presence of the vortices in the sinuses also contribute to stabilise the leaflets' position during the forward flow phase, keeping them away from the aortic lumen[100]. The flow becomes more complex and less characterizable further downstream in the aortic arch[55].

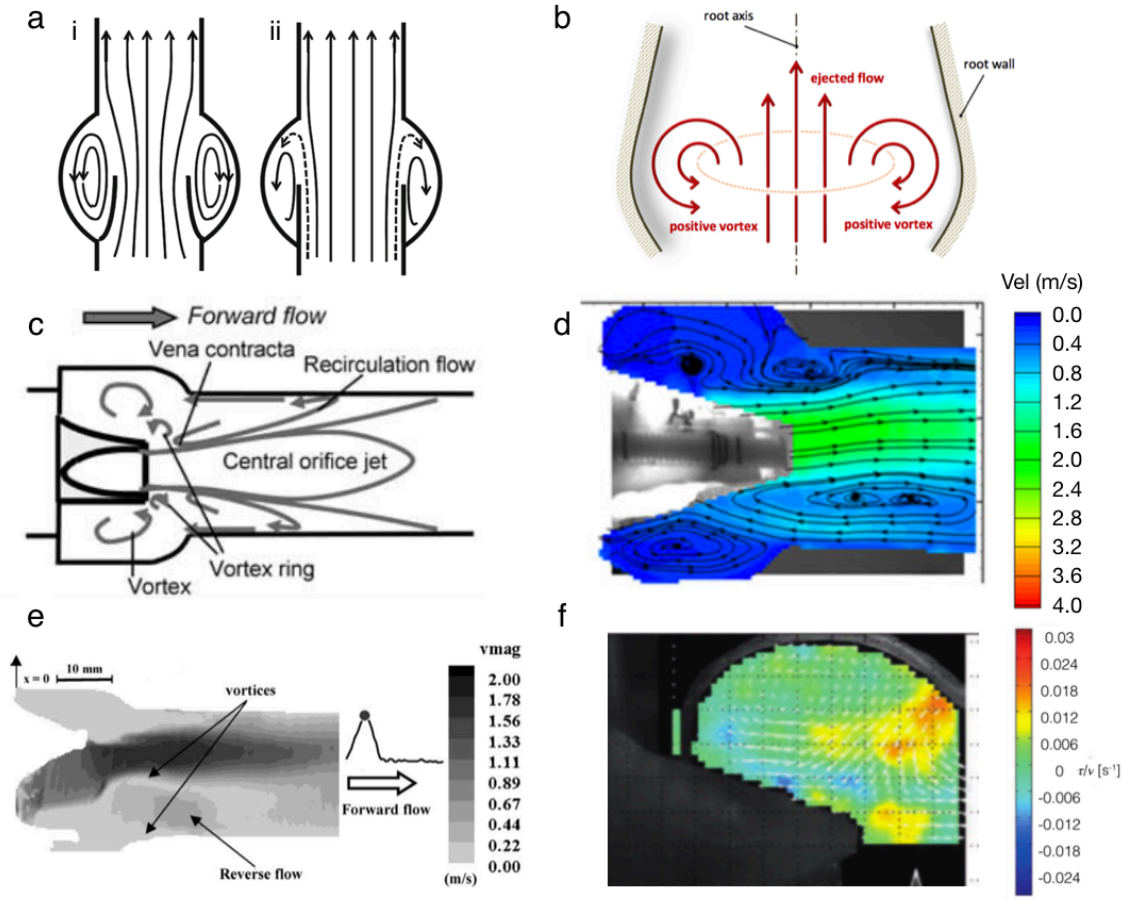

Figure 2-8: Vortices within Sinuses of Valsalva: (a) (i) vortex in sinus generated by shear forces of adjacent forward flow whilst in (ii) vortex caused by forward flow entering sinus after encountering sinotubular junction[102]; (b) initial positive vortex formed during ejection phase[107]; (c) negative sinus vortices[33]; (d) positive and negative vortices[34]; (e) vortex migrating downstream away from sinus[32]; (f) negative sinus vortex[35]

2.1.3.2.2 Fluid Dynamics of the Coronary Arteries

Although there is no significant difference in blood velocity between left and right CAs, the left CA is larger and provides the majority of the blood flow, combining with the right CA for a total flow rate, measured *in vivo*, of around 270 ± 82 ml/min (or 80 ml/min/100 g of heart tissue) at resting heart rate, slightly less than 5 % of the total cardiac output[108]. This flow rate increases as the demands and Cardiac Output (CO) of the heart increase, enabled by the coronary flow reserve[2,40,109,110], and is auto-regulated by myocardial demands[71]. The flow rate variation over the cardiac cycle is disputed, with some claiming that CA flow occurs primarily during diastole, with less than 15% of CA blood flow occurring during the systolic phase of the cardiac cycle, and the sinus vortex present during systole playing a large role in this reduced CA flow[27,40,71,109]. Other literature claims there is a reduced difference between

systolic and diastolic flow of the CA[66,95,111–114], as presented in Figure 2-9. The literature does agree that the flow consists of two peaks, one in systole and one in diastole, and the systolic peak in flow occurs due to the rapid rise in aortic pressure at the beginning of systole[115]. This flow reduces as the muscular tissue of the heart contracts fully, as this results in constriction of the CA[115]. As systole ends and diastole begins, this muscular tissue relaxes, widening the CA lumen and reducing the resistance in the vessels, leading to the second peak of the flow rate[115]. This flow rate peak is higher than the systolic flow peak, and after this diastolic peak flow gradually declines as the aortic pressure lowers throughout diastole[115].

The geometry of the SoV have been linked to affecting systolic flow, although with no direct effect upon the coronary flow reserve, whilst reduced turbulence in the sinus is hypothesised to result in a higher diastolic CA flow[116]. The pulsatile nature of CA flow dominates any secondary flows due to twisting, torsion or cyclic bending of the CAs during each heart beat[117,118]. The narrower diameters of the CAs compared to the upstream regions of the aortic root mean that the corpuscular properties of blood influence the local flow to a greater extent[119].

The literature has not reached a consensus on the effect of the CAs upon sinus fluid dynamics. Some literature reports that the low diastolic CA blood velocity is not related to the diastolic sinus flow[102]. On the contrary, there are reports that the presence/absence of the CAs may alter the sinus flow, predicated on previous reports of a greater tendency of the non-coronary sinus to calcify as a result of lower Shear Stress (SS), due to a lack of diastolic CA flow and increased opening of the coronary leaflets[72,120]. It is reported that due to blood flowing from the base of the sinus into the CAs, there is less stagnation at the base of these coronary sinuses, despite smaller vortices forming during systole[72]. Flow near the sinus wall is directed towards the CA rather than returning toward the root axis and STJ, resulting in increased washout of the sinus[72].

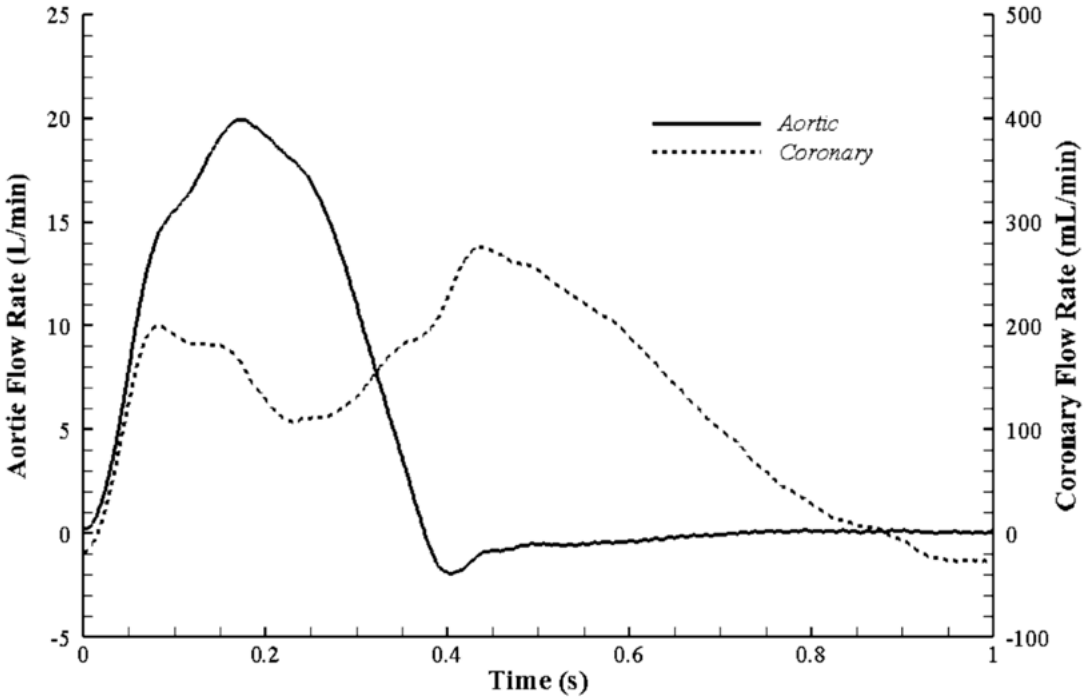

Figure 2-9: Flow rate within coronary arteries[72]

2.1.3.3 Mechanical stresses

The maintenance of the healthy mechanical properties and function of the tissues of the aortic valve and root is strongly related to physiological flow conditions within the region. In order to avoid high shear and bending stresses, which could degrade the tissue, adherence to the physiological opening and closing mechanisms described in Section 2.1.3.2 in conjunction with proper annulus expansion and contraction is vital[98]. The SoV play an important role in lowering flexural stresses[100] in the leaflets as the annulus expands and contracts through the cycle, at peak pressures of 120mmHg for a typical heart at rest. During systolic ejection, the contraction of the myocardial tissue of the ventricle causes the basal annulus to form a circular shape, increasing the GOA despite decreasing the perimeter, thus optimising the systolic flow[12]. Upon muscle relaxation in diastole, the annulus forms a 'D' shaped orifice, which maximises leaflet coaptation[12].

The fast reversal of the pressure gradient across the aortic valve during early systole causes the leaflets to open in a rapid transition[121], opening in a wave from the basal annulus through to the free edges of the leaflets[122]. The decrease in left ventricular pressure during late systole causes this pressure gradient across the valve to invert again, forcing the leaflets back towards

coaptation[121]. The closed leaflets stretch both circumferentially and radially, and this stretching improves the coaptation of the valve, reducing intravalvular leakage[98,123].

The stress-strain response of the leaflets' material to mechanical loading is highly non-linear, and can be described as a J-curve, as proposed by Cohn *et al.*[124]. The tissue initially produces a high amount of strain per unit of stress with an approximately linear stress-strain relationship, labelled as E_L in Figure 2-10(a), until reaching the transition phase of the J-curve, corresponding to a stiffening of the tissue, and the strain produced per unit of stress decreases. Further increase of stress to the tissue eventually produces another approximately linear stress-strain relationship, though with a much higher stiffness modulus than the initial linear region, labelled as E_H in Figure 2-10 (a) [124]. This J-curve behaviour can be ascribed to the properties of the collagen and elastin fibres in the extracellular matrix of the tissue[124]. During region E_L, the collagen fibres are still crimped to an extent, and the response of the tissue is primarily controlled by the stress-strain response of the elastin fibres as the collagen fibres are being straightened[124,125]. In the non-linear transition period, the collagen fibres, much stiffer than the elastin fibres, begin to take up more of the load as each collagen fibre becomes fully straightened[124]. Finally, in E_H all of the collagen fibres have been straightened and the strain response to increasing stress continues in a linear relationship in response to the stretching of both the collagen and elastin fibres, until the tissue fails as the elastin and collagen fibres rupture[124,125].

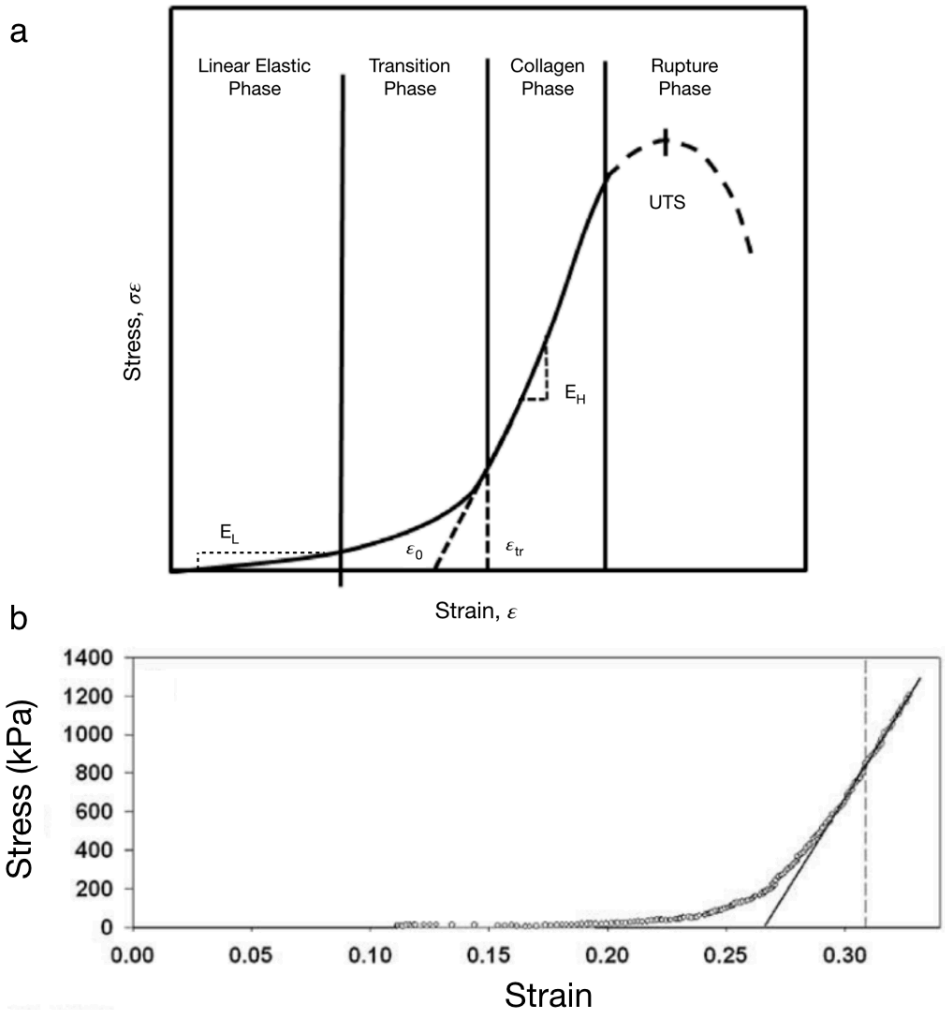

Figure 2-10: Stress-Strain response of native aortic valve leaflets: (a) J-curve presented by Hasan et al. *as a description of the stress-strain behaviour of soft tissues*[125]*; (b) stress-strain response of human aortic valve leaflets, with linear E_H region super imposed*[55]

2.2 Pathologies

2.2.1 Calcific Aortic Stenosis

Aortic stenosis is a degenerative blockage of the blood flow through the aortic valve, and is the most frequent heart valve disease in the western world, affecting 2-3 % of the population above the age of 65[4] and 10 % those above 75[5], and is forecast to increase in prevalence alongside ageing populations in the next 20 years[2,3]. Aortic stenosis can be congenital, acquired, or a combination of both. Congenital stenosis is usually associated with a bicuspid aortic valve, where two of the aortic valve leaflets, typically the left and right coronary leaflets, fuse together and inhibit the performance of the valve,

increasing the susceptibility to calcification[63]. The vast majority of acquired aortic stenosis in Europe and the US is due to calcification of the valve leaflets, stiffening the leaflet to diminish its GOA during systole and preventing complete coaptation of the valve during diastole, increasing intravalvular regurgitation[63]. Current pharmacological treatments of calcific aortic stenosis are unable to reverse or prevent the progression of the pathology, and as such are limited and palliative[6].

2.2.1.1 Cause

A typical stenosis progresses via calcification of the aortic side of the leaflet, initiated in the basal part and extending further, with the commissures affected to a lesser degree[126,127]. Mechanical damage as a result of endothelial stress allows lipids and inflammatory cells into the leaflets, oxidation of which leads to further inflammation and the secretion of proteins (profibrotic cytokines)[3]. These cytokines differentiate connective tissue cells (fibroblasts) into a more muscle-type cell (a myofibroblast), causing disorganised fibrous tissue to accumulate, thickening and stiffening the leaflet[3]. Differentiation of these myofibroblasts into bone-synthesising cells (osteoblasts) causes accelerated calcification, and the formation of these osteoblasts may be accelerated by regions of inflammation around calcific deposits[3]. This calcification thickens and stiffens the leaflet, reducing the leaflet mobility, increasing the jet velocity of the blood flow, and narrowing the geometric orifice area of the valve[3]. Although initially believed to be a passive pathology, due to age-related wear and tear of the leaflet, contemporary studies indicate that it is not simply a degenerative process, showing that aortic valve calcification results from active inflammatory processes, and can be mediated or accelerated by haemodynamic factors[128]. Altered mechanical stimuli on the aortic valve leaflets may lead to deposition of lipoproteins, inflammation of valve tissue, culminating in the expression of bone-related proteins and calcification of the leaflets[128], and areas of leaflet calcification correspond to the sites of greatest flexion stress and strain combined with osteogenic/proinflammatory signalling[129]. The calcification process may also be accelerated by genetic expression and in the presence of certain enzymes, such as angiotensin-converting enzyme and angiotensin II[3,130]. In addition, the aortic side of the valve is more associated with leaflet

calcification, which may be related to the complex and highly dynamic shear stress field on this side of the valve, characterised by low magnitude and a high degree of unsteadiness[3,128,131], and studies have shown an increased density of calcification lesions in these regions of highly heterogeneous shear stress fields[132]. This is reinforced by evidence of increased calcification of the non-coronary sinus, which probably experiences lower SS as a result of no diastolic CA flow[72,120].

2.2.1.2 Resultant Fluid Mechanics

In response to the increased pressure afterload and WSS as a result of aortic stenosis, the wall thickness of the left ventricle increases to restore WSS and preserve left ventricular function[3]. Increased thickness reduces wall compliance and impairs both systolic and diastolic function[3]. The severity of the stenosis is classified as mild, moderate or severe, as shown by the parameters in Table 2-2, with the primary assessment method being catheter-based pressure measurements, with an increased severity of stenosis usually indicated by an increased transvalvular pressure drop[85], as shown in Figure 2-11. Other methods to assess stenosis severity have also been developed, primarily involving echocardiography to determine the GOA[133,134]. There is an increasing need for valve replacement as the severity increases, although it is worth noting that the measurements of these parameters are limited by non-uniformity of flow rates across different patients[135].

Stenosis severity	*GOA (cm^2)*	*ΔP (mmHg)*	*Peak Jet Velocity (m/s)*	*Velocity ratio (LVOT:AV)*
Mild	1.5 – 2.0	< 20	2.5 – 3.0	> 0.5
Moderate	1.0 – 1.5	20 - 40	3.0 – 4.0	0.25 – 0.5
Severe	< 1.0	> 40	> 4.0	< 0.25

Table 2-2: Effect of Severity of Aortic Stenosis. GOA – Geometric Orifice Area; ΔP – transvalvular pressure drop; LVOT – Left Ventricular Outflow Tract; AV – Aortic Valve. The velocity ratio indicates how much the flow is accelerated due to passing from the LVOT through the narrower AV, with a smaller number indicating more flow acceleration[136]. All measurements were taken in vivo.

The effect of the stenosis upon the aortic root shape is shown in Figure 2-12, with increasing stenotic severity resulting in a more exaggerated bulge whose maximum diameter is located further downstream.

Due to the increased leaflet stiffness as a result of calcification, the haemodynamics of the root degrade, with less complete closing of the valve and a reduction of the EOA[100]. As the stenosis' severity increases, the peak velocity of the central jet flow increases due to a reduction in jet cross-section diameter and some return flow back through the valve even at peak systole[98], as illustrated in Figure 2-13 - for a reference STJ diameter of 2.5 cm, a mild stenosis causing a GOA of 1.5 cm^2 (as opposed to 2.5 cm^2 for a healthy condition) results in a transvalvular pressure drop of up to 20 mmHg and an increase of peak jet velocity increases by up to 70 % compared to the healthy condition[137,138], established from *in vivo* measurements.

The altered velocity properties of the flow elevate the levels of SS and turbulence in the region, increasing the probability of damage to the root walls and to the blood itself[138]. The different levels of calcification on each leaflet mean the jet is asymmetrical and typically inclined, resulting in complex conditions specific to each patient, a situation further complicated by the surface irregularities of calcified leaflets[100].

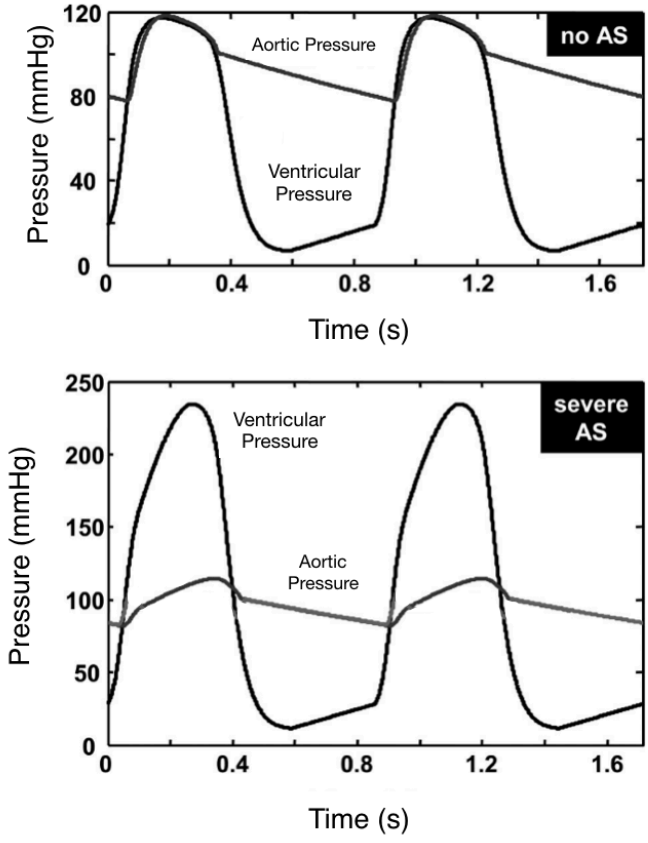

Figure 2-11: Effect of stenosis upon aortic root pressures. A much higher ventricular pressure is required to transfer an equivalent amount of energy to the aortic flow as the healthy condition [image adapted from [139]]

As the stenosis becomes more severe, the pressure drop across the aortic valve may rise above 40 mmHg with a corresponding drop in EOA to beneath 1 cm^2, accompanied by a further decrease in outflow jet diameter at the aortic annulus, leading to a peak velocity greater than 4 times that of the healthy condition[100,137]. The numbers of regions of flow separation around the central jet increase, accompanied by fluctuating shear layers forming between the fast flow and the root walls, potentially causing damage to RBCs and platelets in the flow and to endothelial cells in the aortic walls[100]. As well as elevating the incidence of thrombosis and thromboembolism, the changes in WSS can lead to dilation of the ascending aorta, and the increased force of the higher velocity central jet can, over time, weaken the distal portion of the ascending arch, potentially resulting in aneurysm[138].

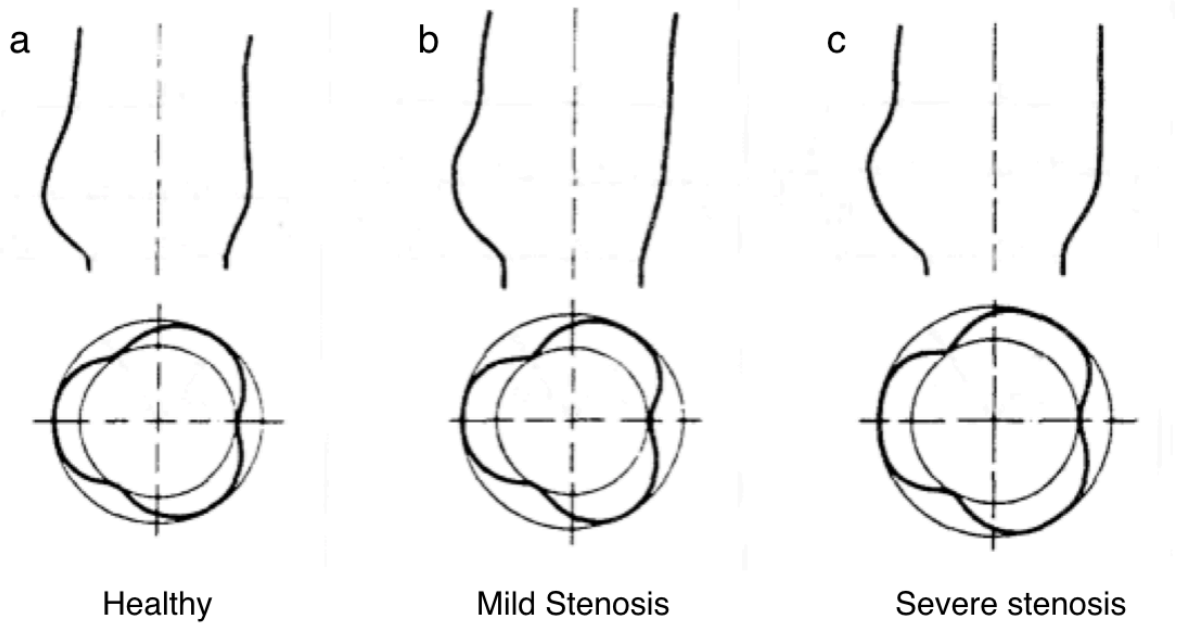

Figure 2-12: Effect of stenosis severity upon aortic root geometry, showing a sagittal cross-section of the root of (a) a healthy aortic valve; (b) a mildly stenotic aortic valve; (c) a severely stenotic aortic valve[65]. Increasing stenotic severity results in a more exaggerated bulge whose maximum diameter is located further downstream.

Even simplified numerical studies have shown that the flow behaviour in the sinuses becomes significantly altered, with the vortices becoming bigger but less intense, and being located further from the leaflet tips soon after generation[79]. As a result, rather than being trapped within the sinuses during valve closing, these vortices disappear during late systole[79]. Coronary flow decreases as leaflet stiffness increases, possibly linked to this reduction in sinus flow recirculation[105].

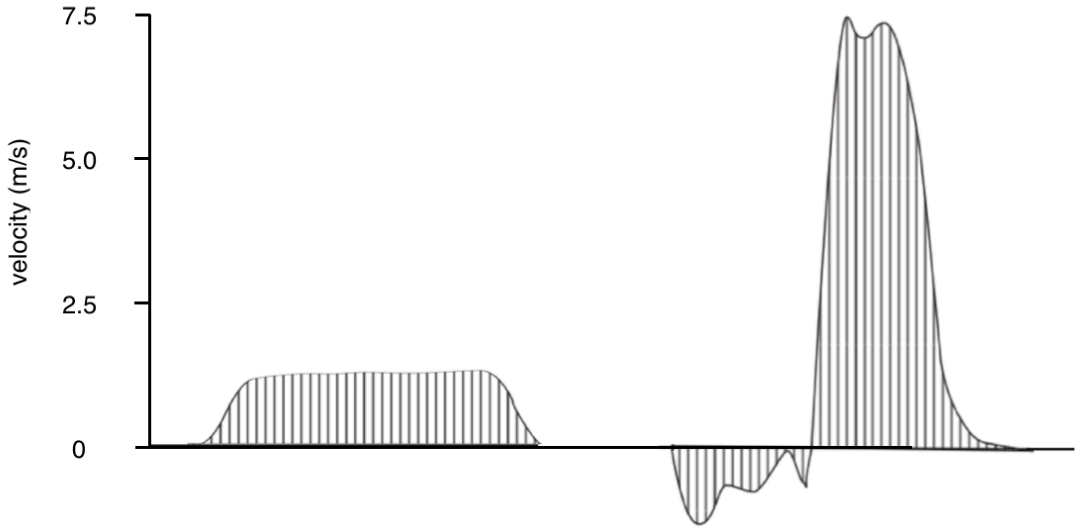

Figure 2-13: Effect of stenosis upon aortic valve velocity profile at the sinotubular junction, adapted from Yoganathan et al.[140]

2.2.2 Root Dilation

Dilation of the ascending aorta is responsible for 50 % of all thoracic aneurysms and can be sub-categorised into easily operable "supra-valvular aortic aneurysms" downstream from the STJ, and "aortic root aneurysms" which require sparing or replacement of the aortic valve[141]. As previously noted, the diameter of the aortic root region naturally increases by about 0.5 % /year in the STJ and sinuses from the age of 40[47,142], but it can also become dilated due to connective tissue diseases, such as Marfan's disease or Ehlers-Danlos syndrome[143]. Root dilation is also associated with aortic stenosis, as can be seen in Figure 2-12, especially of bicuspid aortic valves[65,141,144], and is most likely linked to aortic wall pathology than any dysfunctional valve based haemodynamics[143,144]. Aortic dilation can lead to aortic rupture, which could be catastrophic for the patient, and increased dilation leads to increased wall tension, increasing the likelihood of rupture[85,141,144]. Replacing a defective aortic valve can retard the rate of dilation, as can treatment with β blockers[85,141,144]. During annuloaortic ectasia, a proximal dilation of the ascending aorta characterised by expansion of the root and usually sinus diameter, the leaflets themselves don't necessarily show signs of abnormality other than rolling of free edges, which is an indicator of regurgitation[127]. The presence of aortic regurgitation, or insufficiency, is often associated with the extent of the dilation, due to increased pulse pressure[141]. Interventionist surgery is recommended if

the dilation of the ascending aorta exceeds 55 mm with no other linked pathologies, if it exceeds 50 mm with a diagnosed connective tissue disorder, or if it exceeds 45 mm and the patient has already received aortic valve surgery[143]. Surgery is also recommended if there is growth of the dilation in excess of 1 cm/year despite treatment with β blockers[141]. Surgical intervention either involves remodelling the root, or reimplantation of the aortic valve into a replacement graft[23,43]. Remodelling does not address the dilation of the root as effectively as replacement, but preserves the geometry of the SoV better[141], with the possibility of decreased valve deterioration in the long term[43].

2.2.2.1 Resultant Fluid Mechanics

The dilated aortic root causes numerous deleterious changes to the fluid dynamics in the volume, with much more positional change of enlarged vortical structures that develop alongside and deflect the central jet-like flow during systole[22,145]. Dilation by a third has been shown by *in vivo* research to potentially double the time taken for the valve to fully close[145], indicated by *in silico* studies to increase leaflet stress by 150%, and decrease leaflet coaptation by 8%, increasing regurgitant flow during diastole[146]. Marfan's syndrome has been connected to an increase in the stiffness of the root walls, and, a technique called pulse wave velocity can be used to assess the wall stiffness and, consequently, the progression of dilation[85].

2.2.3 Coronary Disease

Coronary artery disease is a major cause of death in the western world, with approximately one third of people dying as a result of CA disease, and the vast majority of elderly people having some disfunction of the coronary circuit[2]. The most common cause of CA disease is atherosclerosis[40], a hardening of the arteries, which primarily builds up in the side branches and on the inner curvature of the CAs, and it is linked to local low WSS[118,119]. This impairment of the CAs leads to the heart producing an increased systolic flow, in order to maintain the coronary blood flow at a similar level to that of a healthy coronary system, until the CA impairment is so severe that the heart can no longer adequately compensate, and CA flow reduces down to around two thirds that of the healthy condition[109,110,147].

Reduction of the flow in the CAs results in cardiac muscle tissue death (myocardial infarction), and can lead to any or all of the following: reduction in CO; increase in cardiovascular pressure due to blood pooling in veins; fibrillation of ventricular tissue; cardiac tissue rupture[40]. As the flow to the CA decreases, fluid dynamics within the associated SoV will become more reminiscent of those observed in the non-coronary sinus, increasing the likelihood of leaflet calcification and thrombosis due to lower SS in the region[72,120].

2.3 Valve Replacement Treatment

When the performance of the native aortic valve diminishes to a critical level, prosthetic implants can be utilised to restore the functionality of the region. The devices available for implantation have been developed over the last 7 decades, and have been split into three categories for clarity of explanation – mechanical valves, consisting of rigid manufactured materials such as pyrolytic carbon and metals, and displaying outstanding durability[148], requiring open heart surgery for implantation; Surgical bioprosthetic valves, utilising tissue harvested from typically bovine or porcine sources, mimicking the native human aortic valve, and requiring open heart surgery for implantation; Transcatheter valves, again utilising porcine or bovine tissue designed with similarities to the native human heart, but able to be crimped and implanted into the patient without the need for surgery.

2.3.1 Mechanical Aortic Valves

The first implant of a mechanical prosthetic heart valves was by Hufnagel in 1952[149], and was followed by the Starr-Edwards caged ball valve in 1960[150,151]. A sphere is pushed into a retaining cage by the forward flow of the blood, creating a gap between the valve housing and ball through which the blood flows, until the reversal of pressure and flow during diastole cause the ball to return and occlude the housing orifice, preventing regurgitation of blood back in the ventricle[33]. The durability of the cage-and-ball valves is countered by some obstruction of the blood flow by the ball in forward flow, leading to large recirculation/turbulent regions around the axis of the aortic root, as illustrated in Figure 2-14. This results in a large transvalvular systolic pressure drop[33], and the relatively large size of the valve makes it impractical for implantation in

many patients[150,151]. Almost 20% of the blood flow velocity is lost within 30 mm of the annulus before passing through the wake of the ball and cage, leading to a high velocity gradient and turbulent SS measured *in vitro* to be as high as 350 N/m^2, well above the threshold for platelet activation[33].

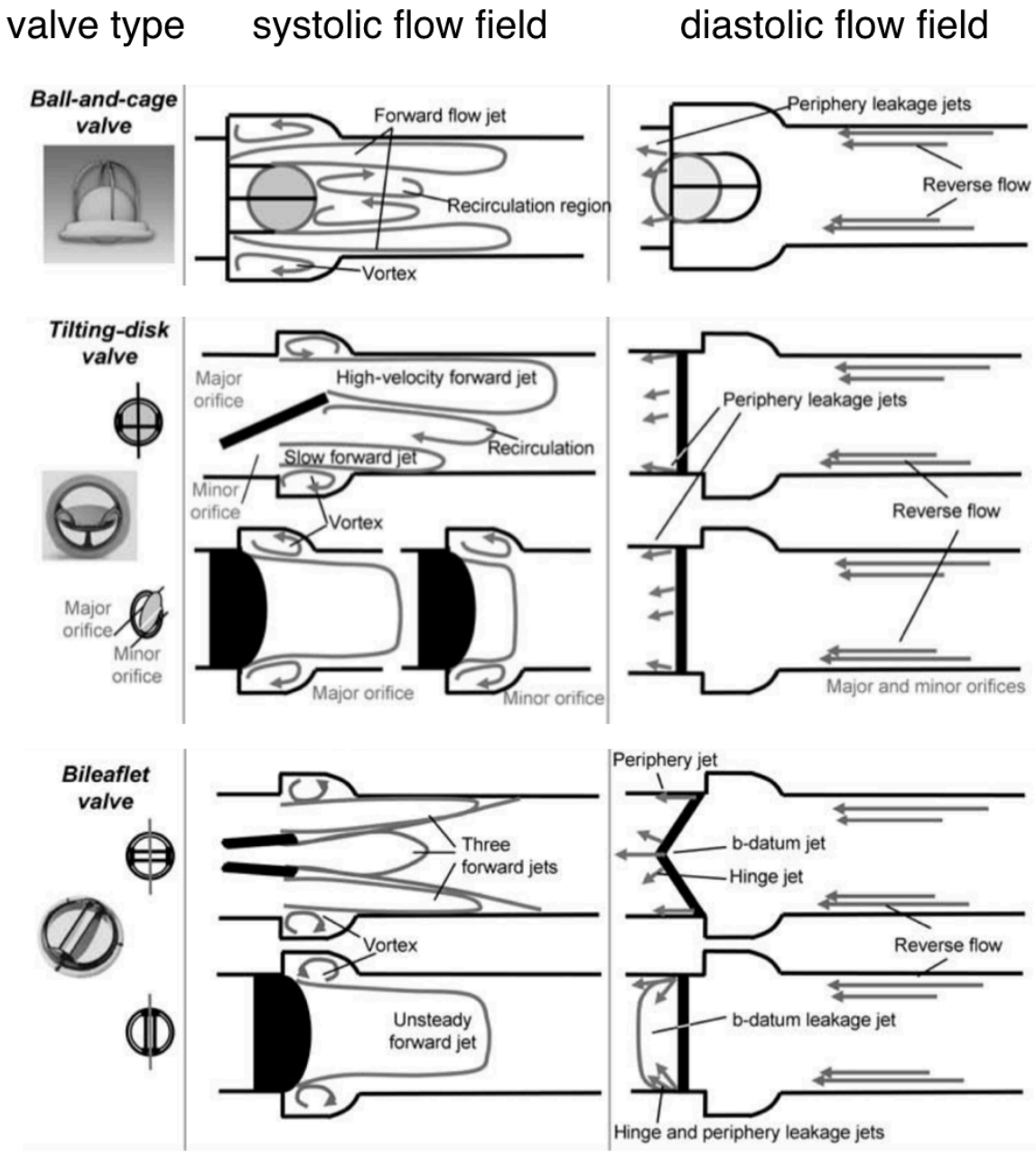

Figure 2-14: Mechanical valve flow diagram during systole and diastole[33]

The second generation of mechanical valves were soon developed, with caged disc and flap disc designs leading into Bjork-Shiley's tilting disc valves in 1967[150,151]. These valves reduce flow abnormalities compared to ball-and-cage valves by having a free-floating disc (reducing contact-based wear) acting as an aerofoil when in the pre-determined open position, between 60 ° and 80 ° relative to the housing. This creates two differently sized orifices for the blood to

flow through, resulting in a larger EOA than in the ball-and-cage design[140,150,151]. Turbulent SSs have been measured *in* vitro to peak at 150 N/m^2 and are typically located at the edge of the major orifice jet, whilst a recirculation region occurs in the sinuses[33]. However, the flow profile generated during systole still has a central recirculation region (although generally reduced from the ball-and-cage design) resulting from a fast and slow forward flow jet emerging from the large and small orifice respectively[33], as presented in Figure 2-14.

The third and most recent group of mechanical valves are bi-leaflet valves, introduced by St Jude Medical Inc. in 1978[152]. Bi-leaflet valves provide improved uniformity of the flow profile, closer to physiological flow[151], as shown in Figure 2-14, with the blood passing through a large central orifice with two smaller semi-circular orifices alongside[33], and the interior positioning of the leaflets reduces the chance of interference with any other architecture in the aortic root[151]. This results in a larger EOA than the tilting disc design, although a larger regurgitant volume means that the valve still suffers from inefficiencies[140]. The recent On-X valve, by the Medical Carbon Research Institute, features leaflets with a similar length-to-diameter ratio to native aortic valve leaflets that open to 90° relative to the valve housing[33]. However, as with all mechanical valves[33], thromboembolytic complications are a major concern, with lifelong anti-coagulation medication necessary for the patient[151,153,154], alongside a degree of leakage back through the closed valve via gaps at the join of the leaflets, the join of housing and leaflet, and possibly the leaflet hinges[33,140,151]. This leakage is an inherent part of the valve, designed to provide washout of the valve to reduce thrombus formation, but can occurs at stress magnitudes that cause damage to RBCs[155], and led to the withdrawal of some devices from the market due to severe thrombosis around the hinges[33]. The flow through the smaller side orifices is slightly faster than the central orifice flow[36], with a peak turbulent SS measured *in vitro* to be as high as 150 N/m^2 similar to that of the tilting disc[33]. Flow patterns in the aortic root are complex, with two recirculations observed in the sinuses, and counter vortices forming in the way of the leaflets at peak systole, degenerating into a chaotic flow field during late systole[156]. There are reports that rigid leaflet valves will also suffer from cavitation, causing damage to the valve itself, leading to a loss of functionality, alongside potential clot formation and detachment arising from damage to the RBCs, which lead to

thrombotic complications, platelet activation, and haemolysis[33,140,151,153,157]. However, this cavitation may be due to analysis of valves after *in vitro* testing, with non-physiologically low pressures and viscosities causing cavitation which has not been reported from explanted *in vivo* mechanical valves.

Polymeric heart valves, made from synthetic materials but replicating physiological haemodynamics, have been used in the short term with assist devices, but shortcomings in valve design and/or material properties have meant that long term implantation has not yet been achieved[151,158]. Susceptibility to calcification, hydrolysis, and oxidation lead to increased occurrence of leaflet malfunction and premature failure[159]. Investigations using high-cycle test machines indicate that the durability and lifetime of these polymeric heart valves are both increasing[159]. Modification of the polymers used can bestow beneficial properties to the valve, such as reduced thrombosis (via addition of cholesterol-modified polyurethane) or improved biocompatibility and durability (via the incorporation of nanomaterials)[159].

2.3.2 Surgical Bioprosthetic Aortic Valves

The first bioprosthetic heart valves were homografts, using antibiotic- or cryo-treated aortic valves from donors to replace the diseased aortic valve, first performed in 1962, whilst the 'Ross procedure' dates from 1967, and involves an autograft of the patient's pulmonary valve in place of the disease aortic or mitral valve, alongside a homografted pulmonary valve - both have satisfactory outcomes but are totally dependant upon donor supply[33,150].

A technique using gluteraldehyde (GA) to fixate tissue developed by Carpentier in 1969 improved the stability and inertness of biological tissue, enabling the use of xenograft tissue combined with mechanical structures to create valves based upon the native human heart valve, with much lower thrombogenicity than their mechanical counterparts, although this treatment leads to a higher likelihood of leaflet tearing or degeneration[33,160]. Porcine tissue mounted on a rigid support (called a stent) was introduced in 1970 in the Hancock Porcine Xenograft, which remains in use today, later joined by the Carpentier-Edwards Bioprosthetic, brought to market in 1976[33]. The flow profile is much more similar to that of a native valve's flow profile than those of the mechanical valves, although representative of a mildly stenotic valve, due to porcine tissue

stiffness, leaflet fixation, presence of a stent, and restriction of movement[140,161]. This results in a decrease in EOA and a larger pressure drop, although the turbulent SS does not exceed the threshold for damaging RBCs[140]. The size similarities of porcine valve leaflets to human valve leaflets enable them to be used ready formed in the xenograft valve, although a large amount of valves need to be obtained to ensure size matching and quality[33].

In order to mitigate these supply issues, and dissatisfied with the haemodynamic performance of available porcine valves, attention turned to pericardial bovine tissue, with the Ionescu-Shiley pericardial xenograft introduced to clinical practice in 1976[162,163]. This valve consisted of GA-fixed bovine pericardium sutured to a titanium frame with a Dacron® coating[162]. However, although initial valve performance was good, progressive structural deterioration within a few years of implantation led to this valve being withdrawn from clinical use by the late 1980s[164]. After a lengthy developmental period, the Carpentier-Edwards pericardial valve was brought to market in 1991, with the pericardial tissue offering improved haemodynamics than the porcine valvular tissue, with a higher EOA, lower pressure drop, and turbulent SSs measured *in vitro* to be < 100 N/m^2, due to reduced tissue stiffness and an improved downstream flow profile[33,140]. There is a degree of regurgitation in all stented bioprosthetics[140].

Increasing the valve orifice, reducing stress at the leaflet-stent attachment, and reducing forward flow obstruction is achievable by removing the stent altogether, made possible by further improvement to tissue fixation techniques in the 1990s and requiring specific matching of patient root and valve geometry[140,161]. Initially designed for full or partial root replacement, the second generation of stentless bioprosthetics, the Shelhigh Super Stentless aortic porcine valves, enabled insertion into a calcified region via suturing of a flexible ring at the base of the valve alongside attachment of the commissures of the valve leaflets to the aortic wall[161]. A pericardial equivalent, the Sorin Pericarbon Freedom, was introduced in 1990, combining ease of implantation with high haemodynamic performance[161], although no improvement in long-term durability has been proven so far[154].

Contemporary bioprosthetic valves usually have leaflets constructed out of GA-fixed porcine or bovine tissue[12], making them vulnerable to leaflet calcification,

which would cause valve stenosis with associated raised transvalvular pressure drops and peak blood flow velocity[140]. The bioprosthetic tissue includes residual antigens from the xenogenic source, which can elicit an immune response from the patient the valve is implanted into, especially younger patients with stronger immune systems[165]. After the host's antibodies enter the leaflet tissue matrix, macrophage deposition, collagen breakdown, and calcification follows, linking the patient's immune system to the presence of calcification[165].

Use of polymeric leaflets to reduce this risk of calcification tends to result in more constricted outflow orifices, with a similar end result to the stenotic valve[32], whilst the polymeric leaflet edge acts as sharp flow separator, increasing residence time of RBCs in the resultant stagnant regions, correspondingly raising the thrombogenicity of the volume[83].

Whilst the resultant fluid dynamics within the aortic region following surgical implantation with a bioprosthetic valve are more similar to the physiological condition than after implantation of a mechanical valve, as presented in Figure 2-15, there are still differences from the native state[75]. The valve frame and implantation strategy result in a shape and positional mismatch between the aortic root and the prosthetic leaflets, and the frame thickness and the valve's sewing ring and pledget-armed sutures, that enable long-term fixation of the prosthetic at the basal annulus, all reduce the GOA[166]. The increased stiffness of the GA-fixed tissue and the man-made commissures of the prosthetic may also affect the flow in the aortic root, with possible alterations to the vortical dynamics and stagnation regions in the SoV[167]. These factors contribute towards producing a valve performance characteristic of a mildly stenotic native valve, characterised by increased peak jet velocity and transvalvular pressure drop, accompanied by a corresponding reduction in EOA, when compared to that of a native valve in the same size aortic root[140].

The forward flow has a relatively flat velocity profile[32] and high distribution of flow, dissipating rapidly downstream of the valve, with velocities higher than in the healthy native valve, reported from *in vitro* research to peak between 2 and 3 m/s[140]. This flat profile becomes parabolic around 45 mm downstream of the valve orifice, reattaching to the aortic wall further downstream[32]. Stented bioprosthetic valves tend to have recirculation regions downstream of the stent posts near the aortic wall, with *in vitro* measurements indicating systolic

recirculation fluid speeds of up to 0.6 m/s and SSs of up to 450 N/m^2 in the shear layer between the central jet and the slow flow and at the trailing edge of the leaflet[32], although many modern devices never exceed 100 N/m^2[140]. Early diastolic recirculation velocities can be as high as 0.4 m/s, but peak fluid velocity is generally no more than 0.04 m/s during diastole[32]. The lack of drainage (that the coronary arteries would otherwise provide) results in increased blood residence time on the non-coronary sinus leaflet of surgical bioprosthetic aortic valves, with the associated increased risk of calcification and thrombosis[167].

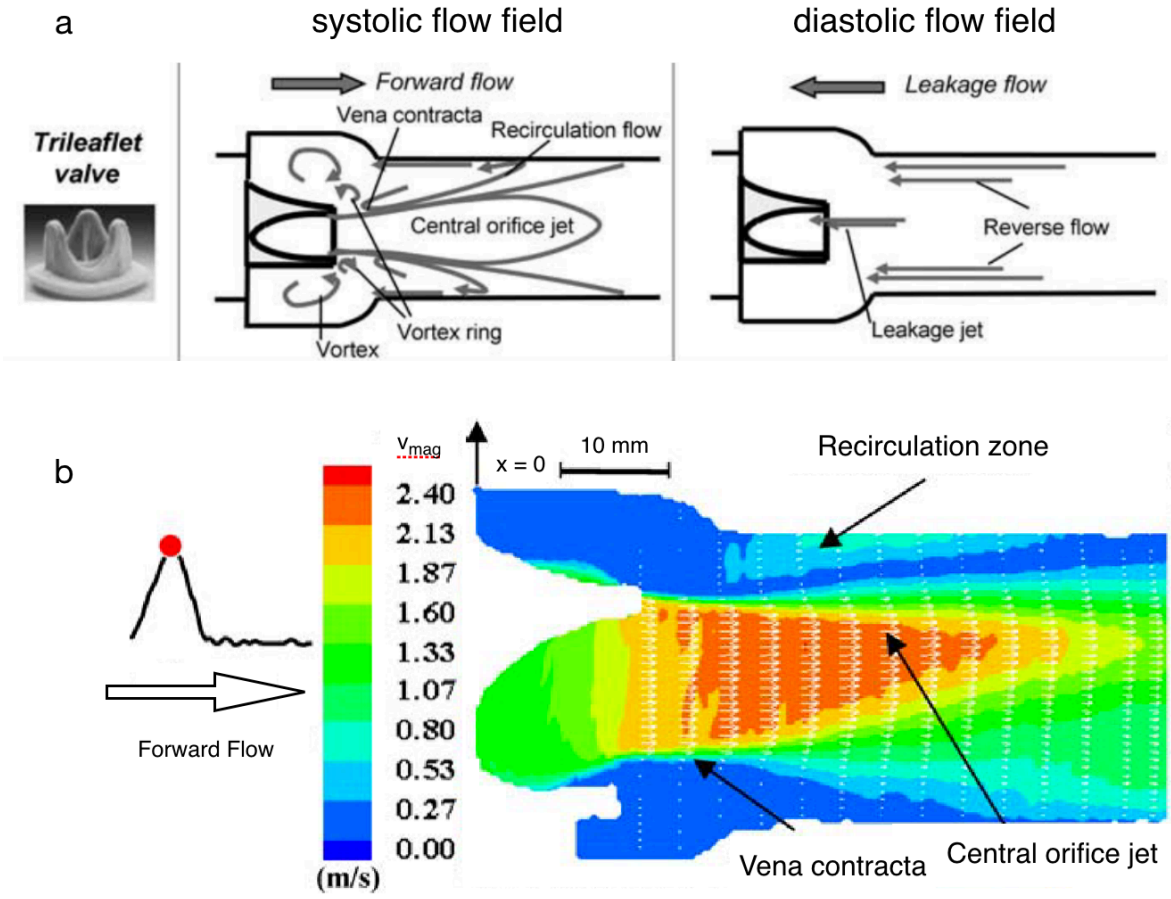

Figure 2-15: Flow field of surgical tri-leaflet aortic valve replacement: (a) summary of flow field during systole and diastole[33]; (b) PIV derived velocity field at peak systole[32]

Stentless bioprosthetic valves display improved performance, offering less forward flow obstruction and superior haemodynamic performance when compared to their stented equivalents[140]. However, their manufacture and surgical procedure are both more complex and costlier, and their performance is more affected by irregularities of the host anatomy (which may distort the shape of the valve away from the ideal) and procedural inaccuracies, due the

absence of a supporting stent which would otherwise enforce a regular circular configuration[140]. However, when suitable for the host anatomy, stentless valves produce flow velocities closest to the healthy native condition, with improved coronary flow compared to their stented equivalent, with a lower transvalvular pressure drop and decreased turbulence downstream from the valve[71].

2.3.3 Transcatheter Aortic Valves

A major drawback of the mechanical and bioprosthetic valves presented so far is the necessity of invasive surgery to remove the old, diseased valve and insert the new prosthetic valve, with up to a third of patients deemed ineligible for surgery due to advanced age and/or pre-existing illness[10,11]. A minimally invasive technique, drawing upon the experiences of balloon aortic valvuloplasty in the 1980s wherein a stenotic aortic valve is widened using a balloon catheter inside the valve[168], has been developed and performed since 2002[6], wherein a transcatheter aortic valve (TAV) is collapsed into a catheter tube, which is percutaneously inserted into the aortic position. The first TAVs were constructed of GA-fixed bovine pericardial leaflets within a tubular stainless steel stent, expanded via the inflation of a balloon located inside the bioprosthetic when the device was in the desired position within the native aortic annulus[169], as illustrated in Figure 2-16(a). The xenogenic tissue leaflets have the same immune-system-led calcification risk as the surgical bioprosthetic heart valves as described in Section 2.3.2, but additional concerns have been raised that the crimping process itself may encourage further acceleration of the calcification process[170]. Whilst balloon expandable devices and bovine pericardium are still commonly used[171], many devices now incorporate porcine pericardium and/or a self-expanding stent, utilising super-elastic metal such as Nitinol™ to deploy the TAV, as shown in Figure 2-16(b). Other, less common, methods of expansion include lateral expansion after retraction of longitudinal Nitinol™ wires (the Boston Scientific Lotus valve) and inflation via a rapid setting polymeric agent (the Direct Flow valve)[172].

Initial TAV deployments were via a femoral artery (trans-femoral or retrograde approach), and this technique has been joined by the recent development of insertion through the apex of the heart (trans-apical approach)[12]. Trans-femoral surgery involves a 1-2 cm incision in the groin to access the femoral artery,

following which a catheter is inserted and fed 70-100 cm through the arterial system including the aortic arch, up to the aortic root region[173]. Trans-apical access requires a longer incision, ~5 cm, but the catheter entry point is much closer, 7-10 cm, to the aortic root[173]. The catheter approaches from the opposite direction compared to the trans-femoral approach, being inserted through the rib cage, into the apex (i.e. the lowest part) of the heart, and through the ventricle to the aortic root region[173]. A trans-apical approach is often required for patients with small, diseased, and/or calcified iliofemoral arteries, as the valve-bearing catheter is too wide to pass through[174]. Both insertion approaches have comparable mortality when comparing patients of similar baselines[13,174].

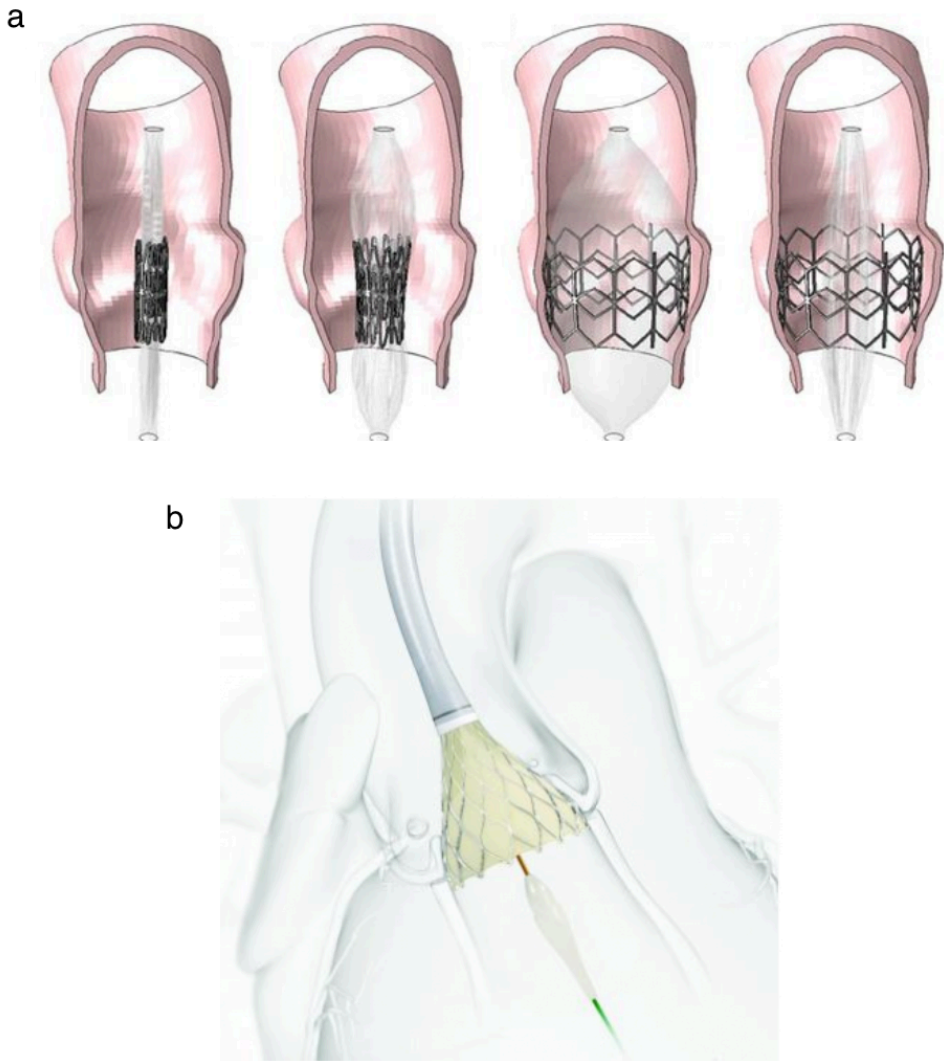

Figure 2-16: Methods of TAV expansion: (a) Balloon expandable – the TAV is inserted with an uninflated balloon located inside, which is then inflated, expanding the TAV. When the balloon is deflated again, the TAV remains expanded and anchored inside the native valve leaflets [image adapted from Auricchio et al[123]*]; (b) Self-expandable – the TAV is made out of super-elastic material, which expands into the desired shape once released from the confines of the catheter [image adapted from Diagnostic and Interventional Cardiology[175]]*

Regardless of insertion point, the catheter is fed into the cardiovascular system until in position, and if necessary, depending on the specific type of TAV, the valve is released from the confines of the catheter tube. The valve expands up to the aortic root wall, forcing the original stenotic valve into a permanently open arrangement, and then the catheter tube is withdrawn from the artery[10,176]. The first generation of TAV devices were not repositionable or retrievable in cases of non-optimal deployment, often resulting in higher than expected paravalvular leakage (PVL) or requiring the insertion of a second TAV device as a result of this erroneous positioning[168]. To address this, the second generation of TAV devices include designs which can be fully or partially re-collapsed after expansion, and/or include guides to enable optimal positioning[168]. PVL has been further reduced in some of the third (the most recent) generation of TAVs, such as the Edwards SAPIEN 3, which includes an outer sealing cuff at the base of the stent[177].

Successful implantation rates have been as high as 97 %[12,51,176]. The benefits of reduced hospital stays, accelerated return of body mobility, decreased major bleeding and onset atrial fibrillation, and improved haemodynamics of TAVs are however offset by the 1-year follow up of patients showing a marked increase in both stroke incidence (from 1.1% to 5.0%) and major vascular complications (from 1.1% to 16.2%), and occasional asymmetric expansion of the valve results in severe leaflet calcification, requiring valve retrieval via surgery[10,178]. The main two TAV technologies that have been commercially available are the Edwards SAPIEN (a balloon expandable TAV) and the Medtronic Corevalve (a super elastic, self-expanding TAV), available in the EU since 2007 and 2011 respectively. Other devices are in various stages of development, such as the JenaValve, the Direct Flow, the Boston Scientific Lotus, the Acurate, and the Portico[10,179].

TAVs include a frame which supports and guides the attachment line of the leaflets, but minimises frame thickness to around 0.5 mm[180,181]. However, the functional orifice area of the device may be impaired due to the presence of the calcified native leaflets, operating in a sub-optimal configuration smaller than the ideal fully expanded geometry[182,183]. Additionally, TAV implantation into a non-spherical annulus, possibly as a result of heavy calcification, can lead to deployment with an oval shape, with less recourse for correction when

compared to a surgical procedure[182,184]. The positioning of the TAV has an increased variability compared to its surgical equivalent, due to the nature of the implantation procedure[185]. A high degree of orifice eccentricity is linked to increased levels of regurgitation, most likely as a result of diminished leaflet apposition[182,186]. TAV oversizing is often utilised to mitigate this issue, as well as attaining more secure device anchoring, but valve haemodynamics can be adversely affected by this approach[51,187], and moderate to severe stenosis of the TAV can occur when there is excess leaflet tissue relative to the stent orifice area, with more associated haemodynamic deterioration[188].

If the device is fixed into position a few millimetres further up- or downstream of the ideal location, any or all of the following can occur: decreased ventricular functionality; alteration of aortic root fluid dynamics; reduced TAV functional lifetime; PVL as a result of seal zone mismatch; CA obstruction; conduction abnormalities; elevated wall stress, potentially resulting in valve embolization or annulus rupture[185,189].

In spite of these limitations, the expansion of TAVs into their destination annulus, including distension of the TAV to conform to the physiology better, results in reduced patient-prosthesis mismatch when compared to surgical procedures[181]. A successful TAV procedure is usually characterised by a larger increase in the systolic performance in comparison to the post-surgical condition, with transvalvular pressure drops below 10 mmHg and EOA up to 2.0 cm^2 for a reference STJ diameter of 2.5 cm[181,190].

2.3.3.1 Specific TAV types

2.3.3.1.1 SAPIEN

The SAPIEN valve family combine bovine pericardium fixed in a tri-leaflet arrangement into a balloon-expandable cobalt chromium frame, resulting in a relatively rapid expansion of the valve once released from the confines of its sheath, radially pushing away the native calcified leaflets, and utilising the elastic recoil of the aortic annulus to fixate the valve[10,12]. The XT valve, approved for use in the US market, is presented in Figure 2-17. The valve is shorter than its diameter, with valve lengths of 14.5, 17, and 19 mm for 23, 26, and 29 mm diameter valves respectively. Less protrusion into the left ventricle and/or the aortic root reduces the amount of non-physiological architecture in

either volume, ideally reducing non-physiological effects on the haemodynamics of the root due to fluid interaction with the bioprosthetic. However, vortices within the sinuses of Valsalva are altered from the physiological condition, to an as yet unascertained degree[12] with the central jet developing a helical flow in mid-systole that results in a mild retrograde flow[187]. According to *in vitro* experiments, 32 % of RBCs remain in the SoV after each cycle, compared to 9 % of RBCs in Corevalve treated regions and 0 % in the healthy native condition, requiring 4 cycles to fully flush the region, with the associated elevated risk of thrombus formation[191]. Sub clinical leaflet thrombosis (SCLT) has been observed at a higher rate in Edwards SAPIEN valves, present in 14 % of follow up examinations, based upon reduced leaflet motion[192], and has been linked to over-expansion of the TAV, as this may cause endothelial damage, larger neo-sinus formation, and reduced washout.

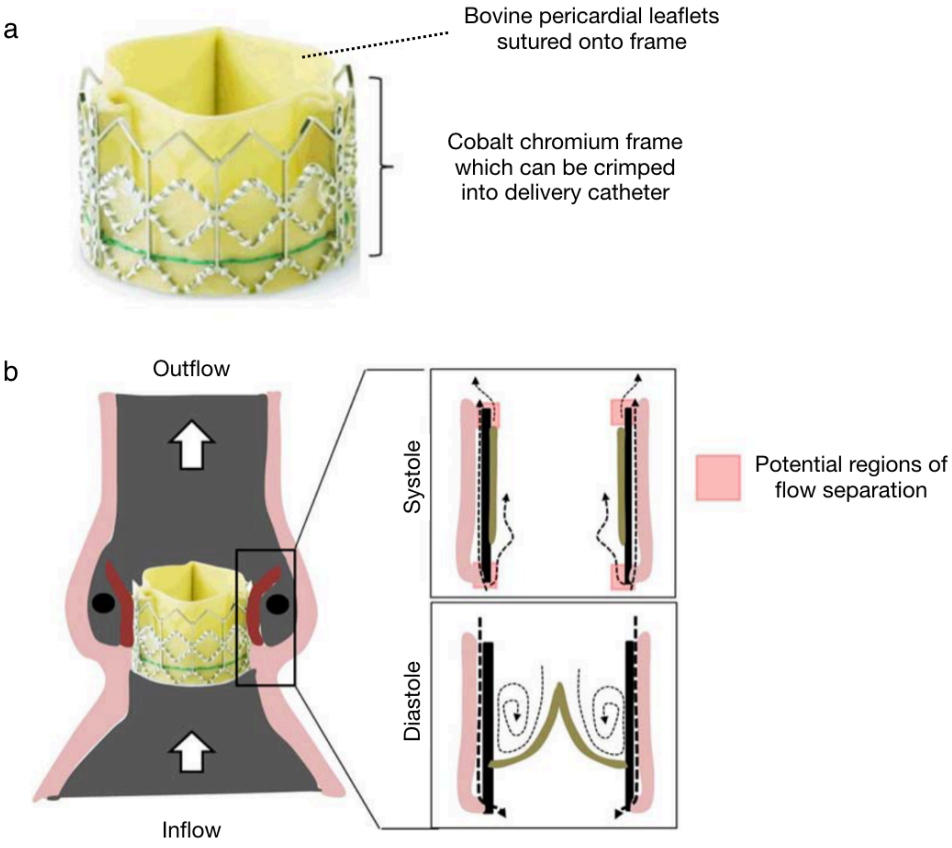

Figure 2-17: Edwards SAPIEN valve: (a) Photo of valve depicting leaflets and frame (reproduced from www.edwards.com); (b) Schematic of flow during systole and diastole[12]

The larger diameter of the crimped Edwards SAPIEN valve, and hence of the catheter used for implantation, often necessitates a transapical approach[174]. The accompanying WSS of the root has been measured during *in vitro*

investigations to be 1 - 1.2 Pa, within the physiological range of 1 - 1.5 Pa, whilst the TAV itself experiences WSS of up to 3.5 Pa during each cycle[184,193]. However, the raised occurrence of asymmetric deployment, present in around 20% of procedures[194], may result in severe leaflet calcification, requiring the valve to be retrieved via surgery, or become the outer component of a Valve-in-Valve procedure[10,178], as described in Section 2.3.3.3.

2.3.3.1.2 CoreValve

The CoreValve family of TAV devices, with an example of the first generation presented in Figure 2-18, can utilise a thinner catheter than the Edwards SAPIEN valve, as the combination of using porcine leaflets, as opposed to thicker bovine pericardial tissue, and a self-expanding Nitinol® stent, as opposed to a balloon expansion, enables tighter crimping for a thinner profile, in turn enabling a higher percentage of transfemoral implantations[12,174]. The longer and tapered profile of the CoreValve relies on self-expansion of the Nitinol® frame rather than the elastic properties of the annulus, which may affect the haemodynamics of the aortic root as the blood flows through the stent mesh, although this is mitigated somewhat by the stent's tapered design[12]. This self-expansion can be affected by leaflet calcification, which is often asymmetric across a valve, with one leaflet more calcified than another, leading to an asymmetric orifice[12]. As Nitinol® conforms to the shape of its containing volume, this asymmetry can be replicated in the deployed valve, possibly leading to unexpected leaflet kinematics in the implanted valve[12,195].

Post mortem examinations of CoreValves show that whilst there is little exhibition of tissue overgrowth in regions of high blood velocity, slow flow regions in contact with the frame results in neo-intimal tissue, particularly where the TAV frame struts contact the aortic wall, suggesting pathological change due to fluid flow alteration[196]. The leaflet position within CoreValves results in a relatively supra annular TAV orifice for a standard implantation height, with the associated haemodynamic performance improvement but also with the associated susceptibility to diminished sinus washout[196].

Regurgitation is at a similar mild-to-moderate level to the Edwards SAPIEN valve, possibly leading to future impairment of left ventricular function, whilst pressure drops across the valves are also similarly mild, in the 5-15 mmHg

range, although long-term effects are still under review[181,197]. The downstream ends of the stent mesh may induce more regions of flow separation and non-physiological flow profiles, whilst RBCs backflowing into the sinuses during diastole may also be damaged and slowed as they travel through the mesh, as indicated in Figure 2-18[12]. Conduction issues are a particular problem following procedures using CoreValves, such as atrioventricular node interference due to the metallic frame, disrupting the signalling of heart beats for up to 40 % of patients[198–200].

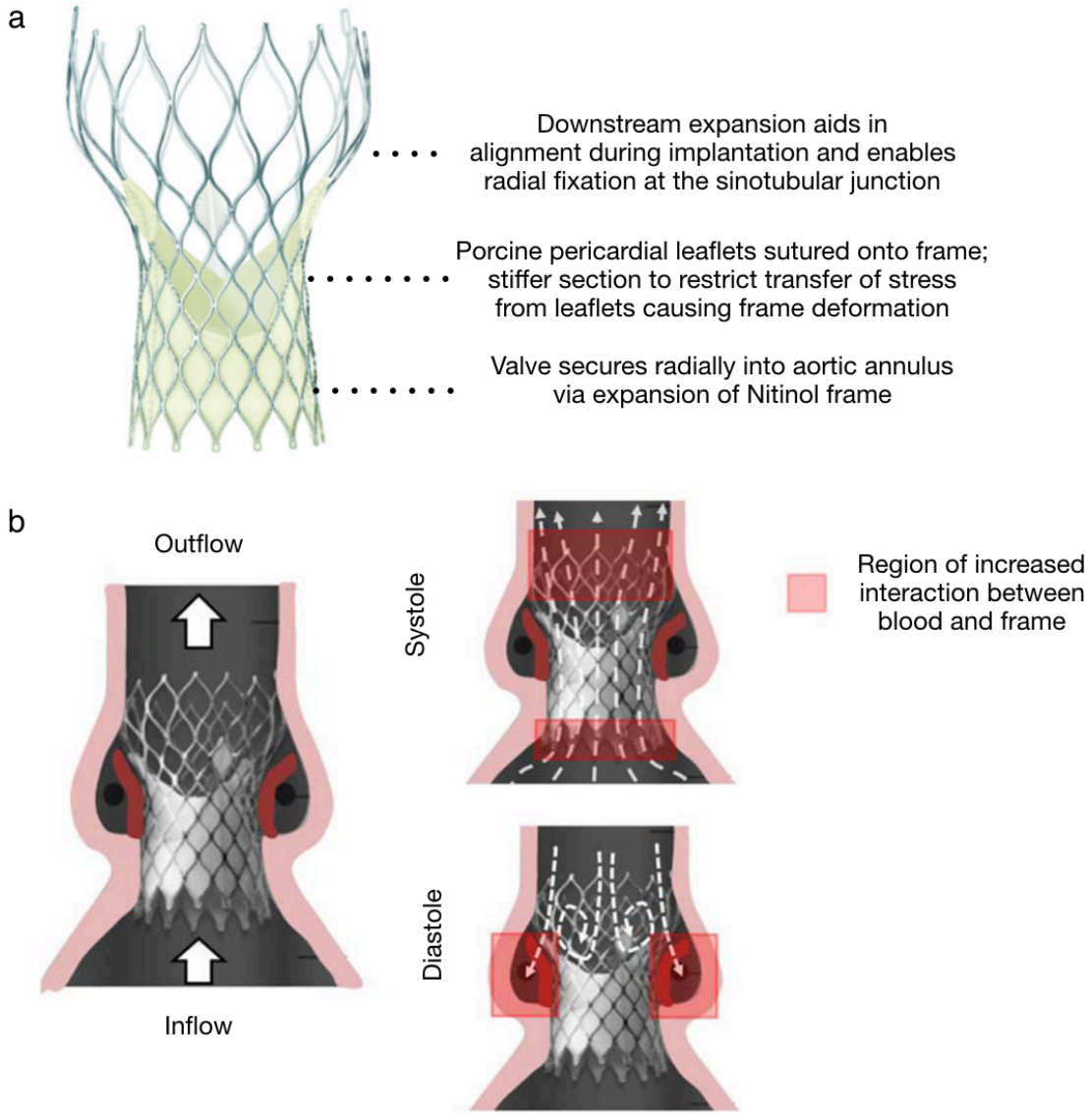

Figure 2-18: Medtronic Corevalve: (a) Photo of valve depicting leaflets and frame, and function of each level of the valve; (b) Schematic of flow during systole and diastole, with regions of increased interaction between blood and frame indicated[12]

2.3.3.2 Flow Alterations

The fluid dynamics of the aortic root following TAV implantation are different to both the healthy native condition and the post-surgical condition, with complications such as flow separation, energy losses, non-physiological CA flow, and PVL[12]. TAV implantation is also associated with serious complications further downstream, such as an increased occurrence of stroke, silent ischemic lesions, and cerebral embolism[14–16,174]. The primary cause of flow pattern difference is the continued presence of the native calcified leaflets, which are not ablated as they would be as part of the surgical procedure, but radially displaced in a permanently open configuration towards the SoV. The available volume of the SoV is reduced by these displaced leaflets, and systolic sinus flow is mostly confined to the upper regions of the SoV, in the vicinity of the cusps of the native leaflets[201], average flow in the SoV is reduced to a quarter that observed in the healthy physiological condition, and peak velocity is halved[35]. Flow within the SoV plays an important role in both CA blood supply and sinus washout[18,96,202], and the associated reduction in shear rate increases the risk of thrombus formation[10,97]. In addition, the start-up vortices generated at the start of systole do not generate at the tip of the dynamic leaflet tips in the upper part of the sinus, but further downstream at the edge of the now static native leaflets[97]. This has been associated with further reductions in sinus washout[97,186], and a delay of ~10 ms in the opening of the valve[35,203].

The volume between the permanently displaced native leaflets and the stent of the TAV can be considered as a neo-sinus, with a size and shape dependent upon the geometry of the native region, the geometry of the prosthesis, and the angular orientation of the TAV with respect to the native architecture, and non-alignment of the opening TAV leaflets with the native SoV may further reduce the SoV flow[204]. Flow within these neo-sinuses may be especially prone to stagnant flow regions, increasing the thrombogenicity of the root[204]. Consequently, clinical thrombotic events are associated with TAVs, especially in the first 3 months after implantation, and most cases happening within 6 months[205,206]. Even if the thrombosis has no direct effect upon quantified haemodynamic performance, SCLT may be occurring, resulting in lesions and reduced prosthesis leaflet motion[192,207]. SCLT is associated with strokes and

transient ischemic attacks, so prevention may improve long-term clinical outcomes[192].

In the majority of TAV designs, the stent prevents the working leaflets from opening beyond 90 °, producing a narrower systolic jet than for an equivalent sized native or surgical valve[35,203], with peak blood flow velocities up to twice as high as for the healthy native condition[55,78,202]. The resultant higher viscous shear stresses, established via *in vitro* investigation to be up to 6 N/m^2[186], remain beneath the haemolytic threshold[201]. The return of fluid during valve closure is not accompanied by the vortical structures reported in the healthy native condition, again reducing wash out of the SoV[97], and fluid suction generated by the closing leaflets has minimal effect upon the sinus volume due to the continued presence of the static native leaflets[201]. Consequently, broadened and drawn out stagnation zones develop in each SoV throughout both the systolic and diastolic cycles, with shear rates lower than 100 s^{-1}[97,185]. Due to the rheology of blood, these regions of permanent low level shear observed at the base of the SoV substantially increase the local dynamic viscosity, extending RBC residence time and enhancing thrombogenic conditions[97], especially in the non-coronary sinus which does not have this low shear mitigated by flow accessing the CA[167].

The effect of TAV implantation upon the coronary flow has not yet reached consensus. As central flow speed is decreased from the pathological condition, some reports claim that a resultant reduced Venturi effect improves systolic CA flow, alongside enhanced coronary bed pressure gradients[71]. However, other findings indicate that patients with coronary ostia positioned closer towards the basal annulus may have a reduction in coronary flow by up to 20%[95,96,208]. As left ventricular efficiency improves, less work is required by the myocardium to generate the pressure required to pump blood around the body, so this loss of coronary efficiency may not be a critical issue on its own, but severity depends on the specific long-term myocardial needs of the patient and combination with other cardiac deficiencies[71]. Ostia also risk being obstructed when close to native leaflets thickened by calcification and/or when an oversized TAV is deployed[10,73]. Fragmentation of the native leaflet during TAV implantation, use of a balloon expansion technique, or high implantation of the TAV can all also cause obstruction of the ostia or increase the chance of coronary ischemia[190].

Low positioning of the TAV carries its own risks of post-procedure conduction abnormalities, with atrioventricular block occurring after 16 % of TAV implantations, contrasted with a 1 % occurrence following surgical implantations[180,198,199,209].

PVL during diastole is more common following TAV implantation than after surgical implantation, due to the reliance of frame expansion to hold the prosthesis in place rather than suturing onto the native tissue[171,205,206]. Eccentric deployment may also lead to intra-valvular leakage, as full leaflet coaptation is prevented by the deployed frame shape[182,210]. Redilation of the TAV can reduce the PVL, and more recent devices use skirts around the upstream base of the frame[203,211], but moderate and severe PVL is still a common occurrence after TAV implantation, and is associated with increased mortality[210]. This regurgitation imposes a high workload upon the left ventricle to maintain a sufficient supply of blood to the body[188]. Tissue overgrowth and/or blood coagulation in the gaps between the TAV and the host tissue of the annulus in the months following the TAV implantation procedure may reduce this PVL, but mild leakages are reported as persisting, and statistics implying severe and moderate PVL improves with time may be biased by the accompanying elevated mortality of increased PVL[210,212].

2.3.3.3 Valve-in-valve

In addition to treating patients with a pathological native valve, TAV implantation can also be used as a non-surgical method of replacing underperforming or dysfunctional prosthetic valves, expanding the new TAV inside the previous prosthetic, referred to as a ‘valve-in-valve’ (ViV) configuration[73,190,210]. The orifice area is further reduced by this approach, and may not be suitable for patients requiring smaller prostheses if this results in critically reduced valve performance[210,213,214]. This orifice reduction can be mitigated to an extent by supra-annular positioning of the TAV, although this does increase the risk of reduced flow within the SoV[213]. Additionally, as the original prosthetic’s stent posts tend to be more flexible than the native annulus, the downstream portion of the new supra-annually positioned TAV tends to splay outwards, creating a ‘flower pot’ arrangement, resulting in the operating leaflets being less constrained at their free margin[187], as displayed in Figure 2-19. The wedge

effect also improves the security of the valve, especially for balloon expandable devices, as the post-ballooning recoil reduces the radial forces at the base of the host stent when the TAV is fitted[215]. However, whilst use of the flower-pot arrangement reduces energy losses during systole, it frequently results in a narrowing of the access to the SoV, reducing sinus washout, especially in the non-coronary sinus[167,191]. The likelihood of coronary obstruction is also raised, especially when: the old prosthesis has badly calcified or damaged leaflets; the coronary ostia are located closer towards the basal annulus; the aortic root and especially the SoV are particularly narrow[71,73,191,212]. RBC residence time increase in the neo-sinuses, both in systole and diastole, raising the risk of thromboembolism[171]. Additional ViV complications include non-ideal positioning of the new TAV (following 15 % more procedures compared to TAV implantation into a native valve), leaflet thrombosis (4 %), CA obstruction (3.5 %) and an increased occurrence of a range of conduction issues[191,210].

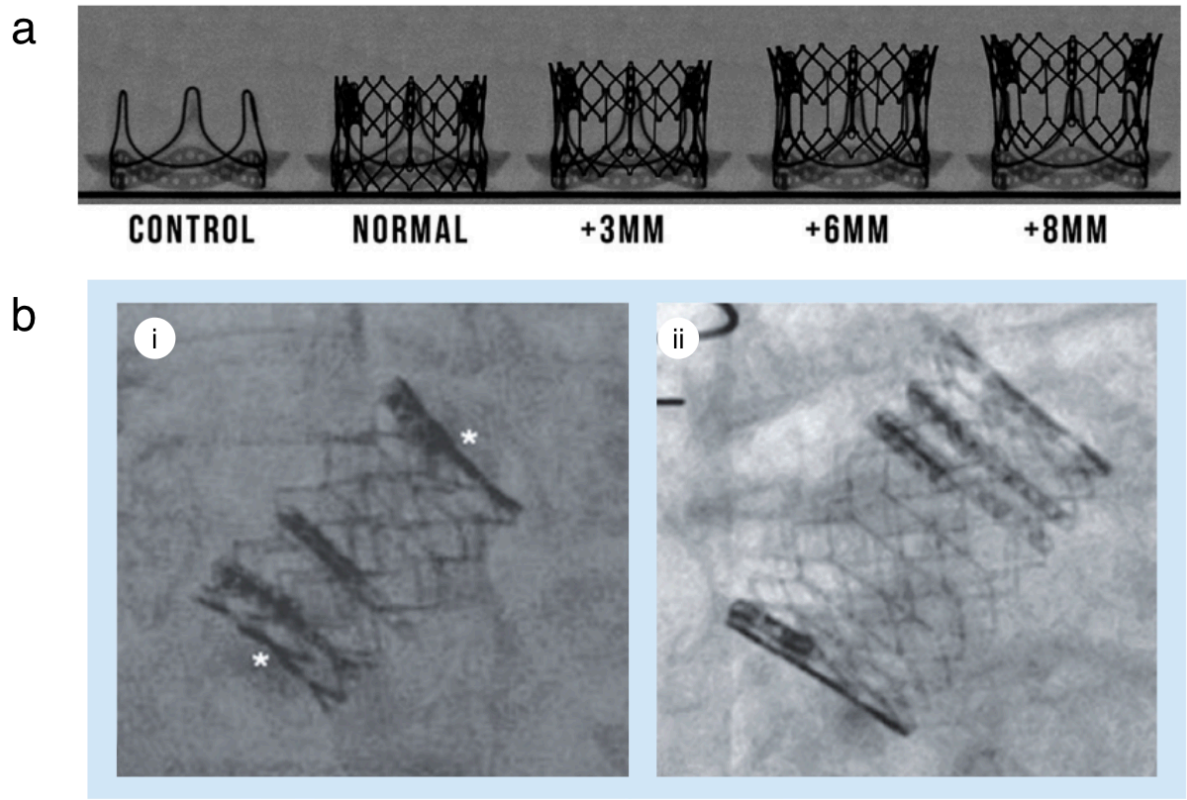

Figure 2-19: 'Flower pot' arrangement as a result of supra-annular deployment: (a) resultant deployments following increasingly supra-annular positioning of the TAV within the failing prosthetic, indicating escalating splaying of the outflow prosthesis orifice[216]; (b) in vivo *images of (i) a regular TAV expansion into the native aortic annulus and (ii) a supra-annular implantation resulting in a conical, or 'flower pot', shape[187]*

2.3.4 Mechanical response of pericardial tissue

The bovine and porcine pericardial tissue used for the bioprosthetic valves have a J-curve relationship between stress and strain, much like the native aortic valve leaflet tissue as described in Section 2.1.3.3. Fixing collagen/elastin based tissue in GA, an agent that preserves and cross-links the tissue, causes changes to the stress-strain relationship of the tissue, but as long as the fixation is not done under pressure, the changes in response are not large, as indicated in Figure 2-20, as fibre crimping during fixation will occur under pressures > 4 mmHg[217]. Whilst consensus has not yet been reached as to the quantified properties of bovine and porcine pericardium, with the reported modulus of the bovine pericardium stress-strain response measured *in vitro* to vary from 10 to 170 MPa and reports of the porcine pericardium modulus ranging from 60 to 130 MPa[218], the response of both tissues can still be described as a J-curve, with a low stretch modulus when the elastin fibres control the stress-strain response, a region of transition as the stiffer collagen fibres are unwound and begin to take the load, and a high stretch modulus when the collagen fibres are fully straightened and dominate the stress-strain response until tissue failure[124,218].

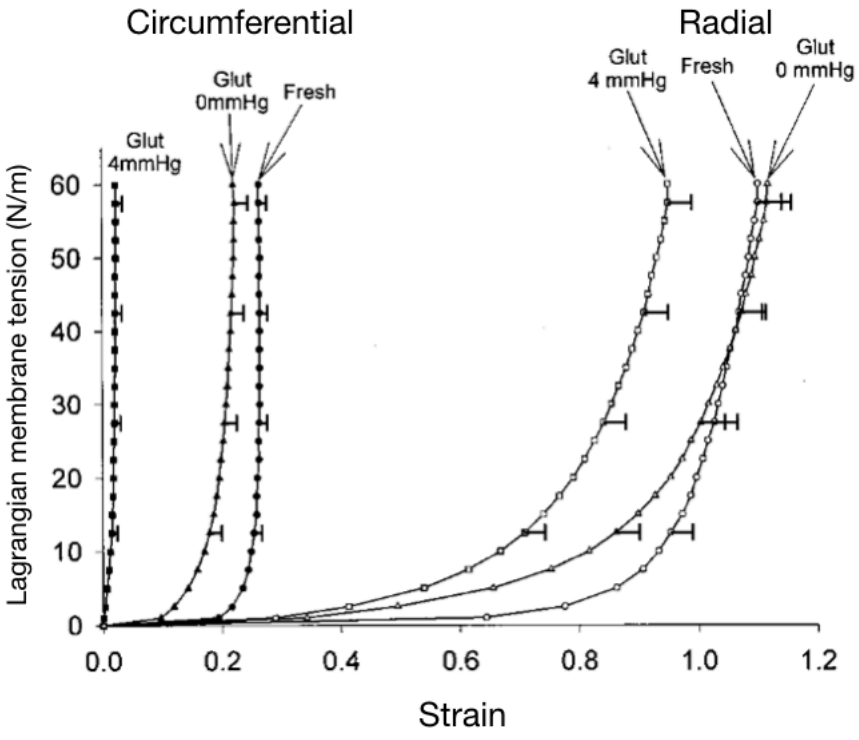

Figure 2-20: Stress-strain response of GA fixed aortic valve tissue[217]

2.4 Conclusions and Objectives

The most relevant parts of the preceding literature review can be summarised by the following brief sections.

2.4.1 Cardiovascular Efficiency and Vortical Dynamics

The role of the aortic valve has a critical effect upon the efficiency of the cardiovascular system, and the valve's efficiency depends upon the surrounding geometry. However, the role of the valve-root system upon the functional mode and hydrodynamics performance of the left side of the heart has not yet been fully revealed. During each cardiac cycle, vortices are generated in the aortic root, and especially in the sinuses of Valsalva, that are involved in the proper function of the aortic valve. Different aortic root geometries relative to the valve have resulted in different vortical patterns, but these patterns have not yet been explained. The mechanics of vortex generation and the vortices' properties and propagation within and out of the aortic root have also not yet found consensus. How these vortices affect the aortic valve, whether a healthy native valve or a prosthetic, has also not been agreed upon.

2.4.2 Post-Surgical Valve-Root Configurations

The implantation of surgical valves can result in a range of relative geometries between valve and root, whilst disorders such as Marfan's syndrome result in distinct changes to the aortic root region, and there is some evidence that these variations result in a change to the local haemodynamics, requiring different and bespoke therapies to encourage healthy blood flow. However, there is little information linking the haemodynamics of these roots with a change in vortical structures or stagnation regions, which could be elucidated via modern methods. Characterisation of these geometries and resulting flow patterns could lead to further classifications of root dilation, leading to improved support for clinicians and/or engineers by informing on the best therapeutic strategy.

2.4.3 Valve-in-valve Architecture produces Flow Alterations

The valve-in-valve architecture present after the majority of TAV implantation procedures results in significant alterations to the fluid dynamics of the aortic root, with the original dysfunctional leaflets permanently held open. These

alterations have been linked to the formation of downstream ischemic lesions and dementia, and the valve-in-valve configuration may also affect the coronary artery flow, in turn having a deleterious effect upon the cardiovascular system. The rotational alignment of a TAV is difficult to control and determine during the implantation procedure, and the effect of prosthesis to native commissure misalignment is as yet unknown.

2.4.4 Coronary Artery Flow linked to Root Dynamics

The flow through the coronary arteries is linked to the fluid dynamics of the aortic root in both the systolic and diastolic phases of the cardiac cycle. However, there are few investigations into what the effect of the presence/absence of the coronary arteries has upon the flow within the aortic root, specifically the sinuses of Valsalva, following TAV implantation.

2.4.5 Objectives

The conclusions of this literature review have led to the following objectives:

2.4.5.1 Objective 1

To investigate the effect of different valve-root geometries upon the fluid dynamics within the aortic root, modelling a native physiological configuration and comparing the resultant flow with a variety of configurations that could result from surgical aortic valve replacement. The research towards this objective is presented in Chapter 4.

2.4.5.2 Objective 2

To characterise the flow resulting from implantation of a TAV into a stenotic aortic valve, and to ascertain whether the rotational alignment of a TAV within its host root has an effect upon the resultant fluid dynamics in the region. This work is reported upon in Chapter 5.

2.4.5.3 Objective 3

To determine whether the presence of the coronary arteries, and the flow into them during each cardiac cycle, has an effect upon the fluid dynamics of the aortic root, particularly within the sinus of Valsalva associated with each coronary artery, following TAV implantation. Chapter 6 elaborates upon this objective.

3 Methods and Materials

3.1 Introduction

This chapter introduces the experimental rigs used in the investigations, and the Particle Image Velocimetry (PIV) used to analyse the flows generated. Firstly, a summary of the bench top pulse duplicator used to generate the desired flow rates and pressures within the valve-root configurations, including explanations of the equations used to calculate the global hydrodynamic parameters which quantify the cycle-to-cycle performance of the valve-root configurations is presented in Section 3.2. Next, the theory and methodology behind the use of PIV in this study is outlined in Section 3.3, describing how the instantaneous flow velocities are calculated. The chapter then continues to detail the materials used in these rigs, describing the aortic valves used in the flow studies in Section 3.4; the design, manufacture and use of the mock roots that these valves were inserted into in Section 3.5; and finally the details of the different testing fluids that have been used in the experiments in Section 3.6.

3.2 Pulse Duplicator – Vivitro Systems Left Heart Simulator

3.2.1 Experimental Rig

The ViVitro Systems left heart simulator (SP3891, ViVitro Systems, Canada) consists of a pump, a mock left heart, pressure and flow transducers, and a computational system, with a photo and schematic shown in Figure 3-1, and reproduces physiologically equivalent pressures and flow rates conforming to the requirements of ISO 5840:2005. A programmable waveform generator (WG5891, ViVitro Systems, Canada) supplies a signal to control the pump head and is sent to the pump (SuperPumpVSI Head SPH5891B, ViVitro Systems, Canada) via electronic signal through a power amplifier (SPA3891, ViVitro Systems, Canada) which designates whether the waveform controls the position or velocity of the pump head. This waveform can be altered to model different cardiovascular systems and states by varying the pump head displacement/velocity, and frequency. The amplitude of the signal is independently adjusted on the power amplifier, with an increase in amplitude

increasing the simulated CO and mean aortic pressure. The rotary motion of the electric motor is converted into linear translation of the piston via a linear actuator and lead screw. Adherence to the input waveform is maintained via feedback from position and velocity transducers situated alongside the piston-in-cylinder pump head.

The pressure changes from the pump head are fed through an impedance adaptor, consisting of a resistive element and two adjustable compliance chambers, to provide greater accuracy when modelling a range of physiological and pathological cardiac systems, and also filter out any high frequency noise during valve or conduit testing. This pressure waveform then acts upon the hydraulic fluid surrounding a silicone sack, representing the left ventricle, which is part of the mock left heart. Testing fluid from the atrium chamber, representing the left atrium, flows into this silicone sack/ventricle through the mitral valve, preventing back flow into the atrium chamber. The atrium chamber is open to the atmosphere, and enables testing fluid, dyes, or particulates to be introduced into the pulse duplicator system. The mitral valve can be replaced to allow for testing of different valves, but as this research was concerned with the aortic root region, a mechanical Sorin Allcarbon 27 mm valve (Sorin Group, Italy), detailed in Section 3.4.2, was used for all tests.

All pressure signals are provided by high-resolution pressure transducers (Millar Mikro- tip®, Millar Inc., USA), and then passed through a bridge amplifier to a tri-pack (TP2001, ViVitro Systems, Canada), which is made up of three amplifiers (VSI AM9991, ViVitro Systems, Canada), before being collected by the computer. The pressure transducers were calibrated by measuring the voltage output of the transducers when placed under gauge pressures of 0 mmHg and 200 mmHg, as measured by a digital manometer (Extech HD750, Nashua, USA) with a range of 0 - 5 psi and a resolution of 0.001 psi. Upstream of the mitral valve is a high-resolution pressure transducer providing the user with the left atrial pressure throughout testing. Another pressure transducer is located in the ventricular chamber, between the flow probe and the aortic valve, measuring the ventricular pressure throughout testing. The final pressure transducer is located approximately 50 mm downstream of the aortic valve, providing measurements of the aortic pressure throughout the cycle.

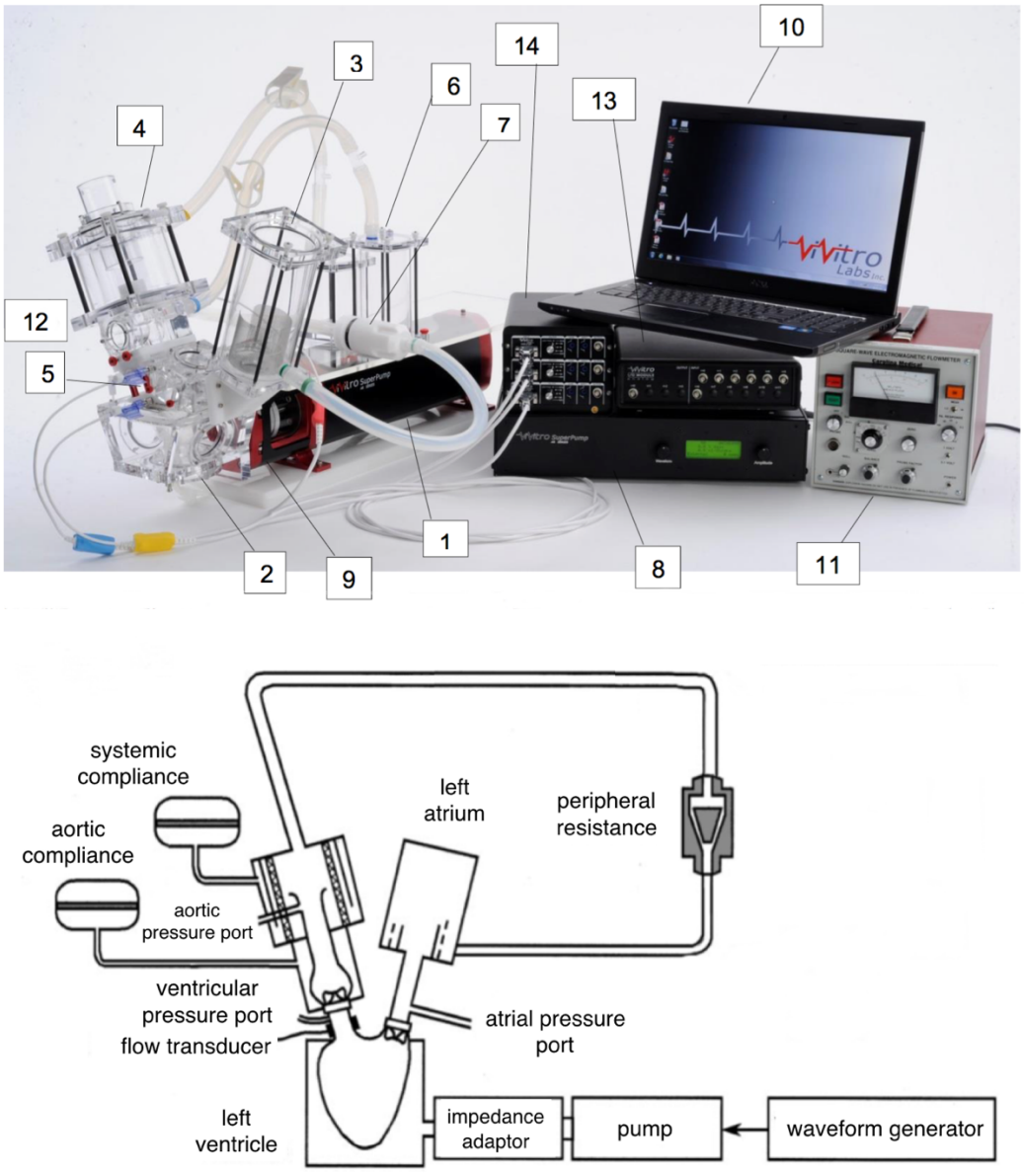

Figure 3-1: Vivitro Labs Pulse Duplicator System SP3891, with schematic (adapted from Lieber 2002[219])

1 - Pump; 2 - Ventricle Chamber; 3 - Atrium Chamber; 4 - Aortic Chamber;
5 - Aortic standoff; 6 - Aortic Compliance chamber; 7 - Peripheral resistance;
8 - Power amplifier; 9 - Viscoelastic Impedance Adaptor; 10 - Computer;
11 – Flowmeter; 12 - Electromagnetic flow transducer; 13 - I/O Module;
14 - Pressure transducer tri-pack

Fluid pumped from the ventricle passes first through a flow transducer and then the aortic valve being tested, until it enters the aortic chamber. The flow transducer is an electromagnetic flowmeter (Carolina Medical Model FM501, Carolina Medical Electronics Inc., USA), and bases its instantaneous volumetric

flow rate upon the rate of ions within the fluid passing through the flow transducer, with an acquisition frequency of 256 samples per simulated heart cycle. The flowmeter is calibrated so that the transducer signal is directly proportional to an output from the pump controller, the piston displacement (L) signal with respect to time ($\frac{dL}{dt}$). This is achieved by applying a 50% sine waveform at a cycle rate of 70 bpm to the pulse duplicator and recording the cumulative voltages over the cycle of both the dL/dt and the flow rate from the flow meter (q_v). The q_v signal then has a calibration factor, C_f, applied to it, so that $q_v = \left(\frac{dL}{dt}.C_f\right)$.

The aortic valve can be replaced to test different valves, and a range of valves were used during this testing, detailed in Section 3.4.1. The aortic chamber is split into two main parts, with the volume immediately downstream of the aortic valve connected to a compliance chamber that allows modelling of various aortic root (or local) compliances by varying the amount of fluid and air within the compliance chamber. An aortic root model can also be fitted into this first aortic chamber volume, imposing predesignated 3D volumes on the fluid flow, allowing for modelling of specific lumen diameters, sinuses of Valsalva, coronary arteries, and surgical grafts. The second aortic chamber volume is connected to the first by a short tube. A second fluid and air compliance chamber connected to this second aortic chamber enables the more general (or global) arterial compliance of the remainder of the vascular system to be modelled.

Outflow from the aortic chamber passes through the heating bath of a heat exchanger (Model HE991, ViVitro Systems, Canada, with pre-set temperature controlled by a compact closed circulator with digital control, Grant FH16-D, Grant Instruments, UK), regulating the temperature of the fluid to a pre-set value. Before returning to the atrial chamber, the testing fluid flows through the peripheral resistance regulator, which can be twisted to increase/decrease the amount of resistance to flow, representing the vascular resistance of the body.

3.2.2 Parameters Measured

The pressure and flow rate waveforms acquired can then be extracted from the Vivitro software, imported into data analysis software (Microsoft Excel, Washington, USA), and converted into a number of different parameters to assess the hydrodynamic performance of the valve-root configuration. The parameters chosen for these experiments were:

- Mean Transvalvular Systolic Pressure Drop (Δp);
- Effective Orifice Area (*EOA*);
- Closing and Leakage Regurgitant Volume (V_c/V_l);
- Forward/Closing/Total Energy Loss ($E_f/E_c/E_t$);

In order to calculate these parameters, each cycle is divided into 4 distinct flow periods and 4 distinct pressure periods, separated by crossover points as indicated in Figure 3-2, as the pulse duplicator simulates each cycle of the heart. The flow cross over points are determined as follows:

F1 – first positive flow from ventricle to aorta; beginning of systolic forward flow

F2 – end of positive flow from ventricle to aorta; end of systolic forward flow

F3 – negative flow through outflow valve, i.e. regurgitant flow from aorta to ventricle, becomes constant, indicating end of valve closure and start of valve leakage

F4 – end of cycle

The flow in period *F1* – *F2* is defined as 'forward flow'; in period *F2* – *F3* as 'closing flow'; and in period *F3* – *F4* as 'leakage flow'.

The pressure drop crossover points are defined as:

P1 – ventricular pressure rises above aortic pressure; beginning of systolic positive pressure

P2 – ventricular pressure falls beneath aortic pressure; end of systolic positive pressure

P3 – ventricular pressure drops beneath atrial pressure; beginning of diastolic pressure

P4 – ventricular pressure rises above atrial pressure; end of diastolic pressure

Period *P1 – P2* is defined as 'systole; Period *P3 – P4* is defined as 'diastole'.

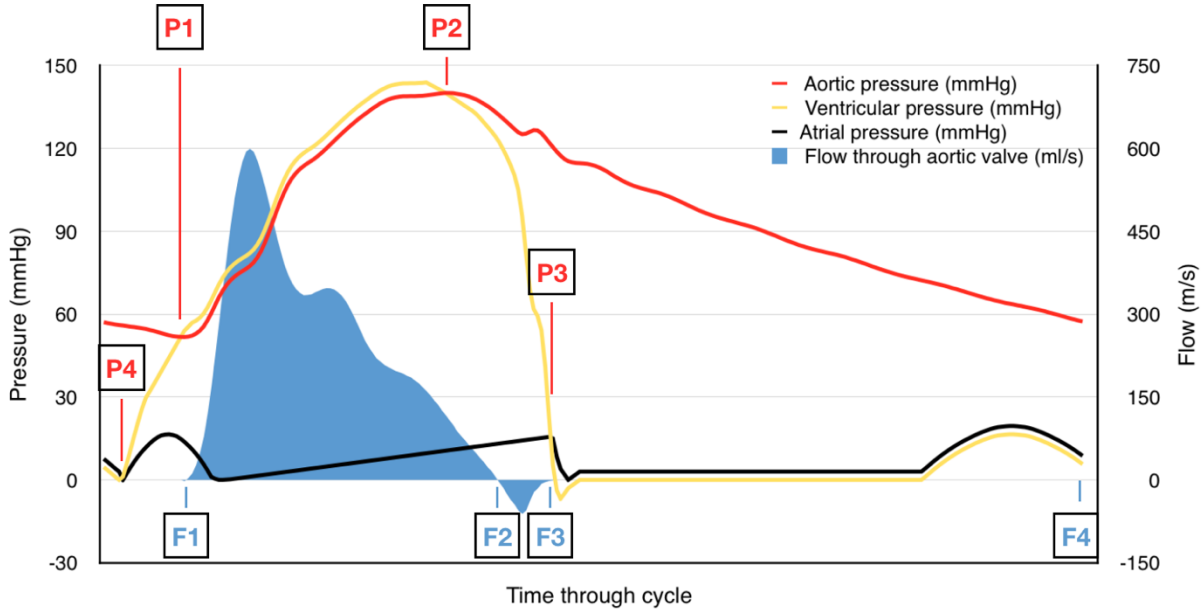

Figure 3-2: Flow-pressure diagram of a typical cardiac cycle, denoting the flow (F1-F4) and pressure (P1-P4) crossover points used to calculate the parameters described in Section 3.2.2

3.2.2.1 Mean Transvalvular Systolic Pressure Drop

The mean pressure drop (Δp) of the flow as it passes from the ventricular to the aortic side of the valve during systole is a commonly used parameter to assess systolic valve performance, with a smaller pressure drop indicating a better performing and more efficient valve. Δp (mmHg) is defined as the mean of the pressure difference between the outflow and inflow pressures (representing the aortic and ventricular pressures respectively) between *P1* and *P2* (i.e. during systole), which can be represented as:

$$\Delta p = \frac{\int_{P1}^{P2}(p_v - p_a)dt}{t_{P2} - t_{P1}} \tag{3-1}$$

where p_v is the ventricular pressure (mmHg), p_a is the aortic pressure (mmHg), t is the time (s), $P1$ is the beginning of the systolic pressure drop, and $P2$ is the end of the systolic pressure drop.

3.2.2.2 Effective Orifice Area

When a uniform flow passes through an orifice, the flow usually separates into three distinct zones – an axisymmetric jet-like flow; a recirculation zone; and a

reattachment zone[220]. The outflow of blood from the left ventricle through the aortic valve can be compared to the flow through a nozzle in a more traditional engineering application[36]. This results in the flow being constricted beyond the orifice, and thus the smallest cross-sectional area of the jet-like flow is further downstream from the orifice, known as the *vena contracta*[37], as illustrated in Figure 3-3.

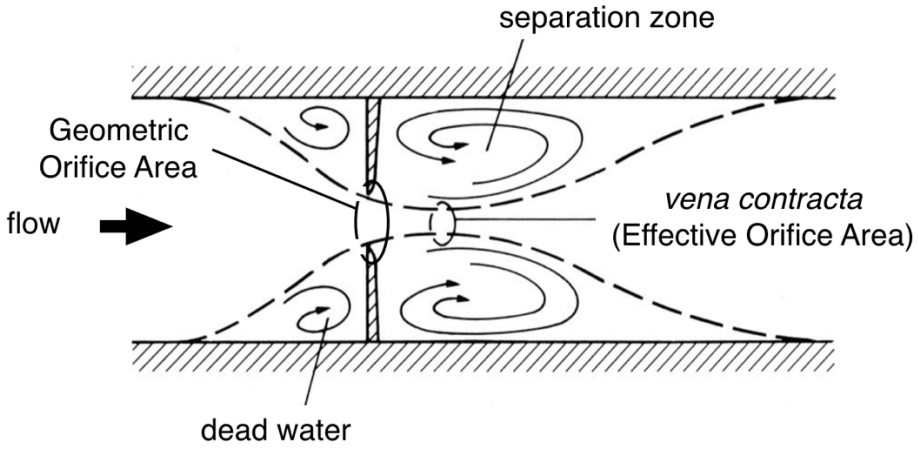

Figure 3-3: the forward flow continues to be contracted once it has passed through the orifice, reaching maximum constriction at the vena contracta [adapted from Caro 2012[37]]

When referring to heart valves, the cross-section of the *vena contracta* is referred to as the Effective Orifice Area (EOA), a commonly used parameter to assess both the severity of aortic stenosis, and the performance of a valve substitute[220]. It is important not to confuse the Geometric Orifice Area (GOA) of the valve with the EOA. The area of this *vena contracta* can be calculated from the Bernoulli and Continuity equations. Assuming inviscid, incompressible steady flow along a streamline under constant gravitational force with a negligible change in height, the pressures and mean fluid velocities over cross-sections 1 and 2 in Figure 3-3, representing a cross-section of the ventricle and the *vena contracta* of the downstream flow from the aortic valve respectively, can be related by the Bernoulli equation:

$$P_1 + \frac{1}{2}\rho v_1^2 = P_2 + \frac{1}{2}\rho v_2^2 \qquad (3\text{-}2)$$

where P is pressure (N/m^2), v is the mean fluid velocity over the cross-section (m/s), and ρ is the fluid density (kg/m^3), and can be rearranged to give:

$$(P_1 - P_2 =)\Delta P = \frac{1}{2}\rho v_2^2 - \frac{1}{2}\rho v_1^2$$

(3-3)

where ΔP is the pressure difference (N/m^2). As $v_1^2 << v_2^2$ [221], this can be further simplified to:

$$\Delta P = \frac{1}{2}\rho v_2^2$$

(3-4)

which can be rearranged to give:

$$v_2 = \sqrt{\frac{2 * \Delta P}{\rho}}$$

(3-5)

The Continuity equation posits that the change of mass in an analysed volume is equal to the mass of the fluid entering the volume minus the mass of fluid exiting the volume, and the mean flow speeds at the in- and out-flow (i.e. cross-sections 1 and 2 in Figure 3-3) are related by:

$$(Q =)v_1 A_1 = v_2 A_2$$

(3-6)

where Q is the constant flow rate (m^3/s) and A is the cross-sectional area of the flow (m^2), and combining and rearranging Equations (3-5) and (3-6) gives:

$$A_2 = \frac{Q}{\sqrt{\frac{2 * \Delta P}{\rho}}}$$

(3-7)

Hence, the flow contraction is associated with a pressure drop in the flow. In order to account for the reduction in section due to viscous effects, it is necessary to apply a discharge co-efficient in line with ISO 5840:2015[222], and so the EOA (cm^2) of the flow in the pulse duplicator is calculated as:

$$EOA = \frac{q_{v_{RMS}}}{51.6 * \sqrt{\frac{\Delta p}{\rho}}}$$

(3-8)

where ρ is the density of the blood analogue fluid (kg/m^3), and $q_{v_{RMS}}$ is the root mean square of the forward flow (ml/s) through the flow meter, defined as:

$$q_{v_{RMS}} = \sqrt{\frac{\int_{F1}^{F2} q_v(t)^2 dt}{t_{F2} - t_{F1}}}$$

(3-9)

where $q_v(t)$ is the instantaneous flow at time t (ml/s), t_{F1} is time at *F1* (s), and t_{F2} is the time at *F2* (s).

3.2.2.3 Regurgitant Volume

Any testing fluid that flows from the aortic chamber back into the ventricular chamber is termed the 'regurgitant volume'. This volume is split into a 'closing regurgitant volume', primarily due to transvalvular (i.e. through the valve) back flow through the leaflets during valve closure, and a 'leakage regurgitant volume', which occurs due to both transvalvular and paravalvular (i.e. around the valve) back flow. The closing regurgitant volume (V_c, ml) is useful as a parameter of the dynamic performance of the valve and is defined as the flow volume with respect to time (s) between *F2* and *F3* (i.e. during valve closure as defined in Section 3.2.2), which is calculated as:

$$V_c = \int_{F2}^{F3} \big(q_v(t)\big) dt$$

(3-10)

The leakage regurgitant volume (V_l, ml) is defined as the flow volume with respect to time (s) between *F3* and *F4* (i.e. during leakage flow as defined in Section 3.2.2), which is calculated as:

$$V_l = \int_{F3}^{F4} \left(q_v(t)\right) dt$$

(3-11)

3.2.2.4 Energy Losses

There are multiple ways in which the aortic valve can lose energy. During forward flow, the transaortic pressure drop across the valve results in a loss of energy in the fluid. Regurgitation back through the valve during valve closure, and leakage around and through the valve when the leaflets are closed are both ways in which the efficiency of the stroke volume is decreased. These energy losses incurred during each simulated cardiac cycle provided a consolidated value of valve performance, and a method of comparing the forward flow inefficiencies of one valve with the regurgitant volumes of another. The following integrals were used to calculate the forward (E_f), closing (E_c), and leakage (E_l) energy losses (in mJ) respectively, in accordance with the findings of Leefe and Gentle[223]:

$$E_f = k_f * \int_{F1}^{F2} \Delta p * \left(q_v(t)\right) dt$$

(3-12)

$$E_c = k_f * \int_{F2}^{F3} \Delta p * \left(q_v(t)\right) dt$$

(3-13)

$$E_l = k_f * \int_{F3}^{F4} \Delta p * \left(q_v(t)\right) dt$$

(3-14)

where k_f is a constant conversion factor of 0.1333, to convert from mmHg*ml to mJ.

3.3 Particle Image Velocimetry – TSI PIV System

Whilst pulse duplicators are ideal for capturing the global flow parameters performed by the tested valve, they give little information about the local flow parameters, i.e. specific instants within each cardiac cycle. The unsteady nature of fluid flow in the aortic region makes full field measurement of instantaneous velocities highly desirable[224]. With careful setup, Particle Image Velocimetry (PIV) can provide information about the velocity fields by seeding the flow with neutrally buoyant particles, and then calculating particle displacement between two images of a cross-section of the flow over a known period of time. If the seeding particles are sufficiently neutrally buoyant and reactive to the flow, the displacement of the particles can be taken as the same as the displacement of the fluid carrying them, thus elucidating information about the flow to enable further valve performance improvements. A schematic of a basic PIV setup is presented in Figure 3-4.

Unlike Particle Tracking Velocimetry, a Lagrangian technique where the seeding of the flow is much less dense and each particle is continually traced as it travels with the flow, PIV is a Eulerian technique that takes a pair of images of the same illuminated cross-section of a flow, separated by a short time interval. A grid is applied to the images, and patterns of particles are identified and matched across the two images via a process known as 'cross-correlation', under the assumption that the pattern of these particles will change minimally over the time period[225]. The displacement of the pattern over the time frame is assumed to be the velocity of the fluid in that particular interrogation spot, and this is repeated across the areas of interest of the image pair of the cross-section[225].

The following sections describe the process of data acquisition and processing to obtain vector fields representing the flow cross-section using the INSIGHT™ 4G-2DTR (TSI Inc., Minnesota, USA, version number 10.0.3.30) software.

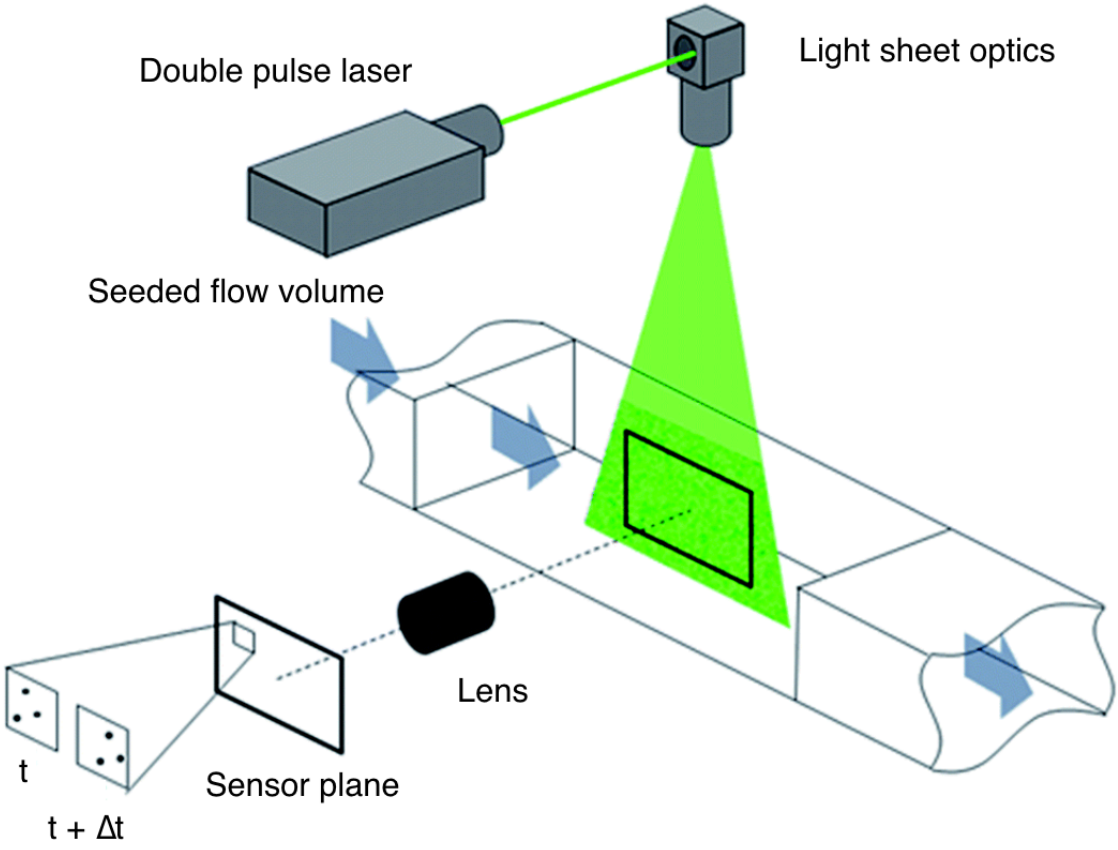

Figure 3-4: PIV schematic [adapted from Sun 2015[226]], showing a seeded flow being illuminated by a laser sheet, and image pairs, separated by a time interval of Δt captured by a CCD camera positioned perpendicularly to this laser sheet

3.3.1 Image Capturing

The PIV measurement system consisted of a laser, a synchroniser, a camera, and vector processing/imaging software, as shown as a schematic in Figure 3-4. The use of a double pulse Nd:YAG laser (YAG70-15-QTL, TSI Inc., Minnesota, USA) was ideal due to its high amplification, good mechanical and thermal properties, ease of use in a triggered mode (allowing for synchronisation with the pulse duplicator system), and fine adjustment of Δt[225]. A laser beam with a wavelength of 532 nm was produced, that was passed through a series of lenses, manipulating the beam into a thin light sheet, with thickness 0.4 mm. To prevent artefacts, external light sources were switched off, and reflective surfaces not directly required for data acquisition were covered up during testing.

As the speed of light changes when it passes from a medium of one density into a medium of another density, any light beams that are not orthogonal to the interface of the two mediums may be displaced, rotated, or distorted[227]. The

Refractive Index (RI, symbolized as n) of a material is the ratio between the velocity of light in free space (or, for practical purposes, in air) and the velocity of light in the material in question, with a greater amount of light beam deflection/distortion/etc occurring when the RI difference between the two mediums is greater. The transparent pulse duplicator chamber wall that the camera imaged through was flat and aligned perpendicularly to the camera, so that the RI difference between the air, the acrylic wall of the pulse duplicator, and the working fluid did not distort the image. Similarly, the transparent pulse duplicator chamber wall that the laser sheet was directed against was also aligned perpendicularly with the laser sheet, to minimise any distortion of the laser sheet shape. However, as the replication of the physiological geometry included curved surfaces, it was important to match the RI of the working fluid to that of the transparent, silicone mock root, in order to reduce optical distortion of the PIV images as a result of light refraction.

The laser was positioned so that the light sheet illuminated the central sagittal plane of the aortic root within the pulse duplicator, as shown in Figure 3-5, and was triggered upon receiving a signal from a synchroniser (LaserPulse™ Synchroniser, Model 610036, TSI Inc., Minnesota, USA). This synchroniser was in turn connected to two computers, one for the PIV system and one for the pulse duplicator. This enabled the PIV system to repeatedly capture images from specific instants within the mock cardiac cycle as detected by the pulse duplicator system, allowing for phase-averaging over multiple image pairs. This synchronisation is denoted as a 'trigger delay' and is referenced in ms from the instant of the first forward motion of the pump in each cycle.

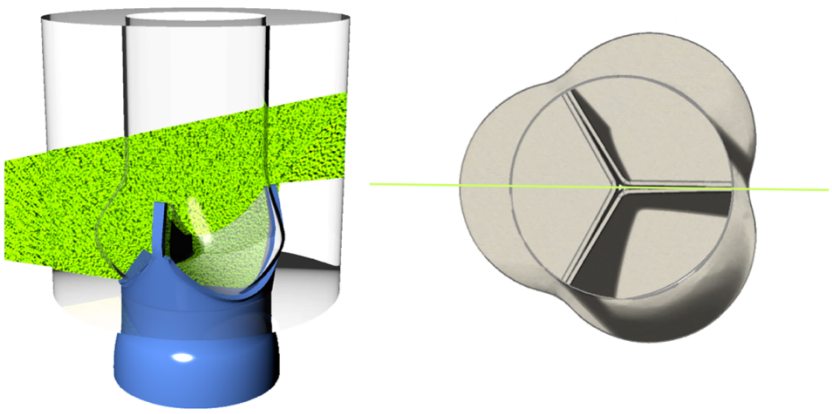

Figure 3-5: Diagram of laser sheet for PIV positioned over cross-section of valve-root configuration under investigation

Once synchronised with the pulse duplicator, two pulses were fired by the laser, separated by time Δt (μs), at specific moments within the pulse duplicator's cycle, e.g. peak forward flow, for a pre-determined number of cycles. Small, neutrally buoyant tracer particles (HGS-10, Dantec Dynamics, Denmark) were added to the testing fluid inside the pulse duplicator, scattering any light incident upon them. The response time, τ_s (s), of these particles to the fluid flow, indicating the delay between a change in motion of the fluid and a complimentary change in motion of the particles moving within that fluid, is calculated by[225]:

$$\tau_s = \frac{d_p^2 \rho_p}{18\mu} \tag{3-15}$$

where d_p is the mean diameter of the seeding particles (1 x 10^{-5} m), ρ_p is the density of the seeding particles (1100 kg/m^3), and μ is the dynamic viscosity of the working fluid (Pa.s). Any difference between the densities of the working fluid and the seeding particles will also lead to a gravitationally induced velocity, $\boldsymbol{U}_g$ (m/s), acting upon the particles, equal to:

$$\boldsymbol{U}_g = \frac{d_p^2(\rho_p - \rho)}{18\mu}\boldsymbol{g} \tag{3-16}$$

where ρ is the density of the working fluid (kg/m^3), and $\boldsymbol{g}$ is acceleration due to gravity (m/s^2). As different working fluids were used at different stages of the investigations, the response times and gravitationally induced velocities of the seeding particles in the various working fluids are calculated and discussed in Sections 3.6.2 and 3.6.3.

A frame-straddling CCD camera (with a resolution of 2048 x 2048 pixels, TSI PowerView™ Plus 4MP, TSI Inc., Minnesota) with a 52 mm lens (Nikon, Japan) is also connected to this system, and takes an image perpendicular to the laser sheet, corresponding to each of the two laser pulses in each cycle, one at time t and one at time $t + \Delta t$. A longer Δt is required for a slower moving flow and is calculated according to the one-quarter rule[225], which suggests that 'the maximum displacement of a particle should not exceed 1/4 of the size of the

interrogation spot' (refer to Section 3.3.2.2.1 for a description of the interrogation spot). This was related to the flow through the aortic valve as:

$$\Delta t = \frac{n_{spot} * k}{4 * v_{max}} \tag{3-17}$$

where n_{spot} is the final interrogation spot size (pixels), k is the μm to pixel ratio (defined in the calibration process below, and which provides the magnification factor from equations (3-21) and (3-23), and v_{max} is the maximum flow velocity detected through the flow transducer (m/s), to give Δt (μs). However, the flow will be considerably slower in the sinuses than in the central jet-like flow during systole. The central jet-like flow may also be faster than the flow past the transducer, as the orifice created by the valve leaflets may be smaller than the orifice created by the flow transducer. As a result, it is necessary to capture images from each instant with various values of Δt to fully reveal the fastest and slowest flow behaviour within the aortic root.

3.3.2 Image Processing

The two images from each cycle are transferred to the computational system for processing. Cross-correlation is used to identify matching particle patterns in the two images, determining the distance these patterns have moved during Δt, and translating this into a velocity measure, as described in Section 3.3.2.2.1. In the practicalities of the experiment, this cross-correlation consisted of pre-processing, processing, and post-processing. A flow chart illustrating the image processing steps is presented in Figure 3-6.

3.3.2.1 Pre-processing

In order to perform the cross-correlation, several steps of pre-processing were needed to prepare the images and extract important information. The magnification factor, M, is required to relate the positions of the particles in the images to the positions of the particles in the interrogation volume and is provided by the μm to pixel ratio. Within the interrogation volume and captured by the images was an object of predetermined physical length, which was used to determine the μm to pixel ratio. This varied according to the focus of the camera lens, and a range of 20-25 μm/pixel was measured across the

experiments. Next, a processing mask was applied to the image pairs, to save computing time by ensuring that only vectors within the processing mask, i.e. the image area of interest, were computed. This mask was altered for the different instants within the cycle, as the physical environment changed position due to the unsteady flow rate and pressures throughout the cycle.

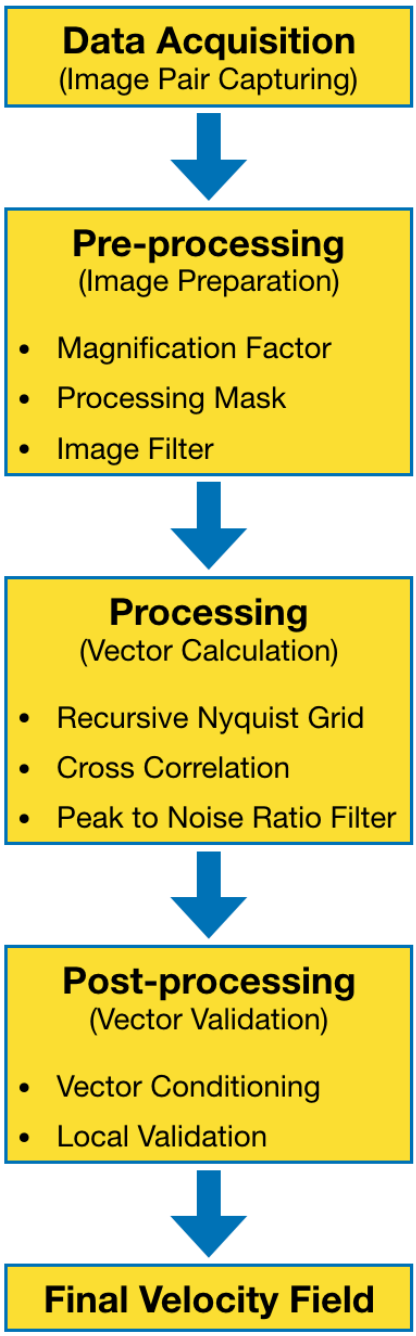

Figure 3-6: Flowchart illustrating the PIV processing protocol

The final step of pre-processing was to apply an image pre-processor, labelled as 'Image Filter', to modify the image for improved vector mapping. The value of any given pixel in the output image is determined by applying an algorithm to

the value of the pixels in the neighbourhood or corresponding input pixel. A Gaussian low-pass filter uses rotationally symmetric kernels and a standard deviation of σ = 0.6 to effectively blur the particles so that they encompass a larger area and encompass more pixels to allow for improved recognition during processing.

3.3.2.2 Processing

Once the images have been prepared via pre-processing, the processing stage begins. The image is divided into smaller spots for vector field processing. In order to achieve the Nyquist sampling criterion required that to adequately reproduce a signal (in this case, the image), it should be sampled at twice the highest resolution required[228]. The interrogation spot size is denoted by n_{spot} from equation (3-17), and the vectors of the grid are set with the x-spacing equal to n_{spot} width divided by 2, and the y-spacing equal to n_{spot} height divided by 2. As all the interrogation spots were square in these experiments, the x-spacing was equal to the y-spacing.

The image pairs are processed in two passes, with the first pass, using a spot size of 64 x 64 pixels, with 50% overlap spacing providing information for the displacement of the correlation group of particles over Δt, which can be used by the second pass to use a smaller spot size, half the height and width of the first spot size, with double the number of vector rows and columns, leading to 4 times the number of vectors calculated. This smaller spot size can be used because the spot analysing the t' image is offset by the pixel displacement calculated from the first pass, so that the centre of the particle pattern is at the centre of the interrogation spot for the t' image. This method of using two or passes that achieve the Nyquist sampling criterion is labelled as a 'Recursive Nyquist Grid'.

3.3.2.2.1 Cross-correlation

A cross-section of the investigated flow is illuminated by a thin laser sheet, and the flow is seeded with particles that are illuminated by this laser sheet. The illuminated volume is split up into many smaller interrogation volumes, where each volume contains between 5 and 15 particles[225]. The position of N particles, $\mathbf{\Gamma}$, in any given interrogation volume at time t is given by[225]:

$$\boldsymbol{\Gamma} = \begin{pmatrix} \boldsymbol{X_i} \\ \vdots \\ \boldsymbol{X_N} \end{pmatrix}$$

(3-18)

where the position of particle i is given by[225]:

$$\boldsymbol{X_i} = \begin{pmatrix} X_i \\ Y_i \\ Z_i \end{pmatrix}$$

(3-19)

If an image of this interrogation volume is taken in the $\begin{pmatrix} x \\ y \end{pmatrix}$ plane, the position of each particle in the image can be represented by[225]:

$$\boldsymbol{x_i} = \begin{pmatrix} x_i \\ y_i \end{pmatrix}$$

(3-20)

Assuming the image of the volume is perfectly in alignment with the $\begin{pmatrix} x \\ y \end{pmatrix}$ plane of the volume, the position of the particles in the volume and in the image are related by a magnification factor, M, specific to the imaging technique[225]:

$$X_i = \frac{x_i}{M} \quad \text{and} \quad Y_i = \frac{y_i}{M}$$

(3-21)

Vector $\boldsymbol{D}$ represents the average of the displacement of the particles within the interrogation spot over incremental time period Δt, so that the position of the particles at time t', where $t' = t + \Delta t$, is given by[225]:

$$\boldsymbol{X_i'} = \boldsymbol{X_i} + \boldsymbol{D} = \begin{pmatrix} X_i + D_X \\ Y_i + D_Y \\ Z_i + D_Z \end{pmatrix}$$

(3-22)

The displacement of the particles, $\boldsymbol{d}$, in the volume within the plane illuminated by the laser field can be related to the displacement of the particles in the image by the same magnification factor, M, as used for the calculation of the position

of the particles in the volume in relation to the position of the particles in the image, given by[225]:

$$\boldsymbol{d} = \begin{pmatrix} MD_x \\ MD_y \end{pmatrix} \tag{3-23}$$

The image intensity field, $\boldsymbol{I}$ representing the light in the image received from the particles in the interrogation spot, for the interrogation spots at time t is given by[225]:

$$\boldsymbol{I}(\boldsymbol{x}, \boldsymbol{\Gamma}) = \sum_{i=1}^{N} V_0(\boldsymbol{X_i}) \tau(\boldsymbol{x} - \boldsymbol{x_i}) \tag{3-24}$$

and the image intensity field at time t', $\boldsymbol{I}'$, by[225]:

$$\boldsymbol{I}'(\boldsymbol{x}, \boldsymbol{\Gamma}) = \sum_{j=1}^{N} V_0'(\boldsymbol{X_j}) \tau(\boldsymbol{x} - \boldsymbol{x_j} - \boldsymbol{d}) \tag{3-25}$$

where $\tau(\boldsymbol{x})$ represents the point spread function of the lens (considered to be identical for all particle positions), and $V_0(\boldsymbol{X_i})$ and $V_0'(\boldsymbol{X_j})$ are transfer functions representing the light energy of the particles in the respective instants.
Considering the light sheet and interrogation volumes as identical, the cross-correlation function, R_{11}, of these two interrogation areas can be written as[225]:

$$R_{11}(\boldsymbol{s}, \boldsymbol{\Gamma}, \boldsymbol{D}) = \frac{1}{a_I} \sum_{i,j} V_0(\boldsymbol{X_i}) V_0\big(\boldsymbol{X_j} + \boldsymbol{D}\big) \int_{a_1} \tau\,(\boldsymbol{x} - \boldsymbol{x_i}) \tau\big(\boldsymbol{x} - \boldsymbol{x_j} + \boldsymbol{s} - \boldsymbol{d}\big) dx \tag{3-26}$$

where $\boldsymbol{s}$ is a separation vector in the correlation plane and a_I is the interrogation area.
By assuming that the $i \neq j$ terms represent the randomly distributed particles, i.e. primarily noise in the correlation plane made up from the convolution of the mean intensities and a fluctuating noise component, and that the $i = j$ terms contain the sought-after displacement information, i.e. the detection of an

identical group of particles in both times t and t', equation (3-26) can be re-represented so that the two term types can be distinguished from each other[225]:

$$R_{11}(\boldsymbol{s},\boldsymbol{\Gamma},\boldsymbol{D}) = \sum_{i\neq j} V_0(\boldsymbol{X_i})V_0\big(\boldsymbol{X_j}+\boldsymbol{D}\big)\,R_\tau\big(\boldsymbol{x}-\boldsymbol{x_j}+\boldsymbol{s}-\boldsymbol{d}\big)$$

$$+R_\tau(\boldsymbol{s}-\boldsymbol{d})\sum_{i=1}^{N} V_0(\boldsymbol{X_i})V_0(\boldsymbol{X_i}+\boldsymbol{D})$$

(3-27)

This component of R_{11} can be represented by R_D, given by[225]:

$$R_D(\boldsymbol{s},\boldsymbol{\Gamma},\boldsymbol{D}) = R_\tau(\boldsymbol{s}-\boldsymbol{d})\sum_{i=1}^{N} V_0(\boldsymbol{X_i})V_0(\boldsymbol{X_i}+\boldsymbol{D})$$

(3-28)

which provides a maximum cross-correlation peak at $\boldsymbol{s}=\boldsymbol{d}$, as illustrated in Figure 3-7, and the location of this peak gives the average in-plane displacement and hence the U and V components of the velocity of the group of particles analysed.

For each interrogation spot, the highest correlation map pixel was assumed to be the particle image displacement peak, with the other peaks in the correlation map taken to be noise peaks created by random pairings of different particle patterns. The correlation peak was found by fitting a Gaussian curve to the highest pixel and its four nearest pixels. 3-point fits in the x-direction and y-direction were done, on the peak pixel and each pixel to the left and right of (for the x-direction) or above and below (for the y-direction) this peak pixel, was done. The Gaussian peak equation was defined as:

$$dx = x + \frac{(\log(l)-\log(r))}{2(\log(l)+\log(r)-2\log(c))} - x_0$$

(3-29)

where the intensity values for left, right and peak pixels in the correlation map are denoted by l, r, and c respectively, x is the integer shift and x_0 is the zero-shift location. A Peak to Noise-Peak ratio threshold of 1.3 was applied, so any correlation peaks less than 1.3 times the height of the biggest noise peak in the

same correlation map were rejected and labelled as ‘bad’ vectors. Those that passed this requirement were labelled as ‘good’ vectors.

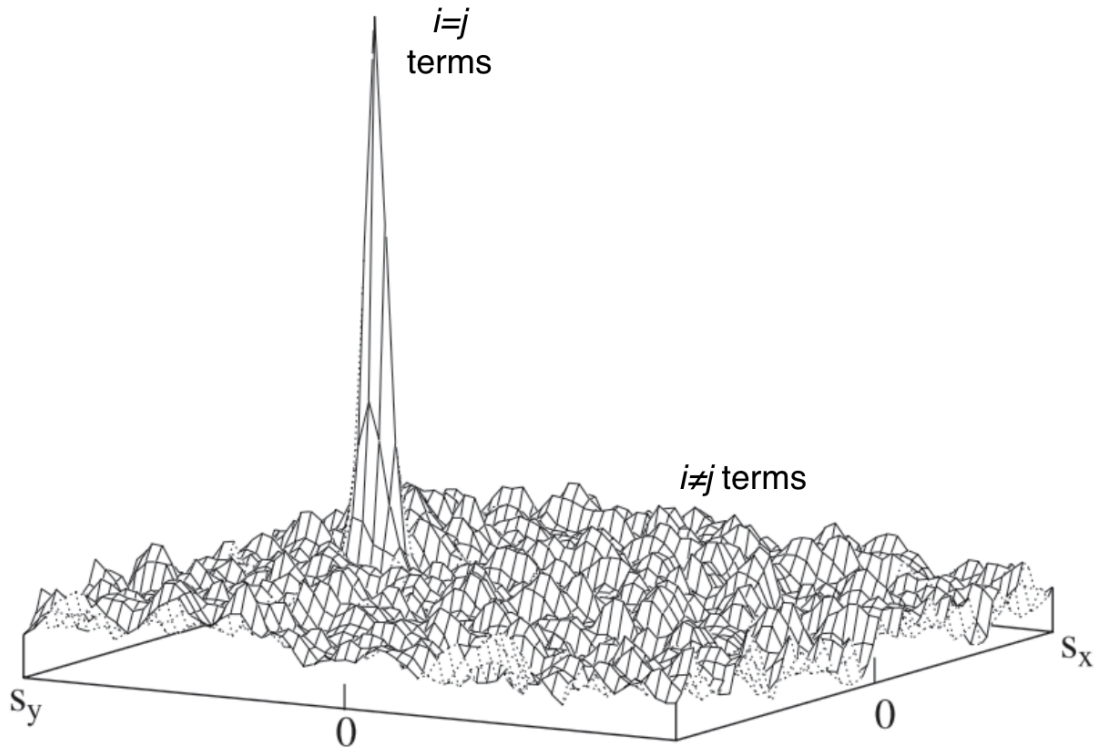

Figure 3-7: Composition of peaks in the cross-correlation function [adapted from Raffel 2007[225]]

3.3.2.3 Post-processing

After this processing, vector validation, or post-processing, is undergone, with two post-processor functions utilised. The first function was labelled as ‘Vector Field Conditioning’, and the resultant vectors were labelled as ‘interpolated’ vectors. These ‘interpolated’ vectors were then validated by the second post-processor function, which compared each new vector with a reference vector equal to the median velocity of all the vectors within its 5 x 5 neighbourhood. The new vector was re-designated as ‘bad’ if its value was not within a tolerance range of the reference vector, with a tolerance of $dU = dV = 2$ pixels. The second function, ‘Local Validation’, filled holes in the vector field, which were primarily due to vectors failing the Peak to Noise-Peak ratio requirements. The holes were filled by the mean vector of neighbourhood vectors, with a minimum of 3 ‘good’ neighbour vectors needed in a 5 x 5 neighbourhood.

After post-processing, the calculated vectors designated as ‘good’ or ‘interpolated’ were included in the exported vector field, with the ‘bad’ vectors excluded from this matrix.

3.3.3 Data Analysis

3.3.3.1 Vector Properties

The vector fields generated by the processes of Section 3.3.2 were used to quantify and illustrate the investigated flow. The velocity fields derived from all of the image pairs for a given instant were averaged. Calculating the velocity of the flow enables elucidation of the flow structures present in the flow, such as vortical structures, separation regions, and stagnant volumes, and was derived from the vectors by the following equation:

$$v_{mag} = \sqrt{U^2 + V^2} \tag{3-30}$$

where v_{mag} is the velocity magnitude of the vector (m/s), U is the x component of the vector (m/s), and V is the y component of the vector (m/s).

When a flow is laminar, the fluid flows in parallel layers, with little disruption between the layers of flow, and little lateral mixing. As a flow speeds up and traverses more complex geometry, the flow may become turbulent, characterised by eddies and mixing of the layers of flow. As turbulence has been linked with elevated wall and blood stress, leading to increased endothelial damage, blood damage and thrombosis[37,85–89], information on the level of turbulence within a flow is desirable. The Reynolds equation can be used in steady (as opposed to pulsatile) flows, characterising flow according to the density, viscosity, and average speed of the flow alongside the diameter of the vessel it is flowing through, to dichotomise flows as laminar or turbulent, but is of less applicability in the pulsatile flows generated by a pulse duplicator, and give little discrete information across a cross-sectional image. By assuming that regions of greater turbulence will have a greater amount of cycle-to-cycle variation in the phase-resolved calculations of velocity for each node in those regions, the standard deviation of the velocity can be related to the turbulence of the flow, with a greater standard deviation of velocity for a particular node

over the image pairs of a specific pass indicating a greater fluid turbulence in that part of the flow. The presence of turbulence in blood flow results in a loss of energy and can lead to blood damage and haemolysis[88,89]. This standard deviation was calculated via:

$$SD_{turb} = \sqrt{U'^2 + V'^2} \tag{3-31}$$

where SD_{turb} is the standard deviation representing turbulence in the flow, and U'^2 and V'^2 are the standard deviations of the u and v components of the velocity respectively. U' for each node is calculated via:

$$U' = \sqrt{\frac{\sum(U - \overline{U})^2}{n}} \tag{3-32}$$

where $\overline{U}$ is the mean u component of velocity for that node across the image pairs, and n is the number of image pairs. The V' component of SD_{turb} is worked out in the same way, but for the v components of the velocity.
The Reynolds shear stress (RSS) (derived from the effect of convective acceleration upon the mean velocity profile, i.e. related to the shear stresses between layers of the fluid caused by temporal variations in the velocity field) has been related to blood damage potentially leading to haemolysis[37,89,90], as detailed in Section 2.1.3.1.2, and so provides useful information for the investigation. By establishing the fluctuating component of the x- and y-velocities at node i,j ($u'_{i,j}$ and $v'_{i,j}$ respectively) from:

$$u'_{i,j} = u_{i,j} - U_{i,j} \tag{3-33}$$

and

$$v'_{i,j} = v_{i,j} - V_{i,j} \tag{3-34}$$

where $u_{i,j}$ and $v_{i,j}$ are the instantaneous x- and y-velocities at node i,j (i.e. at location x_i, y_j), and $U_{i,j}$ and $V_{i,j}$ are the mean x- and y-velocities at node i,j, the RSS is derived from the vector field by multiplying the following equation by the density of the fluid:

$$(-u'v')_{i,j,avg} = \frac{1}{N}\sum -u'_{i,j}v'_{i,j}$$

(3-35)

The vorticity of the flow describes the spinning motion of the flow at each point, giving an indication of the intensity of a vortex or the degree of washout of a volume within the flow. The vorticity component orthogonal the plane of measurement for each point, ω_z (s^{-1}), is defined as:

$$\omega_z = \frac{dv}{dx} - \frac{du}{dy} = \frac{v_{i+1,j} - v_{i-1,j}}{x_{i+1,j} - x_{i-1,j}} - \frac{u_{i,j+1} - u_{i,j-1}}{y_{i,j+1} - y_{i,j-1}}$$

(3-36)

3.3.3.2 Streamlines

Calculating and illustrating the streamlines of the velocity fields generated provided enhanced visualisation of the cross-section, highlighting wash-out regions, vortices, and stagnant, unstructured regions of flow. A streamline is defined as a line which is tangent to the instantaneous velocity field, as illustrated in Figure 3-8.

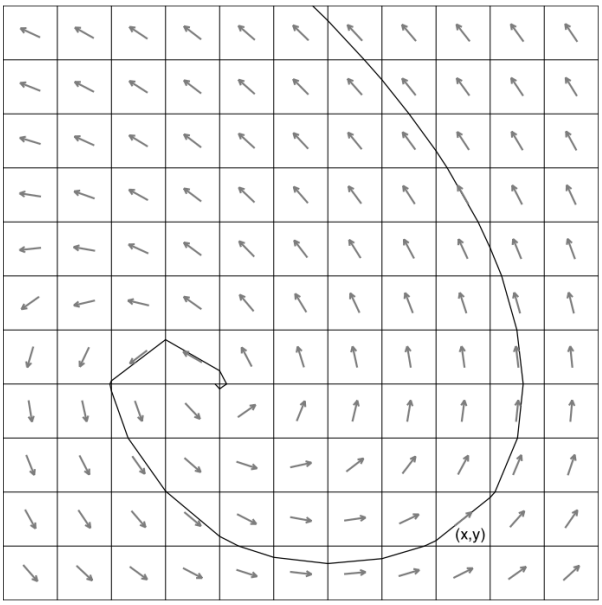

Figure 3-8: Example of a streamline derived from instantaneous velocity field[229]

3.3.3.3 PIV Velocity Uncertainty

An error on the velocity calculated by the above methodology is inherently present, due to the random error on the determination of the finite interrogation windows within sub-pixel accuracy, and this uncertainty is calculated as the smallest measurable displacement divided by the time spacing at each acquisition point[225]. As the maximum absolute uncertainty of the measured displacement is around 0.1 pixels[225], the velocity uncertainty, v_ϵ, is calculated via:

$$v_\epsilon = \frac{k * 0.1}{\Delta t} \qquad 3\text{-}37$$

3.3.3.4 Image Pair Quality

Due to the practicalities of testing, a balance between the time taken to acquire and process the data and the quality of the final vector maps was required. 1000 image pairs were captured as described in Section 3.3.1 and processed as described in Section 3.3.2, at peak flow of the ideal surgical configuration, described fully in Section 4.2. The velocity component for each node of the cross-section was calculated as described in Section 3.3.2, and then the standard deviation of the velocity magnitudes across the image pairs for each equivalent node was calculated. The average standard deviation of each quantity of image pairs was then calculated by taking the mean of the standard deviations for all of the nodes of the cross-section across the chosen quantity of image pairs. The resultant mean standard deviations for each quantity of image pairs are displayed in Table 3-1 and Figure 3-9.

As a result of this analysis, a selected number of 100 image pairs for each value of Δt being investigated at each instant, as this was a good balance of acquisition and processing time with quality of results, with an error $< 0.19\%$ compared to the standard deviation of the average of 1000 image pairs for each value of Δt.

Image Pairs	*Standard Deviation (%)*
20	2.6762
50	2.6819
100	2.6383
200	2.6339
350	2.6337
500	2.6334
750	2.6334
1000	2.6334

Table 3-1: Standard deviation of velocities calculated via PIV

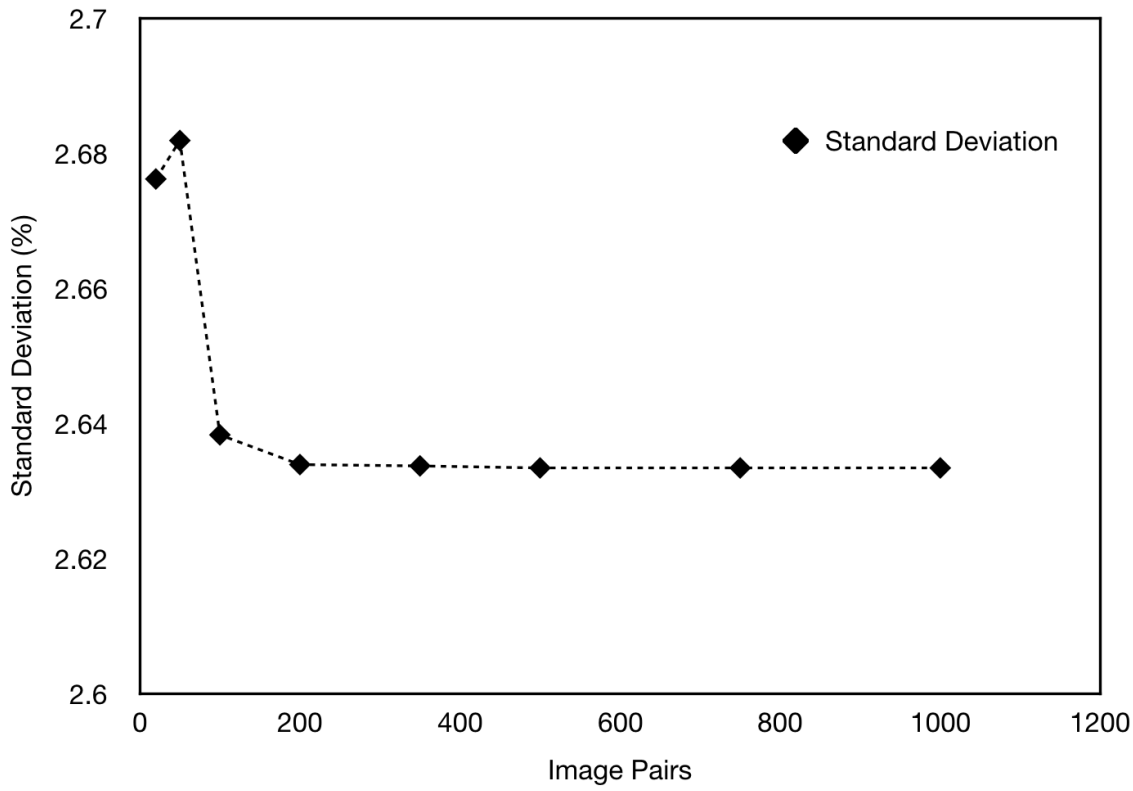

Figure 3-9: Variation of standard deviation of velocity with quantity of image pairs

3.4 Valves

3.4.1 Aortic Valves

Four different aortic valves were used to represent the various root-valve configurations in these studies - two surgical porcine valves with external diameter 25 mm and 29 mm, a transcatheter aortic valve replacement, and an integrated mock root-valve manufactured from silicone.

3.4.1.1 Labcor TLBP Surgical Valves

The two bioprosthetic surgical valves used in this report, a TLPB 25 aortic valve, Model TLPB A Supra, size 25, and a TLPB 29M mitral valve, Model TLPB M, size 29 (Labcor Laboratórios Ltda, Brazil). These valves are currently in usage as aortic and mitral valve surgical replacements, with over 100,000 implanted worldwide, and demonstrate good haemodynamic performance in comparison with other bioprostheses[230,231]. The valves are presented in Figure 3-10, with the relevant dimensions given in Table 3-2. The valves consist of a stented frame, to which three separated and GA treated porcine valve leaflets are attached in a tri-composite arrangement, mounted upon an acetal copolymer frame and covered with polyester fabric. The positioning of the sewing ring at the inflow level of the valve allows for supra- or intra-annular valve implantation.

The TLPB 25 aortic valve was used to model the aortic valve in the following experiment setups:

- Chapter 4, setup ii – optimal surgical aortic root
- Chapter 4, setup iii – sinusless aortic root
- Chapter 4, setup iv – sub-annular aortic root
- Chapter 4, setup v - dilated root/undersized valve aortic root

The TLPB 29 aortic valve was used to model the aortic valve in the following experiment setup:

- Chapter 4, setup i – physiological aortic root

Valve	*Diameters (mm)*			*h_p (mm)*
	D_i	*D_o*	*D_{sr}*	
TLPB 25	23	25	27	13
TLPB 29M	26	29	31	9

Table 3-2: Dimensions of surgical valves. D_i – inner diameter; D_o – outer diameter; D_{sr} – suture ring diameter; h_p – downstream projection from basal annulus after implantation

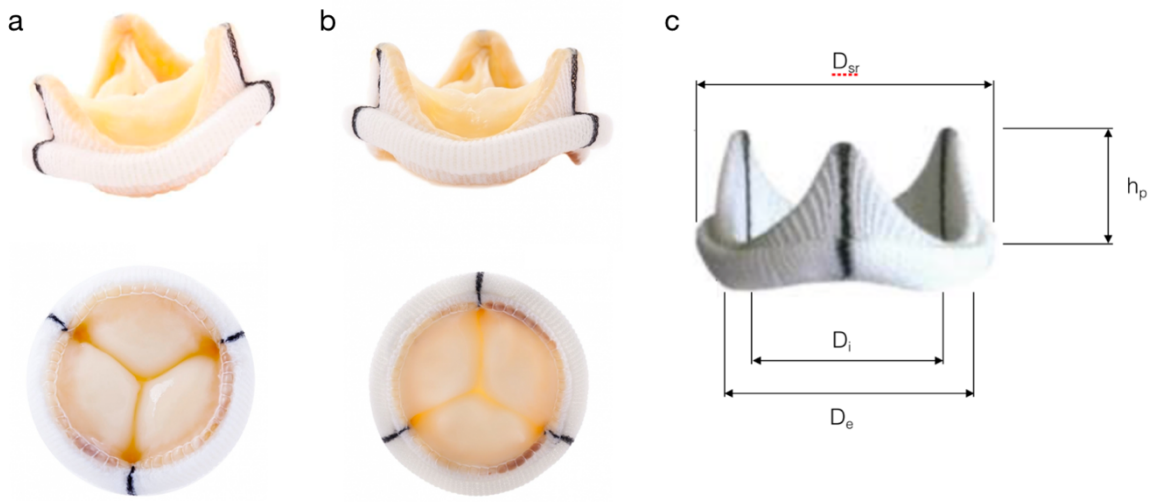

Figure 3-10: Surgical aortic valves: (a) TLPB A Supra; (b) TLPB M; (c) description of valve dimensions, for reference with Table 3-2, where D_{SR} is the suture ring diameter, D_i and D_o are the inner and outer diameters of the leaflet frame respectively, and h_p is the downstream projection of the valve from the basal annulus.

3.4.1.2 Sorin Bicarbon Mechanical Valve

The mechanical aortic surgical valve utilised in this report was the Sorin Bicarbon 25 (Sorin Group, Italy), a bi-leaflet mechanical valve, composed of two curved pyrolytic carbon leaflets in a titanium housing ring, surrounded by a PET suture ring cover, and coated with Carbofilm. The valve and its dimensions are shown in Figure 3-11. There is no protuberance of the leaflets into the upstream (ventricular) chamber. The valve was used with its suture ring removed, and an o-ring fitted instead, which was then put into a custom-made housing for use in the pulse duplicator.

The Sorin Bicarbon 25 mechanical valve was used to model the aortic valve in the following experiment setup:

- Chapter 4, setup vi – mechanical aortic root

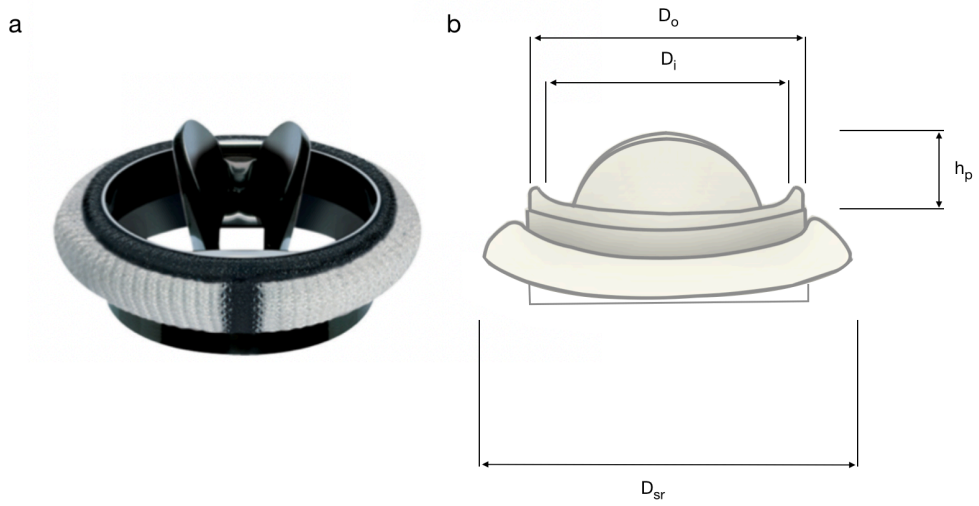

Figure 3-11: Mechanical aortic valve. (a) Sorin Bicarbon 25; (b) description of valve dimensions D_i is the diameter of the orifice (21.3 mm), D_o is the outer diameter of the rigid carbon frame (25.6 mm), D_{sr} is the outer diameter of the suture ring (28.2 mm), and h_p is the distance the fully open disc axially projects into the downstream (aortic) chamber from the basal annulus (6.0 mm). The semilunar leaflets are convex–concave shaped and tilt up to 80° and close at 20°, with a maximum central orifice width of 10.0 mm, and side orifices with a maximum width of 6.7 mm

3.4.1.3 Edwards SAPIEN XT Valve

The transcatheter valve used in this report was a 26 mm Edwards SAPIEN XT, a transcatheter valve system clinically utilised around the world[232]. The valve and its dimensions are presented in Figure 3-12, and it consists of a cobalt-chromium balloon-expandable cellular frame into which three separate and GA fixed pieces of bovine pericardium are attached. A fabric polyethylene terephthalate skirt is attached to the upstream side of the valve, to reduce leakage.

The 26 mm Edwards SAPIEN XT was used to model the aortic valve in the following experiment setups:

- Chapter 5, all aortic root configurations (TA1-4)
- Chapter 6, all aortic root configurations (NoCA, LCA, RCA, and NCA)

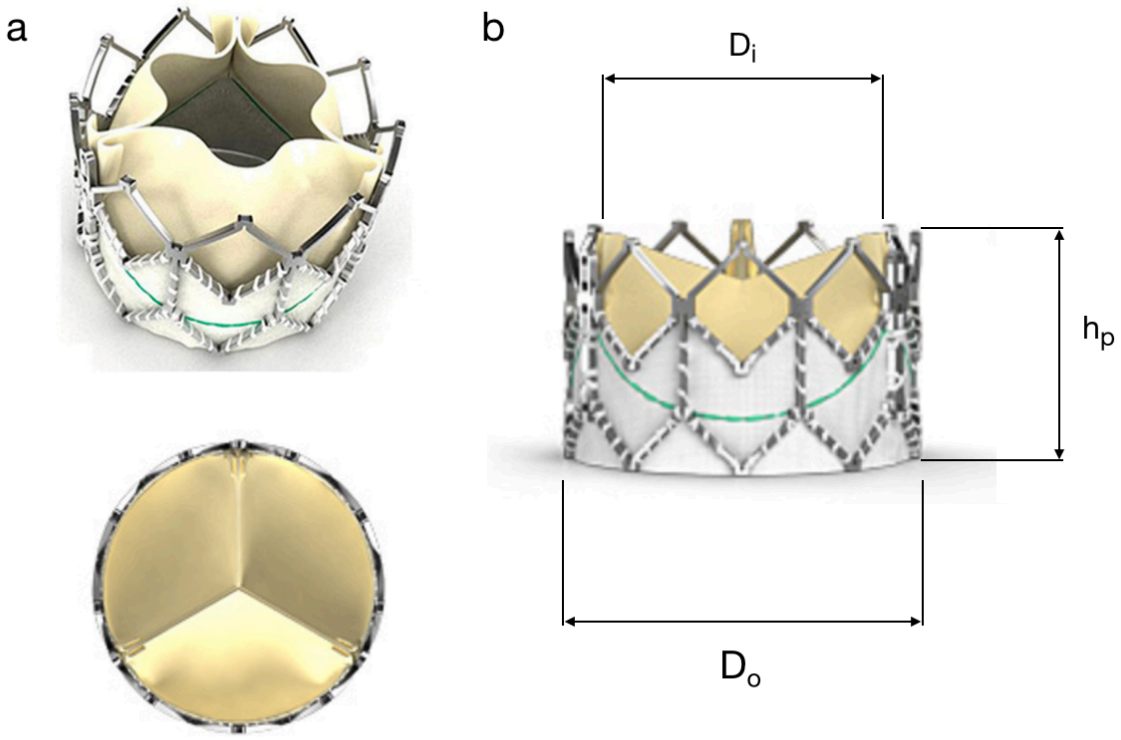

Figure 3-12: Transcatheter Aortic Valve: (a) Edwards SAPIEN XT 26 valve, in open and closed configurations; (b) description of valve dimensions, where D_e and D_i are the external and internal diameters of the frame (26.0 mm and 25.2 mm respectively), and h_p is the total height of the frame(17.2 mm).

3.4.1.4 Mock Human Healthy Aortic Valve

To simulate the native root-valve system, a silicone valve was integrated into one of the silicone roots described in Section 3.5. The valve was based upon the description of an idealised healthy human closed valve as provided by Thubrikar[126], scaled to a basal annulus size of 25 mm, shown in Figure 3-13(a). A 3D-model of the valve was produced using SolidWorks (Dassault Systemes, France). As the TLBP bioprosthetic valve described in Section 3.4.1.1 is characterised by a semi open shape when at rest in saline solution, and silicone has a micro structure different to that of fibrous tissue (affecting the opening dynamics of the leaflet, in particular the change in leaflet shape from closed to open), a pre-expansion procedure was undertaken on the 3D model, undertaken by Anna Maria Tango (PhD candidate, Mechanical Engineering, UCL), using a pre-expansion Fluid Structure Interaction procedure in the explicit finite element software LS Dyna (Release 9.2, LSTC, Livermore, CA, USA). The leaflets were modelled as linearly elastic, with a Young's modulus of 1 MPa, a Poisson's ratio of 0.45, and a uniform thickness of 0.5 mm. The expansions

were achieved by applying a uniformly distributed opening pressure of 5 mmHg to the leaflets' belly, resulting in the model presented in Figure 3-13(b). The annulus of the modelled valve was then modified to transition into a tapered lower part, matching the lower parts of the root cores described in Section 3.5.2, as shown in Figure 3-13(c).

This 3D model was converted into an .stl file, and printed on a stereolithographic 3D printer (Form 2, Formlabs, USA) to produce a polymerized resin model of the closed valve, as presented in Figure 3-13(d). This was dip-coated with silicone (Transil 40-1, Mouldlife, Bury St Edmunds, UK) than that used for the roots as described in Section 3.5.2, as the resultant cured silicone would need to be dynamically responsive and operate as a working valve, but did not need to be optically clear. The dip coated mould was inverted and left to cure for 24 hours at 25°C, before removing the cured silicone from the mould, and trimming away unwanted material, resulting a final silicone valve as displayed in Figure 3-13(d), with leaflet thickness of 0.39 ± 0.04 mm.

This silicone valve-root was used to house the 26 mm Edwards SAPIEN XT valve in the following experiment setups:

- Chapter 6, all aortic root configurations (NoCA, LCA, RCA, and NCA)

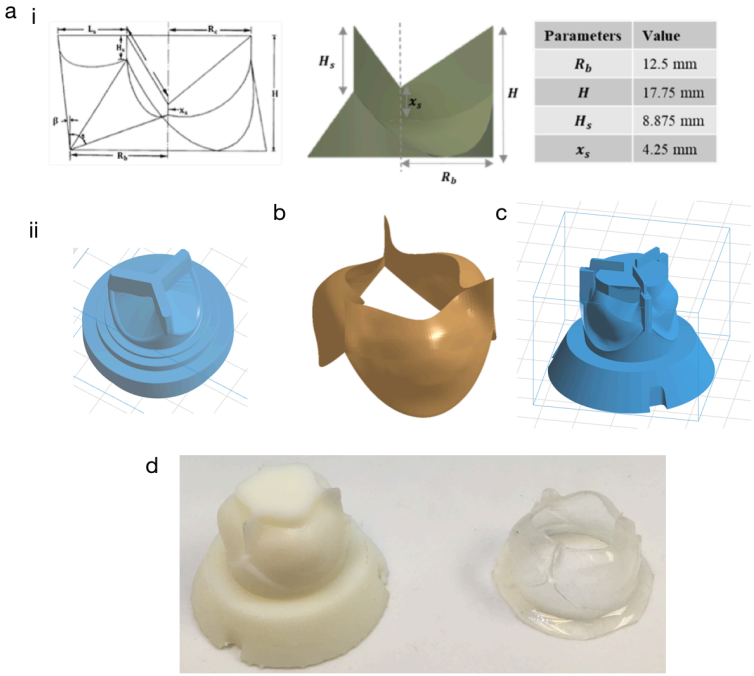

Figure 3-13: Design and manufacture of silicone valve: (a) i - dimensions of closed Thubrikar valve, scaled to a basal annulus size of 25 mm, ii - .stl model of closed valve; (b) semi open valve after numerical expansion; (c) .stl model of semi-open valve; (d) 3D printed model of valve and resultant cured and trimmed silicone valve

3.4.2 Mitral Valve

A mechanical surgical mechanical valve was used to represent the mitral valve throughout all investigations using the pulse duplicator.

3.4.2.1 Sorin Allcarbon

A Sorin Allcarbon 29 mm (Sorin Group, Italy) was employed in the mitral valve position of the pulse duplicator. This is a tilting disc valve, with a pyrolytic carbon disc housed in a cobalt-chrome ring, surrounded by a knitted polytetrafluoroethylene (PTFE) suture ring, and coated with a thin film of pyrolytic carbon (Carbofilm™). The valve and its dimensions are presented in Figure 3-14.

The Sorin Allcarbon 29 mm was used to model the mitral valve in the following experiment setups:

- Chapter4, all aortic root configurations (physiological, optimal surgical, sinusless, sub-annular, dilated root/undersized valve, mechanical)
- Chapter 5, all aortic root configurations (TA1-4)
- Chapter 6, all aortic root configurations (NoCA, LCA, RCA, and NCA)

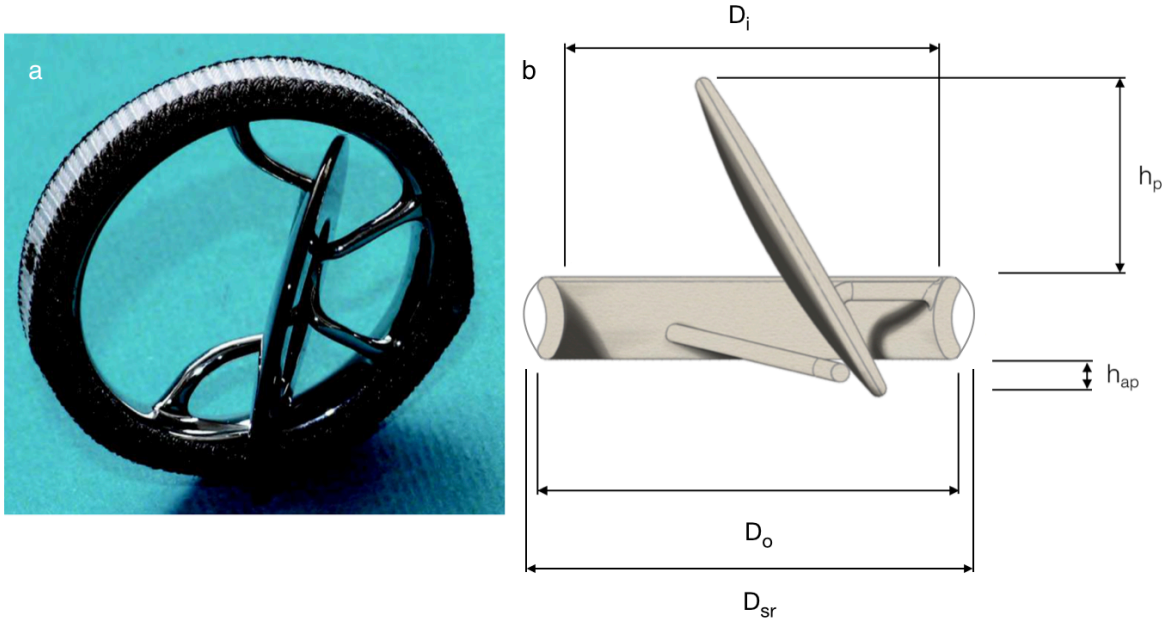

Figure 3-14: Mitral valve: (a) Sorin Allcarbon 27 mm; (b) description of valve dimensions, where D_{SR} is the suture ring diameter (35.4 mm), D_i and D_o are the inner diameter (26.7 mm) and outer diameter (31.6 mm) respectively, h_p is the distance the fully open disc axially projects into the downstream direction (14.5 mm), and h_{ap} is the distance the fully open disc axially projects in the upstream direction (2.7 mm). The carbon disc is 1.8 mm thick, with a diameter of 23.3 mm.

3.5 Roots

3.5.1 Size and Shape

The size and shape of the sinus roots were modelled based on the geometric proportions described by Swanson & Clark[27], the epitrocoidal top view profile defined by Reul et al.[65], and the size and shape of the interleaflet triangles at the base of the root was taken from leaflet angles identified by Thubrikar et al.[45], as illustrated in Figure 3-15. Idealised root geometry represents the population average, which is useful for initial investigations of particular phenomena in the region. However, as the physiology varies between aortic roots, the modelling of blood flow within patient specific models should be carried out to establish how the fluid dynamics of the region alter in comparison to this idealised model, as well as quantifying the usability and validity of the idealised geometry, although this is beyond the scope of the work in this thesis.

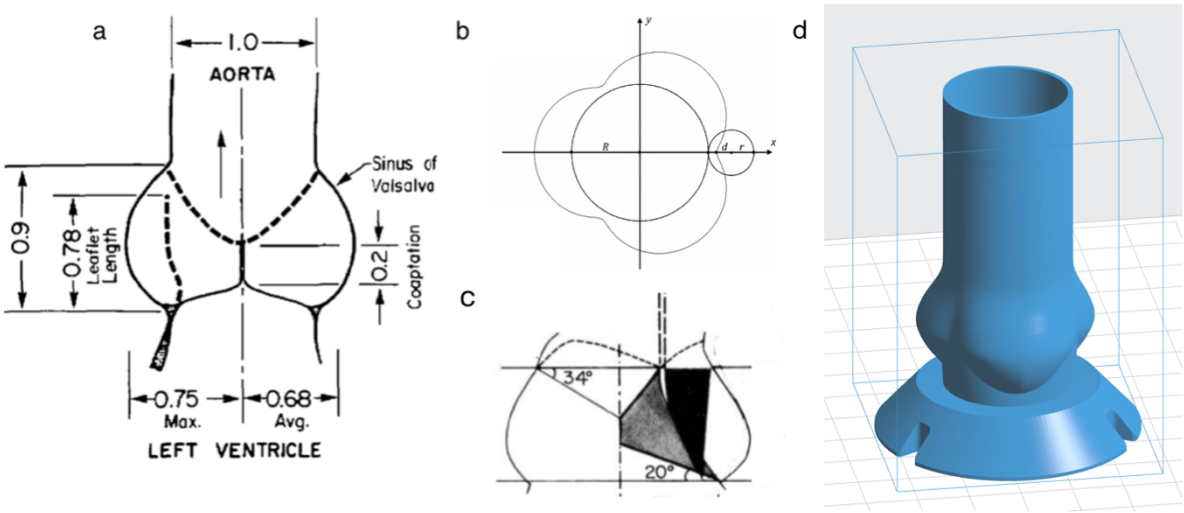

Figure 3-15: the geometry of a normal aortic root: (a) a sagittal cross-section of the root shown in proportions of the STJ diameter[27] (b) the epitrochoidal shape of a transversal cross-section of the sinuses of Valsalva[233]; (c) the angles of the basal interleaflet triangle[45]; (d) Resultant 3D model of the root with sinuses of Valsalva and base for assembly into silicone mould

An epitrochoid profile is defined as a curve produced by a point within a circle (radius b_{ep}) which rolls around the perimeter of a second circle (radius a_{ep}), with the circles related by the diameter ratio of 3:1, due to anatomical symmetry between the 3 sinuses, and whose x- and y-coordinates are defined by the equations[65]:

$$x = (a_{ep} + b_{ep}) \cos \alpha - \left(d * \cos \left(\frac{a_{ep} + b_{ep}}{b_{ep}} \alpha \right) \right)$$

(3-38)

And

$$y = (a_{ep} + b_{ep}) \sin \alpha - \left(d * \sin \left(\frac{a_{ep} + b_{ep}}{b_{ep}} \alpha \right) \right)$$

(3-39)

where d is a constant (m), equal to:

$$d = \lambda b_{ep}$$

(3-40)

where λ is a dimensionless constant that varies with the condition of the root, equal to 0.5 for healthy, normal human hearts[65]. This results in the maximum and minimum radii (r_{min} and r_{max} respectively) of the epitrochoid profile being related to each other by the following equation[65]:

$$r_{min} = \frac{4 - \lambda}{4 + \lambda} r_{max}$$

(3-41)

where r_{max} is also equal to the radius of the modelled sinuses at their largest diameter. The sagittal plane sinus profile was obtained from Grigioni et al. and their approximation of the Swanson, Clark, and Reul geometry[234]. The location of the ostia for the coronary arteries was taken from Knight et al[70], where for an average sinus height (from the basal annulus) of 20.9 mm, the ostium height was in the range of 15.9 – 18.0 mm, i.e. an average of 17.0 mm, equal to 81 % of the sinus height, and centrally located around each section of the epitrochoid profile. The diameter of each ostium was 4.1 mm, as reported by Sirikonda and Sreelatha[74]. Each sinus had an ostium included, so that the same root model could be used for a variety of coronary configurations by clamping or opening the tubing connected to the various ostia, without the need to remove the root and valve from the pulse duplicator and PIV setup.

The roots were labelled by their sinotubular junction (STJ) diameter, e.g. a root labelled as '25' has a diameter of 25 mm at the STJ. Five roots were made:

- 25P - a physiological root with a 25 mm STJ and no mock coronary ostia. The 25P root was used to represent the aortic root in the following experiments:
    - Chapter 4, setup ii (optimal surgical)
    - Chapter 4, setup iv (sub-annular)
    - Chapter 4, setup vi (mechanical)
    - Chapter 5, all setups;
- 25G - a root identical to the 25P, but with the inclusion of a groove, in the shape of the frame of the TPPB 29M valve, in the root wall around the basal annulus of the root, as illustrated in Figure 3-16(a). This groove allowed for the embedding of the TLPB 29M valve, as without the groove the stent of the valve would not fit into the root without considerable distortion of valve and/or root. The 25G root was used to represent the aortic root in the following experiment:
    - Chapter 4, setup i (physiological);
- 29P - a root with the same internal shape as the 25P, but scaled up to an STJ diameter of 29 mm. The 29P root was used to represent the aortic root in the following experiment:
    - Chapter 4, setup v (dilated root/undersized valve);
- 25C – a root identical to the 25P, but with a mock coronary ostium included on each sinus. The 25C root was used to represent the aortic root in the following experiments:
    - Chapter 6, all setups;
- 25S - a sinusless mock root, modelled as a simple 25 mm diameter tube. 3D models of the root were made using SolidWorks, and then converted into .stl files for use with a 3D printer, as illustrated in Figure 3-15(d). The 25S root was used to represent the aortic root in the following experiment:
    - Chapter 4, setup iii (sinusless).

3.5.2 Manufacture

3D models of the various root sizes and shapes were printed out of polymerized resin on a Form2 3D printer, based on the CAD models described in Section 3.5.1. For all of the roots with the exception of the 25C, the printed models consisted of a mould core and a mould exterior, as shown in Figure 3-16(b-e). The outer surface of the core was designed so that it would match the contours of the lumen of the modelled root, and the core itself was hollow and thin-shelled, so it would be easily crushable if the core was not easily extractable from the silicone after curing. The mould exterior was designed as three identical parts that fit together around the core for the casting procedure, so that the outer surface of the resultant silicone root would fit into the pulse duplicator's first aortic chamber, immediately downstream of the left ventricle chamber and aortic flow transducer. The external surface of the mock root block was characterised by flat faces on planes parallel to the root axis, on each commissure-to-commissure plane, to reduce distortion and refraction of the laser sheet during image capture for PIV. The bottom of the core and exterior sections including complimentary tapering to reduce leakage, and locating grooves to enable alignment of core and exterior. Teflon tape was placed in between each exterior section before assembly, and the bottom of the core-exterior assembly was sealed with modelling clay to prevent leakage.

The roots were manufactured from an optically clear, solvent free, low viscosity silicone elastomer (MED-6015, NuSil Technology, Carpinteria, CA, USA), with a refractive index of n = 1.4. Although the cured silicone has different mechanical properties to that of the endothelial tissue that makes up the aortic root walls, its casting, durability and optical properties mean it is well suited to: accurately produce the desired geometry specified in Section 3.5.1; be placed in the pulse duplicator for long period of testing; work within the context of a PIV study. Use of a native porcine aortic root, for example, would not enable the projection and photography of a laser plane over the cross section of the root. After mixing of Part A and Part B in a 10:1 ratio, the resultant solution was de-bubbled in a vacuum chamber (4.2 L Stainless Steel Degassing Vacuum Chamber and Hose, HVac Store Ltd, UK) to ensure optimal optical properties after casting. Use of silicone grease to facilitate ease of removal from the mould was

investigated, but it was found that this penetrated into the silicone during the curing process, resulting in a thin, cloudy layer next to any application of the grease, which had a deleterious effect upon the optical properties. The solution was poured into the assembled mould, and then placed in an oven at 50°C for 12 hours, which is a lower temperature than the curing temperature recommended by the manufacturer but prevented mould damage/warping from heat exposure during curing. After this period, the mould exterior was separated and removed, whilst the central core mould was either crushed or pushed out, depending on the elastic deformability of the resultant silicone model and shape of the core used. The resultant mock root was then ready for insertion into the pulse duplicator.

Due to the integration of the silicone valve described in Section 3.4.1.4 and the modelling of coronary arteries, the manufacture of the 25C root included some additional and modified steps compared to the other roots.

The 3D model of the root was made up of the same sinuses and aortic tract as the 25P root, but with cylindrical nubs included to allow modelling of the coronary arteries, as shown in Figure 3-17(a). One end of these nubs was located at the position of the ostia, described in Section 3.5.1. In order to reduce any optical distortion, the path of each nub was individually modified to lead away from the sagittal cross-section of the root to be analysed, indicated in Figure 3-17(b), and towards the downstream end of the mock root. These nubs were hollowed out at the join with the mock sinuses, to allow for easier fragmentation of the 3D printed model during disassembly, and included a cupped end on the downstream end. Brass rods (4 mm diameter) with connector moulds (4 mm internal diameter, 8 mm external diameter) were placed into these cups, creating mock coronary arteries leading away from each sinus in the final mock root and allowing for connection to the outflow tubing. The same outer core as for the other mock roots was assembled around this central collection, before pouring in the uncured silicone and curing with the same method as for the other roots.

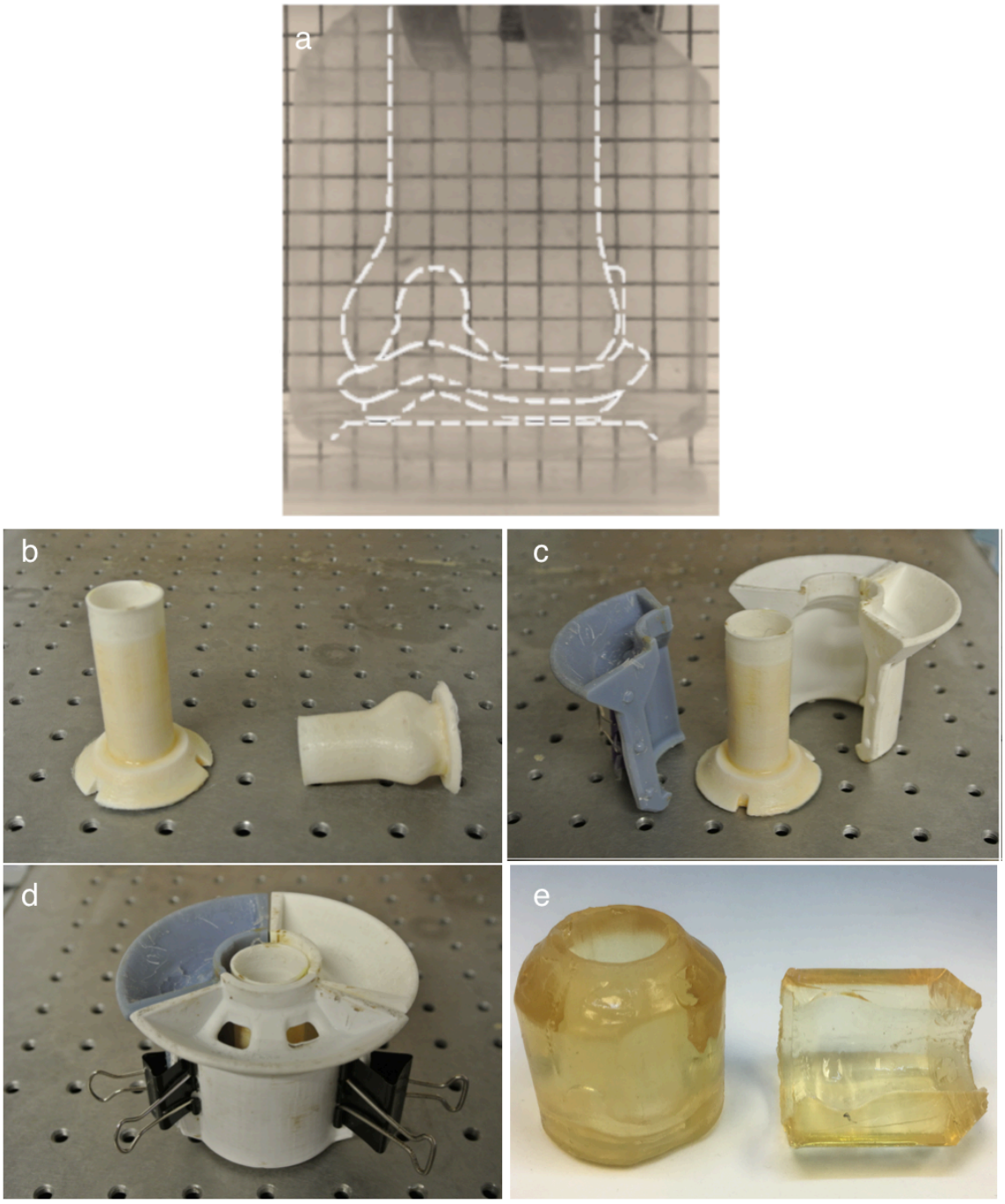

Figure 3-16: Manufacture of root: (a) illustration of groove in 25G root, required to fit 29 mm valve; (b) 25S and 25P 3D printed root cores; (c) Root core and exterior; (d) Assembled core and exterior, prior to addition of silicone; (e) finished silicone cast, ready for use, alongside halved silicon root

Once cured, the brass rods and connector moulds were removed and the 3D printed 25C model was carefully crushed, followed by removal of the resulting fragments. The silicone valve had its commissures and tapered base coated in Med-6015, and was inserted into the silicone root, aligned commissure to commissure, and was cured in at 50°C for 12 hours. The resultant root is displayed in Figure 3-17(c).

Upon assembly within the pulse duplicator, each downstream end of these mock arteries had a tubing connector inserted, and a 500 mm length of silicone tubing (6 mm external diameter, 4 mm internal diameter) attached. This tubing was then passed through the aortic compliance port of the pulse duplicator, to drain into either the open atrial chamber, as shown in the schematic presented in Figure 3-18, or a container on top of a computer attached balance (ADAM PGW 253e, Adam Equipment Co Ltd, Milton Keynes, UK) for coronary flow assessment.

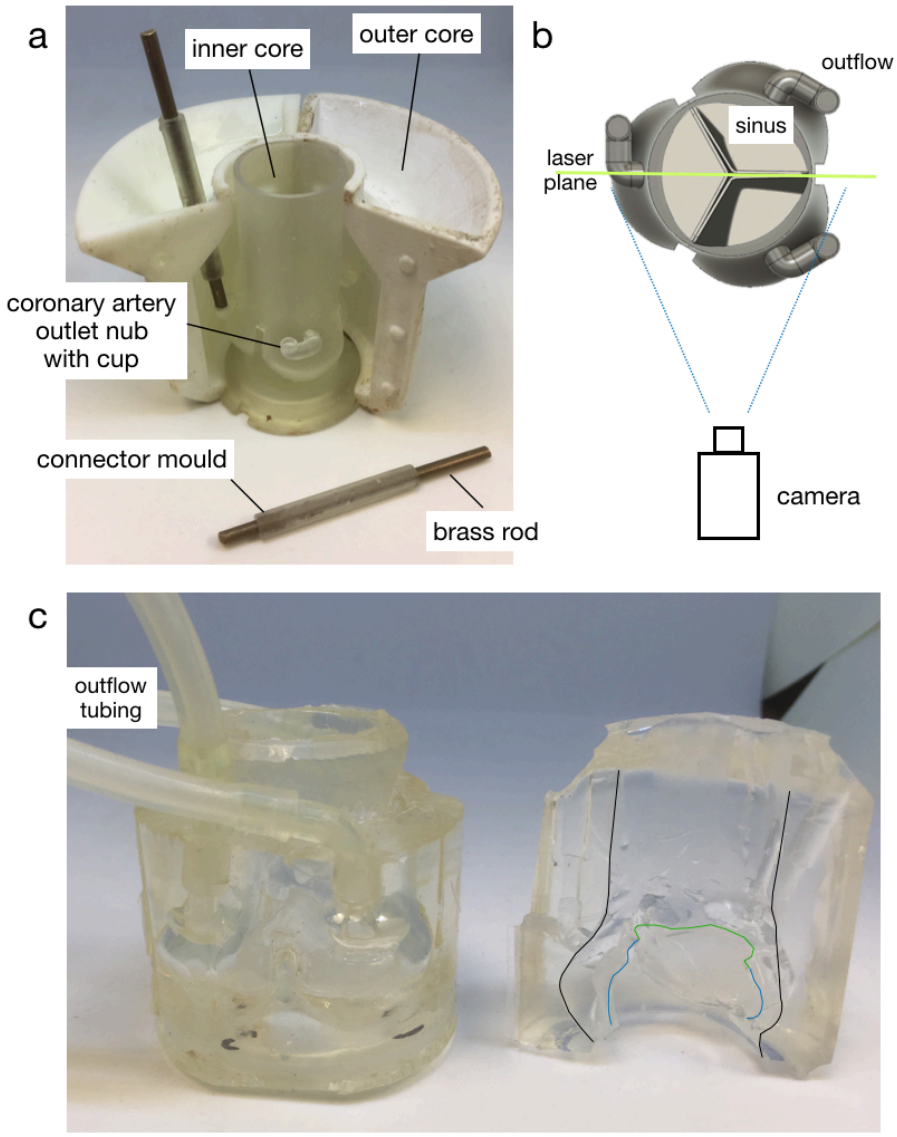

Figure 3-17: Design and manufacture of mock aortic root with coronary arteries: (a) 3D printed model of aortic root with coronary artery nubs inside outer mould, with rod and tubing connector mould insert; (b) proximal schematic of 25C root, showing path of each mock coronary artery from its sinus to the outflow tubing in relation to the laser sheet and camera angle used for PIV; (c) resultant silicone mock aortic root with coronary arteries, alongside cross-section showing valve placement. The wall of the root in the cross section is highlighted with black, the outflow cusp of the valve in green, and the cross sectioned edge of the valve leaflet in blue.

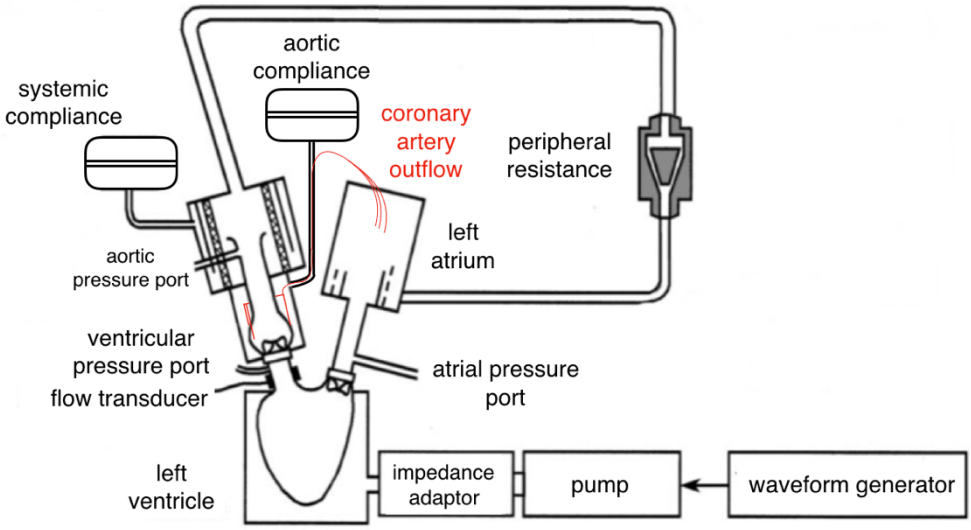

Figure 3-18: Schematic of the route of the coronary artery outflow from aortic root, through aortic compliance tubing, flowing out into left atrium

3.6 Testing Fluids

3.6.1 Properties of Analogue Fluids

As blood itself is not transparent and would cause operating difficulties as it dried and coagulated inside the pulse duplicator, an analogue fluid is required. ISO 5840 requirements state that[235] "testing shall be performed using a test fluid of isotonic saline, blood, or a blood-equivalent fluid whose physical properties are appropriate to the test being performed". The analogue fluids used needed to fulfil 3 exclusive criteria:

i. presence of ions;
ii. viscosity matched to that of blood;
iii. refractive index (RI) matched to that of the silicone elastomer used to construct the mock roots.

3.6.1.1 Presence of Ions

In order for the flow transducer of the pulse duplicator to detect and quantify the fluid flow, ions were required to be present in the flow so that the electromagnetic. The FM501 flowmeter required a final concentration of > 0.9% NaCl[236].

3.6.1.2 Viscosity

As noted in Chapter 2, the non-Newtonian nature of whole blood leads to many discrepancies with a Newtonian testing fluid when comparing flow profiles and

behaviour, and an ideal testing fluid would replicate the shear-thinning properties[119,237,238]. However, as this investigation requires the use of an optically transparent fluid to enable PIV, it is beyond the scope of this project to model the non-Newtonian nature in great detail, especially as the effects are less pronounced in relatively large diameter vessels such as the sinuses of Valsalva or the STJ[237], and so it is preferred to replicate the viscosity of blood for a given shear. Blood viscosity tends towards 3.5 - 4.0 cP at a shear > 100 s^{-1} and a temperature of 37 °C, which is normally reached by the relatively fast flow of blood as it exits the aortic valve[81]. Some investigations have used glycerol to increase the viscosity of a buffered saline to this range[21,102,239], but there have been reports of the glycerol causing changes in the mechanical properties of the leaflet tissue of bioprosthetic valves[240,241]. This may represent a major limitation for the proposed tests, as these tests typically require several hours, and for comparison reasons they may need to be repeated on the same valve on different days. It was therefore decided to study the effect of glycerol upon the leaflets to establish the reliability of bioprosthetic valves after prolonged immersion before using glycerol as a blood analogue fluid, which is reported in the appendices in Section 9.1.

3.6.1.3 Refractive Index

As the interface between the silicone mock aortic root and the surrounding analogue fluid is curved, mismatch of the RI of the blood analogue fluid and the silicone would lead to distortion of the images used in cross-correlation, leading to subsequent errors in the fluid velocities reported over the cross-section. Accordingly, it was important to reduce these errors by matching the RI of the analogue fluid to that of the silicone used to construct the mock root (n = 1.4).

3.6.2 Refractive Index Matched – Water and Potassium Iodide

In order to raise the RI of the fluid to match that of the silicone mock root, n = 1.4, potassium iodide (KI) can be added[97,242], attaining the required RI at a ratio of 100:77 by weight of water and KI. A small amount of sodium thiosulphate was mixed into the water-KI solution to make it completely transparent. The resultant clear, colourless solution had the same dynamic viscosity as buffered phosphate saline at 25 °C, η_R = 0.001 Pa.s), but a much great density (ρ_R =

1.77g/cm^3). Photos displaying the image distortion before and after the RI matching are presented in Figure 3-19 (a) and (b).

Due to the difference in density between this fluid and the seeding particles used to capture PIV data, the response time of the seeding particles in the water-KI solution, τ_{s_R}, was 6.11 x 10^{-6} s, and the gravitationally induced velocity, $\boldsymbol{U}_{g_R}$, was a maximum of 6.00 x 10^{-5} m/s. As these values were well outside of the expected scale of results, they were deemed to be acceptable.

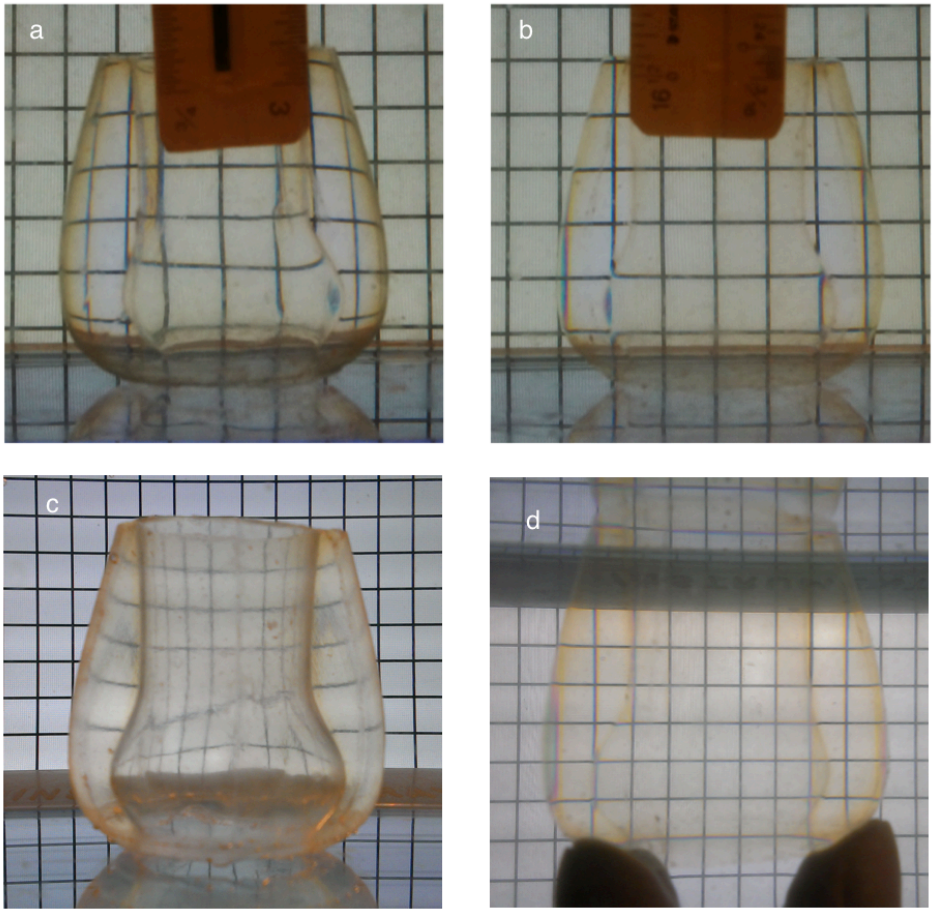

Figure 3-19: Refractive Index (RI) matching of the working fluids, with a square grid showing the optical distortion due to the difference in RI of the silicone and the surrounding fluid: (a) RI matching of silicone root in saline; (b) RI matching of silicone root in saline and KI solution described in 3.6.2; (c) RI matching of silicone root in saline; (d) RI matching of silicone root in saline, KI and glycerol solution described in 3.6.3

3.6.3 Viscosity and Refractive Index Matched – Water, Glycerol and Potassium Iodide

In order to realise a working fluid with a viscosity of 3.5 – 4.0 cP, glycerol can be added to water[191,242–244]. Addition of glycerol also raises the RI of the solution, but as glycerol has a natural RI of n = 1.47, matching the RI of the silicone

would require a very large proportion of the fluid to be glycerol, raising the viscosity of the fluid to non-physiological levels at testing temperatures. However, when used in conjunction with KI salt in a ratio of 1000:314:746 (by weight) of water, KI, and glycerol, a working fluid with a viscosity matching that of blood at high shear and a RI matching the silicone mock root when testing at 25°C was achieved[97]. The solution also has a much lower density than if the RI is raised with just KI alone (ρ_{VR} = 1.29g/cm^3). Similar to the water and KI working fluid described in Section 3.6.2, sodium thiosulphate was added to prevent yellowing of the solution. Photos displaying the image distortion before and after the RI matching are presented in Figure 3-19 (c) and (d).

As again there was a difference in density between this fluid and the seeding particles, the response time of the seeding particles in the water-KI-glycerol solution, $\tau_{s_{VR}}$, was 1.74 x 10^{-6} s, and the gravitationally induced velocity, $\boldsymbol{U}_{g_{VR}}$, was a maximum of 1.71 x 10^{-5} m/s. Similar to the particles in the water-KI working fluid, these values were deemed to be acceptable.

4 Physiological Vortices in the Sinuses of Valsalva and the Effect of Surgical Valve Replacement[1]

4.1 Introduction

As far back as the early 16th century, the propagation of vortical structures with the sinuses of Valsalva (SoV) have been reported[59,245], and the development of replacement heart valve prosthetics during the 1960s prompted further research to improve the understanding of the fluid dynamics within the aortic root during the cardiac cycle[18,67,96]. As a result of these investigations, it is now well accepted that the geometry of the SoV influences the kinetics of the opening and closing valve leaflets, as well as the flow of blood into the coronary arteries, the ostia of which are located in two of the SoV[20,37,40,69,246]. However, the specific flow conditions that these chambers promote within the root are not yet fully understood, with multiple and often contradictory interpretations within the literature[32,102,247].

The mechanism proposed by Bellhouse and Bellhouse[18] suggested that the SoV host and expand a vortex ring generated at the downstream exit of the valve in the early stages of systole, and that this vortex persisted through systole, eventually aiding in leaflet closure. In the proximity of the root axis, this vortex follows the direction of the ejected central fast flow, with opposite direction alongside the arterial wall, as indicated in Figure 4-1, and this direction will be referenced henceforth as 'positive'. These vortical dynamics have been

[1] The research presented in this chapter has been published in two articles:

- 2016, Physiological vortices in the sinuses of Valsalva: an in vitro approach for bio-prosthetic valves, R. Toninato, J. Salmon, F. M. Susin, A. Ducci, and G. Burriesci, J. Biomech. Sep 6;49(13):2635-2643
- 2018, Validation and Extension of a Fluid-Structure Interaction Model of the Healthy Aortic Valve, A.M. Tango, J. Salmonsmith, A. Ducci, and G. Burriesci, J. Cardiovasc Eng Tech. Dec;9(4):739-751

And has been presented by the author at:

- 4th European Society for Vascular Surgery Spring Meeting 2016, London, UK

Research from this chapter has also been included in a chapter of a book currently in press:

- Chapter 1.8, Hemodynamic Issues with Transcatheter Aortic valve Implantation, J. Salmonsmith, A. Ducci, and G. Burriesci., Transcatheter Aortic Valve Implantation: Clinical, Interventional, and Surgical Perspectives, A. Giordano, G. Biondi-Zoccai, G. Frati, Springer International Publishing, Cham Switzerland) *Due for publication May 13, 2019*

observed in recent *in vivo* high intensity Magnetic Resonance Imaging (MRI) studies[22–26], although these studies are restricted by the spatial and temporal resolution of the imaging to provide a conclusive answer. The same fluid response has also been identified by a number of numerical investigations from different research groups[27–31]. However, despite agreement within the scientific community that valve opening is accompanied by a vortex ring, recent *in vitro* work has reported different and more complex fluid dynamics, where this initial vortex ring is convected away from the valve opening and towards the ascending aorta. In its stead, a secondary vortex with opposite rotational direction forms, remaining within the chambers of the SoV for the remainder of systole until the valve begins to close[32–35,248]. These alternate vortical dynamics have also been revealed *in silico*, which also reported that the number and strength of the vortices generated within the SoV during systole are dependent upon the extension and depth of the chambers[103]. As stated in section 2.4.1, different aortic root geometries relative to the valve have resulted in different vortical patterns, but these patterns, nor the mechanics of vortex generation and the vortices' properties and propagation within and out of the aortic root have not yet been explained. The effect of these various vortices upon the aortic valve itself has also not been agreed upon.

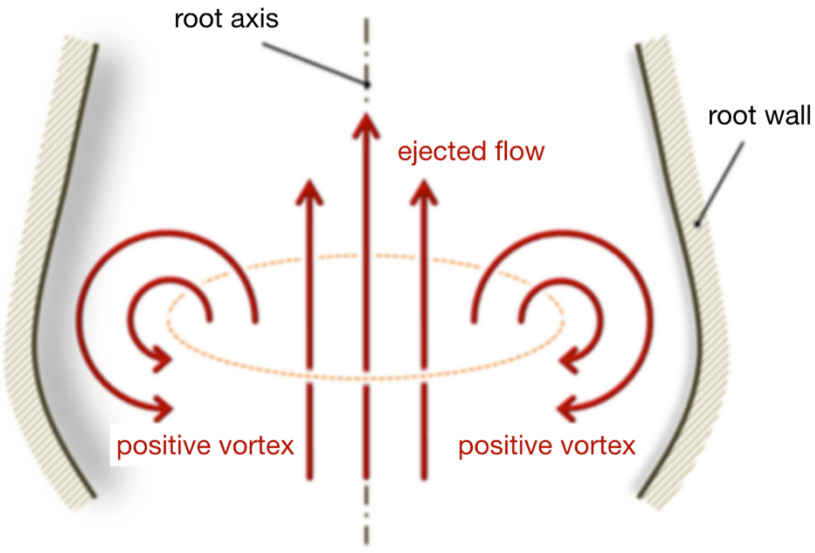

Figure 4-1: Diagram indicating the direction of a positive vortex ring during systole

Following replacement of the aortic valve with a bioprosthetic tri-leaflet valve, the forward flow retains a relatively flat velocity profile[32], with a high distribution of flow, dissipating rapidly downstream of the valve, but with peak blood flow

velocities peaking between 2 and 3 m/s[140], approximately twice that of the physiological range of 1.1 – 1.7 m/s[55,98]. In addition, the stent posts of these surgical valves often produce recirculation regions close to the aortic wall[140]. As the instability of the flow conditions of the aortic side of the valve have been linked to diseases in the region[100], adding further recirculation volumes to the flow may increase the susceptibility to pathologies, such as endothelial remodelling and alterations to the root geometry as a result of abnormal shear stresses at the root lumen[101]. Use of mechanical surgical aortic valves instead of bioprosthetics is sometimes preferred due to their durability[249], but although bi-leaflet valves produce a more physiological flow than their tilting disc or ball and cage brethren[151], the resultant flow patterns are reported to be complex, with multiple recirculations in the SoV, and a chaotic flow field in late systole[156]. As stated in section 2.4.2, there is little information linking the haemodynamics of post-surgical roots with changes to the vortical structures or stagnation regions of the volume. Characterising these geometries and the resulting flow patterns could lead to improved support for clinicians and/or engineers by informing on the best therapeutic strategy.

The aim of this chapter is to provide an in-depth investigation into the fluid dynamics within the aortic root in a number of different configurations with the aortic valve, justifying the various haemodynamics reported in the aforementioned previous studies and investigating the first objective presented in Section 2.4.5.1, 'to investigate the effect of different valve-root geometries upon the fluid dynamics within the aortic root, modelling a native physiological configuration and comparing the resultant flow with a variety of configurations that could result from surgical aortic valve replacement'. Various combinations of aortic root geometries and prosthetic valves were studied *in vitro* on a pulse duplicator which was used to extract global haemodynamics, whilst local flow characteristics were analysed via the use of 2D Particle Image Velocimetry (PIV). The configurations chosen to be investigated were representative of an idealised healthy native valve, an 'ideal' surgical treatment, and three common departures from this ideal treatment, modelling a mismatch of valve-root size, a sub-annular valve fixation, and a valved-graft (resulting in the absence of the SoV). This work presented in this chapter is an adaptation of work previously

published by the author in the Journal of Biomechanics[107], and was also as part of an article involving *in vitro* validation of a numerical model[250].

4.2 Methods

4.2.1 Valve-root Configurations

The following five different valve-root configurations were modelled and studied, as illustrated in Figure 4-2:

i. A physiological configuration, describing an idealised, healthy, native aortic valve and root region;
ii. An optimal surgical configuration, representing an aortic root region following an ideal implantation of a bioprosthetic valve sized to be sutured into the basal annulus of the physiological configuration described above. Due to the presence of a stent in the bioprosthetic, which must fit inside the patient's aortic root and are required to give the leaflets their shape for valve functioning, the functioning leaflets of this SAV are smaller than the leaflets of the original native valve that it is replacing[251];
iii. A sinusless surgical configuration, describing the fluid flow downstream of a surgical bioprosthetic in the absence of sinuses, which are sometimes occluded by synthetic grafts used as vascular substitutes[252];
iv. A sub-annular surgical configuration, reproducing an infra-annular implantation of the bioprosthetic valve. This is also the default positioning for the valve housing in many commercial pulse duplicators[21,60,253];
v. An oversized surgical root/undersized SAV configuration, describing the optimum implantation of a bioprosthetic valve in an enlarged root, common in testing situations[32–35,248]. This configuration was also representative of root dilation as a result of pathologies such as Marfan's Syndrome or Ehlers-Danlos syndrome[143], or the undersizing of a SAV.
vi. A mechanical configuration, representing the use of a typical mechanical valve instead of a bioprosthetic valve, sutured into the basal annulus of the aortic root

One of the porcine bioprostheses described in Section 3.4.1.1, the TLPB Mitral 29 valves, was used to model the physiological healthy human aortic valve, due to its similarity in terms of material, shape and thickness[126], and the other, the

TLPB Aortic 25, was used to represent the valve used in the various surgical bioprosthetic configuration. The mechanical valve used was the Sorin Bicarbon 25, as presented in Section 0. A selection of the mock aortic roots described in Section 3.5 were used to investigate the impact of the various SoV and aortic root proportions on the fluid dynamics of the region, replicating common testing arrangements and post-surgical configurations.

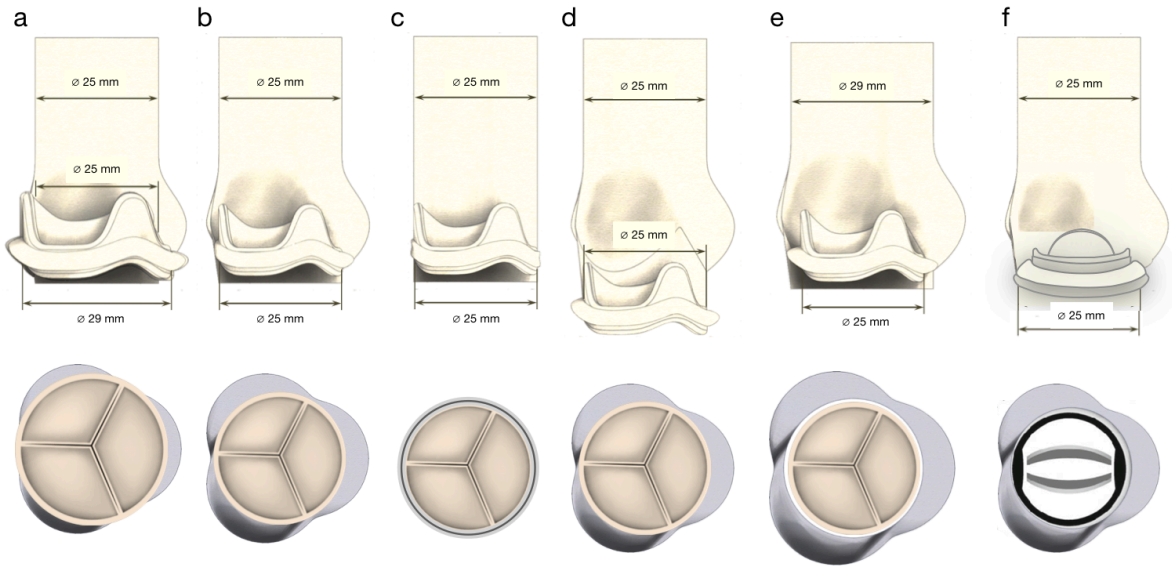

Figure 4-2: Valve-root configurations investigated in the study. (a) Physiological; (b) Optimal surgical; (c) Sinusless; (d) Sub-annular; (e) Oversized/Dilated root; (f) Mechanical

For ease of reference, the 4 roots used are summarised below:

- The 25P root, a physiological root with a 25 mm STJ diameter, for use with the TLPB Aortic 25 valve;
- The 25G root, identical to the 25P root, but with the addition of a groove to house the TLPB Mitral 29 valve without distortion of the root;
- The 29P root, with the same internal shape as the 25P, but scaled up to an STJ diameter of 29 mm, for use with the TLPB Aortic 25 valve;
- The 25S root, which did not reproduce the SoV, instead modelled as a simple 25 mm diameter tube, for use in combination with the TLPB Aortic 25 valve.

The reference diameter of 25 mm at the STJ was representative of an average size for a healthy adult human[46], with the scaled up 29P root used to verify the effect of valve under sizing and/or root dilation. The physiological condition was represented by using the 25G root in combination with the TLPB Mitral 29 valve,

as the leaflets of this larger valve were originally extracted from a porcine aortic root with a STJ diameter equal to about 25 mm, thus better representing the native human anatomy of equivalent size. The influence of the stent of the larger bioprosthetic valve was minimised by its housing within the groove of the 25G root, located at the basal annulus of the mock root. The optimal surgical configuration consisted of the TLPB Aortic 25 valve within the 25P root, again at the level of the mock root's basal annulus, matching the sizing used in a typical surgery. The same valve was positioned 8.5 mm lower within the same root to represent the sub-annular configuration, whilst using the valve positioned at the basal annulus of the 25S root produced the sinusless configuration. The oversized/dilated root configuration was produced by placing the TLPB Aortic 25 valve at the basal annulus of the larger 29P root. Finally, the mechanical valve configuration consisted of the Sorin Bicarbon 25 mechanical valve secured into the basal annulus of the 25P root.

As described in Section 3.5.2, all the roots were made of optically clear, solvent free, low viscosity silicone elastomer with refractive index $n = 1.4$. The physiological elasticity of the root wall depends upon a number of *in vivo* factors, including the age and healthiness of the tissue or the prosthetic materials and degree of cellular infiltration following the surgical introduction of a graft. The geometry of the different chamber sizes would also produce varying compliance, and so it was decided to exclude this variable from the experiment, with the thick walls of the silicone roots resulting in negligible compliance, representative of older patients[254].

4.2.2 Global Parameters

In this study, all experiments were carried out using the hydro-mechanical pulse duplicator described in Section 3.2.1, using pressure transducers positioned within the mock ventricular and aortic chambers, i.e. upstream and downstream of the aortic valve respectively. Combined with instantaneous volumetric flowrate data provided by the electromagnetic flowmeter positioned just upstream of the aortic valve, this allowed estimation of the following haemodynamic data:

- The systolic transvalvular pressure drop (Δp) across the valve, in mmHg
- The Effective Orifice Area (EOA) of the valve, in cm^2

- The closing regurgitant volume (V_c) of the valve, in ml
- The energy losses during forward flow (E_f) and valve closure (E_c), and the combination of these to give the total systolic energy loss (E_s), in mJ.

The calculation of these parameters from the various data acquired from the pulse duplicator is detailed in Section 3.2.2, with an average cycle calculated from 20 cycles for each experimental setup, taken from the first and last 10 cycles during the PIV data acquisition. As the investigation described in Section 9.1 in the appendices was still on-going, the decision was made not to include glycerol in the testing fluid, in order to minimise the chance of the testing fluid affecting the dynamic response of the valve as the testing proceeded, as suggested by previous investigations in the literature[240,241]. This resulted in the dynamic viscosity of the testing fluid not matching that of blood. Though this limitation is accepted by international regulations for the testing of bioprosthetic valves (ISO 5840:2009), it may have resulted in some departure in fluid dynamics from the physiological environment. However, as the local flow characteristics to be elucidated by the PIV study were expected to be critical to the findings of the experiment, the testing fluid did contain potassium iodide, in order to match the Refractive Index (RI) of the testing fluid to that of the silicone mock roots to be used, as detailed in Section 3.6.2.

A heart rate of 70 bpm was simulated using the pulse duplicator, controlling the displacement of the piston head of the pump with respect to time, applying an FDA approved displacement waveform with 35 % systole per cardiac cycle. A physiological flowrate of 4 l/min, calculated as the net flow through the flowmeter each cycle multiplied by the number of cycles per minute, at a mean aortic pressure of 100 mmHg was imposed across the valve by combination of adjusting both the amplitude of the pump's piston head movement and the resistance of the system via constriction or expansion of a hose clamp.

4.2.3 Local Fluid Property Acquisition

The systolic cycle for each root-valve configuration was characterised by the elucidation of a velocity field for each of 5 instants, representative of a distinct part of the systolic cycle. These reference instants could occur at different times of the cycle for the various configurations, as they were dictated by the flow displayed by each configuration as opposed to a predetermined time interval.

These flow conditions, presented in Table 4-1 for all configurations and illustrated for the Optimal Surgical configuration in Figure 4-3, were defined as the instants of:

A. Maximum increasing flowrate
B. Peak flowrate
C. Maximum decreasing flowrate
D. The most significant change of curvature of the flowrate during late systole
E. The end of forward flow

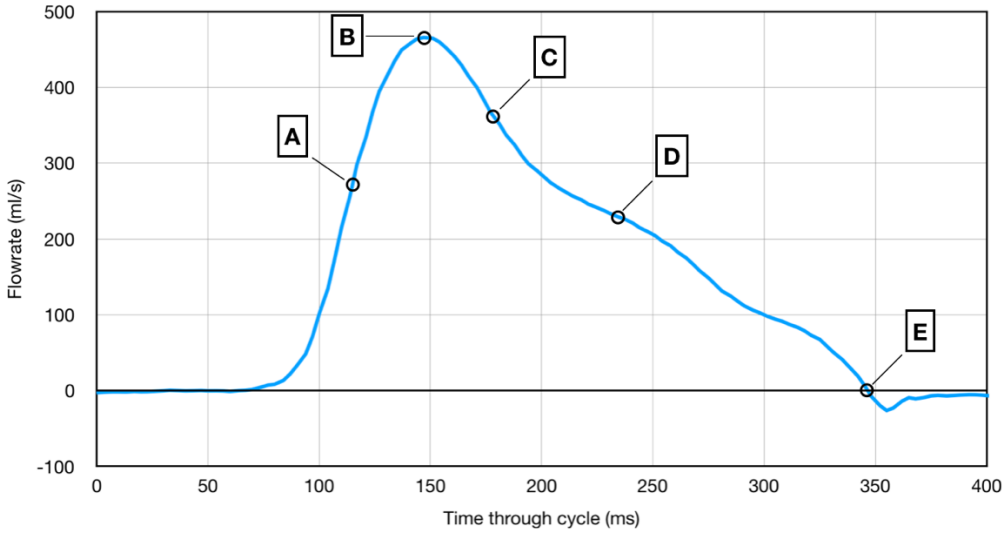

Figure 4-3: Typical diagram of the flowrate vs the time through the heart cycle with the analysed instants shown.

Configuration	*Instant Time through Cycle (ms)*				
	A	B	C	D	E
Physiological	110	147	174	234	342
Optimal Surgical	117	154	174	234	354
Sinusless	114	154	177	228	348
Sub-annular	114	147	171	228	352
Dilated	110	151	174	234	347
Mechanical	117	151	174	231	352

Table 4-1: Time elapsed through cycle for each analysed instant for PIV data acquisition for each valve-root configuration

The local fluid dynamics at each of these instants were captured via 2D PIV using the bench top equipment and techniques presented in Section 3.3. As

detailed in Section 3.3.3.4, 100 image pairs were captured for each instant, allowing for phase-resolved processing of the resultant velocity fields, in order to identify and compare the large-scale flow features for the different valve-root configurations. The choice of the time interval between the images of each image pair (Δt) for the fast fluid flow of each instant was chosen by estimation of the fluid velocity through the flowmeter at that time, in accordance with the equation (3-17). This initial fluid velocity estimation was carried out by dividing the flowrate at that particular instant by an approximated valve orifice area, assuming each of the two bioprosthetic valves formed a triangular orifice during systole[255], with dimensions in accordance to an equilateral triangle inside the circular suturing annulus of the bioprosthetic. As a result, the different image pair time intervals were used for the specified instants across the various configurations, as displayed in Table 4-2. In order to capture the anticipated slower fluid flow in the sinuses, a second set of 100 image pairs with a Δt of 250 μs was captured at instants A-E for each configuration.

Configuration	*Time interval of image pair, Δt, at each Instant (μs)*				
	A	B	C	D	E
Physiological	158	88	108	184	250
Optimal Surgical	154	100	120	200	250
Sinusless	162	95	114	195	250
Sub-annular	177	104	126	194	250
Dilated	187	100	116	101	250
Mechanical	183	94	109	204	250

Table 4-2: Time interval for image pairs at specified instants. NB - as, by definition, the fluid flow speed was calculated as 0 m/s for Instant E, a Δt of 250 μs was used for this instant across the valve-root configurations

The maximum PIV velocity uncertainty for each instant was then calculated from these image pair time intervals and the k value (the μm to pixel ratio) for each PIV setup for each valve-root configuration, presented in Table 4-3.

Configuration	*PIV Velocity Uncertainty for each Instant (m/s)*				
	A	B	C	D	E
Physiological	0.0133	0.0237	0.0195	0.0114	0.0084
Optimal Surgical	0.0149	0.0231	0.0192	0.0115	0.0092
Sinusless	0.0136	0.0232	0.0194	0.0113	0.0088
Sub-annular	0.0142	0.0241	0.0199	0.0129	0.0100
Dilated	0.0107	0.0201	0.0172	0.0099	0.0080
Mechanical	0.0120	0.0233	0.0201	0.0108	0.0088

Table 4-3: Maximum PIV Velocity Uncertainty for each instant in each configuration

Measurements were carried out on a root cross-section (sagittal plane), bisecting one of the sinuses, as illustrated in Figure 4-4(a). As the bileaflet design of the mechanical valve results in 2 segments of symmetry and the root has 3 segments of symmetry, each sinus does not have its own valve leaflet associated with it. The mechanical valve was aligned as shown in Figure 4-4(b), with the laser cast over where the line of symmetry for the root and valve aligned, as recommended by the manufacturer in order to avoid a prosthetic valve hinge being in the vicinity of one of the coronary ostia. In order to study the cross-sectional downstream flow of the valve at 90 ° rotation to this, the PIV setup illustrated in (c) was also used for image pair acquisition.

After image pair acquisition, cross correlation processing was carried out, as detailed in Section 3.3.2, to produce velocity fields for each instant across the 6 configurations. These fields were then converted into velocity magnitude, Reynolds shear stress (RSS), standard deviation (as an indication of turbulence), and vorticity, as described in Section 3.3.3.1. The velocity fields had streamlines applied to them, as described in Section 3.3.3.2, in order to enhance the visualisation of the fluid flow dynamics.

The peak velocity was identified as the highest velocity magnitude calculated via the PIV process, across the entire investigation region for each flow condition, A-E. The average sinus velocity, v_{si}, was calculated by averaging the velocity magnitudes for any non-zero vectors within the sinus area of the PIV cross-sectional image.

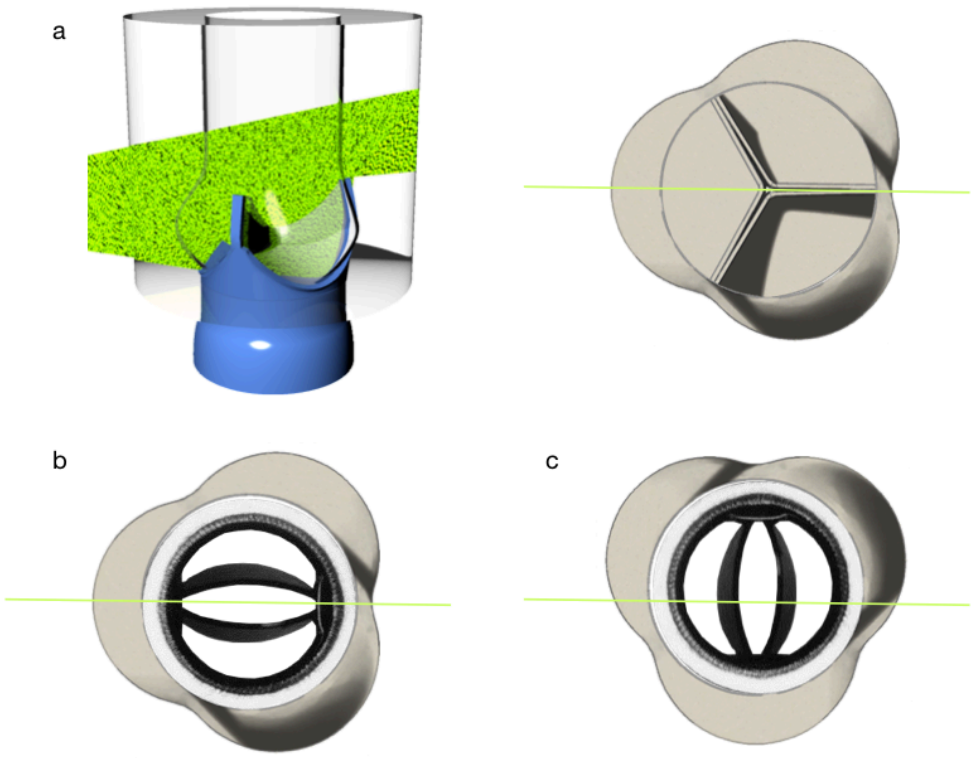

Figure 4-4: Laser sheet positioning. (a) Diagram of laser sheet for PIV positioned over sagittal equivalent cross-section of valve-root configuration under investigation, in this instance the optimal surgical configuration; (b) Laser sheet position across the mechanical configuration, splitting the sinus where the root and valve share a line of symmetry; (c) Laser sheet position at 90 ° rotation to this.

The sinus area is indicated as the green shaded region in *Figure 4-5*(a), and is defined as the region of the cross-section that is downstream of the basal annulus and upstream of the STJ of the mock root, and radially positioned in relation to the mock aortic wall downstream of the STJ. To quantitatively measure and compare the central jet flow width resulting from each configuration, the fast flow width (x_f) of the flow was defined as the width of the velocity profile across the mock STJ where the downstream velocity magnitude, v_{STJ}, is higher than one third of the peak velocity detected via PIV analysis for the whole cross-section at peak flow, v_p, for each configuration, measured from the PIV data, as indicated in *Figure 4-5*(b).

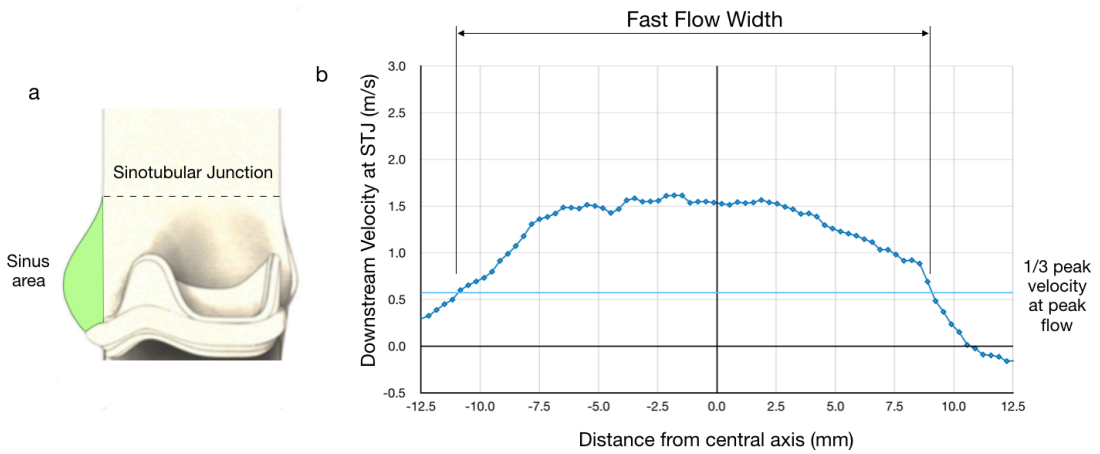

Figure 4-5: Sinus and Sinotubular Junction regions of PIV cross-section: (a) Sinus area of cross-section for calculation of average sinus velocity from PIV data; (b) Calculation of fast flow width (x_f) from velocities across the STJ profile

4.3 Results

4.3.1 Global Data

The global haemodynamic data across the 6 configurations, in terms of EOA, mean systolic transvalvular pressure drop (Δp), closing regurgitant volume (V_c), and systolic energy losses (E_f, E_c and E_s) components), alongside the maximum velocity (v_p) and the maximum RSS measured for each configuration at peak flow (instant B) from the PIV data, is presented in Table 4-4. The haemodynamic performance of each configuration is compared to that of the physiological setup, as this configuration was designed to reproduce the most similar flow conditions to those expected for a healthy native anatomy. The variation of flow and pressure throughout a typical cycle during PIV acquisition for each configuration is illustrated in Figure 4-6. Bar diagrams to enable visual comparison of the variation of Δp, V_c, and the energy losses for each configuration are shown in Figure 4-7. Errors in the haemodynamic data are equal to the range of pressure over the 20 cycles and the resolution of the pressure and flow transducers, and are indicated both in the table and the figures above.

Global Parameter	*Physiological*	*Optimal Surgical*	*Sinusless*	*Sub-annular*	*Dilated*	*Mechanical*
Effective Orifice Area (cm^2)	2.43 ± 0.02	1.65 ± 0.01 *(68 %)*	1.56 ± 0.02 *(64 %)*	1.41 ± 0.01 *(58 %)*	1.53 ± 0.01 *(63 %)*	1.56 ± 0.02 *(64 %)*
Pressure Difference (mmHg)	5.27 ± 0.08	8.63 ± 0.13 *(164 %)*	11.16 ± 0.23 *(212 %)*	10.91 ± 0.07 *(207 %)*	9.29 ± 0.15 *(176 %)*	15.82 ± 0.34 *(300 %)*
Closing Volume (ml)	3.52 ± 0.16	0.36 ± 0.08 *(10 %)*	0.70 ± 0.09 *(20 %)*	0.16 ± 0.04 *(5 %)*	0.37 ± 0.11 *(11 %)*	1.27 ± 0.12 *(36 %)*
Forward Energy Loss (mJ)	33.96 ± 1.1	63.35 ± 1.01 *(187 %)*	100.88 ± 2.32 *(297 %)*	86.59 ± 1.56 *(255 %)*	73.67 ± 1.71 *(217 %)*	134.21 ± 3.11 *(395 %)*
Closing Energy Loss (mJ)	15.18 ± 0.56	1.28 ± 1.22 *(8 %)*	2.74 ± 0.29 *(18 %)*	0.50 ± 0.12 *(3 %)*	1.57 ± 0.41 *(10 %)*	7.04 ± 0.76 *(46 %)*
Systolic Energy Loss (mJ)	49.14 ± 1.66	64.63 ± 1.23 *(132 %)*	103.62 ± 2.61 *(211 %)*	87.09 ± 1.68 *(177 %)*	75.24 ± 2.12 *(153 %)*	141.25 ± 3.87 *(287 %)*
Peak Velocity (m/s)	1.7 ± 0.024	2.9 ± 0.021 *(171 %)*	3.0 ± 0.022 *(176 %)*	2.9 ± 0.020 *(171 %)*	2.8 ± 0.021 *(165 %)*	1.9 ± 0.023 *(112 %)*
Peak Reynolds shear stress (N/m^2)	53 ± 0.75	223 ± 1.60 *(421 %)*	276 ± 2.01 *(521 %)*	159 ± 1.08 *(300 %)*	191 ± 1.43 *(361 %)*	138 ± 1.03 *(260 %)*

Table 4-4: Hydrodynamic global data for all configurations: mean value, ± standard deviation, and percentage value with respect to physiological configuration.

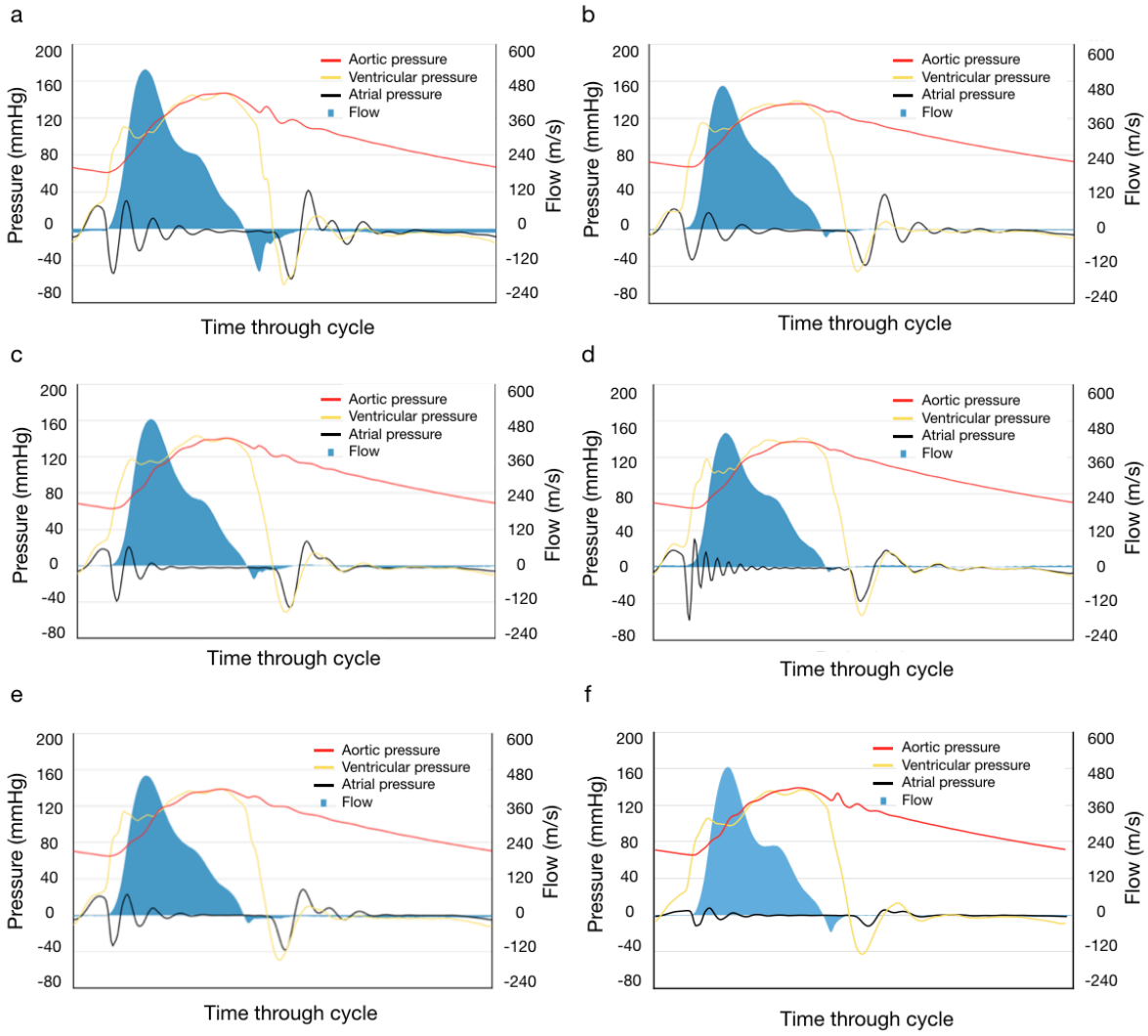

Figure 4-6: Pressure-time and pressure-flow charts for each configuration throughout a typical cardiac cycle during PIV acquisition. (a) Physiological; (b) Optimal surgical; (c) Sinusless; (d) Sub-annular; (e) Oversized/Dilated root; (f) Mechanical.

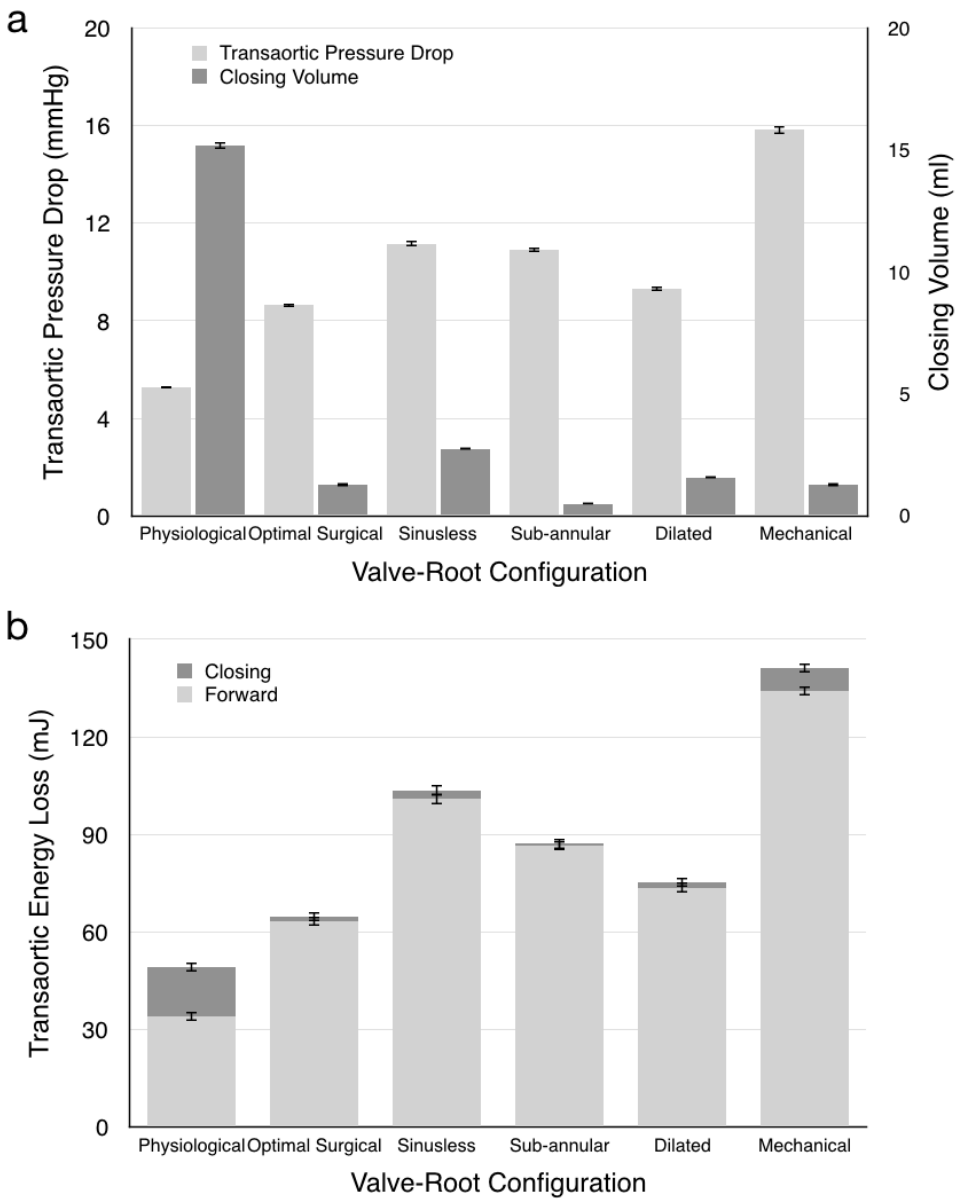

Figure 4-7: (a) Transaortic pressure drop and closing volume for each configuration; (b) Transaortic energy losses during forward flow and closing phases for each configuration.

4.3.2 PIV data

PIV data for the fast flow width (x_f) and average sinus velocity (v_s) for each instant of each configuration is presented in Table 4-5. Visual comparison of these parameters is provided via line charts in Figure 4-8. The velocity profile of each instant of each configuration is also displayed via line charts in Figure 4-9.

Parameter	*Instant*	*Physiological*	*Optimal Surgical*	*Sinusless*	*Sub-annular*	*Dilated*	*Mechanical*
Fast Flow Width (mm)	A	23.8	18.5	15.6	3.2	0.0	22.1
	B	18.9	15.2	15.6	11.2	17.7	11.1
	C	13.8	13.9	14.2	9.9	8.4	4.7
	D	7.7	11.1	12.4	6.1	4.3	0.0
Average Sinus Velocity (m/s)	A	0.199	0.516	n/a	0.186	0.239	0.294
	B	0.108	0.298	n/a	0.117	0.100	0.332
	C	0.147	0.186	n/a	0.171	0.108	0.444
	D	0.085	0.166	n/a	0.110	0.138	0.134
	E	0.049	0.090	n/a	0.050	0.104	0.198

Table 4-5: Instantaneous data from PIV analysis for all configurations at all instants, with the exception of instant E for the fast flow width (as this was zero for all configurations)

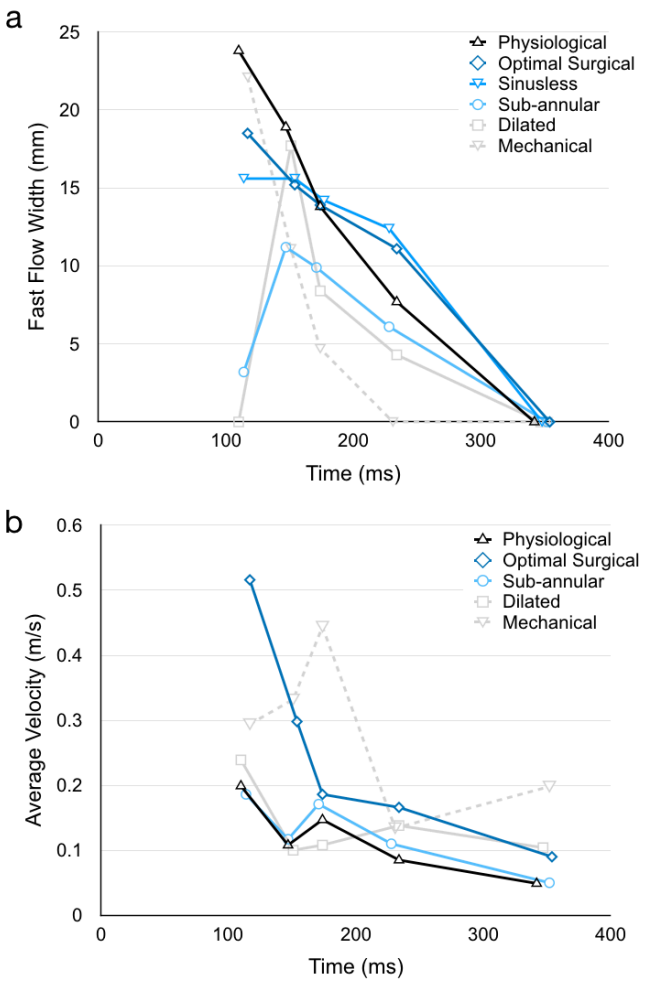

Figure 4-8: (a) Fast flow width at instants A-E of each configuration; (b) Average sinus velocity for each instant of each configuration

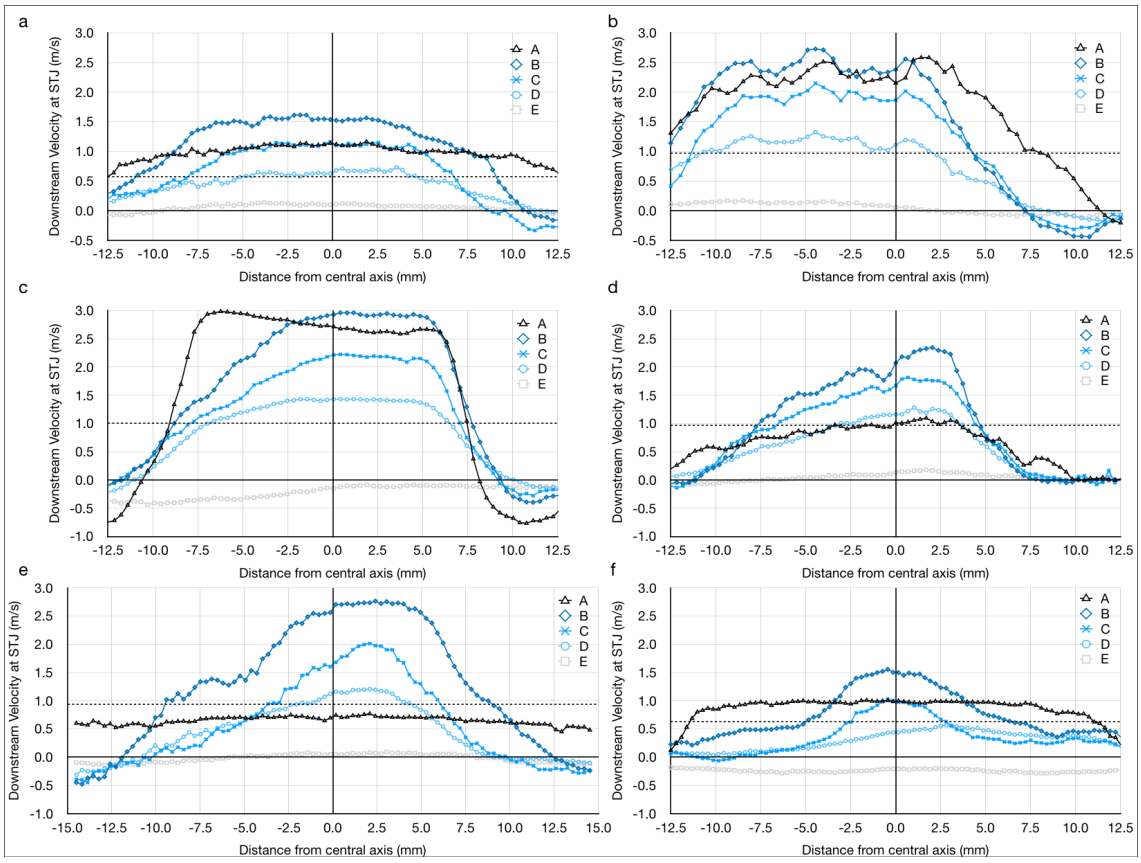

Figure 4-9: Velocity profiles across sinotubular junction at each instant analysed for each configuration, with the 1/3 peak velocity line used to calculate the fast flow width indicated by a dotted line on each plot. (a) Physiological; (b) Optimal surgical; (c) Sinusless; (d) Sub-annular; (e) Oversized/Dilated root; (f) Mechanical

4.3.2.1 Physiological configuration

The contour maps for velocity are presented in Figure 4-10, whilst a contour map for the Reynolds shear stress (RSS) at peak flow (instant B) for each configuration is presented in Figure 4-11. Contour maps of the RSS, turbulence, and vorticity captured by the PIV analysis process for each instant of the physiological configuration are presented in the appendices, in Section 9.2. At the beginning of the ejection phase, a positive start-up vortex forms, which is captured within the sinus chamber throughout the systolic cycle until valve closure, only dissipating once the valve has fully shut (instant E in Figure 4-10). The valve leaflets extend into the SoV during the early stages of systole, whilst the central fast flow jet has a slightly divergent profile, occupying the majority of the root cross-section above the STJ, excepting a small vortical region which forms above the commissures of the leaflets, which can be most clearly observed at peak systole in Figure 4-10. The peak velocity detected throughout the cycle was 1.7 m/s, with an uncertainty error of 1.41 %, whilst the average

sinus velocity peaked during early systole at around 0.2 m/s, dropping to 0.05 m/s at valve closure. The fast flow width was also at its maximum as the flow increased (23.8 mm at instant A), shrinking as systole progressed.

The RSS remains low throughout the systolic cycle, with just a small region above the commissural side of the valve during peak systole (displayed in Figure 4-11) at a maximum magnitude of 50 N/m^2. The turbulence, indicated by the standard difference of the velocity calculated for each image pair within the 100 image pairs captured for each instant, is indicated to be at the greatest at the edge of the central jet flow during peaks systole, particularly on the sinus side of the valve, reaching a standard deviation of 0.9 m/s. The regions of vorticity greater than 500 /s are restricted to two volumes, close to and downstream of the exit to the opening leaflet and the valve commissure.

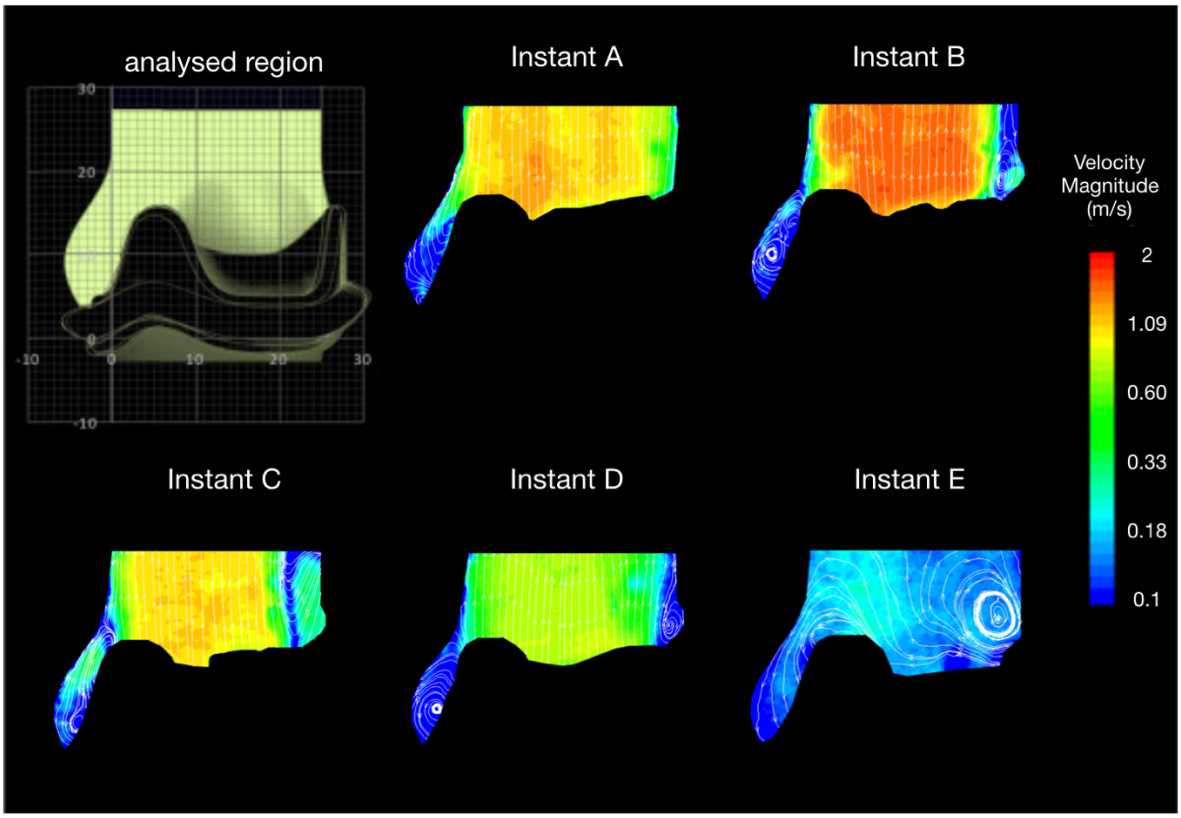

Figure 4-10: Velocity contour maps and streamlines for the physiological configuration.

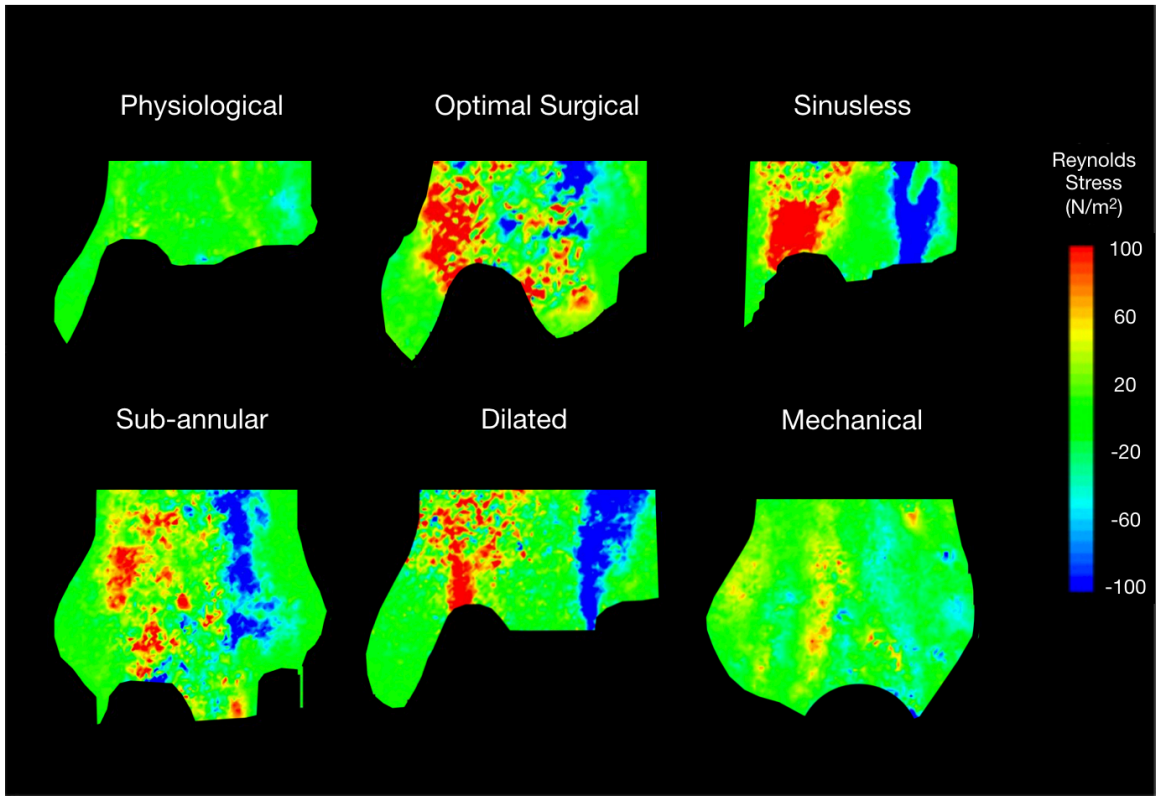

Figure 4-11: Reynolds shear stress contour maps for the various configurations at peak flow (instant B).

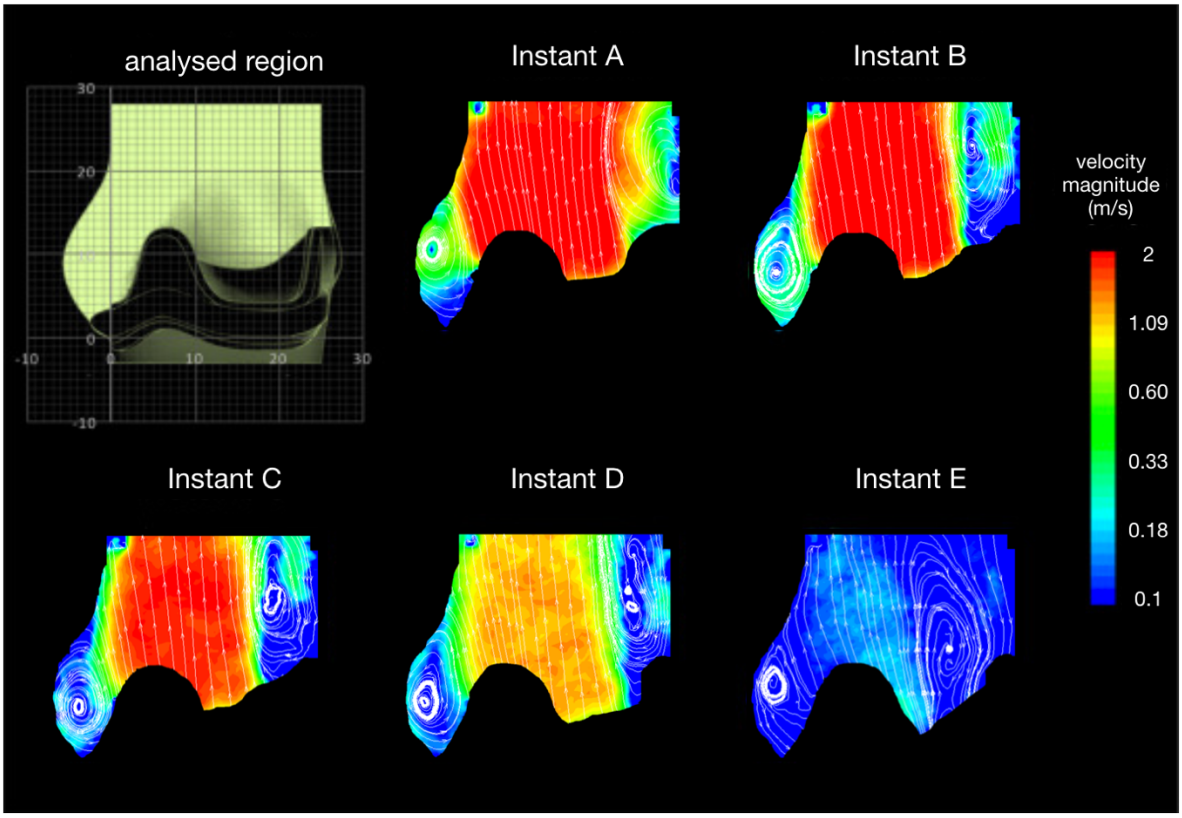

Figure 4-12: Velocity contour maps and streamlines for the optimal surgical configuration.

4.3.2.2 Optimal surgical configuration

Figure 4-12 illustrates the resultant optimal surgical configuration velocity field, whilst the RSS, turbulence, and vorticity contour maps are presented in the appendices, in Section 9.2. The streamlines shown on the velocity contour maps suggest similar fluid flow to the physiological configuration, with a stronger positive start-up vortex generating on the sinus side of the root cross-section during valve opening, which remains within the SoV chamber throughout systole, with diminishing intensity, and having shrunk in size at valve closure (instant E in Figure 4-12). The commissural vortex is again present from the beginning of systole, although in this configuration the vortex is larger and more intense than that observed in the physiological case, expanding towards the centre of the root to a much greater degree, especially as the flow decreases, most clearly shown during instants B, C, and D in Figure 4-12. Peak velocity through the cycle was detected as 2.9 m/s, observed during peak flow, with a velocity uncertainty of 0.82 %. The fast flow width was initially smaller than that observed in the physiological configuration (18.5 mm as compared to 23.8 mm at instyant A) in the early stages of systole, but did not shrink as much as each cycle progressed, and in fact was still as wide as 11.1 mm in late systole (instant D). Average sinus velocity was much higher than the physiological configuration as the flow through the valve increased (0.516 m/s in contrast to 0.199 m/s at instant A), and remained twice as high on average throughout systole.

The RSS of the configuration is much higher than that of the physiological setup, with regions of positive and negative stress, up to the magnitude of 225 N/m^2, mixed together downstream of the valve within and in the vicinity of the central jet flow, particularly at the start of the cycle, shown in Figure 4-11. A standard deviation of at least 0.5 m/s throughout the central part of the aortic root is indicative of the turbulence accompanying the forward flow through the valve, with peak standard deviation up to 1.5 m/s at the valve exit in early systole (instants A and B). The vorticity either side of the central jet flow during early systole is also higher than in the physiological configuration, reaching 900 /s in both regions.

4.3.2.3 Sinusless configuration

The contour maps for the velocity of the sinusless configuration are presented in Figure 4-13, and the RSS, turbulence, and vorticity contour maps are again provided in the appendices, in Section 9.2. Although there are no sinuses in the root model for this configuration, a positive start-up vortex generates in a similar position to the previous configurations, above the exit of the opening leaflet and in close proximity to the aortic wall. However, contrary to the first two cases examined, this vortex is then translated along with the ejected central flow, away from the valve, a mechanism which appears to repeat several times during the ejection phase, as shown in instants A-D in Figure 4-13, ceasing only with valve closure (E in Figure 4-13). In line with the two previous configurations, a positive vortex also generates above the commissural stent post, remaining throughout systole. The central jet flow has a narrower cross-section than is observed for the previous two setups. The highest velocity in the cycle was 3.0 m/s during peak flow, with an accompanying PIV uncertainty of 0.77 %, whilst the fast flow width was broadly similar to that obtained from the optimal surgical configuration.

Well defined regions of RSS are observed either side of the central jet, initially quite narrow, but growing in both size and magnitude as systole progresses (Figure 4-11), peaking at 275 N/m^2, until reducing to negligible quantities at valve closure (instant E). Little turbulence is indicated in the central fast flow of the root throughout the cycle, although a standard deviation of around 1.0 m/s can be observed above the exit of the valve leaflet and the commissure stent post at peak flow, gradually reducing in size and magnitude after peak systole (instants C and D). The vorticity on the sinus side of the valve peaks as the flow increases, reaching 850 /s, but the rest of the cycle exhibits low levels of vorticity on this side of the valve. On the commissural side, a constant region of vorticity can be observed, also peaking in early systole at a level of 900 /s, but this region persists throughout the forward flow phase of the cardiac cycle.

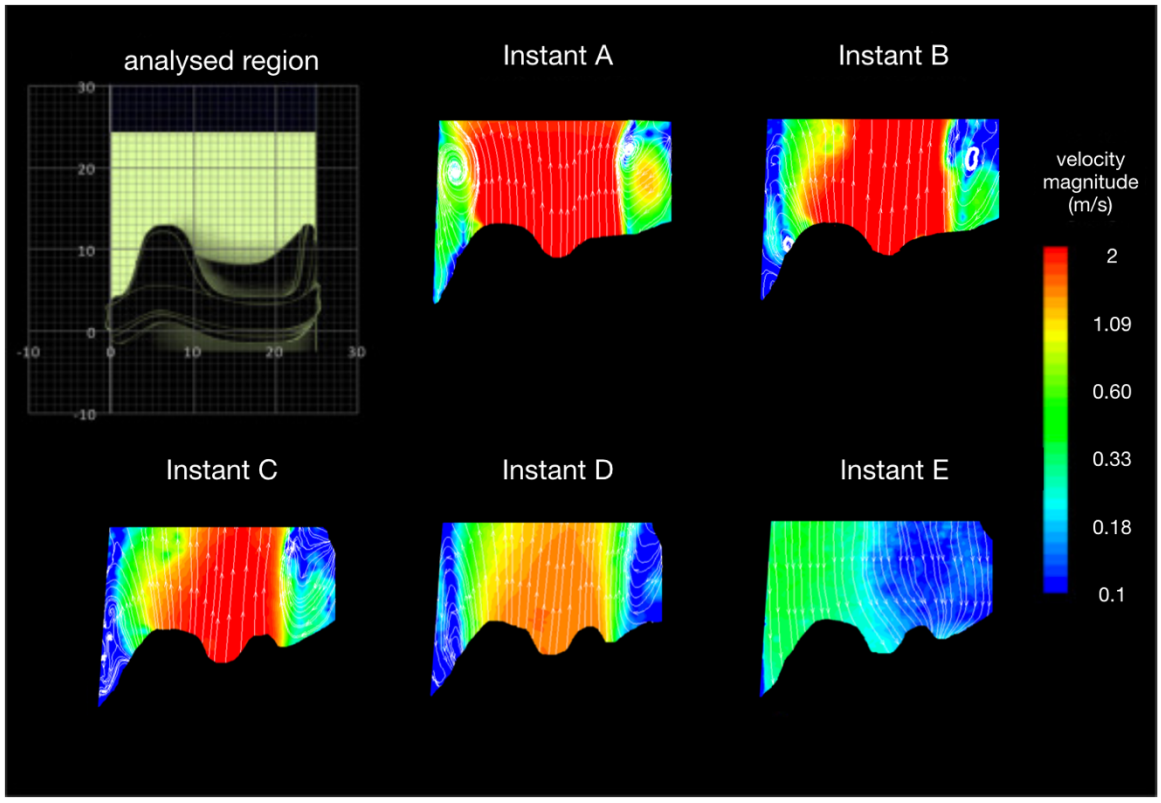

Figure 4-13: Velocity contour maps for the sinusless configuration.

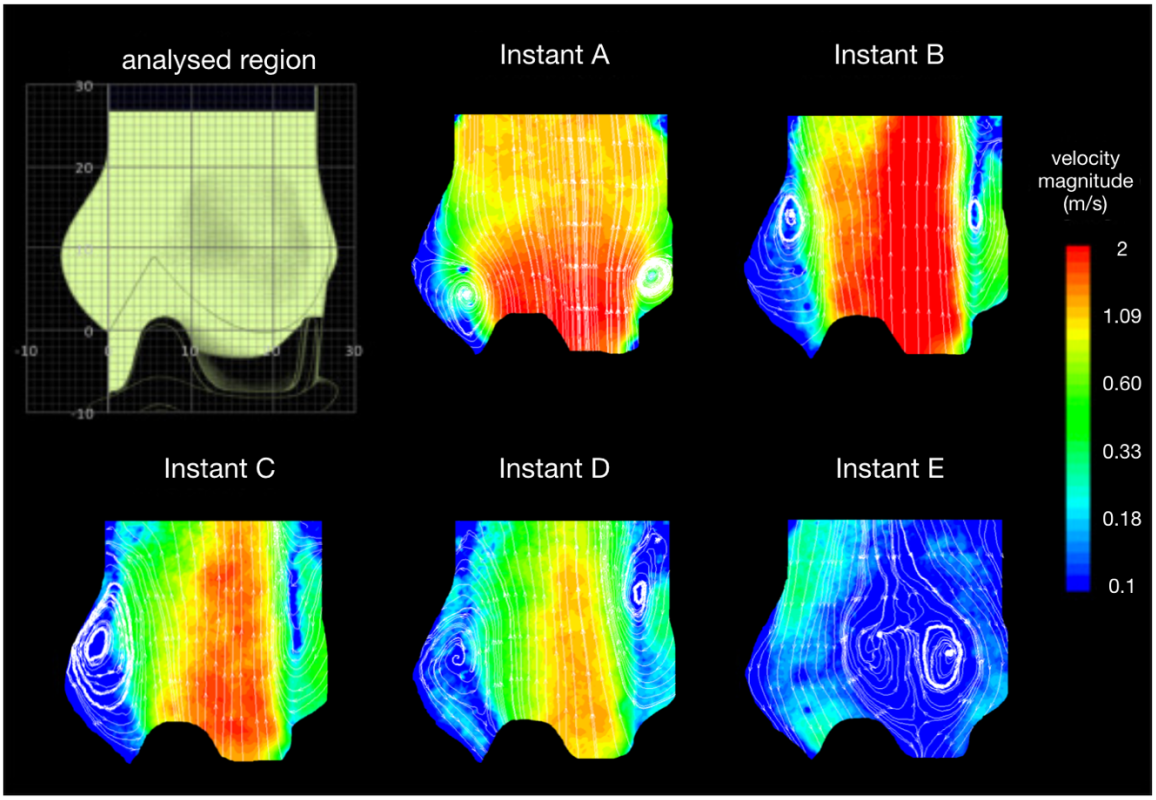

Figure 4-14: Velocity contour maps for the sub-annular configuration.

4.3.2.4 Sub-annular configuration

The velocity contour maps for the sub-annular configuration are represented in Figure 4-14, with the RSS, turbulence, and vorticity provided in the appendices, in Section 9.2. Once more, a positive start-up vortex ring develops on the sinus side of the valve, although in this case the vortex is generated at the base of the SoV chamber, from where it moves towards the STJ during peak flow, as shown in instant B of Figure 4-14. Remaining at a relatively low intensity, the vortex then expands to fill the entire sinus cavity (instants C-D in Figure 4-14), before dissipating at valve closure (instant E). A positive vortex forms above the commissural stent post again (instants B-D of Figure 4-14), with similar dimensions and intensity to that observed in the optimal surgical case (instants B-D of Figure 4-12), expanding towards the root axis at the end of systole.
During peak flow, the greatest velocity detected was 2.9 m/s, with an uncertainty of 0.83 %, and fast flow width was narrower than for the previous configurations, peaking at 11.2 mm during maximum flow (instant B). The average sinus velocity was very reminiscent of that measured for the physiological setup throughout the cycle, remaining on average within 10 % of the physiological values, and peaking at 0.186 m/s as the flow increased (instant A).
The RSS measured in the sub-annular setup are reminiscent of those in the optimal surgical configuration for the same instants, made up of much less distinct regions than the equivalent for the sinusless root, with intermixing of the positive and negative stresses in the central part of the flow (Figure 4-11), and reaching magnitudes of 160 N/m^2. The turbulence detected is spread across the fast flow portions of the cross-section, reaching a maximum standard deviation of 0.8 m/s at peak flow (instant B). Similar to the optimal surgical and sinusless configurations, a region of negative vorticity persists throughout systole on the commissural side of the valve, although closer to the base of the root, reflecting the sub-annular fixation of the valve, reaching 800 /s in early systole (instants A-C).

4.3.2.5 Dilated/oversized root configuration

Figure 4-15 presents the velocity contour maps obtained for the dilated root configuration, whilst the contour maps for the RSS, turbulence, and vorticity are

again located in the appendices, in Section 9.2. The forward flow spreads across the entire aortic cross-section at the STJ as the valve opens, accompanied by the formation of a positive start-up vortex in the SoV chamber. However, this vortex soon escapes the sinus, moving towards the ascending aorta and increasing in intensity at peak flow, as can be seen in instant B of Figure 4-15, before stabilising in position alongside the aortic wall at the level of the STJ (instants B-D in Figure 4-15). With the absence of this first vortex, a second vortex generates towards the base of the sinus as the forward flow decreases, with opposite direction (i.e. a negative vortex) to the initial vortex, evidenced in instants C and D of Figure 4-15. As with the optimal surgical and sub-annular configurations, a positive vortex also forms above the commissural stent post, moving downstream during systole, with the centre of the vortex positioned about 20 mm downstream of the distal portion of the stent just after peak systole (instant C). The maximum velocity in the cycle was detected at 2.8 m/s at peak flow, with a velocity uncertainty of 0.72 %, with a fast flow width that varied greatly through the systolic cycle – at peak flow, this was within 7 % of that measured for the physiological case (17.7 mm compared with 18.9 mm at instant B), but diminished very quickly, dropping to 72 % of the physiological at the next measured instant (9.9 mm in contrast to 13.8 mm at instant C). The average sinus flow followed a different trend to the other configurations – after similar sinus flow speeds to the physiological and sub-annular setups in the early stage of systole (instants A and B), the sinus velocity remains fairly constant at high flow through the valve, and then increases in late systole (instant D), in contrast to the slowing of sinus flow velocity in the other configurations.

The RSS distribution is more distinct than for the optimal surgical or sub-annular setups, but less than that observed for the sinusless configuration. Regions reaching 190 N/m^2 are observed either side of the central jet flow at maximum flow (Figure 4-11), diminishing in both size and magnitude as the flow decreases, before dissipating completely at valve closure. The turbulence is highest in the regions downstream of the valve leaflet exit and the commissures at and just after peak systole, at similar levels to that observed in the sub-annular configuration, whilst the vorticity is highest at peak flow, reaching -950 /s on the commissural side of the valve in a similarity to the 3 previous post-

surgical configurations, with little vorticity observed in the rest of the systolic cycle.

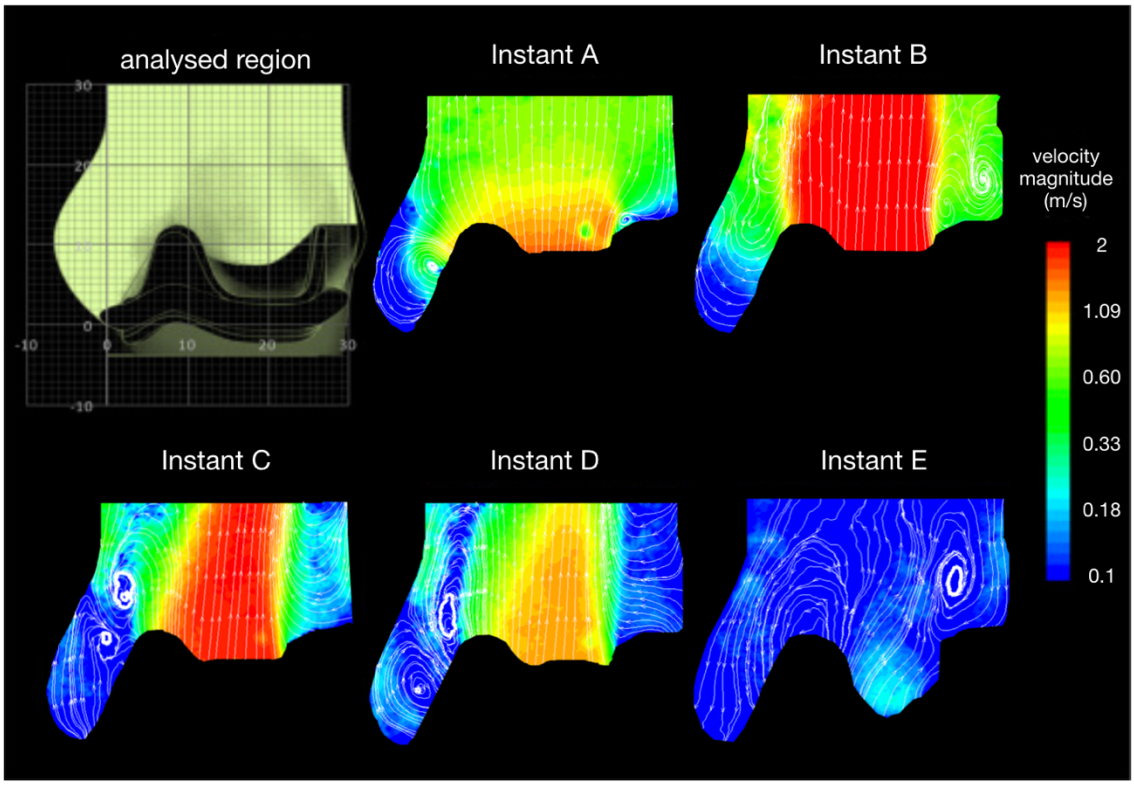

Figure 4-15: Velocity contour maps for the dilated/oversized root configuration.

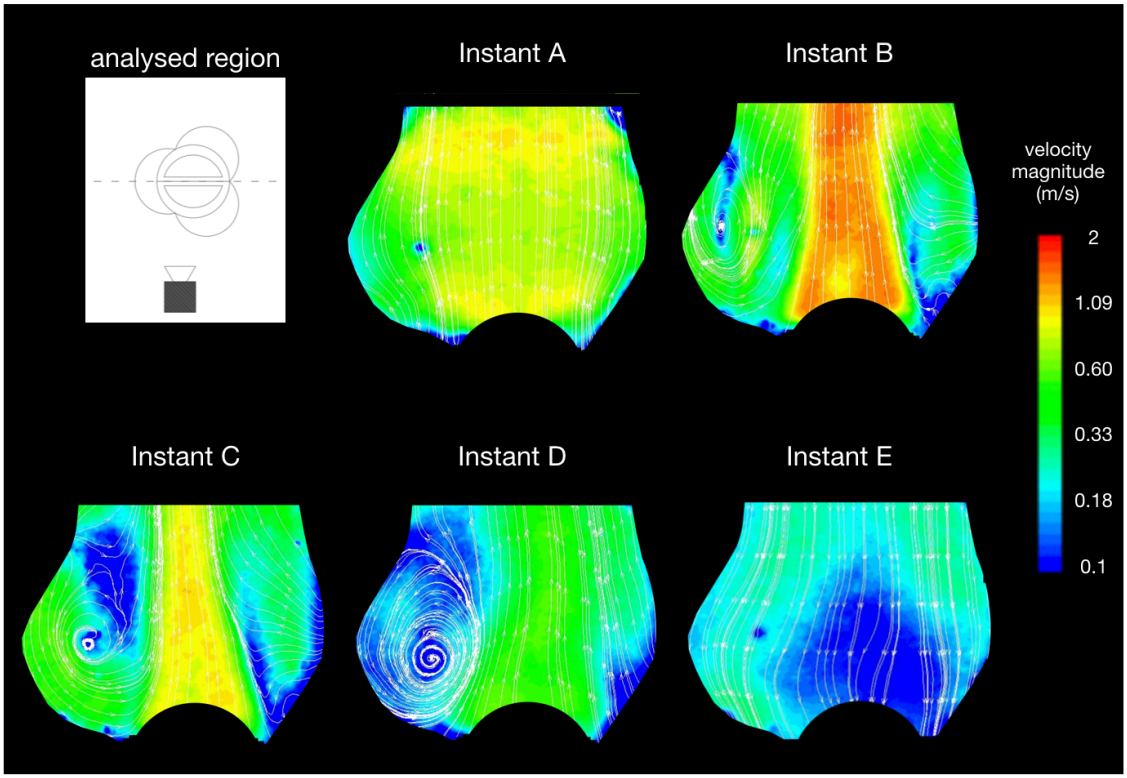

Figure 4-16: Velocity contour maps for the mechanical valve configuration, with the PIV laser sheet across the shared line of symmetry of the root and valve.

4.3.2.6 Mechanical valve configuration

The velocity fields for the mechanical valve configuration are illustrated in Figure 4-16, and contour maps of the RSS, turbulence and vorticity for each instant, alongside the velocity measurements for the rotated cross-section, are provided in the appendices, in Section 9.2.

Once developed at peak flow, the central jet flow is narrower than in any of the previous configurations, with a similar peak flow (instant B) forward flow width (11.1 mm) to that of the sub-annular configuration (11.5 mm). This jet width then shrinks quickly, down to 4.7 mm in mid-systole (instant C), less than half that of any other fast flow width at this point, and then reducing to zero at the next data acquisition point. A positive vortex is apparent from peak systole, in a similar position to that observed in the sub-annular setup. The vortex grows in size, filling more and more of the sinus as systole progresses (instants C and D in Figure 4-16), although no vortex is captured at any instant on the non-sinus side of the root cross-section. The average sinus velocity is generally the highest of any of the configurations, reaching a maximum of 0.444 m/s and averaging 0.280 m/s across the 5 analysed instants. The greatest velocity detected during peak flow (instant B) was 1.9 m/s, with an uncertainty of 1.21 %.

The peak RSS captured by the PIV analysis did not cover a large area of cross-section, concentrated on the outside of the central jet flow as indicated in Figure 4-11, although they did reach a magnitude of 138 N/m^2, slightly less than that measured for the sub-annular configuration. The turbulence of the analysed region is indicated to reach a maximum either side of the jet at peak flow (instant B), reaching a standard deviation of 0.8 m/s, although much of the cross-section appears to experience turbulence from early- to mid-systole (instants A-C). Similar to the RSS measured, regions of high vorticity across the region are small, with small areas reaching a magnitude of 800 /s either side of the central jet flow at peak systole (instant B).

4.4 Discussion

To enhance the clarity of the PIV findings, summaries of the various flow within each root are presented in Figure 4-17.

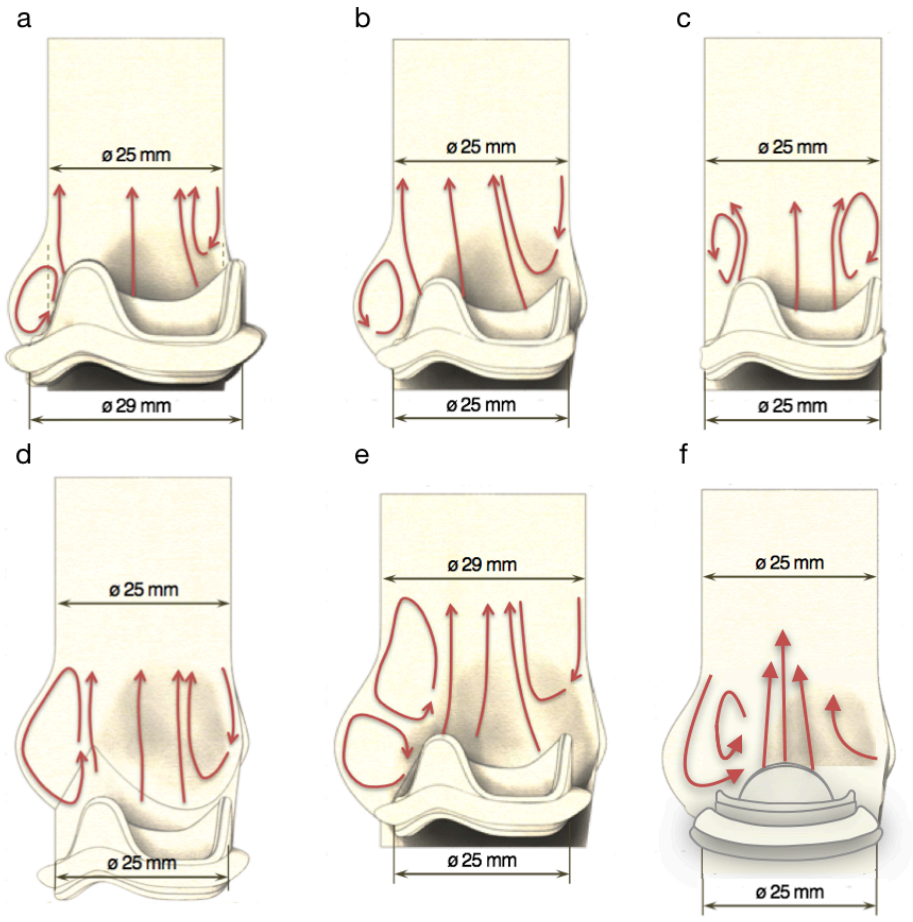

Figure 4-17: Summary of the fluid flow for each configuration. (a) Physiological; (b) Optimal surgical; (c) Sinusless; (d) Sub-annular; (e) Oversized/Dilated root; (f) Mechanical

The physiological setup, which represents the healthy native anatomy the most closely, is characterised by a start-up vortex which becomes entrapped within the sinus chamber for the majority of systole. The ejected flow is accordingly relatively unrestricted as is passes from the open valve to the STJ, leading to the largest x_f and an evenly distributed flow profile in the early stages of systole compared to the other configurations. RSS throughout the cycle remain well below any reported haemolysis thresholds, ranging from 150 – 520 N/m^2 in the literature[37,89,90] and measured at values no greater than 53 N/m^2 across all instants for this configuration.

The optimal surgical configuration - modelling the same root geometry as the physiological setup but following the ablation of the native valve and replacement with an ideally sized and positioned bioprosthetic valve, with necessarily smaller leaflets than the physiological valve - has a very similar opening mechanism to the physiological case, with the start-up vortex captured

and contained within the SoV in early systole. However, the vortices within the sinus and just downstream of the valve stent commissures are larger, due to the smaller valve leaflets and increased presence of the stent inside the root lumen, constraining the systolic jet flow and decreasing the haemodynamic performance of the setup. Specifically, the EOA is 32 % smaller than for the physiological configuration, corresponding to an increase in ΔP of 64 %, and the v_p increasing by 70 %. The smaller valve displays an improved closing energy efficiency, due to the reduced distance of leaflet travel and diminished geometric orifice area, but this cannot compensate for the systolic losses, and the E_s for the setup is 32 % higher. The peak RSS measured during the early stages of systole were higher than the lower threshold of haemolysis reported in the literature, indicating a risk of blood damage and platelet activation in the region after even an ideal surgical procedure. The increased sinus velocities for this case in comparison to the other setups may mitigate this to an extent however, indicating increased washout and reducing the thrombogenicity of the SoV chambers during systole.

Whilst the sinusless configuration appears to be an extreme scenario, it is representative of clinical cases of an aortic valve being implanted into a tubular aortic graft, and could be analogous to the case of transaortic valves, for which the native leaflets (which are not ablated as in surgical valve implantation) held open by the surrounding TAV frame act as a containing tube[35]. This setup is characterised by the repeated formation and migration of vortices on the sinus side of the valve, constricting the central flow and, in comparison to the physiological case, leading to an increase in both v_p and ΔP of 76 % and 112% respectively, and a corresponding reduction of EOA of 36%. This configuration also displayed the highest levels of RSS acquired, up to 276 N/m^2 which was more than 5 times that measured in the physiological setup, and well above the lower threshold of haemolysis reported in the literature.

A major function of the SoV appears to the systolic hosting of the start-up vortex that generates as a result of the associated leaflet opening, enabling the central fast flow to reattach to the aortic wall at the STJ, as illustrated in Figure 4-12. The absence of the SoV chambers also causes a significant decrease in the closing efficiency when compared to the optimal surgical configuration, as

shown by the increased V_c and E_c, most likely due to the reduction of the radial aspect of the flow, which develops in the sinuses and promotes the closure of the leaflets. Over the whole cycle, E_s is more than twice that of the physiological configuration, and 60 % higher than the optimal surgical case. This is in agreement with findings in the literature stating that the geometry of the root and the presence of the SoV chambers have a major impact upon the flow characteristics downstream of the aortic valve[18,20,69,246]. Improvements in the performance of the valve due to the presence of the SoV has been reported in other *in vivo* and *in vitro* studies[68,256], and a clear and reasonable explanation is provided by the fluid dynamics mechanisms identified here.

The remaining 2 configurations indicate that the dimensional parameters of the valve and root as well as the positioning of the valve have a strong influence upon the valve performance. In the sub-annular case, the start-up vortex moves away from the low position of the valve into the upper region of the sinus, which, due to the absence of the leaflets adjacent to the upper portion of the chamber, cannot provide effective containment. The vortex is resultingly pushed away from the sinus by the central fast flow, escaping towards the ascending root, which confines the ejected flow from the valve onto the other side of the root and narrows the *vena contracta* of the flow. In comparison to the physiological case, the EOA is reduced by 42 % and x_f is diminished throughout the cycle, particularly in early systole, and the configuration produces a ΔP very similar to that measured in the sinusless setup, whilst the levels of RSS acquired indicate that very little of blood exceeds the haemolysis threshold. However, the increase of space available in the sinuses enables the formation of a larger vortex, supporting the closure of the valve leaflets and resulting in the lowest V_c of any of the investigated cases, although across the systolic cycle as a whole, energy losses were 77 % higher than for the physiological setup. Sub-annular configurations are common in *in vitro* testing, where the prosthetic is often clamped into a housing component situated beneath the mock aortic root with sinuses, and the observed mechanism of vortex migration shows similarities to those reported in the literature in some benchtop studies[21,60,253]. This study therefore implies that the axial positioning of the valve needs to be replicated with care within the test rig, as it can significantly affect the

haemodynamic performance. These results also suggest that the current supra-annular implantation approach used clinically, as opposed to infra-annular positioning, may result in significantly improved haemodynamics as well as a more favourable geometric orifice area.

The STJ root diameter was increased by 16 % for the dilated root configuration, which impaired the potential of the sinus to constrain the start-up vortex to its chambers. The vortex escapes downstream, narrowing the central flow and decreasing the EOA by 37 % and increasing the ΔP by 76 % in comparison to the physiological case, whilst the RSS briefly exceeds the lower reported haemolysis threshold during peak flow, reaching a maximum of 191 N/m^2, although this soon subsides and remains well below any reported threshold for the rest of the cycle. Once the vortex has escaped the SoV, x_f is diminished, as shown in instants C and D in Figure 4-15. Once this initial vortex has moved away from the sinus, a secondary negative vortex forms in its stead, increasing sinus flow velocity and supporting valve closure, and leading to values of V_c similar to those acquired from the optimal surgical setup. Accordingly, E_s for this configuration is in between those obtained for the optimal surgical and sinusless cases. Despite a much larger transversal aortic root cross-sectional area (35 % larger) than in the other cases investigated, the vortical mechanism observed results in a significant reduction in EOA when compared to the optimal surgical case, which is otherwise identical in valve size and position. Similar root-valve geometries can be expected in clinical situations where the implanted valve is under-sized, or when the aortic root dilates due to either pathological scenarios or ageing[47,142], and oversized roots (relative to the valve used) are common in *in vitro* tests, where a universal root is used for various valve sizes[33,34,155,248], with the mechanism identified for this case often observed.

Replacing the surgical bioprosthetic with a mechanical valve resulted in the greatest ΔP during systole, 3 times that of the physiological level, with correspondingly high systolic energy losses. V_c was higher than any of the surgical bioprosthetic setups, possibly indicating that any vortices present in late systole have less effect upon the rigid pyrolytic carbon material than on the flexible biological tissue leaflets. The vortical patterns within the sinus during mid-late systolic flow is reminiscent of those observed in the sub-annular

configuration, which correlates with the relative low outflow of the mechanical valve in comparison to the standard bioprosthetic fixation. With no leaflet containment within the sinus, the vortex spreads and impinges upon the central jet flow of the root in this cross-section. Although the small x_f measured during peak flow does not appear to correspond with the relatively low v_p, it must be considered that the bileaflet mechanical valve does not align with the 3 sinuses in the same manner as the trileaflet bioprosthetics, as shown in Figure 4-4. Examination of the velocity fields from the alternate mechanical valve-root cross-section, as described in Figure 4-4 (c) and which can be referred to in the appendix in Section 9.2, shows a much larger x_f, accompanied by very little vortical patterns. The RSS measured remains below the majority of the thresholds described in the literature, and the sinus flow speed is high in comparison to the bioprosthetic surgical configurations, indicating that the high levels of blood damage reported for mechanical valves is not related to the RSS observed in the flow downstream of the valve outlet, but may be more associated with the mechanical valve itself, primarily the shear stress around the hinge joints, the systolic backflow jets, and the thrombogenicity of the material surface, possibly worsened with wear[9]. Despite the associated lifelong anti-coagulant therapy required after implantation, mechanical valves are sometimes used instead of bioprosthetic valves due to their high durability in comparison to current bioprosthetic valves[9].

4.4.1 Limitations

The investigation included some limitations, which need to be taken into account when considering the above discussion. The blood analogue used in the experiment is Newtonian, with a lower dynamic viscosity than that measured in human blood at high shear. There may accordingly be some departure from the physiological fluid dynamics. The PIV system used is both phase-averaged, therefore unable to reveal cycle-to-cycle variations of the flow patterns, and 2D, rendering it unable to capture out of plane fluid structures. Imaging of the hinge joints of the mechanical heart valve, indicated to be a region of high turbulence and shear stress in previous research[9], was not possible. Finally, the roots constructed for this investigation were designed from an idealised physiology, with no presence of coronary ostia of vessel compliance, and only one set of

pressure and flow conditions, representing a typical healthy physiological condition at rest, were used throughout the analysis. Inclusion of root compliance and different operating conditions could provide further insight into the flow mechanics of the valve. The limitations described here do not overly detract from the work, which clearly identifies varying fluid mechanisms for the same valve, as a result of alterations to the system configuration.

4.5 Concluding Remarks

The results acquired from this investigation clearly show the important role that the relationship between the aortic valve and root plays on the functional mode and haemodynamic performance of the left side of the heart, and clarify the reasons for the contrasting mechanisms reported in the literature. The setup of the physiological configuration was considered successful, with peak blood velocity, effective orifice area, pressure drop across the valve, and RSS representative of measurements taken from *in vivo* studies[55,98,137,138]. The setup designed to replicate the native condition produces superior hydrodynamic performances to the other cases, and any significant alteration to the valve position or variation to the geometric proportions of the root in relation to the valve results in major changes to the fluid dynamics downstream of the valve, negatively affecting the haemodynamic performance. This rationale could explain the difference in the number and direction of the vortical structures identified in previous reports in the literature, elucidating the experimental complications previously encountered in the assessment of prosthetic heart valve performance, even when these reports are limited to the calculation of whole cycle parameters such as the effective orifice area, the transvalvular pressure drop, and regurgitant volumes.

The systolic vortical patterns of the model of the physiological aortic root and valve can be summarised as follows – the interaction between the central fast flow and the lower inertial flow in the surrounding boundary layer result in the generation of vortices at the exit of the valve, which are soon captured by the encompassing SoV chambers and remain here throughout systole, dissipating only after complete valve closure. With the vortices confined to the sinuses, the central flow is broadly unrestricted and spreads across the root at the STJ,

filling most of the root cross-section, before the flow becomes more complex further downstream in the aortic arch. This summary can now be used to compare and contrast the resultant fluid flow patterns acquired from the investigations of a TAV setup, revealing the haemodynamic changes as a result of the interventional treatment, which will be presented in Chapter 5, ‘Does Transcatheter Aortic Valve Alignment Matter?’.

5 Does Transcatheter Aortic Valve Alignment Matter?[2]

5.1 Introduction

As described in the previous chapter, the fluid dynamics of the healthy native valve exploits the possibility of vortical generation within each of the sinuses of Valsalva. This allows the systolic ejected flow to pass through to the STJ relatively unrestricted with an evenly distributed flow profile, and the blood is indicated to remain well below the haemolytic shear stress threshold, when blood is at risk of rupturing due to the shear stress imposed on it, indicated by the literature to be as low as 150 N/m^2, throughout the cardiac cycle[37,89,90]. However, degenerative conditions such as aortic stenosis, a common disease in the world's elderly population[4,5], are often irreversible[6], and require the native aortic valve to be replaced in order to restore the region's functionality. Replacement of the native valve with a prosthetic via surgery is deemed to be ineligible for around a third of patients, due to advanced age and/or co-morbidities[10,11], and so a minimally invasive technique, involving delivery of a crimped bioprosthetic valve – known as a Transcatheter Aortic Valve (TAV) - to the aortic annulus via a catheter[12], has been developed and has been performed on over 200,000 patients since 2002[189].

The fluid dynamics of the aortic root region are different to those observed for the healthy native valve, and complications such as energy losses, non-physiological CA flow, and PVL[12] frequently follow TAV implantation, and serious downstream pathologies such as an increased occurrence of stroke, silent ischemic lesions, and cerebral embolism[14–16,174] have been linked to the procedure. The native leaflets are not ablated as they often would be during surgery, but instead are permanently radially displaced into a pseudo-cylindrical

[2] The research presented in this chapter is under review for publication as an article in the Journal of Cardiovascular Research

- Does Transcatheter Aortic Valve Alignment Matter?, J. Salmonsmith, A. Ducci, and G. Burriesci, *submitted December 2018*

And has been presented by the author at:

- British Cardiovascular Society Conference 2017, Manchester, UK
- UCL Institute of Healthcare Engineering Autumn Research Symposium 2018, London, UK

configuration. As the TAV stent restricts the opening of the working leaflets to 90 °, the systolic jet is narrower than for an equivalently sized native of surgical valve[35,203], potentially doubling the peak blood velocity[55,78,202] and raising the shear stresses of the flow[186], although these remain beneath haemolytic thresholds[201].

It has been reported that the systolic vortices no longer generate within the SoV at the start of forward flow through the valve, but instead form at the edge of the now static native leaflets[97], reducing sinus washout[97,186], particularly the shorter TAV style such as the Edwards SAPIEN XT valve[191], associated with a delay in valve closure of ~ 10 ms[35,203]. Similarly, it has been reported that vortices are not present following the return of fluid during valve closure, again reducing chamber washout[97]. The decreased shear stress and increased red blood cell (RBC) residence time in the native sinuses[97,185] enhance the thrombogenic conditions within[97]. Additionally, the 'neo-sinus', formed between the native leaflets and the stent of the TAV, may also promote fluid dynamics that are prone to stagnation[204]. This would increase the thrombogenicity of the region, enhancing the risk of sub clinical leaflet thrombosis (SCLT), which could lead to lesions and diminished TAV leaflet motion[192,207] and has been associated with strokes and transient ischemic attacks, and has been observed in 14 % of follow up examinations after implantation of Edwards SAPIEN XT valves[192]. Reduction of these stagnation regions may improve long-term clinical outcomes[192], which are currently affected by thrombotic events in the first 6 months following TAV implantation[205,206].

Placement of the TAV device into the native aortic annulus is typically achieved using intra-operation 2D imaging techniques, such as angiography or fluoroscopy. These techniques, whilst adequate in ensuring a sufficiently accurate depth of implantation, are not ideal in identifying the angular position of the TAV, and methods which would establish the rotation of the device, such as real-time 3D Computed Tomography-fluoroscopy or 3D transoesophageal echocardiography-fluoroscopy fusion imaging, are not commonly used[257,258]. Correspondingly, orientation of the TAV in the same leaflet-to-sinus arrangement as the native valve is rather haphazard[259], raising concerns about the effect of non-alignment of the commissures of the TAV with the commissures of the host root[204], as stated in section 2.4.3. The interaction of

the leaflets and fluid flow with the geometry of the sinuses has been shown *in vivo*, *in vitro*, and numerically within the literature, as well as in the previous chapter of this thesis, to have significant effects upon the haemodynamics[18,20,21,246]. Alignment of the commissures has already been shown to minimise the stress experienced by the TAV's leaflets, and although non-alignment has been indicated *in vivo* to result in similar global haemodynamic features[259], commissural alignment may improve the flow dynamics of the native- and/or neo-sinuses[204], and have implications for the central fast flow systolic jet.

The aim of this chapter is to investigate the effect of the angular alignment of TAVs upon the hydrodynamics produced within the host aortic root and ascertain whether non-alignment of the bioprosthetic can result in sub-optimal haemodynamics and performance, in-line with the second objective of this thesis, presented in Section 2.4.5.2, 'to characterise the flow resulting from implantation of a TAV into a stenotic aortic valve, and to ascertain whether the rotational alignment of a TAV within its host root has an effect upon the resultant fluid dynamics in the region'.

A widely adopted TAV, the Edwards SAPIEN XT, was placed into a mock aortic root in 2 extreme rotations:

1. prosthetic and mock host root perfectly aligned (commissure-upon-commissure), within mock native leaflets;
2. prosthetic and mock host root at maximum misalignment (commissure-upon-sinus), for a maximum angular misalignment of 60 °, within mock native leaflets.

The presence of the native leaflets is commonly neglected for *in vitro* experiments[78,182,184,186], and therefore it is useful to verify if this assumption is acceptable. Consequently, 2 additional configurations were also investigated:

3. prosthetic and mock host root perfectly aligned (commissure-upon-commissure), with no mock native leaflets present
4. prosthetic and mock host root at maximum misalignment (commissure-upon-sinus) of 60 °, again with no mock native leaflets present.

For each configuration, the global haemodynamics were assessed via pressure transducers and a flowmeter, and local fluid dynamics were again characterised

using Particle Image Velocimetry (PIV), providing information on the flow structures (using the same methods as Chapter 4). This work presented in this chapter is an adaptation of work which is under review at the Journal of Cardiovascular Research.

5.2 Methods

5.2.1 Valve Configurations

The bovine bioprosthesis described in Section 0, the 26 mm Edwards SAPIEN XT valve, was selected for this study. A widely implanted TAV device, the valve consists of a cobalt chromium balloon-expandable cellular frame, which houses a trileaflet bovine pericardial valve. One of the mock aortic roots described in Section 3.5, the 25P, was used to replicate the idealised geometry of a native aortic region characterised by a 25 mm STJ diameter, representative of a healthy human adult[46].

As in the previous chapter, the root was made of optically clear, solvent free, low viscosity silicone elastomer with refractive index $n = 1.4$, the thick walls of which resulted in negligible compliance, representative of older patients[254]. Expanded native leaflets were modelled by including a cylindrical vinyl wrap around the TAV, 0.45 mm thick, which prevented the flow of any fluid through the mesh of the TAV. The distal edge of the wrap was 17.5 mm from the sinus base, with the shape matching a fully open native human aortic valve as described by Thubrikar[126] for an aortic root with 25 mm STJ. The expanded Edwards SAPIEN XT valve was placed into the mock aortic root, with the midpoint of the valve between 1 and 2 mm downstream of the basal annulus of the root[51], as recommended for the clinical procedure[214]. The following four different valve-root configurations were modelled and studied, as illustrated in Figure 5-1:

TA1. Aligned, native leaflets: each commissure of the TAV aligns with a commissure of the aortic root model, resulting in each TAV leaflet's belly opening out into its associated Valsalva sinus; mock native leaflets were included in the aortic root model.

TA2. Misaligned, native leaflets: the valve is 60 ° out of phase with the ideal alignment with the root, resulting in the belly of each TAV leaflet

aligning with a commissure of the aortic root model; mock native leaflets were included in the aortic root model.

TA3. Aligned, no native leaflets: the same valve-root alignment as used in configuration TA1; No native leaflets are included in the model.

TA4. Misaligned, no native leaflets: the same valve-root alignment as used in configuration TA2; No native leaflets are included in the model.

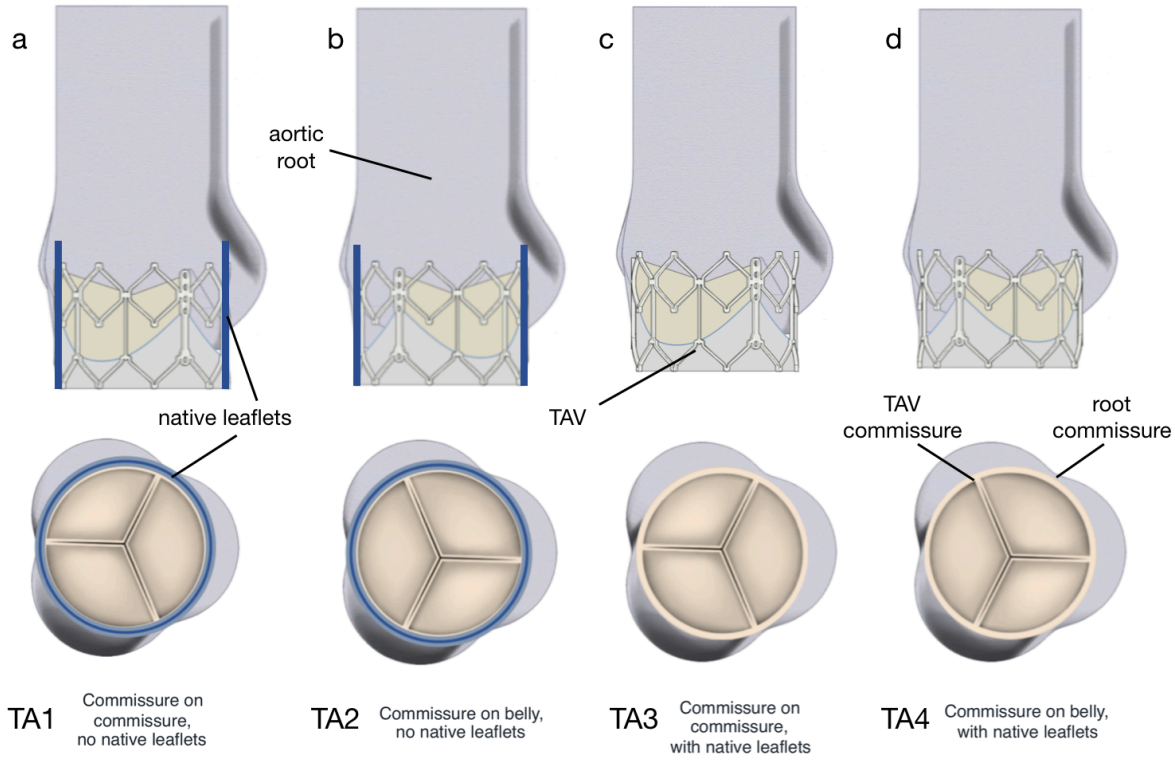

Figure 5-1: Valve-root configurations considered in TAV Alignment study. (a) Configuration TA1; (b) Configuration TA2; (c) Configuration TA3; (d) Configuration TA4

As the investigation presented in Chapter 4 had been concluded before the commencement of this experiment, it was decided that the use of glycerol or KI in the blood analogue would not alter the properties of the bioprosthesis during the span of the tests. Accordingly, the solution described in Section 3.6.3, utilising KI, glycerol, and deionised and filtered water, was used as the blood analogue, matching the blood viscosity of 4.0 cP at 37 °C, and the refractive index of the silicone material used in the mock aortic root.

5.2.2 Global Parameters

Assessment of the various configurations was again carried out on the hydro-mechanical pulse duplicator detailed in Section 3.2. Tests were performed at a heart rate of 70 beats per minute, with 35% of systolic duration and a mean aortic pressure of 100 mmHg. In order to reduce the effect of the different diastolic leakages, and to produce comparable systolic flows more appropriate for this study, the stroke volume rather than the cardiac output was considered in this investigation. As a result, 4 different stroke volumes, representing the amount of blood pumped from the left ventricle in one contraction (i.e. the blood per cycle), 28.6, 50, 71.4, and 92.9 ml (corresponding to cardiac outputs of 2.0, 3.5, 5.0, and 6.5 litres per minute (lpm) respectively). Measurements from pressure transducers up- and down-stream of the TAV combined with volumetric flowrate data acquired from an electromagnetic flowmeter downstream of the aortic valve allowed estimation of:

- The systolic transvalvular pressure drop (Δp) across the valve, in mmHg
- The Effective Orifice Area (EOA) of the valve, in cm^2
- The closing regurgitant volume (V_c) of the valve, in ml
- The energy losses during forward flow (E_f) and valve closure (E_c), and the combination of these to give the total systolic energy loss (E_s), in mJ.

As detailed in Section 3.2.2 and as in the previous chapter, an average cycle of pressure and flowrate fluctuations was calculated from 20 cycles, taken from the first and last 10 cycles of the PIV image acquisition for each configuration.

5.2.3 Local Fluid Flow Properties

2D PIV, as detailed in Section 3.3, was again used to investigate instantaneous fluid dynamics of each configuration, at a standard stroke volume of 71.4 ml/cycle (corresponding to a systolic cardiac output of 5 lpm), to produce a contour map describing the instantaneous fluid motion across the measurement plane. The laser sheet was projected over the sagittal plane, as in the previous investigation, at the centre of the root-valve configuration. Velocity fields for each of 5 instants across the systolic portion of the cardiac cycle were captured, enabling characterisation of the fluid flow dynamics. As in the previous chapter, these reference instants could potentially alter their timing position within the

cardiac cycle due to the changes between the various configurations, and therefore the instants corresponded to the following conditions:

A. Maximum increasing flowrate
B. Peak flowrate
C. Flowrate decreased to 75 % of peak flowrate
D. The most significant change of curvature of the flowrate during late systole
E. Flowrate decreased to 25 % of peak flowrate

These instants are presented for all configurations in Table 5-1, and illustrated for configuration TA1 in Figure 5-2(a).

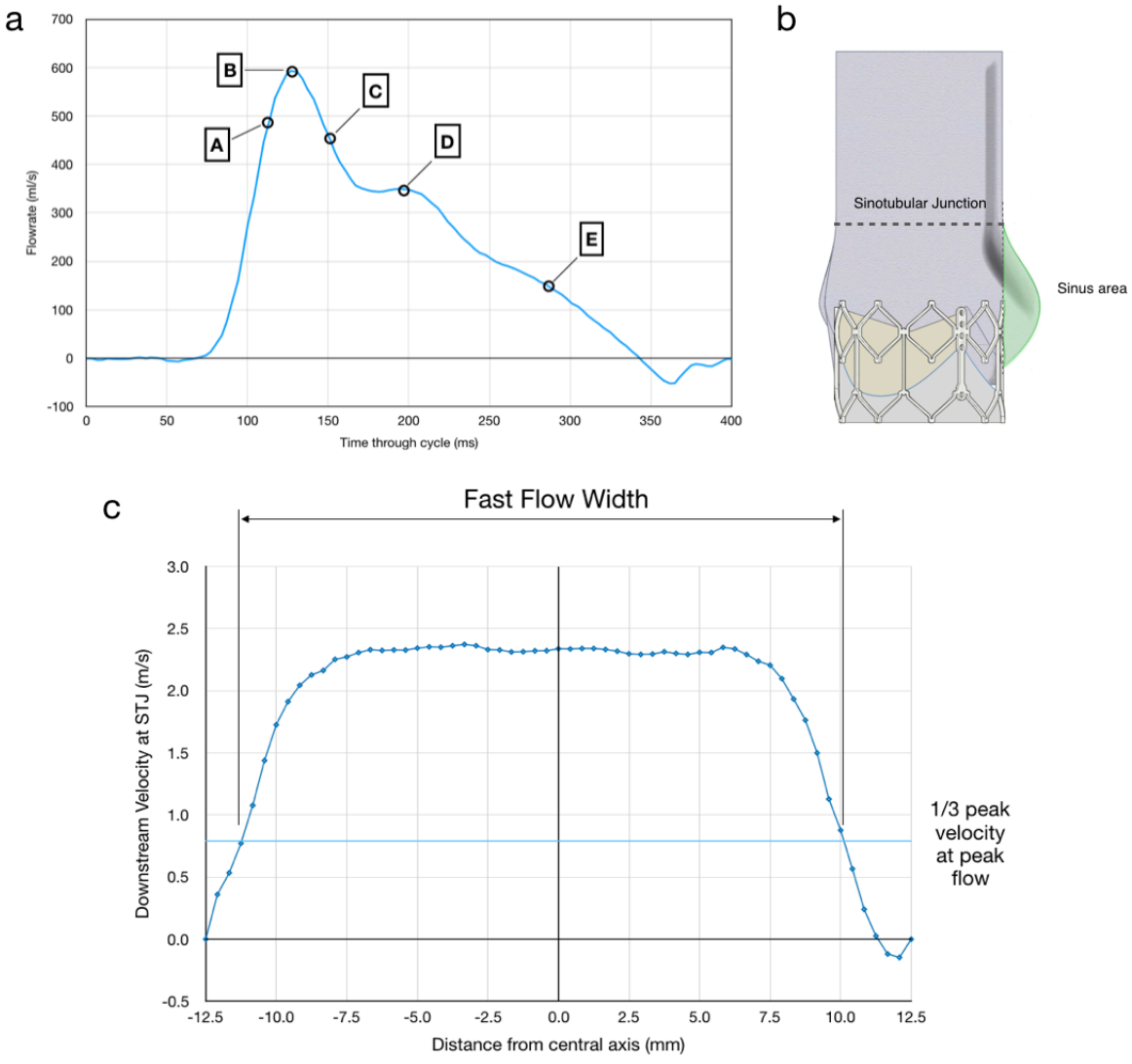

Figure 5-2: PIV data properties: (a) Typical diagram of the flowrate vs the time through the heart cycle with the analysed instants shown; (b) Sinus area of cross-section for calculation of average sinus velocity from PIV data; (c) Calculation of Fast Flow Width (x_f) from velocities across the STJ profile.

Configuration	*Instant Time through Cycle (ms)*				
	A	B	C	D	E
TA1	112	127	152	194	287
TA2	112	127	150	191	286
TA3	111	127	152	193	285
TA4	111	127	151	191	281

Table 5-1: Time elapsed through cycle for each analysed instant for PIV data acquisition for each configuration

Phase resolved processing was carried out on 100 image pairs for each instant of each configuration, as detailed in Section 3.3.3.4. Identification of the time interval of the image pairs (Δt) for the anticipated relatively fast flowing central jet was calculated via equation (3-17), assuming the formation of an approximately triangular orifice[255] inside the frame of the Edwards SAPIEN XT valve. The image pair time intervals used to capture the fast flow dynamics during each instant for the various configurations is displayed in Table 5-2. In order to capture the expected slower sinus flow, a second set of 100 image pairs with a Δt of 250 μs was captured at instants A-D for each configuration.

Configuration	*Time interval of image pair, Δt, at each Instant (μs)*				
	A	B	C	D	E
TA1	74	67	89	133	267
TA2	64	58	77	116	231
TA3	71	63	85	127	254
TA4	63	57	75	113	226

Table 5-2: Time interval for image pairs at specified instants

These image pair times alongside the magnification factor k for each PIV setup enabled calculation of the PIV velocity uncertainty, describing the velocity error due to the randomness of the determination of the finite interrogation windows within sub-pixel accuracy[225] as defined in Section 3.3.3.3, for each analysed instant of each configuration, the results of which are shown in Table 5-3.

Configuration	*PIV Velocity Uncertainty for each Instant (m/s)*				
	A	B	C	D	E
TA1	0.0324	0.0360	0.0270	0.0180	0.0090
TA2	0.0327	0.0463	0.0273	0.0182	0.0091
TA3	0.0326	0.0362	0.0272	0.0181	0.0091
TA4	0.0334	0.0371	0.0278	0.0186	0.0093

Table 5-3: Maximum PIV Velocity Uncertainty for each instant in each configuration

Cross correlation processing, as explained in Section 3.3.2, was undertaken after the acquisition of image pairs for each instant, resulting in velocity fields, which were then converted, as detailed in Section 3.3.3.1, into velocity magnitude, RSS, turbulence as indicated by standard deviation, and vorticity, including the application of streamlines to improve the elucidation of the fluid flow at each analysed instant, as presented in Section 3.3.3.2.

Quantitative comparison of the configurations was achieved by recording the greatest velocity magnitude measured for the entire cross-section for each instant of each configuration, labelled as the peak velocity, v_p. Further analysis was carried out by extracting the mean of the velocity magnitudes within the sinus area of the images, indicated by the green shaded region in Figure 5-2(b), was recorded as the average sinus velocity, v_s. As there have reports in the literature[97] that the flow at the base of the sinuses is particularly affected by the implantation of the TAV, the sinus data was categorised further into the upper and lower half of the sinus, divided by the median y-value of the sinus area as illustrated in Figure 5-3, to give an average upper- and lower-sinus velocity (v_{us} and v_{ls} respectively). Finally, the fast flow width (x_f) of the flow was defined as the width of the velocity profile across the mock STJ where the downstream velocity magnitude, v_{STJ}, is higher than one third of the peak velocity detected via PIV analysis for the whole cross-section at peak flow, v_p, for each configuration, measured from the PIV data, as indicated in Figure 5-2(c).

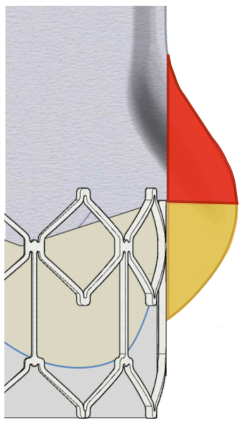

Figure 5-3: Illustration of upper- and lower-sinus regions. The upper sinus is shaded red, and the lower sinus is shaded orange, split around the centre line of the sinus, halfway between the basal annulus and the STJ.

5.3 Results

5.3.1 Global Data

The global haemodynamic data across the 4 configurations for each of the 4 stroke volumes are presented in two separate tables for clarity, with the EOA and mean systolic transvalvular pressure drop (Δp) presented in Table 5-4, with line charts to enable visual comparison of the variation of Δp and the systolic energy losses for each configuration at each stroke volume shown in Figure 5-4, and the closing regurgitant volume (V_c), and systolic energy losses (E_f) are displayed in Table 5-5. The haemodynamic performance of each configuration is compared to that of the maximally aligned valve within native leaflets, as this configuration was designed to reproduce the fluid dynamics of an ideal implantation of a TAV. The variation of flow and pressure throughout an average cycle during systole for each configuration at a stroke volume of 71.4 ml (the equivalent of a cardiac output of 5 lpm) is illustrated in Figure 5-5, followed by the flow-time and pressure-time outputs for configuration TA1 at all 4 stroke volumes investigated in Figure 5-6. Errors in the haemodynamic data are equal to the range of pressure over the 20 cycles and the resolution of the pressure and flow transducers, and are indicated both in the table and the figures above.

Global Parameter	*Stroke Volume (ml)*	*TA1*	*TA2*	*TA3*	*TA4*
Effective Orifice Area (cm^2)	28.6	1.71 ± 0.02	1.98 ± 0.02 *(115 %)*	2.36 ± 0.02 *(138 %)*	2.03 ± 0.02 *(119 %)*
	50.0	2.21 ± 0.02	2.24 ± 0.02 *(101 %)*	2.51 ± 0.03 *(114 %)*	2.35 ± 0.02 *(106 %)*
	71.4	2.35 ± 0.02	2.32 ± 0.02 *(99 %)*	2.55 ± 0.03 *(109 %)*	2.44 ± 0.02 *(104 %)*
	92.9 (86.2 for TA2)	2.33 ± 0.02	2.42 ± 0.02 *(104 %)*	2.52 ± 0.03 *(108 %)*	2.40 ± 0.02 *(103 %)*
Pressure Difference (mmHg)	28.6	3.3 ± 0.08	3.1 ± 0.08 *(94 %)*	2.1 ± 0.06 *(63 %)*	2.8 ± 0.07 *(85 %)*
	50.0	4.8 ± 0.11	4.4 ± 0.10 *(92 %)*	3.8 ± 0.09 *(78 %)*	4.3 ± 0.10 *(90 %)*
	71.4	8.1 ± 0.14	8.2 ± 0.14 *(101 %)*	7.1 ± 0.12 *(88 %)*	7.8 ± 0.13 *(96 %)*
	92.9 (86.2 for TA2)	14.1 ± 0.21	11.9 ± 0.18 *(84 %)*	13.5 ± 0.20 *(96 %)*	14.7 ± 0.23 *(104 %)*

Table 5-4: Effective Orifice Area and Transvalvular Pressure Drop for all configurations at all stroke volumes: mean value, ± standard deviation, and percentage value with respect to configuration representing an aligned valve within native leaflets

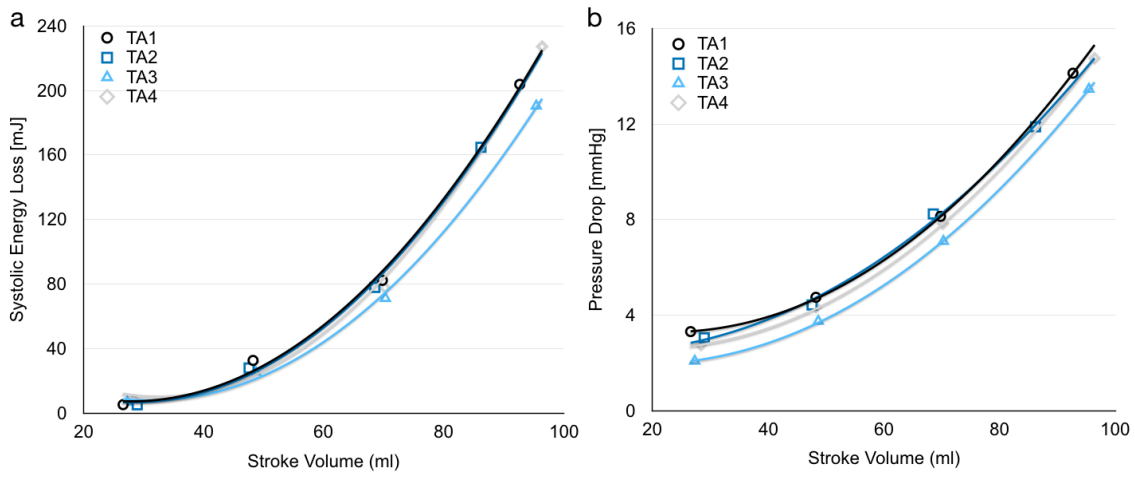

Figure 5-4: Haemodynamic Performance. (a) Transaortic energy losses during forward flow and closing phases for each configuration at each stroke volume; (b) Systolic transaortic pressure drop for each configuration at each stroke volume.

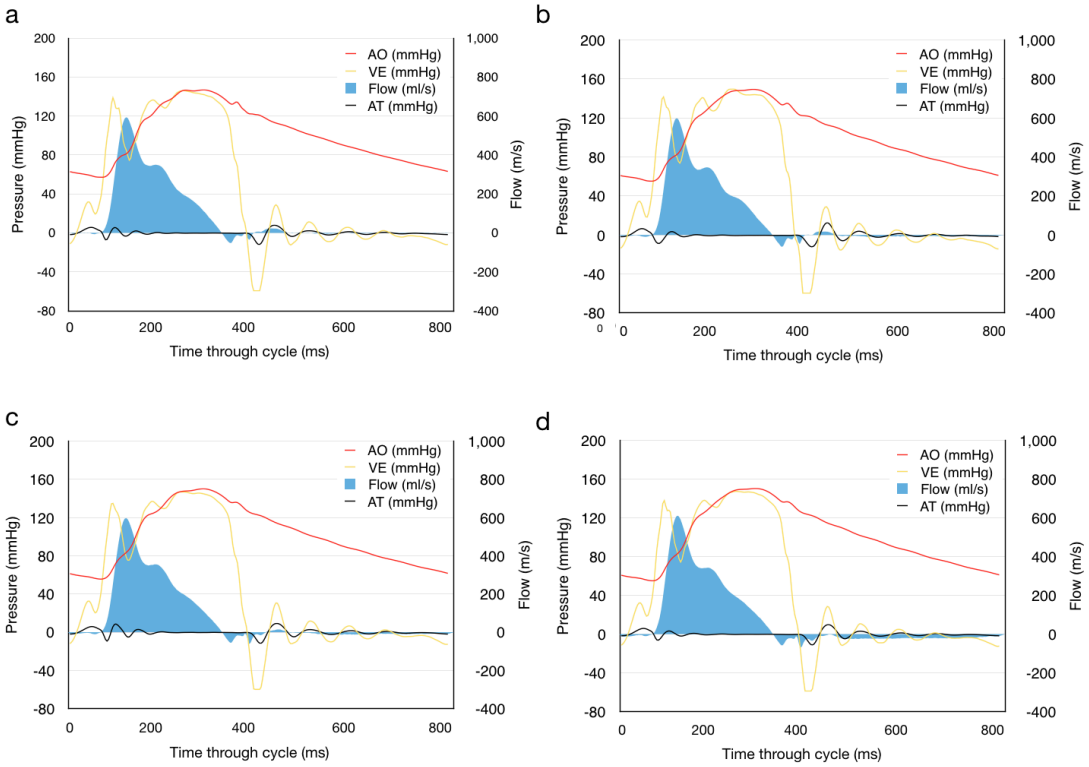

Figure 5-5: Pressure-time and flow-time charts for each configuration throughout a typical cardiac cycle during PIV acquisition. (a) Configuration TA1; b) Configuration TA2; (c) Configuration TA3; (d) Configuration TA4

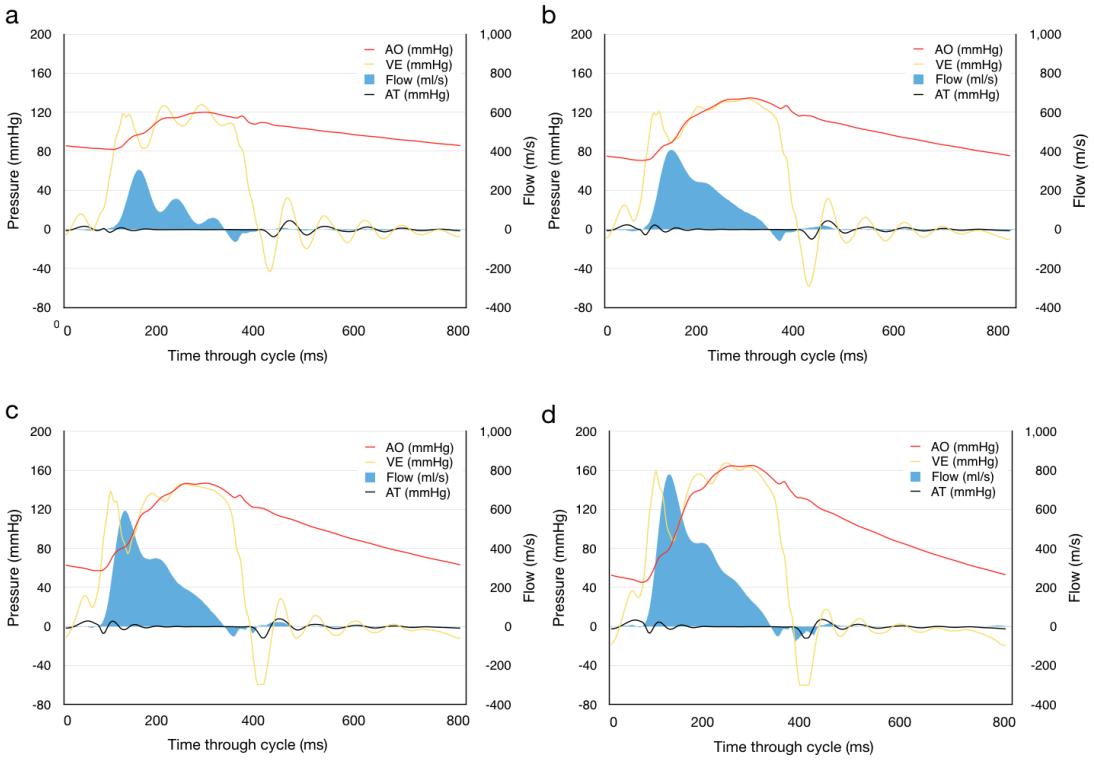

Figure 5-6: Pressure-time and flow-time charts for the aligned valve within native leaflets configuration throughout a typical cardiac cycle for each stroke volume investigated. (a) 28.6 ml ; (b) 50.0 ml ; (c) 71.4 ml ; (d) 92.9 ml

Global Parameter	*Stroke Volume (ml)*	*TA1*	*TA2*	*TA3*	*TA4*
Closing Volume (ml)	28.6	1.6 ± 0.32	2.5 ± 0.46 *(153 %)*	1.7 ± 0.33 *(106 %)*	2.1 ± 0.41 *(131 %)*
	50.0	1.4 ± 0.24	1.5 ± 0.24 *(104 %)*	1.5 ± 0.25 *(107 %)*	1.6 ± 0.27 *(114 %)*
	71.4	1.1 ± 0.21	1.2 ± 0.22 *(106 %)*	1.3 ± 0.23 *(118 %)*	1.3 ± 0.23 *(118 %)*
	92.9 (86.2 for TA2)	1.1 ± 0.21	1.1 ± 0.21 *(83 %)*	1.4 ± 0.26 *(127 %)*	1.4 ± 0.24 *(127 %)*
Systolic Energy Losses (mJ)	28.6	5.4 ± 0.3	5.3 ± 0.2 *(98 %)*	7.1 ± 0.3 *(131 %)*	8.2 ± 0.4 *(152 %)*
	50.0	32.8 ± 0.7	28.1 ± 0.6 *(85 %)*	25.8 ± 0.6 *(78 %)*	31.7 ± 0.7 *(97 %)*
	71.4	82.4 ± 2.0	78.0 ± 1.8 *(95 %)*	71.3 ± 1.8 *(87 %)*	77.8 ± 1.9 *(94 %)*
	92.9 (86.2 for TA2)	203.8 ± 4.8	164.8 ± 4.5 *(71 %)*	190.5 ± 5.2 *(93 %)*	227.2 ± 5.8 *(111 %)*

Table 5-5: Closing Volume and Systolic Energy Losses for all configurations at all stroke volumes: mean value, ± standard deviation, and percentage value with respect to configuration representing an aligned valve within native leaflets

5.3.2 PIV Data

PIV data for the maximum velocity (v_p) and the maximum RSS measured for each configuration at peak flow (instant B) alongside the fast flow width (x_f) and average velocity for the upper-, lower-, and full-sinus (v_{us}, v_{ls}, and v_s respectively), as defined in Section 5.2.3, for each instant of each configuration is presented in Table 5-6. Visual comparison of the fast flow width and the average sinus velocity is provided via line charts in Figure 5-7. The velocity profile at the STJ of each instant of each configuration is also displayed via line charts in Figure 5-8.

Parameter	*Instant*	*TA1*	*TA2*	*TA3*	*TA4*
Peak Velocity (m/s)	B	2.51	2.59	2.64	2.64
Peak Reynolds Shear Stress (N/m^2)	B	159	127	223	191
Fast Flow Width (mm)	A	18.8	18.3	18.5	16.0
	B	20.8	20.6	18.5	18.8
	C	12.5	9.9	14.2	9.0
	D	3.75	2.0	0.0	0.0
Average Full Sinus Velocity (m/s)	A	0.066	0.033	0.182	0.114
	B	0.072	0.068	0.217	0.197
	C	0.047	0.024	0.182	0.087
	D	0.025	0.028	0.046	0.067
	E	0.058	0.029	0.209	0.079
Average Upper Sinus Velocity (m/s)	A	0.134	0.045	0.315	0.177
	B	0.133	0.104	0.380	0.286
	C	0.061	0.035	0.258	0.116
	D	0.043	0.059	0.034	0.117
	E	0.124	0.052	0.274	0.126
Average Lower Sinus Velocity (m/s)	A	0.032	0.027	0.089	0.067
	B	0.041	0.049	0.103	0.123
	C	0.039	0.017	0.129	0.066
	D	0.013	0.011	0.054	0.030
	E	0.021	0.013	0.164	0.043

Table 5-6: Instantaneous data from PIV analysis for all configurations at all instants, with the exception of instant E for the fast flow width (as this was zero for all configurations), and only instant B is presented for the peak velocity and Reynolds shear stress.

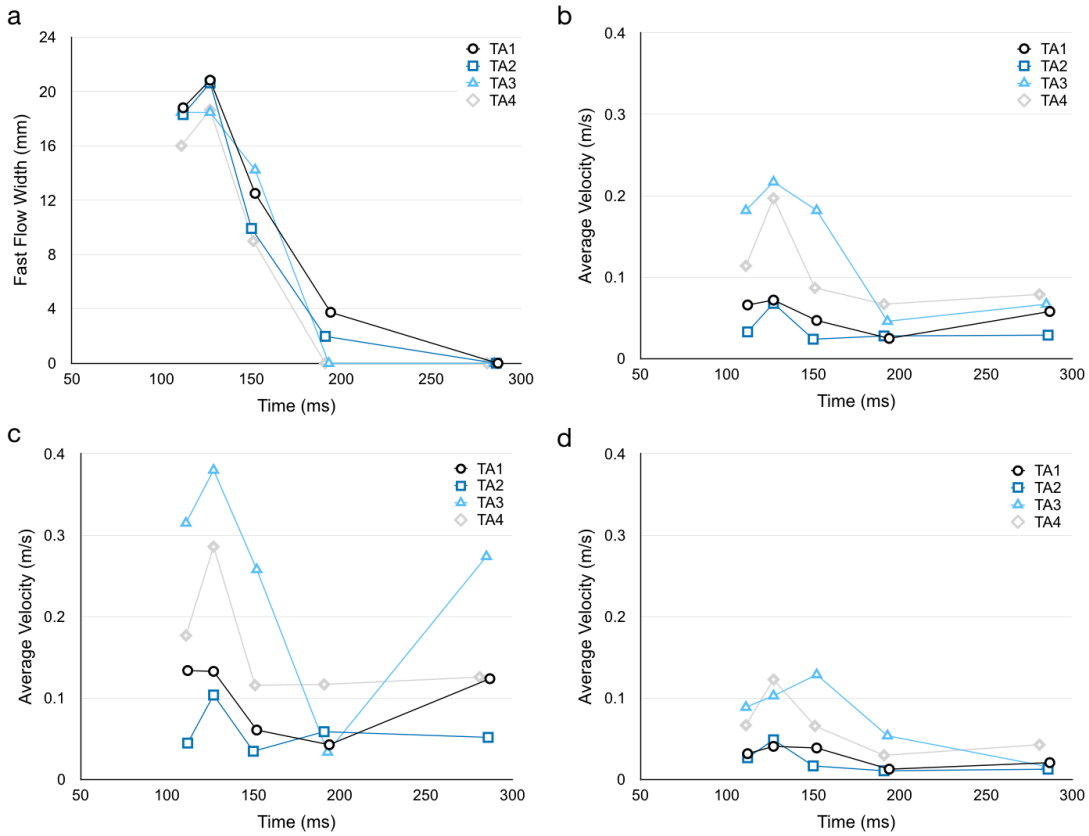

Figure 5-7: PIV derived data. (a) Fast flow width at instants A-E of each configuration; Average velocity within the (b) whole- (c) upper- and (d) lower- sinus for each instant of each configuration

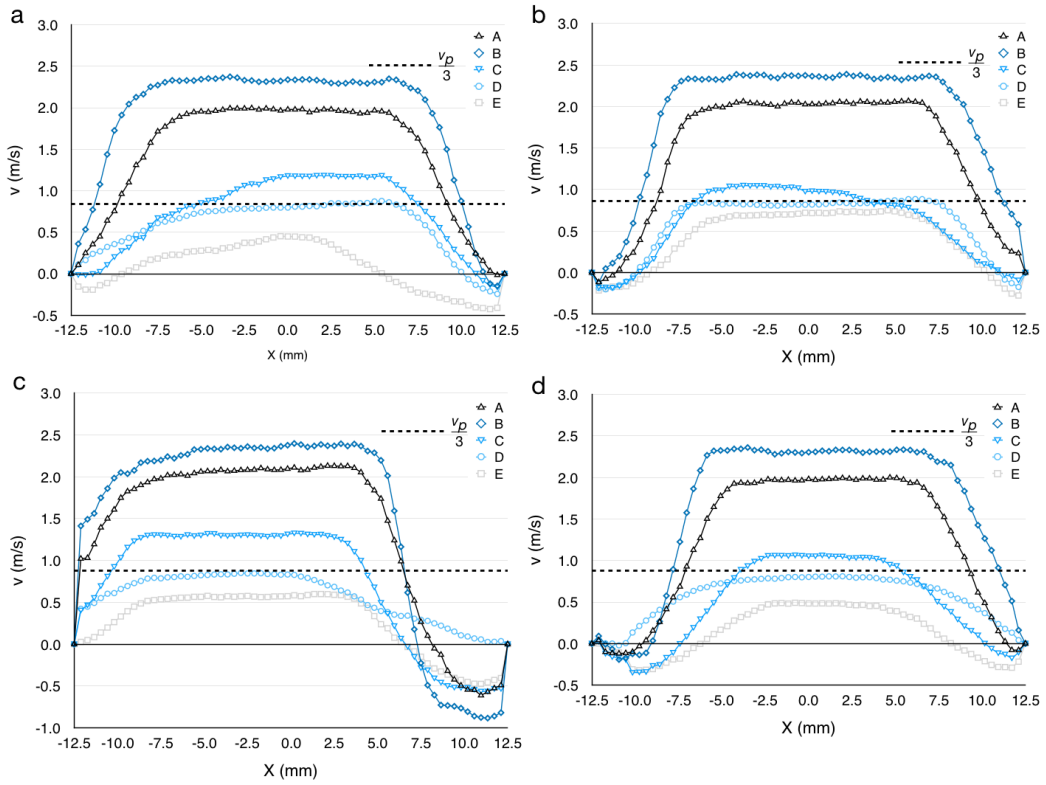

Figure 5-8: Velocity profiles across sinotubular junction at each instant analysed for each configuration, with the 1/3 of peak velocity for each configuration indicated. (a) Configuration TA1; b) Configuration TA2; (c) Configuration TA3; (d) Configuration TA4

5.3.2.1 TA1, Aligned Valve within Native Leaflets

The velocity fields of configuration TA1 are presented in Figure 5-9, whilst a contour map for the Reynolds shear stress (RSS) at peak flow (instant B) for each configuration is presented in Figure 5-10. Contour maps of the RSS, turbulence, and vorticity captured by the PIV analysis process for each instant of the physiological configuration are presented in Section 9.3, within the appendices.

In early systole, the central fast flow expands after exiting the valve, extending to the root wall on the commissural side of the valve and occupying much of the STJ. The largest x_f is reached during peak flow (instant B), equal to 20.8 mm, with a v_p of 2.4 m/s across the STJ and an almost symmetrical distribution with flat central profile until late systole. Peak velocity across the entire cross-section was detected as 2.51 m/s ± 1.4 %, within the threshold for acceptable prosthesis performance[260]. The central jet is accompanied throughout systole by a small vortex at the exit of the native leaflets, on the sinus side of the valve at the level of the STJ, which appears to promote structured flow into the sinus. A vortex is apparent in the widest part of the sinus during mid-late systole. This sinus flow suggests washout of the chamber during the whole systolic cycle, with v_s always between 0.025 and 0.072 m/s. Flow in the upper sinus is considerably higher than in the lower, with return flow at the end of systole raising v_{us} to a much greater extent than v_{ls}. On the commissural side of the TAV, the flow extends to the root wall until late in systole, when another vortex is generated, again positioned at the exit of the native leaflets, but this structure does not appear to significantly affect the central jet flow at this time.

Peak RSS occurs during peak flow, reaching a magnitude of 159 N/m^2, concentrated downstream of the native leaflet on the sinus side of the TAV, which also coincides with the highest vorticity measured during the cycle (900 /s). Turbulence is indicated to be highest during early systole, downstream, of the native leaflets on both sides of the TAV, with relatively little turbulence implied over the cross-section during late systole.

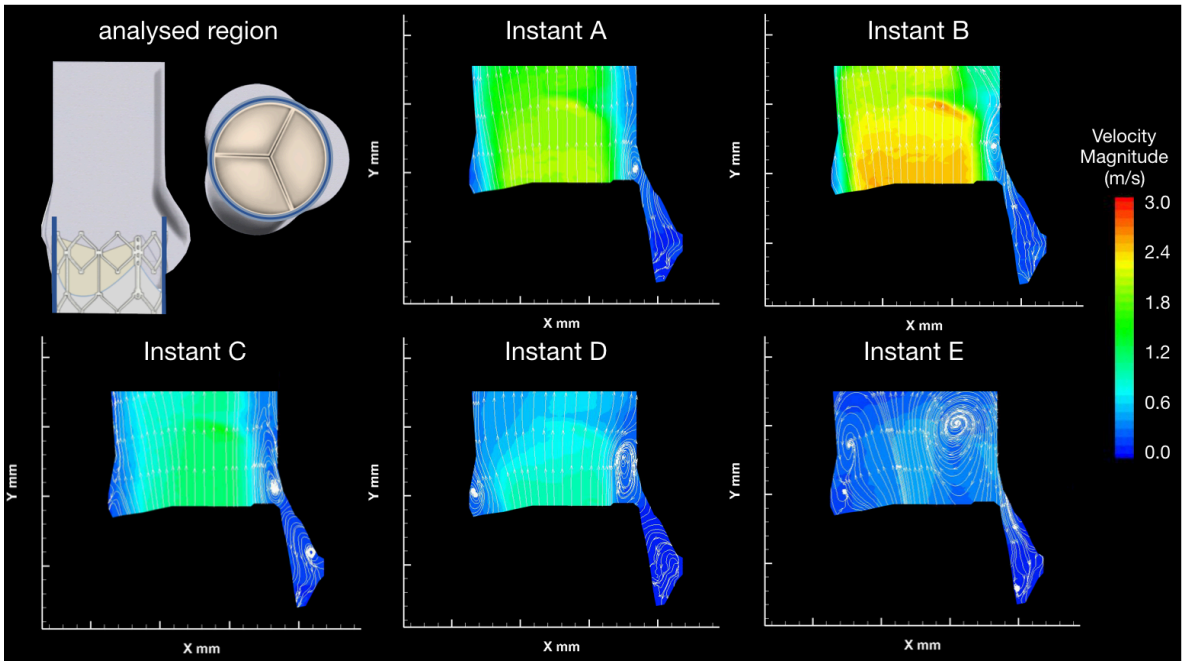

Figure 5-9: Velocity contour maps and streamlines for the aligned valve with native leaflets, configuration TA1.

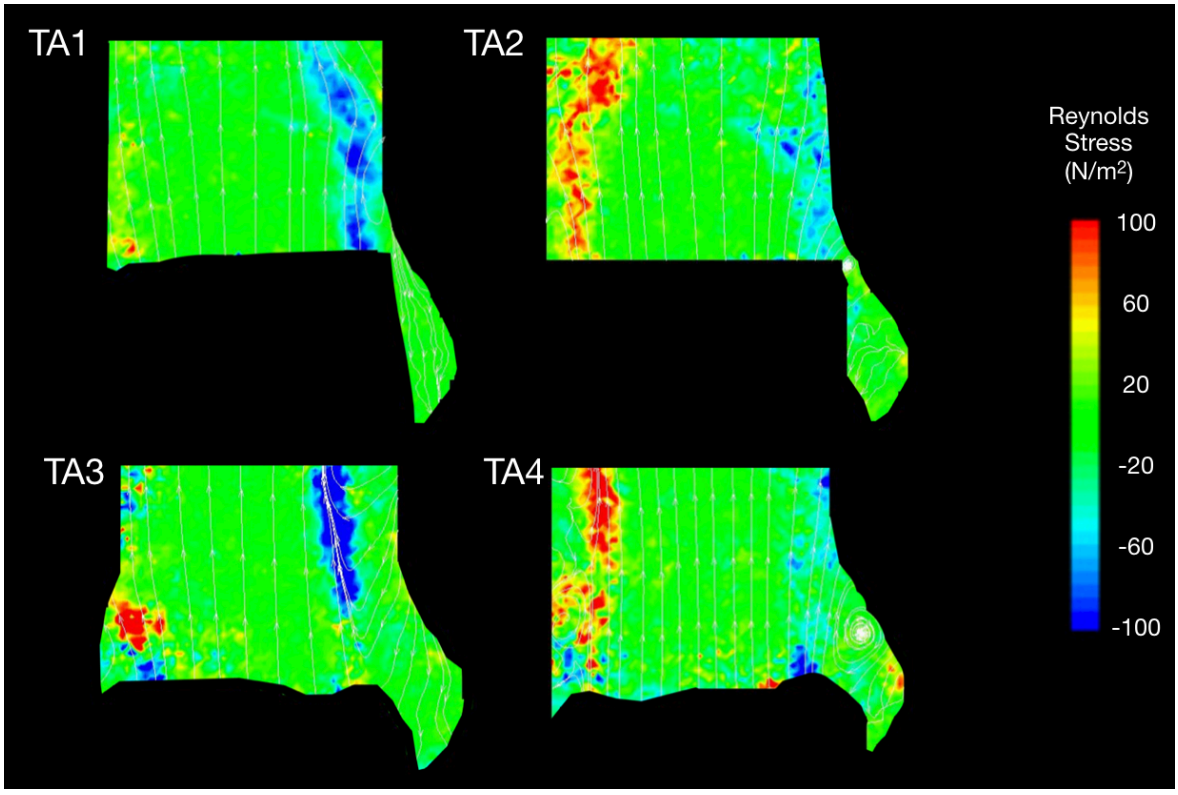

Figure 5-10: Reynolds shear stress contour maps for the various configurations at peak flow (instant B)

5.3.2.2 TA2, Non-aligned Valve within Native Leaflets

The velocity maps obtained from the PIV data for configuration TA2 are presented in Figure 5-11. Non-alignment of the TAV, rotating it 60° out of phase compared to configuration TA1, resulted in little change to the global haemodynamic performance, as can be seen in the Δp and E_s line charts presented in Figure 5-4. The v_p for the cross-section throughout the cycle, 2.59 ± 1.8 %, and x_f throughout the cycle are both similar to the aligned configuration, although the fluid flow at the edge of the central flow is altered. A vortex is indicated above the cusp of the TAV leaflet, now on the commissural side of the root, as illustrated in Figure 5-11(a), with no equivalent vortex on the sinus side of the valve until late systole. The upper sinus flow is accordingly reduced during the cycle, as indicated in Figure 5-7(c), particularly during the high flow portion of the cycle, whilst lower sinus flow remains at similarly low levels to that observed for configuration TA1. The central jet flow no longer extends to the root wall on the commissural side of the valve – on the contrary, a region of unstructured slow flow, with oscillatory features evident from the downstream translation of vortices along the mock aortic tract and the changing location of where the central jet flow extends to the wall, is observed between the root wall and jet flow throughout systole.

RSS of up to 120 N/m^2 was measured on both sides of the valve in early systole, peaking during instant B, particularly concentrated on the commissural side. The relatively high magnitude regions of vorticity do not extend as far downstream as in TA1, but reach a similar intensity (up to 900 /s) near the valve outflow on the commissural side of the TAV, whilst remaining below 650 /s on the sinus side. Turbulence is indicated to affect similar areas as in the aligned configuration, but to a greater extent, especially on the commissural side of the valve.

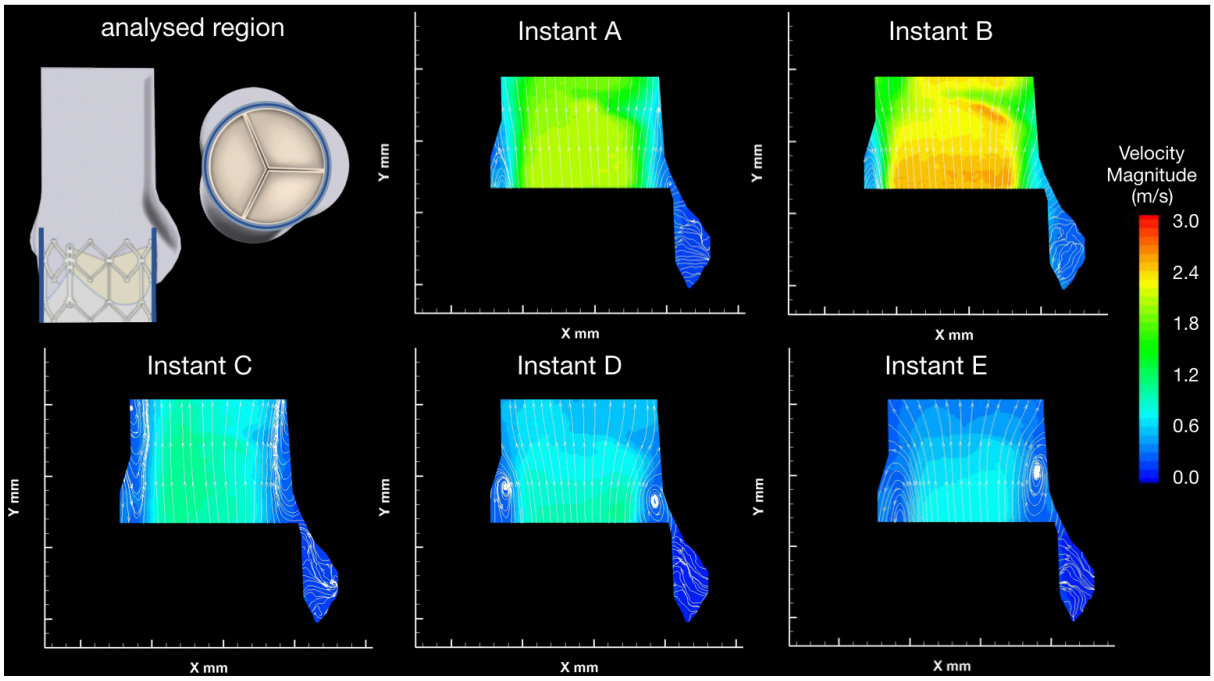

Figure 5-11: Velocity contour maps and streamlines for the non-aligned valve with native leaflets, configuration TA2.

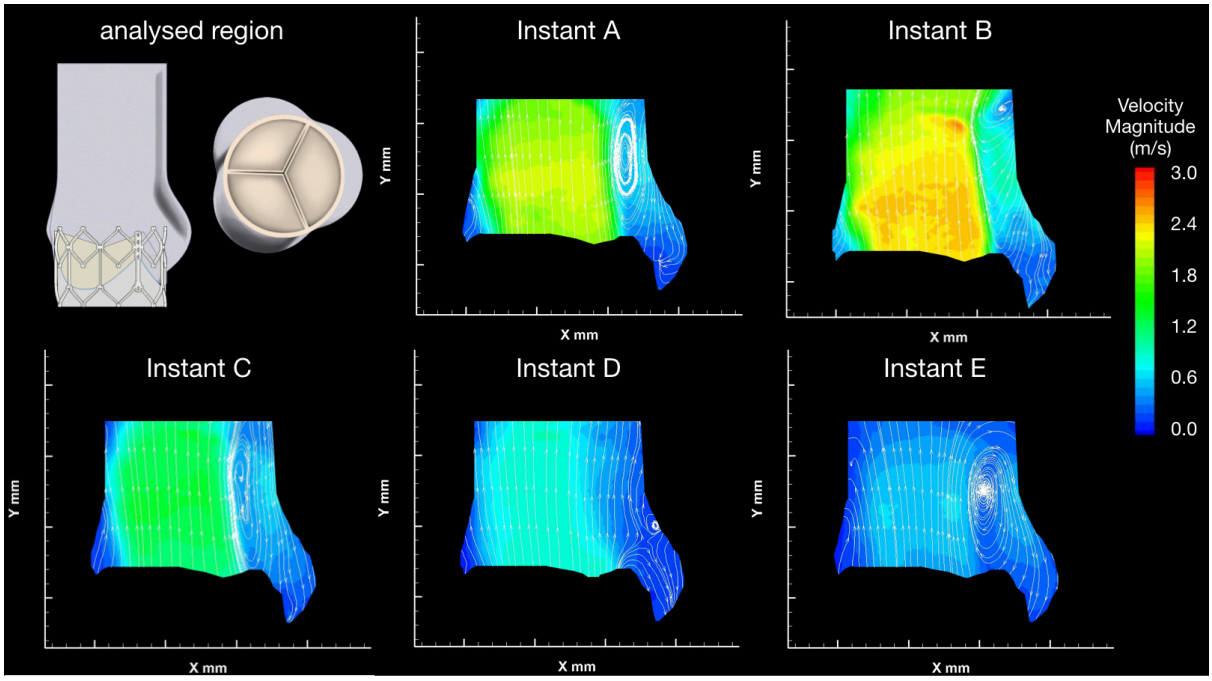

Figure 5-12: Velocity contour maps and streamlines for the aligned valve in the absence of native leaflets, configuration TA3.

5.3.2.3 TA3, Aligned Valve in the Absence of Native Leaflets

The fluid velocities captured at the various instants throughout the cycle for configuration TA3 are illustrated in Figure 5-12. Absence of the native leaflets

from the experimental setup results in a reduced Δp and E_s for all stroke volumes, as presented in Figure 5-4, although a slightly increased V_c, up to 25 % greater, at higher stroke volumes.

A v_p of 2.64 ± 1.4 %, similar to both previous setups, is measured, with the central jet establishing closer to the commissural wall. Although the maximum x_f is slightly reduced compared to the previous two cases, the central jet span is maintained longer into the systolic phase, justifying the larger EOA measured via the Gorlin's equation. On the sinus side of the root, a vortex generates early in systole, much larger than that observed for TA1, narrowing the jet flow of the central region. Consequently, flow in the sinus is much greater than for any other configuration, appearing to be well-defined and providing wash-out of the sinus, both upper and lower, throughout systole. There is no evidence of a commissural side vortex at any stage of systole for configuration TA3.

A maximum RSS of 223 N/m^2 was measured at peak flow (instant B), as presented in Figure 5-10, 40 % higher than for the equivalent configuration with native leaflets (TA1), and this relatively large region of elevated RSS persisted through early-mid systole, with RSS as high as 85 N/m^2 observed at instant C on the sinus side of the root. This area was indicated to have with a persistent region of turbulence above the native leaflets on the SoV side, accompanied by relatively high vorticity (1300 /s) at peak flow. A smaller region of similarly intense vorticity was also observed on the commissural side of the TAV, which also displayed RSS acting in opposing directions during peak flow, as illustrated in Figure 5-10.

5.3.2.4 TA4, Non-aligned Valve in the Absence of Native Leaflets

Velocity fields for each analysed instant from the PIV analysis for configuration TA4 are shown in Figure 5-13. Removing the native leaflets from the experimental set up results in a bigger difference between the aligned and misaligned configurations than was observed in the cases that included the native leaflets. Global haemodynamic performance was similar to the two setups that included the native leaflets, with the exception of the V_c, which was similar to that of configuration TA3.

The same v_p, 2.64 ± 1.5 %, was detected as in TA3, but there were differences in the fluid flow dynamics. Two comparably sized vortices were present on

either side of the valve through systole, narrowing x_f. Sinus flow, though slower than in TA3, was considerably faster than for the native leaflet configurations, as shown in Figure 5-7(b-d), with well-defined streamlines detected throughout systole. A region of unstructured slow flow separates the central jet flow from the commissural side root wall throughout systole, including the transfer of vortices in a similar fashion to that observed in TA2.

A large region of high RSS, reaching magnitudes of 190 N/m^2, 58 % higher than the equivalent configuration with native leaflets, was present above the commissural side of the TAV frame until mid-systole (instant C), as well as smaller regions of similar magnitude on the sinus side. Turbulence was indicated to be less than in configuration TA3 and was predominantly on the commissural side of the root, where the flow also reached a vorticity of 1100 /s during peak flow (instant B).

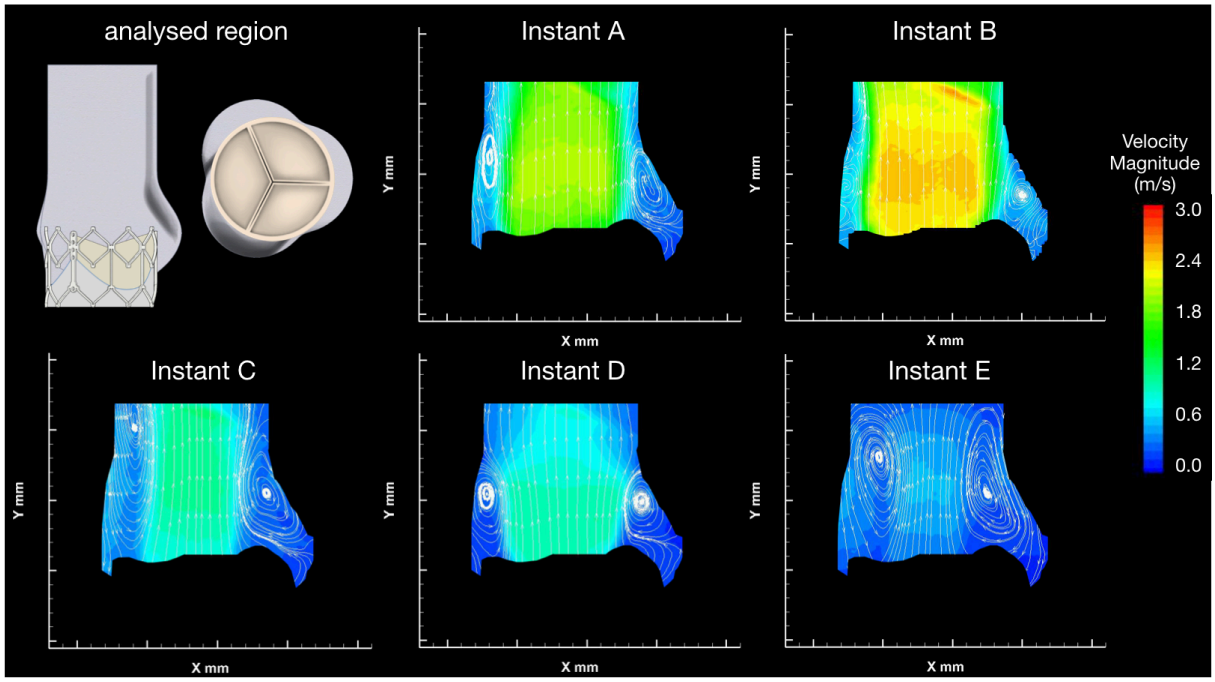

Figure 5-13: Velocity contour maps and streamlines for the non-aligned valve in the absence of native leaflets, configuration TA4

5.4 Discussion

The fluid flow of the post-TAV implantation aligned configuration has some differences to the flow observed in the healthy physiological setup of Chapter 4, which are primarily due to the continued presence of the native leaflets after valve replacement. In the healthy native aortic root, the modelling of which is

described in section 4.2.1 and the fluid dynamics summarised in section 4.4 the sinus side vortex that generates as the associated leaflet opens is confined within the chamber throughout systole, enabling the central jet flow to extend to the root wall and maximising its width, as illustrated in Figure 5-14 (a), minimising the peak velocity and shear stresses of the outflowing blood. The location of this vortex also contributes to the washout of the sinus, minimising stagnation and thrombogenic conditions. In contrast to this, the post-TAV central flow is separated from the sinus side root wall by a region of return flow, in a similar manner to the sub-annular SAV implantation or the undersized SAV as shown in Figure 5-14 (b-d). The RSS of the TAV within native leaflets flow reaches a peak of 159 N/m^2, which is at the lower end of the 150-520 N/m^2 threshold indicated in the literature[37,89,90], implying little or no haemolysis due to high shear at this resting heart rate. However, the thrombogenicity of the sinus could potentially increase, due to the diminished flow speeds measured in this region, and the lack of vortical dynamics providing washout of the chamber during systole.

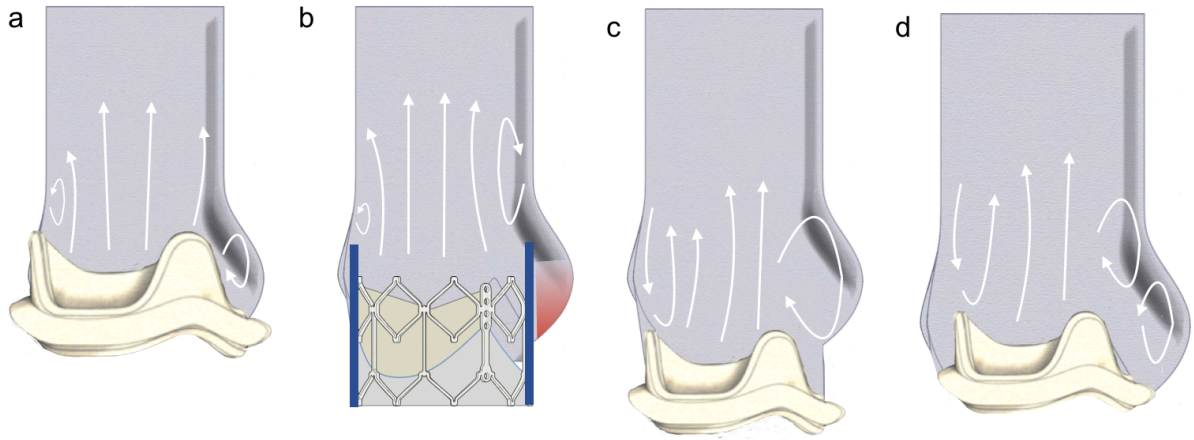

Figure 5-14: Alteration of fluid flow as a result of TAV: Fluid flow patterns for (a) healthy native valve, as described in section 4.4; (b) Post-TAV implantation, with TAV in correct alignment and slowed sinus flow indicated by red shading; (c) sub-annular implantation of a surgical bioprosthetic, previously characterised in section 4.4; (d) implantation of an undersized surgical bioprosthetic, as described in section 4.4

The non-alignment of the implanted TAV within its host leaflet leaflets has little effect upon global haemodynamic performance indicators such as EOA or ΔP. The velocity fields show that the central jet flow properties of the aligned and misaligned configurations are also similar, following the trend of the global haemodynamics. However, the slower flow in the aortic root during systole is

modified as the rotation of the TAV in relation to the host root varies, resulting in reduced flow within the SoV, especially at the base of these chambers, and alterations to the flow in the vicinity of native commissures. The central jet flow of the TAV may be relatively unaffected by commissural alignment due to the presence of the native leaflets, extending beyond the downstream exit of the TAV in a pseudo-cylindrical shape. This relatively uniform geometry may mean the orientation of the TAV has little effect upon the central flow, with the cusp of this cylinder leading to vortex shedding all around the valve, as evidenced by the vortices present on both sides of the valve in late systole, as opposed to vortices primarily generating in the vicinity of the opening leaflets in the case of roots with surgical or native aortic valves.

However, the dynamic leaflets of the TAV do have an effect upon the location of the circulations at the edge of this jet flow, with the strength of the resultant vortices affected by the orientation of the TAV with respect to the aortic root. Vortical dynamics in the sinus of the physiological root are connected to both the vortex shedding from the cusp of the moving leaflet[102] and, as established in Chapter 4, the geometry of the root in relation to the valve. When the sinus bulge coincides with the centre of the moving leaflet, as in the aligned configurations, the resultant vortex on the SoV side of the root is stronger, as illustrated in Figure 5-15, resulting in increased flow back into the sinuses and improved washout of these chambers. On the other hand, non-alignment of the valve, common in TAV procedures[259], may reduce this overlap of vortical factors, producing a weaker vortex in the vicinity of the largest part of each SoV and lessening the associated sinus washout. The jet flow no longer extends to the root wall, and the translation of vortices through the systolic cycle and related unstructured slow flow outside of the fast central flow is reminiscent of both the resultant root flow of a stenotic aortic valve[100] and that of a dilated aortic root, previously characterised in section 4.4, as shown in Figure 5-16. Non-physiological vortices and blood recirculation of this type has been associated with intraluminal thrombosis, leaflet cusp deterioration or aneurysm[129,261,262], whilst oscillatory low wall shear stress and flow separation have been linked to plaque formation and enhanced atherogenesis[263].

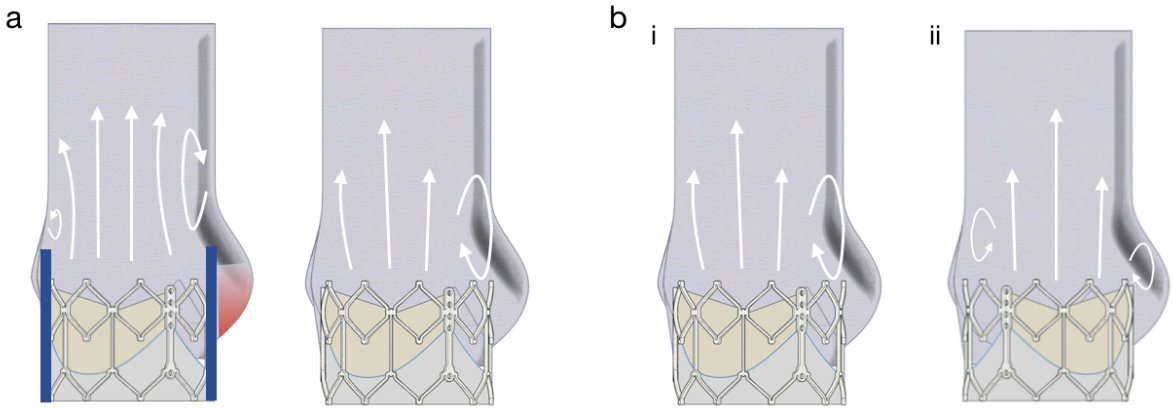

Figure 5-15: Vortical behaviour changes. (a) due to presence/omission of native leaflets, where the native leaflets reduce the influence of the valve orientation and result in a significant region of stagnation in the native sinuses. (b) due to valve alignment. (i) commissure to commissure alignment results in centre of moving leaflet and maximum sinus bulge being aligned, resulting in a single, larger vortex next to the sinus; (ii) Non-alignment of the commissures means the factors are not aligned, resulting in 2 weaker vortices forming, one next to the bioprosthetic commissure and one next to the sinus.

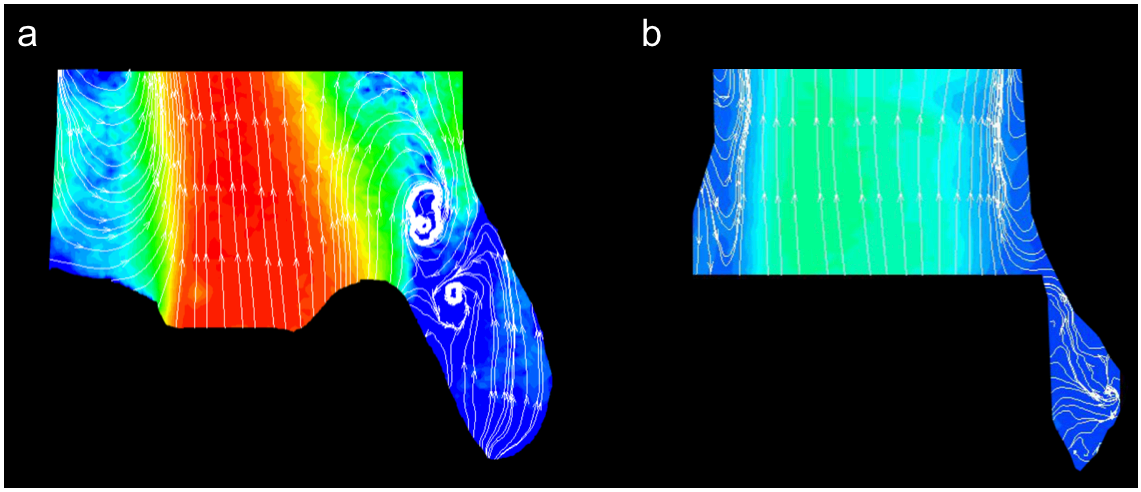

Figure 5-16: Similarities between the (a) dilated root and (b) non-aligned TAV PIV analyses – the central fast flow does not extend to the root wall in either case, and is surrounded by return flow and migrating vortices.

Although the haemodynamic performance of the valve does not appear to be significantly affected, it is apparent that non-alignment of TAVs, which occurs in approximately 25 % of TAV procedures[259], may result in some long-term consequences for the patient and a reduced functional life for the bioprosthesis, especially when considered in conjunction with the increased stresses experienced by non-aligned TAVs[264].

Removing the mock native leaflets from the investigational setup resulted in a greater difference between the performance of an aligned and non-aligned configurations, as removal of the barrier between the TAV and the SoV enabled the 2 vortical generation factors described in Figure 5-15 to act in greater confluence, which may explain the higher levels of RSS observed at peak flow for both non-native leaflet configurations compared to their equivalents. The differences between the flow patterns and improved valve performance between the configurations with and without the mock native leaflets indicate that the inclusion of native leaflets during *in vitro* tests of TAVs is important for accurate results, and could be considered into the regulatory requirements. The presence of native leaflets has often been neglected in previous *in vitro* and *in silico* studies, possibly resulting in unrealistically optimistic flow patterns and valve performance indicators[78,182,184,186].

The presence of the native leaflets, necessary in most TAV implantations, appears to severely impair the washout of the sinuses, reducing the average sinus velocity to about 1/3 of that observed in equivalent configurations without native leaflets. Reduction and stagnation of blood flow is associated with an increase in thrombogenicity, providing a possible reason for the high incidence of subclinical leaflet thrombosis in TAVs[265]. Maximum misalignment of the bioprosthesis is indicated to further reduce this blood flow in the upper sinus during systole, particularly during early systole when the flow in the upper sinus is slowed to similar magnitudes as that in the lower sinus, already implicated as an area of thrombotic concern[97,186]. It can be extrapolated that the effect would be less severe for intermediate commissural misalignment. Although current imaging methods capable of identifying the rotational alignment of the TAV during the implantation procedure, such as real-time 3D Computed Tomography-fluoroscopy or 3D transoesophageal echocardiography-fluoroscopy fusion imaging, are not commonly used[257,258], a combination of multi-planar MRI and markers on the TAV could be used to reduce the incidence of misalignment.

Recording the orientation of TAVs implanted into patients would be useful in providing some clinical support to the presented argument, and possible identify an association between the instances of subclinical leaflet thrombosis and misalignment of the TAV.

5.4.1 Limitations

Some limitations were present in this study, and the interpretation of the results needs to take these into consideration. Firstly, the analysed cases are idealisations, where the model for the native leaflets was at the lower range of aortic leaflet thickness with a more uniformly cylindrical shape than calcified native leaflets would be expected to take[266] with reduced potential for expansion away from the TAV during the cycle due to the adhesion to the TAV stent, and the deployment of the TAV was assumed to be circular, even though irregularities in the anatomical shape of the leaflets and calcification distribution can lead to asymmetrical expansions and altered fluid dynamics[12,186]. The consequence of a deployment that resulted in a TAV that was both non-aligned and asymmetrical could be an interesting future study. No coronary flow was modelled in the aortic root, which may result in a degree of asymmetry across the root, particularly in the sinuses. No aortic root compliance was modelled, but it should be considered that many TAV recipients are elderly patients[189] with correspondingly lower compliance aortic roots[267], making the findings of this investigation representative of a significant proportion of the patient population. The fluid used in this study was Newtonian, resulting in some departure from the flow behaviour of shear-thinning blood. All of these factors may affect the small difference observed in the wash-out flow associated with valve alignment. Finally, no out of plane motion or flow structures can be detected with the PIV setup used, although it is expected that the plane investigated in this study captures the most relevant flow structures of the aortic root.

It must be noted that comparison of the flow dynamics acquired via PIV between the physiological, surgical, and percutaneous (TAV) models is limited by the flow rates imposed upon them, the forward flow rate of which was 4 lpm for the former two cases and 5 lpm for the latter setup. Whilst this makes quantitative comparison of data such as peak velocity and pressure drop inappropriate, it is expected that the qualitative comparisons of vortical generation and relative flow dynamics are still reasonable.

5.5 Concluding Remarks

The introduction of a TAV to the aortic root produces alterations to the flow dynamics of the region, displacing the central jet flow away from the sinus side

aortic wall and diminishing the sinus flow, increasing the thrombogenicity of the volume, especially at the end of the chamber closest to the aortic basal annulus. The presented study also indicates that the misalignment of a TAV within native leaflets has a negligible effect upon the quantified haemodynamic performance of the implanted valve, but does affect the flow patterns by the root wall, particularly in the vicinity of the native commissures, and within the sinuses, where the average flow velocity is particularly reduced in the volume of the chamber closest to the STJ. This suggest that correct alignment of TAVs may lead to some advantage in terms of sinus flow and reduction of non-physiological vorticity in the neighbourhood above the native commissures. The design of novel devices improving the rotational control of TAVs, together with the use of advanced medical imaging, such as real-time 3D Computed Tomography-fluoroscopy or 3D transoesophageal echocardiography-fluoroscopy fusion imaging[257,258] could bear some benefit.

In addition, this investigation indicates that simulations involving TAVs in unrealistic setups where the native leaflets are omitted may be characterised by substantially different flow features, with significant sensitivity to the prosthesis' orientation. This implies that the presence of mock native leaflets is essential in determining veridical results, and reveals a need for the explicit requirement of this feature in the regulations for preclinical testing of these devices.

6 The Effect of Coronary Arteries upon Post-TAVI Flow

6.1 Introduction

The coronary arteries (CAs) supply the muscle tissue of the heart itself with oxygenated blood[40], and originate in two of the SoV of the aortic root, typically just upstream of the STJ, although this position varies from person to person[42,70]. The haemodynamics of the aortic root influence CA flow[71,72], with increased turbulence in the SoV reported to reduce the flow though the CAs during diastole[116]. Reversing this consideration,has not yet reached consensus amongst previous reports, with few investigations into the effect of the coronary arteries upon the flow within the aortic root, especially within the sinuses of Valsalva, following TAV implantation, as stated in section 2.4.4. Some literature reports that the low velocity of blood flow through the coronaries during diastole has little effect upon the sinus that the relevant CA ostium is situated in[102]. On the other hand, other investigations report that, as the aortic valve leaflet associated with non-coronary artery (NCA) sinus has a greater tendency to calcify in comparison to the other two leaflets, the absence of diastolic CA flow results in lower shear stresses in the region[72,120]. The suctioning effect from the CAs results in an increased volume of the central root flow entering the associated sinus, reducing the stagnation at the base of these chambers, and flow towards the ostium, rather than the root axis and STJ, causes increased washout of the two coronary sinuses[72].The enlarged regions of low shear observed in the NCA sinus substantially increase the residence time of the RBCs, increasing the thrombogenicity of the volume[167].

The post-TAV implantation effect upon coronary flow has been reported to depend upon the specific patient, with improved systolic CA flow in comparison the stenotic condition resulting from a reduced Venturi effect from the central flow and enhanced coronary bed pressure gradients[71]. However, patients with relatively low coronary ostia, situated closer to the basal annulus of the aortic root, have been reported to have up 20 % reduction in coronary flow in comparison to other recipients of TAV intervention[95,96,208]. Due to the improved efficiency of the left side of the heart after the prosthesis implantation, this

reduction may not be a critical issue on its own, but the severity for each patient depends upon long-term myocardial needs in combination with other cardiac deficiencies[71]. The volume of the sinus chambers is reduced by the displaced native leaflets, and systolic sinus flow is primarily in the region of each sinus closest to the STJ, in the vicinity of the cusps of the native leaflets[201]. The regions of permanently low level shear at the base of the SoV following TAV implantation may be exacerbated by the lack of coronary flow during diastole[97], but as yet, there has not been any PIV investigation of the fluid dynamics within an aortic root, complete with CA, containing a TAV implanted into native leaflets. The modelling of CA has been included in previous PIV studies of SAV and TAV within an aortic root, but these studies did not model the presence of natives leaflets[72,167].

The aim of this chapter is to investigate the effect that coronary flow has upon the fluid flow of the aortic root, particularly within the sinuses, after TAV implantation, throughout a typical cardiac cycle, researching the third objective of this thesis, as stated in Section 2.4.5.3, 'to determine whether the presence of the coronary arteries, and the flow into them during each cardiac cycle, has an effect upon the fluid dynamics of the aortic root, particularly within the sinus of Valsalva associated with each coronary artery, following TAV implantation'. This was achieved by developing a mock aortic root that included an outflow tube on each sinus, exiting the chamber in the equivalent position of a typical coronary ostium. Each tube could be individually narrowed or blocked off, enabling the setup to model the left, right, and non-coronary sinuses and associate artery outflow observed in the normal human anatomy, as well as the common *in vitro* configuration where coronary arteries are not represented at all. The mock root included silicone leaflets of a mock native aortic valve, into which a TAV device was placed. The entire assembly was then loaded into a pulse duplicator, obtaining global haemodynamic performance data from pressure and flow transducers, and PIV acquisitions were taken, elucidating local fluid fields for specific instants within the pulse duplicator imposed cardiac cycle.

6.2 Methods

6.2.1 Setup of Coronary Arteries

A 26 mm Edwards SAPIEN XT valve, as described in Section 0, was again used as the TAV, and was placed inside the 25C root, designed and manufactured as presented in Sections 3.5.1 and 3.5.2, which incorporated a silicone Thubrikar valve, detailed in Section 3.4.1.4, representing the calcified native valve hosting the bioprosthesis. The resultant mock coronary ostia were positioned 17.0 mm downstream of the same basal annulus, the average position in healthy adult humans as reported by Knight *et al.* [70] which located them just upstream of the STJ, with a diameter of 4 mm, and were attached, via a 4.0 mm diameter bore through the silicone root and tubing connectors with a 3.0 mm internal diameter, to 0.5 m long silicone tubing with a 4.0 mm internal diameter, as illustrated in Figure 6-1(a). The route of the silicone bore had been designed with this PIV laser sheet in mind, leading away from the plane of the laser sheet as described in Section 3.5.2, so that the resultant PIV images had the minimum interference from the mock CAs. The outflow of the silicone tubing passed through the aortic compliance port of the pulse duplicator, and then poured into the open atrial chamber of the pulse duplicator during PIV data acquisition. Diverting the outflow of these silicone tubes to a chamber on top of a balance, attached to a computer, enabled coronary flow assessment by taking measurements from the balance at 5.35 Hz. The resulting measurements were then phase matched, so that each reading corresponded to a time through each cycle imposed by the pulse duplicator. To match up the coronary flow with the flow and pressure data acquisition from the pulse duplicator, a video was taken of the outlet of the coronary flow alongside the piston head of the pulse duplicator, enabling the peak CA outflow to be identified in relation to the position of the piston head imposing the simulated cardiac cycle.

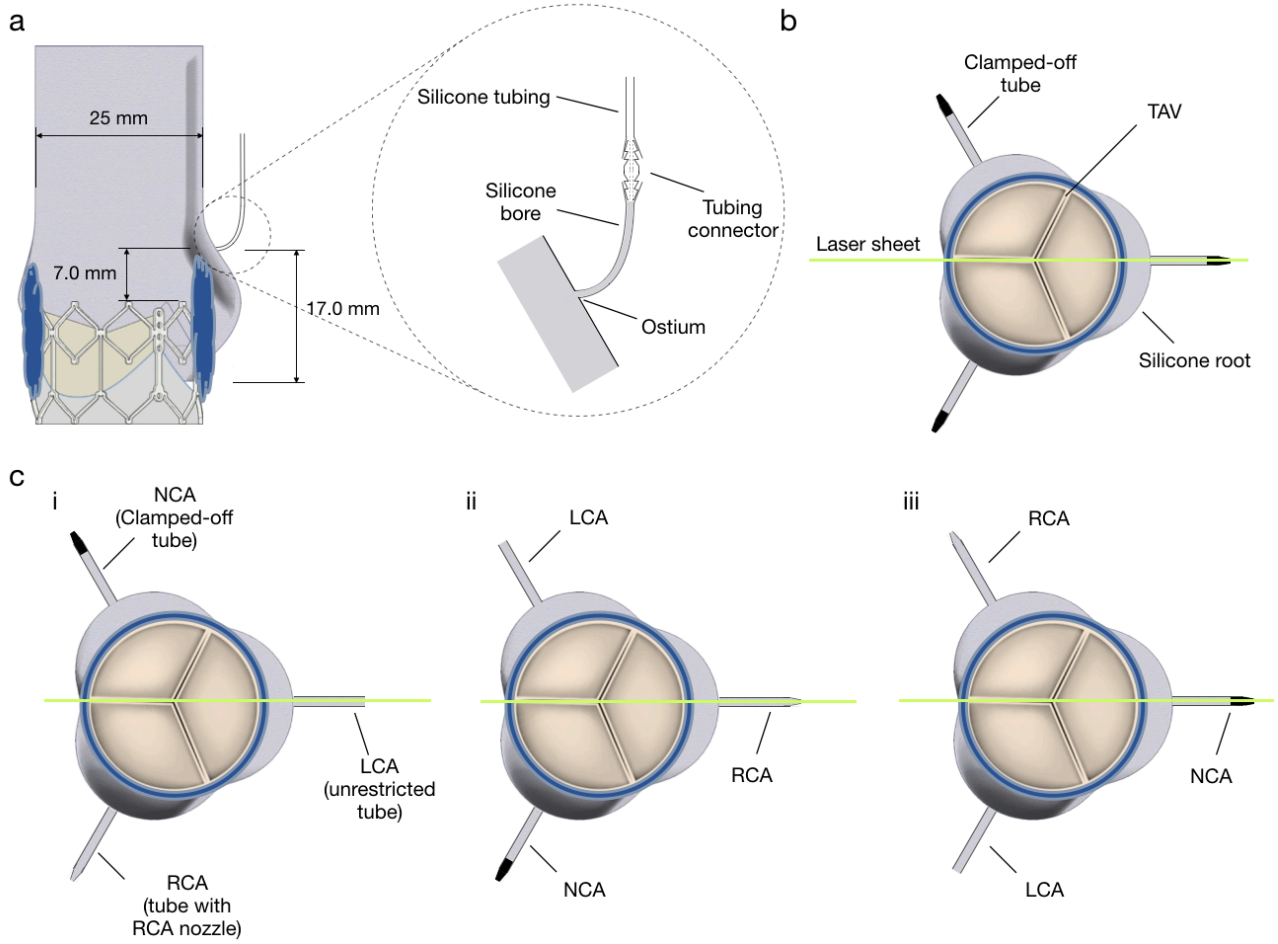

Figure 6-1: Coronary Artery configurations for PIV analysis. (a) Height of mock ostia in relation to root annulus and TAV frame, with enlargement of tubing connection; (b) All mock CA are clamped off for the NoCA configuration; (b) The LCA (i), RCA (ii) and NCA (iii) configurations have the same combination of obstructed silicone tubing, but are rotated in relation to each other in order to analyse the LCA sinus, the RCA sinus, and NCA sinus respectively via PIV.

6.2.2 Root Configurations

In order to represent PIV investigations that do not model the coronary arteries, and to provide direct comparison of the setup to the aligned TAV within native leaflets configuration (TA1) from Chapter 6, the 3 silicone tubes connected to the mock coronary ostia were clamped shut, preventing any flow through them. The physiological condition was represented by clamping shut one of the tubes (modelling the NCA), reducing the internal diameter of another via the insertion of the RCA nozzle (to portray the lesser coronary flow of the Right Coronary Artery, RCA), and leaving the third tube fully open (to represent the higher coronary flow of the Left Coronary Artery, LCA). The larger LCA provides the majority of the blood flow for most people, although there is a lot of variation in the dominance of this artery, resulting in a flow rate of 156 ± 77 ml/min for the

LCA, 91 ± 70 ml/min for the RCA, and 270 ± 82 ml/min (or 80 ml/min/100 g of heart tissue) for the coronary flow as a whole[108]. The midpoint of the TAV was placed between 1 and 2 mm downstream of the basal annulus of the Thubrikar valve, as recommended for the clinical procedure[214].

The configurations studied in this investigation are illustrated in Figure 6-1(b and c), and were as follows:

- NoCA – all mock CA silicone tubing clamped shut, representing common *in vitro* studies with no modelling of the CA flow, including configuration TA1 from Chapter 6;
- LCA – the mock CA whose ostium is located within the sinus bisected by the laser sheet is left fully open. The mock CA situated clockwise of this (from a downstream transversal perspective) has the RCA nozzle inserted, and the last mock CA is clamped shut;
- RCA – the mock CA associated with the sinus analysed by PIV has the RCA nozzle located at its outflow, the mock CA clockwise of this is clamped off, and the final length of silicone tubing is unobstructed;
- NCA – the silicone tubing leading away from the analysed sinus is clamped off, the mock CA clockwise of this is unobstructed, and the final tubing has the RCA nozzle inserted.

As the clamps and RCA nozzle were attached to the tubing outside of the pulse duplicator, it was possible to change between these configurations without taking the TAV or silicone root out of the pulse duplicator or altering the PIV data acquisition setup.

As with the previous 2 PIV investigations presented in this thesis, the root was made of optically clear, solvent free, low viscosity silicone elastomer with refractive index $n = 1.4$, the thick walls of which resulted in negligible compliance, representative of older patients[254]. The solution described in Section 3.6.3, utilising KI, glycerol, and deionised and filtered water, was again used as the blood analogue, matching both the blood viscosity of 4.0 cP at 37 °C, and the RI of the silicone material used in the mock aortic root.

6.2.3 Global Haemodynamics

The hydro-mechanical pulse duplicator presented in Section 3.2 was again used to impose the equivalent of a physiological cardiac cycle upon the setup. All tests were performed at a heart rate of 70 beats per minute, with a mean aortic pressure of 100 mmHg, 35 % systole, and a stroke volume of 71.4 ml producing a cardiac output of 5 lpm. Pressure readings were obtained from transducers situated up- and down-stream of the TAV, whilst the electromagnetic flowmeter positioned just downstream of the valve provided flowrate data throughout each cycle. As detailed in Section 3.2.2 and as in the previous investigations, an average cycle of pressure and flowrate fluctuations was calculated from 20 cycles, taken from the first and last 10 cycles of PIV image acquisition for each configuration. This enabled calculation of:

- The systolic transvalvular pressure drop (Δp) across the valve, in mmHg
- The Effective Orifice Area (EOA) of the valve, in cm^2
- The closing regurgitant volume (V_c) of the valve, in ml
- The energy losses during forward flow (E_f), valve closure (E_c), and valve leakage (E_l), the combination of these to give the total energy loss (E_t), in mJ.

6.2.4 Local Fluid Flow

Velocity fields of the central cross-section of the root, bisecting one of the sinuses, were obtained via 2D PIV, the process and theory of which is described in Section 3.3. 8 instants were identified within the cardiac cycle, to characterise the fluid flow dynamics of the full cardiac cycle. These instants corresponded to:

A. Flow rate through the basal annulus of the root, as detected by the pulse duplicator flowmeter, increased to 1/3 of Peak flowrate
B. Peak flowrate
C. Flowrate decreased to 2/3 of peak flowrate
D. Flowrate decreased to 1/3 of peak flowrate
E. Flowrate decreased to zero
F. Taken after 1/4 of the duration of diastole
G. Taken after 2/4 of the duration of diastole
H. Taken after 3/4 of the duration of diastole

I. Taken at the end of diastole, indicated by the first positive flow through the valve

These instants were all the same for the LCA, RCA, and NCA configurations, as the valve-root-CA setup is the same but rotated for each, and the instants for the NoCA and the 3 CA setups are presented in Table 6-1, and illustrated for the CA configuration in Figure 6-2(a).

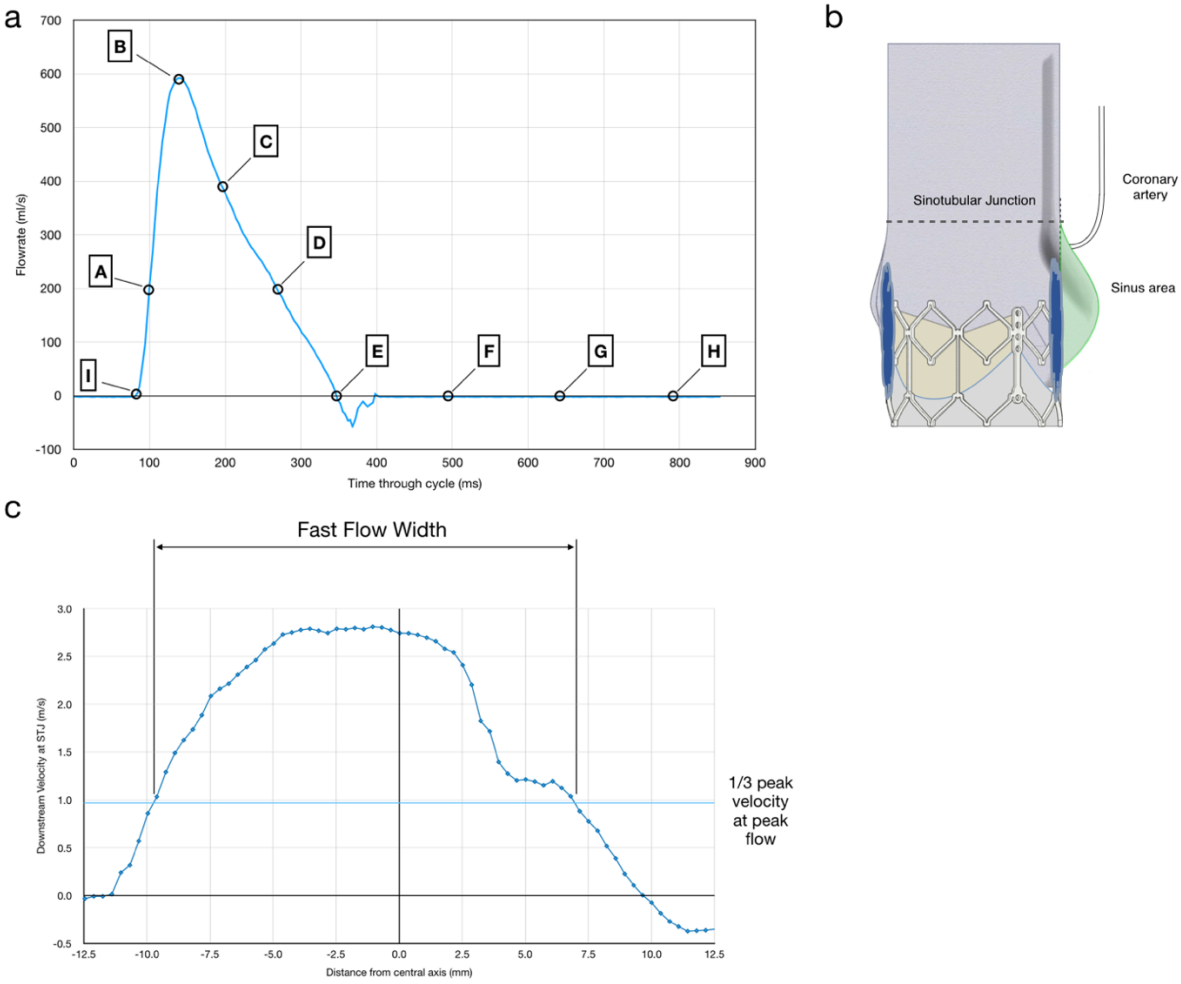

Figure 6-2: PIV data properties: (a) Typical diagram of the flowrate vs the time through the heart cycle with the analysed instants shown; (b) Sinus area of cross-section for calculation of average sinus velocity from PIV data; (c) Calculation of Fast Flow Width (x_f) from velocities across the STJ profile.

Setup	*Instant Time through Cycle (ms)*								
	A	B	C	D	E	F	G	H	I
NoCA	99	137	197	269	347	494	642	790	84
CA	100	141	194	268	347	494	642	790	84

Table 6-1: Time elapsed through cycle for each analysed instant for PIV data acquisition for each configuration

Phase resolved PIV processing was carried out on 100 image pairs acquired for each instant of each configuration, as described in Section 3.3.3.4. As in the previous PIV investigation in this thesis, the time interval of the image pairs (Δt) for the systolic instants was calculated via equation (3-17), utilising the measured flowrate through the flowmeter, alongside a second set of image pairs taken with a Δt of 250 μs in order to capture the expected slower sinus flow. However, using the same methodology for the diastolic instants was not possible, as by definition there was very little, if any, flow through the flowmeter at these times. Therefore, it was decided to again acquire image pairs at 2 Δt values, 100 at 250 μs, the same as for the instant at the end of systole, and a further 100 image pairs at 1000 μs, to maximise the accuracy of the PIV measurements during even very slow diastolic flow. The resultant image pair time intervals used to capture the fast flow dynamics during instants A-D for the various configurations is displayed in Table 6-2.

Setup	*Time interval of image pair, Δt, at each Instant (μs)*			
	A	B	C	D
NoCA	243	81	122	243
CA	244	81	122	244

Table 6-2: Time interval for image pairs at instants A-D

The maximum PIV velocity uncertainty for each instant and each setup was then calculated from these Δt values and the magnification factor from the PIV setup, as presented in Table 6-3. As the camera was moved in between data acquisition for each configuration to get access to the pulse duplicator, the magnification factor had to be remeasured for each of the configurations, including the individual CA setups.

Setup	*PIV Velocity Uncertainty for each Instant (m/s)*				
	A	B	C	D	E - I
NoCA	0.0090	0.0271	0.0181	0.0090	0.0088
LCA	0.0090	0.0271	0.0181	0.0090	0.0088
RCA	0.0091	0.0270	0.0180	0.0091	0.0088
NCA	0.0090	0.0269	0.0179	0.0090	0.0088

Table 6-3: Maximum PIV Velocity Uncertainty for each instant in each setup

Velocity fields were derived from the image pairs via cross correlation, as described in Section 3.3.2, from which the RSS, vorticity, and standard deviation (as an indicator of turbulence) were calculated in accordance to the process defined in Section 3.3.3.1. Streamlines were also applied to the velocity images, as described in Section 3.3.3.2, enhancing the visualisation of the fluid flow for each instant. Extracting the peak velocity value, v_p, across the cross-section enabled quantitative comparison between the setups, and identification of the sinus region, illustrated in Figure 6-2(b), allowed the average sinus velocity, v_s, to be determined. The investigation presented in Chapter 6, alongside previous reports from the literature[97], indicated that flow at the base of the sinuses is particularly affected by TAV implantation inside the native leaflets, so this sinus data was further divided by the median y-value of the sinus co-ordinates into the upper (closer to the STJ) and lower (closer to the basal annulus) sinus, as illustrated in Figure 6-3, enabling the calculation of the average upper and lower sinus velocities, v_{us} and v_{ls} respectively. The velocity values across the STJ were also extracted, enabling the quantification of the fast flow width (x_f), defined as the span of the stream where the downstream velocity, v_{STJ}, is greater than 1/3 of the peak velocity, v_p, detected across the entire cross-section, as indicated in Figure 6-2 (c).

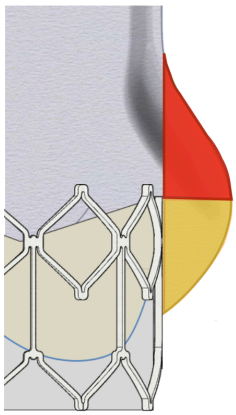

Figure 6-3: Illustration of upper- and lower-sinus regions. The upper sinus is shaded red, and the lower sinus is shaded orange, split around the centre line of the sinus, halfway between the basal annulus and the STJ.

6.3 Results

6.3.1 Coronary Flow

The outflow of the mock coronary arteries throughout a typical cardiac cycle during PIV acquisition is presented alongside measurements from previous *in vitro* and *in vivo* in the literature in Figure 6-4. Peak coronary flow was identified as occurring 350 ± 20 ms through the imposed cardiac cycle, which correlated with the end of systole and valve closure.

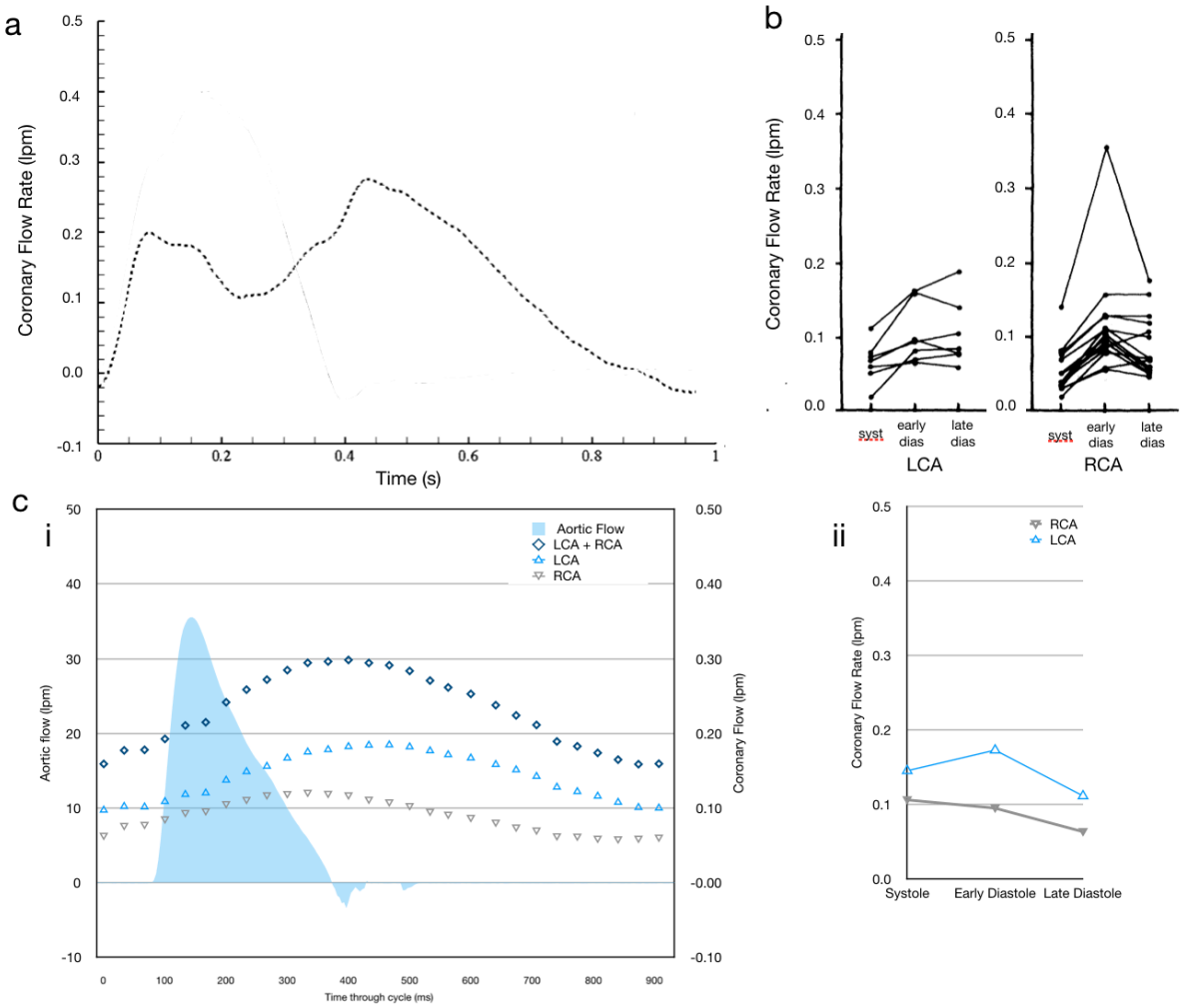

Figure 6-4: Coronary Flow rates: (a) in vitro *measurements reported by Moore* et al.[72]*; (b)* in vivo *measurements reported by Spiller* et al.[111]*; (c) Phase-averaged coronary flow measurements from the presented investigation, presented as (i) aortic and coronary flow vs time and (ii) coronary flow vs. cardiac phase.*

6.3.2 Global Data

The hydrodynamic data for the 4 setups, in terms of the EOA, mean systolic transvalvular pressure drop (Δp), closing regurgitant volume (V_c), and forward, closing, leakage, and total energy losses throughout the cycle (E_f, E_c, E_l and E_t respectively), alongside the peak velocity (v_p) and the maximum RSS for the

whole cross-section throughout the cycle, is presented in Table 6-4. The flow and pressure acquisitions throughout a typical cycle during PIV acquisition for each setup are illustrated in Figure 6-5. Errors in the haemodynamic data, resulting from the range of pressure readings acquired over the 20 cycles in combination with the resolution of the pressure and flow transducers, are indicated in the table above. The data for each parameter is compared to that of the mean of the 3 CA setups, and with the exception of leakage energy losses, all data acquired from the pressure and flow transducers of the pulse duplicator, EOA, Δp, V_c, E_f, and E_c, were within 10 % of all the values from the other setups.

Global Parameter	*NoCA*	*LCA*	*RCA*	*NCA*
Effective Orifice Area (cm^2)	2.58 ± 0.02 *(101 %)*	2.56 ± 0.03		
Pressure Difference (mmHg)	8.36 ± 0.13 *(99 %)*	8.44 ± 0.21		
Closing Volume (ml)	1.29 ± 0.12 *(100 %)*	1.29 ± 0.23		
Forward Energy Loss (mJ)	64.92 ± 1.01 *(96 %)*	67.87 ± 2.31		
Closing Energy Loss (mJ)	4.85 ± 0.54 *(108 %)*	4.48 ± 0.87		
Leakage Energy Loss (mJ)	14.99 ± 0.72 *(158 %)*	9.46 ± 0.93		
Total Energy Loss (mJ)	84.76 ± 2.27 *(104 %)*	81.81 ± 4.11		
Peak Velocity (m/s)	2.5 ± 0.027 *(89 %)*	2.8 ± 0.027	2.5 ± 0.027 *(89 %)*	2.8 ± 0.027 *(100 %)*
Peak Reynolds shear stress (N/m^2)	127 ± 1.37 *(120 %)*	106 ± 1.14	124 ± 1.33 *(120 %)*	95 ± 1.03 *(90 %)*

Table 6-4: Hydrodynamic global data for all configurations: mean value, ± standard deviation, and percentage value with respect to LCA configuration.

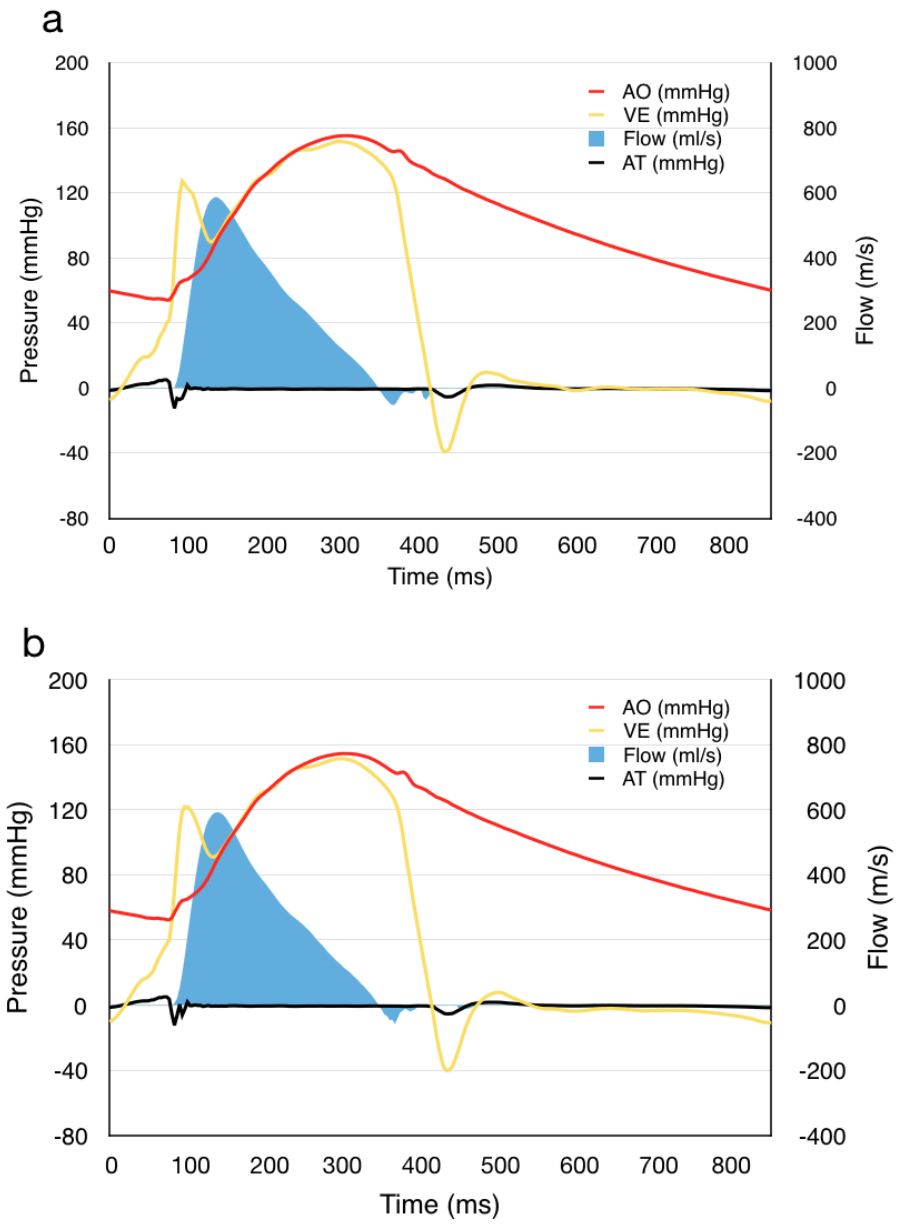

Figure 6-5: Pressure-time and flow-time charts for each configuration throughout a typical cardiac cycle during PIV acquisition: (a) NoCA; (b) mean results of the 3 CA setups.

6.3.3 PIV Data

PIV data for the fast flow width (x_f) and average velocity for the upper-, lower-, and full-sinus (v_{us}, v_{ls}, and v_s respectively) as described in Figure 6-3, for each instant of each setup are presented in Table 6-5. Line charts in Figure 6-6 provide visual comparison of the fast flow width and the average sinus velocity throughout the cycle of each configuration, and the velocity profiles at the STJ for instants A - E in each setup is displayed via line charts in Figure 6-7.

Parameter	*Instant*	*NoCA*	*LCA*	*RCA*	*NCA*
Fast Flow Width (mm)	A	7.9	12.5	19.0	13.6
	B	13.8	16.4	14.0	14.3
	C	13.2	13.9	12.2	10.4
Average Full Sinus Velocity (m/s)	A	0.016	0.022	0.017	0.016
	B	0.044	0.075	0.034	0.057
	C	0.047	0.045	0.036	0.030
	D	0.015	0.027	0.022	0.016
	E	0.017	0.020	0.013	0.021
	F	0.020	0.028	0.018	0.015
	G	0.013	0.024	0.014	0.004
	H	0.011	0.021	0.021	0.008
	I	0.015	0.019	0.009	0.014
Average Upper Sinus Velocity (m/s)	A	0.025	0.039	0.031	0.020
	B	0.066	0.135	0.069	0.100
	C	0.066	0.072	0.072	0.041
	D	0.019	0.052	0.043	0.023
	E	0.016	0.040	0.029	0.035
	F	0.024	0.049	0.040	0.022
	G	0.016	0.049	0.031	0.006
	H	0.012	0.042	0.032	0.013
	I	0.020	0.036	0.022	0.025
Average Lower Sinus Velocity (m/s)	A	0.009	0.009	0.008	0.013
	B	0.024	0.033	0.016	0.027
	C	0.029	0.026	0.019	0.022
	D	0.012	0.010	0.011	0.012
	E	0.018	0.007	0.005	0.011
	F	0.017	0.012	0.007	0.011
	G	0.010	0.007	0.006	0.002
	H	0.009	0.006	0.016	0.004
	I	0.010	0.006	0.004	0.006

Table 6-5: Instantaneous data from PIV analysis for all setups, presenting the fast flow width at instants A – C, and the average full-, upper-, and lower-sinus velocities at all instants.

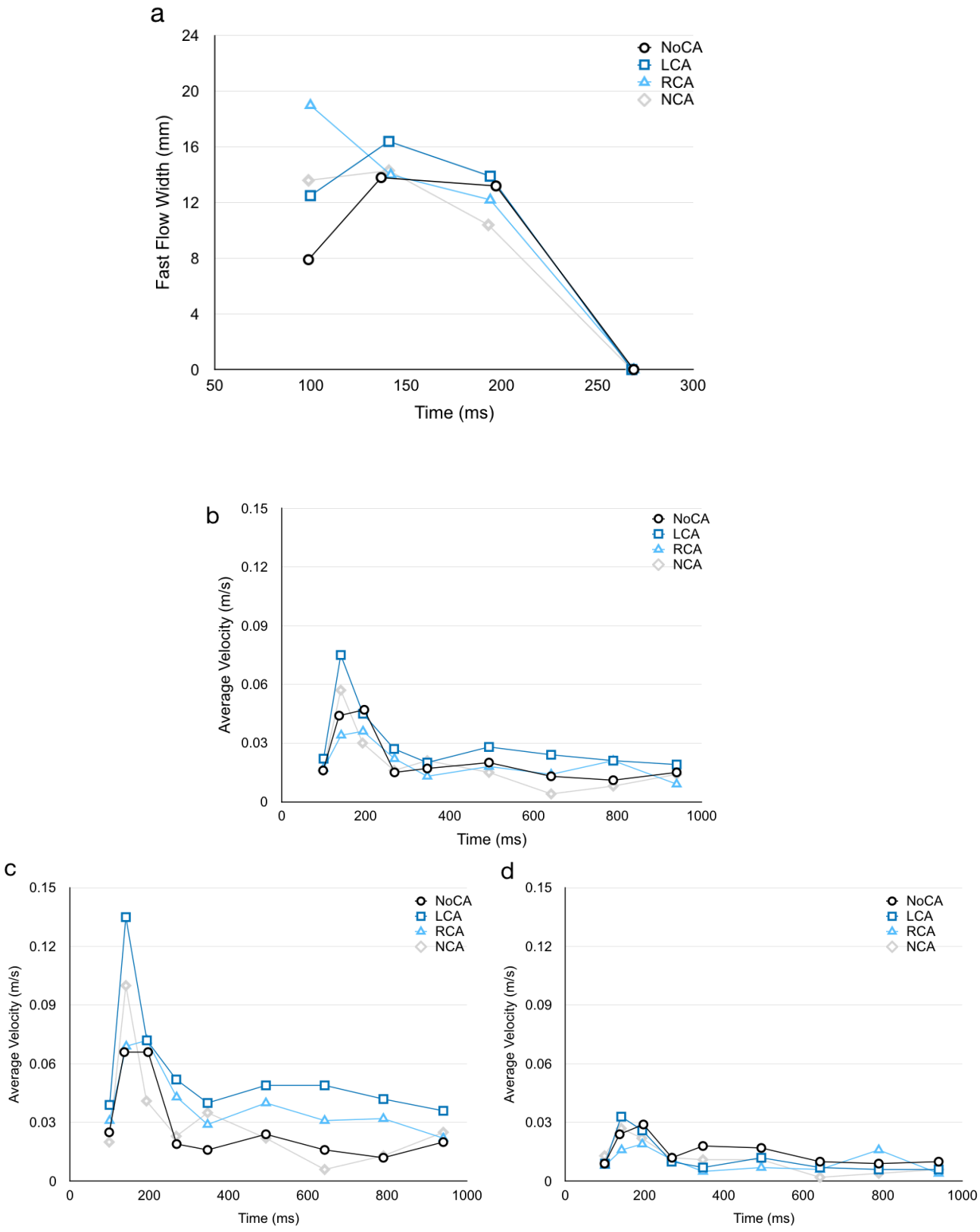

Figure 6-6: PIV derived data. (a) Fast flow width for instants A-D of each setup; Average velocity within the (b) whole- (c) upper- and (d) lower- sinus for each instant of each setup

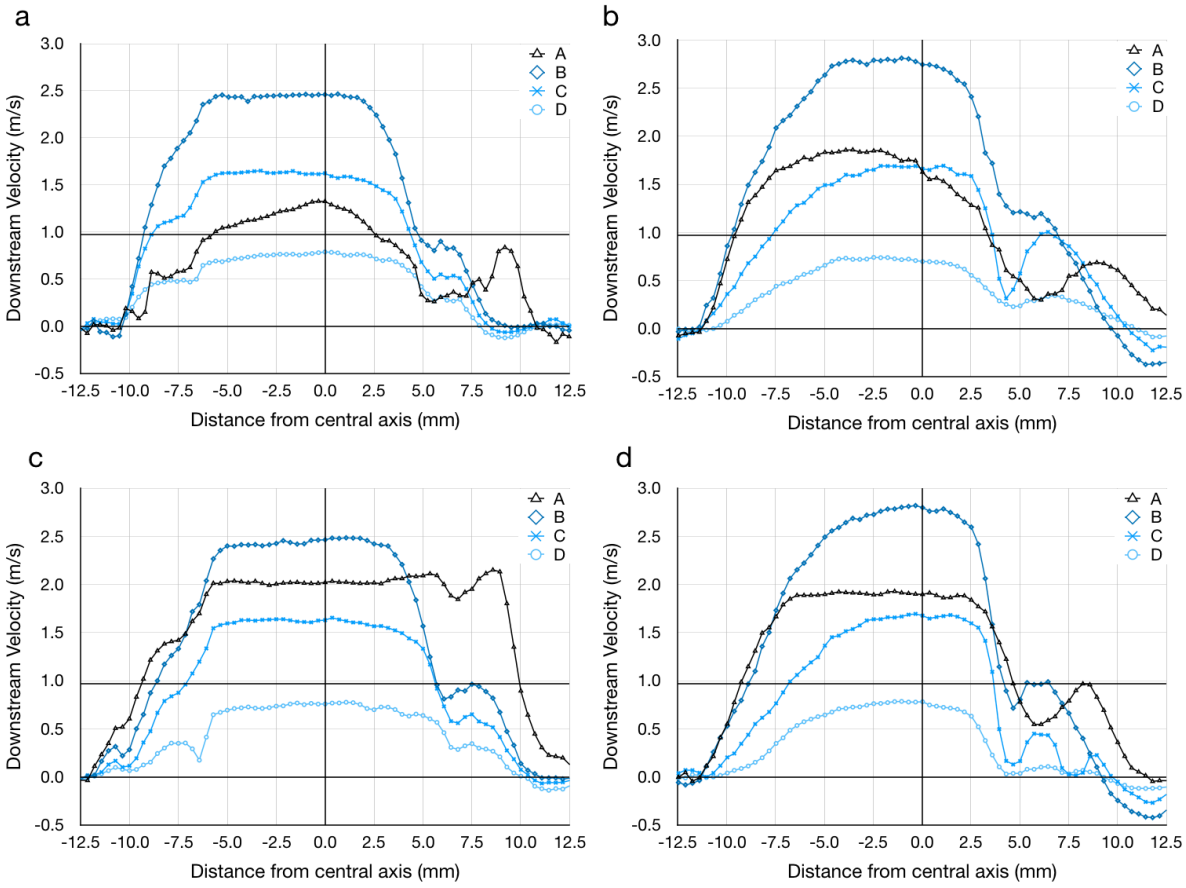

Figure 6-7: Velocity profiles across sinotubular junction at each instant analysed for each configuration, with the 1/3 of peak velocity for each configuration indicated. (a) NoCA b) LCA; (c) RCA; (d) NCA.

6.3.3.1 NoCA

The velocity fields of the NoCA setup are presented in Figure 6-8, with a contour map for the Reynolds shear stress (RSS) at peak flow (instant B) shown in Figure 6-9(a). Colour maps for the vorticity, standard deviation, and RSS during instants A-D are provided in the appendices. The fast flow is initially very centralised along the root axis with an arched velocity profile across the STJ, before gradually shifting towards the commissural side of the cross-section while the STJ velocity profile flattens out, with X_f reaching 13.8 mm at peak systole (instant B). A vortex is generated at peak systole, downstream of the native leaflet cusp next to the sinus side root wall, which dissipates at the end of systole. Whilst the PIV images do not indicate a commissural side vortex, the velocity profile across the STJ does show some return flow on this side of the root cross-section during peak systole, and the fast flow never extends to the commissural root wall throughout the cycle. v_p, acquired during peak systole,

was measured at 2.5 m/s, at which time the peak RSS and vorticity were also obtained, reaching 127 N/m^2 and 850 /s respectively, primarily distributed downstream of the native leaflet cusp on the commissural side. Turbulence was indicated to be highest in the regions downstream of the native leaflet cusps during mid systole (instants B and C), in a roughly symmetrical distribution around the central flow, reaching a standard deviation across the acquired image pairs of each instant of 0.75 m/s.

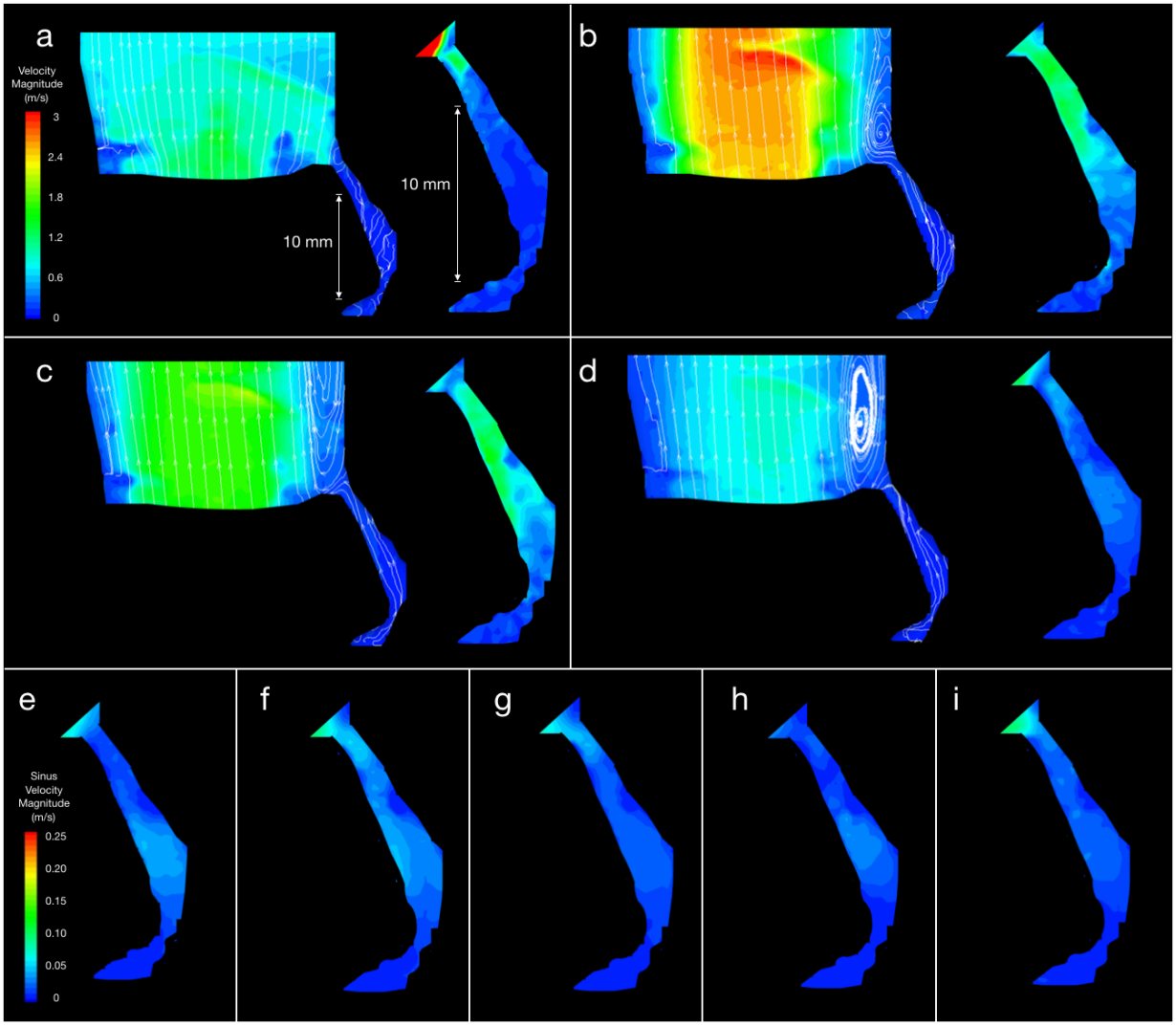

Figure 6-8: Velocity contour maps and streamlines for the NoCA setup. The full cross-section velocity field is displayed for instants A – D, and enlarged sinus velocity fields, at a smaller velocity scale, are shown for all instants.

Systolic flow does not establish a distinct pattern within the sinus, indicating alterations to the sinus flow from cycle to cycle, and peaks at 0.15 m/s within the sinus throughout the cardiac cycle. v_{us} is 0.045 m/s during systole (instants A – D), and v_{ls} is equal to 0.020 m/s. Flow is reduced during early diastole in the upper sinus, lowering v_{us} to 0.0198 m/s over instants E and F, although

there is little reduction in flow in the lower sinus, which averages v_{ls} at around 0.019 m/s during these same instants. As diastole proceeds, v_{ls} does decrease with time, approximately halving from that observed in the first half of diastole. Upper sinus flow, after the initially deceleration in early diastole, remains higher than the lower sinus, with a diastolic (instants G - I) v_{us} of 0.0165 m/s.

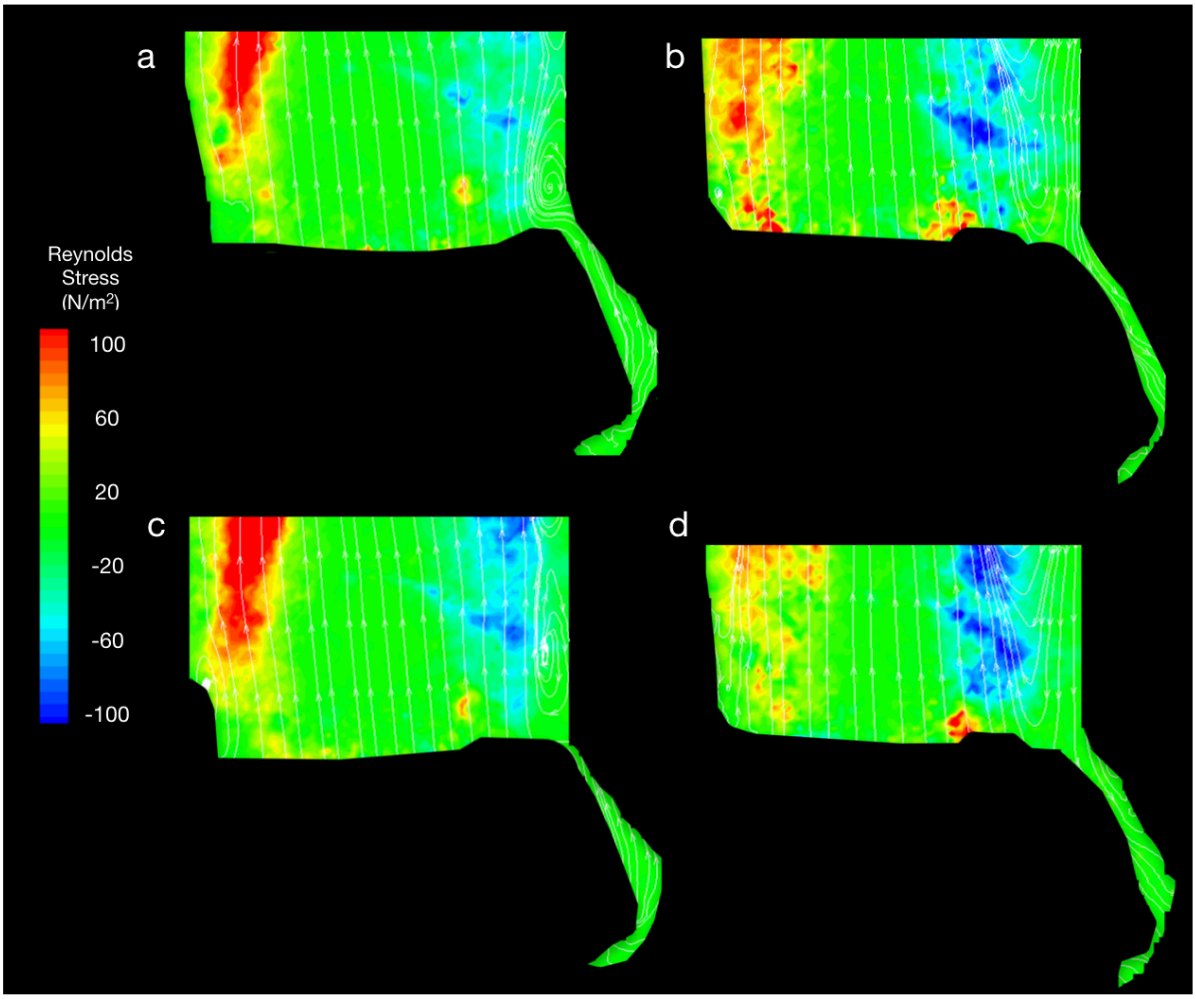

Figure 6-9: Reynolds shear stress contour maps for the various setups at peak flow (instant B): (a) NoCA; (b) LCA; (c) RCA; (d) NCA

6.3.3.2 LCA

The velocity maps obtained from the PIV data for setup LCA are presented in Figure 6-10, and a colour field of RSS at peak flow (instant B) shown in Figure 6-9(b). Colour maps for the vorticity, standard deviation, and RSS during instants A-D are provided in the appendices. The fast flow is initially skewed away from the sinus side of the root cross-section, with an arched velocity profile throughout systole, and X_f is always higher than at the equivalent instant for the NoCA setup, reaching 16.4 mm at peak systole (instant B), when v_p is

acquired, equal to 2.8 m/s. The peak RSS is also measured at this instant, equal to 106 N/m^2, and 900 /s respectively. Turbulence distribution is indicated to be similar in both magnitude and distribution to that of the NoCA setup during mid systole (instants B and C), but in contrast to the previous configuration, there is also a large region of turbulence at the STJ level on the sinus side of the cross-section. A sinus side vortex is again present, although it only fully coalesces later in the cycle (instant C), with a less structured region of return flow indicated in the same area during peak flow (instant B). A commissural side vortex can be observed during late systole (instant D), forming adjacent to the native leaflet cusp on this side.

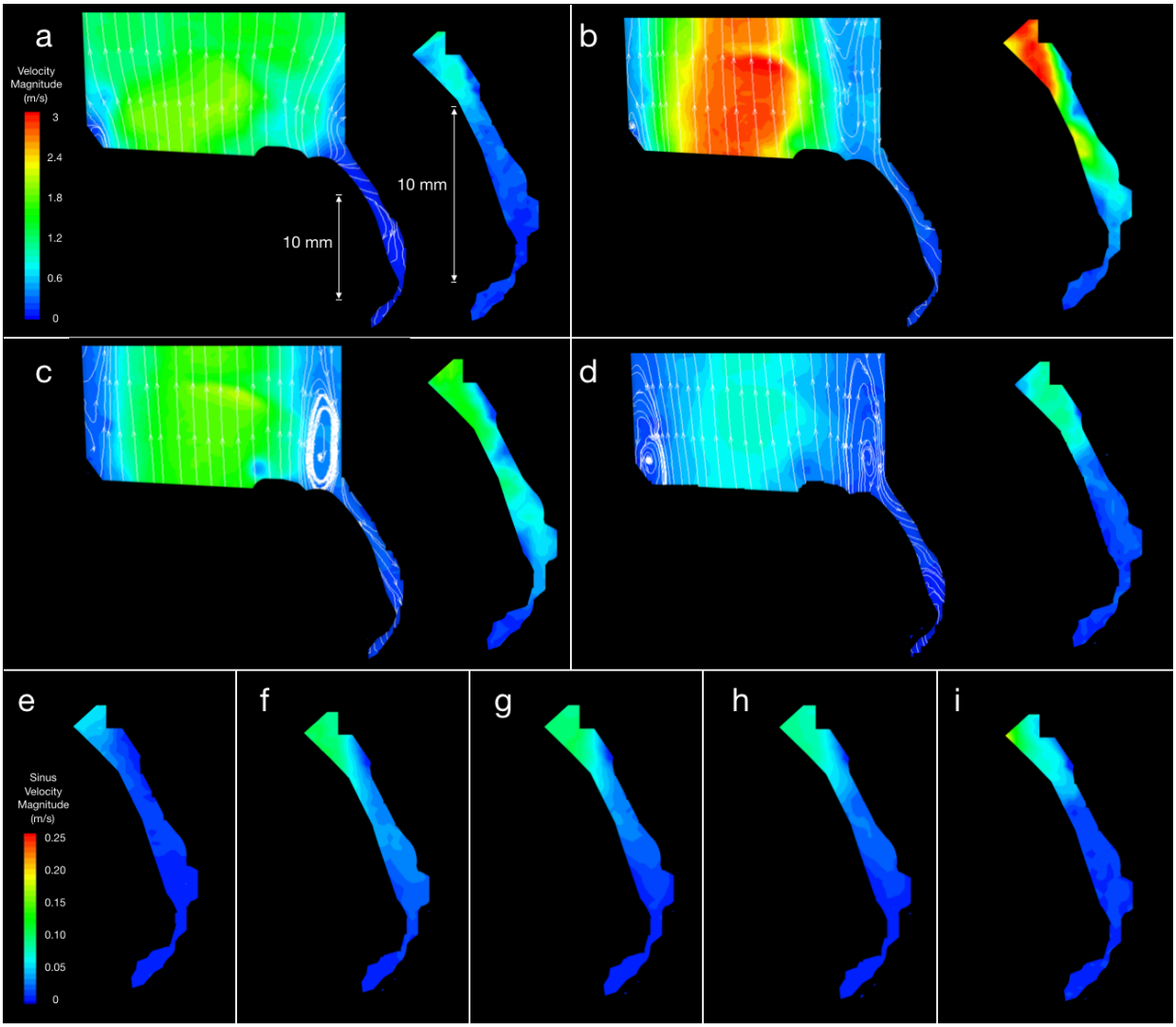

Figure 6-10: Velocity contour maps and streamlines for the LCA setup. The full cross-section velocity field is displayed for instants A – D, and enlarged sinus velocity fields, at a smaller velocity scale, are shown for all instants.

Systolic fluid flow in the LCA sinus is relatively structured and at a greater velocity compared to the NoCA setup, especially within the upper sinus, with a maximum velocity magnitude of 0.28 m/s measured and v_{us} averaging 0.0423 m/s throughout the entire cycle. v_{us} is equal to 0.0745 m/s during systole in the upper sinus, with flow towards the mock CA from the upper sinus, and v_{ls} is equal to 0.0195 m/s during this same period. Flow towards the CA continues during early diastole (instants E and F), although slowing to a v_{us} of 0.045 m/s, and flow at the base of the sinus has become very slow, v_{ls} = 0.0095 m/s. The flow towards the CA becomes reduced during late diastole (instants G – I), although v_{us} remains fairly constant during this time, v_{us} remaining above 0.036 m/s throughout. The sinus flow further away from the STJ and ostium also remains fairly constant, at the much slower rate of v_{ls} = 0.0063 m/s during this period.

6.3.3.3 RCA

The PIV derived velocity fields for the various instants throughout the RCA setup cycle are illustrated in Figure 6-11, and a contour map of the RSS at peak flow (instant B) shown in Figure 6-9(c). Colour maps for the vorticity, standard deviation, and RSS during instants A-D are provided in the appendices. The fast flow is more centrally aligned with a flatter profile than for the LCA setup, with a region of high velocity flow apparent in the STJ profile on the sinus side of the cross-section during early systole (instant A), as can be observed in Figure 6-7(c), which contributes to the largest X_f (19.0 mm) observed across all configurations, and may contribute to a reduced v_p over the cross-section, equal to 2.5 m/s. For the remainder of systole (instants B – D), X_f is lower than that observed for the LCA, and a sinus side vortex forms downstream of the native leaflet cusp, whilst a commissural vortex is indicated by the PIV images throughout systole. The maximum RSS is again observed during peak systole (instant B), reaching 124 N/m^2, slightly higher than that observed in setup LCA, but with a similar distribution, downstream of both sides of the native leaflet cusps in the cross-section. However, the highest vorticity for this configuration is observed during early systole (instant A), on both sides of the central flow, reaching magnitudes of 980 /s. The turbulence pattern during mid systole (instants B and C) is similar to that of both the NoCA and LCA setups, with large

distributions indicated downstream of the native leaflet cusps on both sides of the jet flow, whilst the turbulence during early systole (instant A) is more prevalent than in the NoCA setup, but not as extensive as that observed in the LCA sinus, again downstream of the native leaflet cusps on both sides of the cross-section.

Similar to the LCA setup, there is structured flow in the upper sinus and towards the CA during systole, peaking at 0.27 m/s, with much slower flow in the lower sinus. However, this flow speed is on average only 71 % of the magnitude of that observed in the LCA, with a v_{us} = 0.058 m/s during diastole, with this value equal to 64 and 68 % of the average LCA flow across the sinus during early (instants E and F) and late (instants G – I) diastole respectively. Flow in the lower sinus is also diminished until late diastole in comparison to the LCA setup, with v_{ls} = 0.016 m/s in systole and v_{ls} = 0.0062 m/s in early diastole. In late diastole, this flow at the base of the sinus has an average magnitude greater than late of the LCA, but v_{ls} remains below 0.016 m/s at all instants in this period, and averages 0.0084 m/s overall from instants G – I. A vortex is generated around the mid-point of the sinus in mid-diastole (instants F and G), although with very low vorticity, never rising above 10 /s.

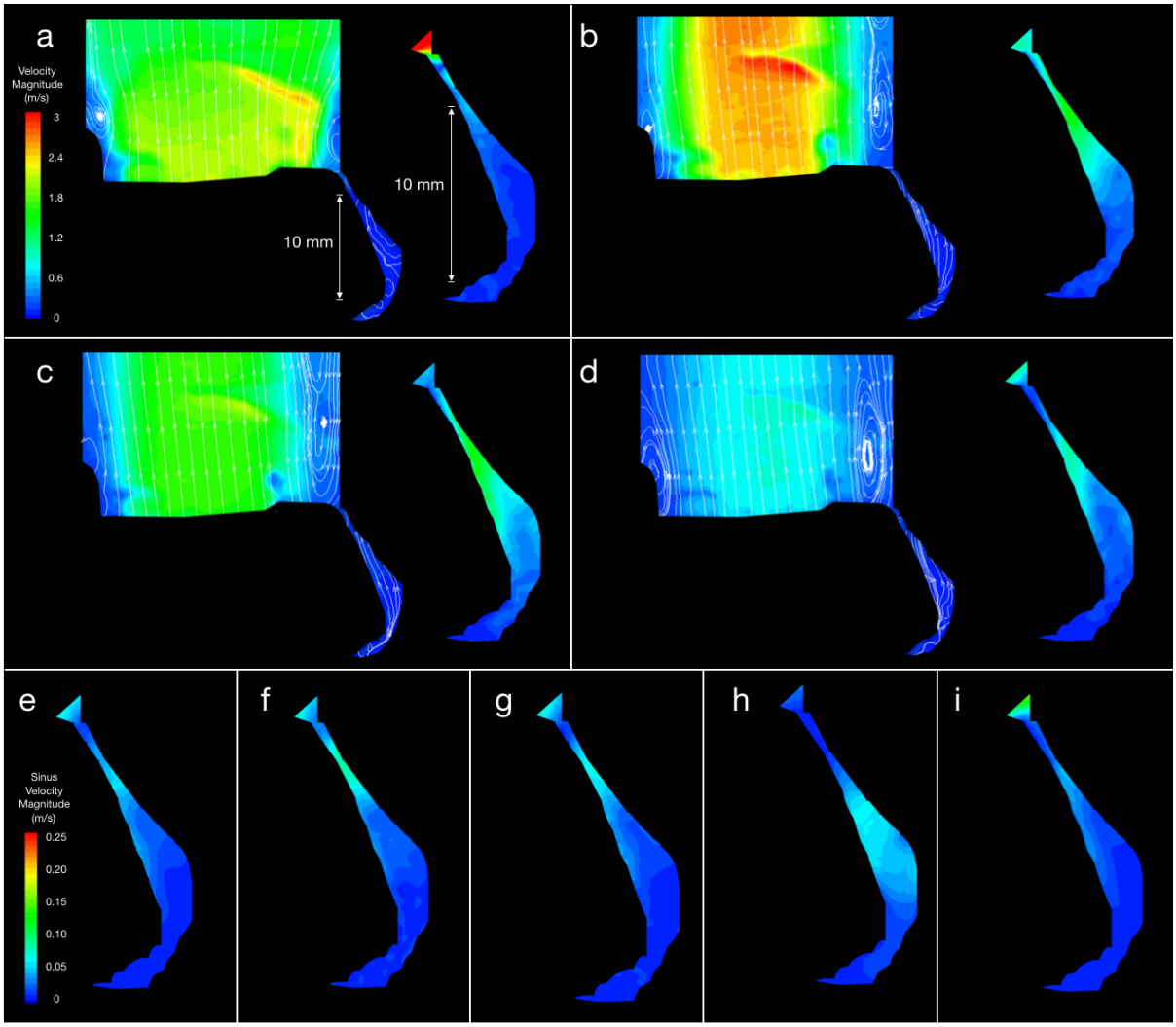

Figure 6-11: Velocity contour maps and streamlines for the RCA setup. The full cross-section velocity field is displayed for instants A – D, and enlarged sinus velocity fields, at a smaller velocity scale, are shown for all instants.

6.3.3.4 NCA

Velocity fields for each analysed instant from the PIV analysis for the NCA setup are shown in Figure 6-12, and a colour field of the RSS at peak flow (instant B) shown in Figure 6-9(d). Colour maps for the vorticity, standard deviation, and RSS during instants A-D are provided in the appendices. The central flow is again skewed towards the commissural side of the root, in similarity with the LCA cross-section, with an initially flat velocity profile across the STJ which becomes more arched as systole progresses, reflected by the NCA X_f being initially greater than the LCA equivalent before shrinking to a narrower central flow. v_p is equal to that of the LCA setup, 2.8 m/s during peak systole (instant B), and RSS reaches 95 N/m^2 at this time, the lowest RSS across the configurations, concentrated more on the sinus side of the cross-

section. The vorticity is also lower than the previous setups, peaking at 750 /s in the same region as the maximum RSS. The turbulence distribution is very similar to that observed in the LCA composition, reaching a maximum during mid systole (instants B and C) in the regions downstream of the native leaflet cusps with additional turbulence observed in early systole (instant A) on the sinus side of the cross-section. Return flow accompanied by a vortex downstream of the native leaflet cusp on the sinus side of the root is present throughout the mid-late systolic cycle (instants B – D), and a commissural side vortex is indicated in the relatively wide slow flow during late systole (instant D). Unlike the LCA and RCA sinuses, and in similarity to the NoCA setup, NCA sinus flow is initially unstructured, and very slow throughout systole, with velocities approximately 57 % of LCA, at similar magnitudes to that observed for the NoCA configuration. Flow remains very slow at the base of the sinus throughout the cycle, $v_{ls} < 0.027$ m/s during systole and $v_{ls} < 0.011$ m/s throughout diastole. For the upper half of the sinus, v_{us} averages 0.042 m/s in diastole, 57 % of the LCA and 78 % of the RCA equivalent velocity magnitudes, and a vortex present in the sinuses at the equivalent position of the CA in the LCA and RCA setups seems to direct returning flow away from the sinus. The average velocity of the upper sinus remains below both of the other two physiological setups in the remainder of the cycle, with v_{us} = 0.029 m/s during early diastole for the NCA sinus (66 % of the LCA v_{us} and 86 % of the RCA v_{us}), and diminishing further during late diastole, v_{us} = 0.0159 m/s (38 % of the LCA v_{us} and 57% of the RCA v_{us}), and comparable to the equivalent value of the NoCA setup.

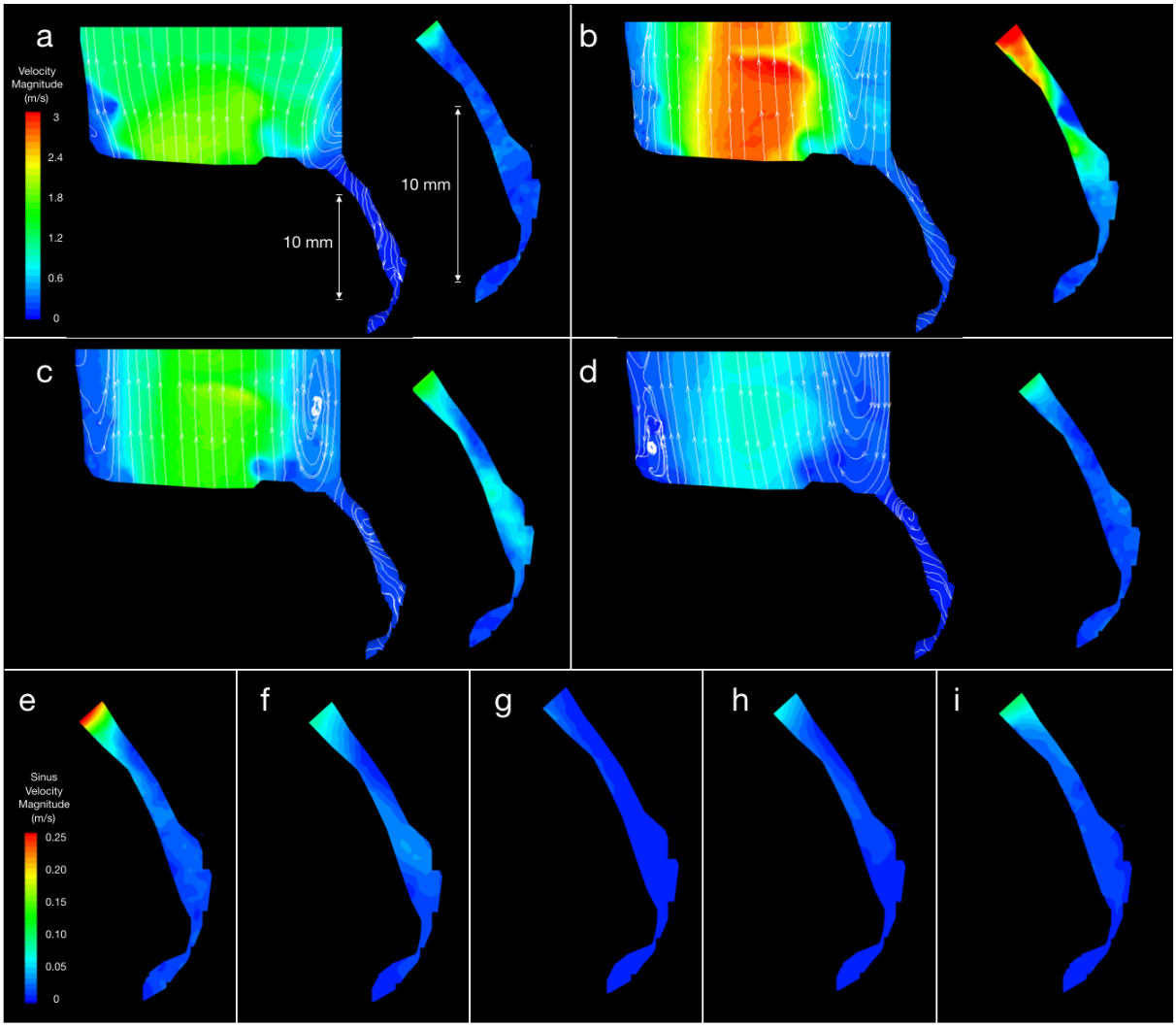

Figure 6-12: Velocity contour maps and streamlines for the NCA setup. The full cross-section velocity field is displayed for instants A – D, and enlarged sinus velocity fields, at a smaller velocity scale, are shown for all instants.

6.4 Discussion

For the first time, the flow within an aortic root containing native leaflets and an implanted TAV has been modelled and analysed via PIV, elucidating local fluid flow fields of instants throughout the systolic and diastolic cycles. The CA flow rates observed throughout the cycle were within the upper and lower extremes of the flows reported in the literature, with a similar flow pattern consisting of peak CA flow during very late systole and early diastole observed[72,111]. The average CA flowrates, 114.2 ml/min for the LCA and 52.1 ml/min for the RCA, were also within the *in vivo* ranges previously reported (79-233 ml/min for the LCA and 19-162 ml/min for the RCA, measured via angiography and intravascular ultrasound and the contrast transit time)[108]. This degree of

agreement with the data published in the literature is considered acceptable, especially when considering that the variability between patients results in a wide range of physiological coronary waveforms[72].

The global haemodynamic data acquired was very similar across the 4 setups, suggesting that the presence or otherwise of the CA has little effect upon the cycle to cycle performance of TAVs in terms of forward flow efficiency and valve function. The EOA, Δp, and E_f varied by less than 4 % across the setups, whilst the V_c and associated E_c were within 10 % for the configurations, equating to an additional 0.11 ml of regurgitation in the NCA setup in comparison to the LCA setup, marginally greater than the experimental error of ± 0.09 ml, but still well within the ISO requirements for a bioprosthetic implant[268]. This was expected for the 3 physiological setups (LCA, RCA, and NCA) as the only difference between these configurations was the location of the fully open, partially obstructed, and fully closed tubing in relation to the camera used for PIV image acquisition. The similarity of the global data of the NoCA setup to the 3 physiological setups implies that *in vitro* testing where the primary/sole aim of the experiment is to obtain these performance indicators, the inclusion of CAs in the model is not necessary to achieve physiologically relevant findings.

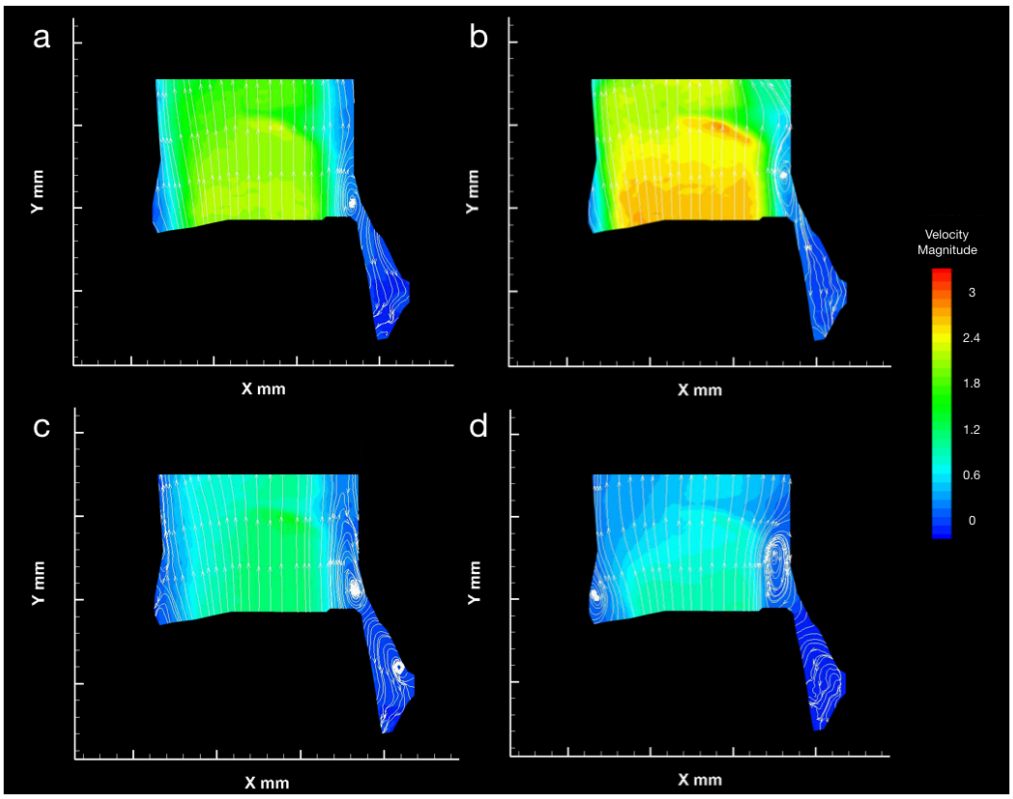

Figure 6-13: The velocity fields for instants A – D from configuration TA1 from Chapter 6

The leakage during the diastolic part of the cycle was greater for the NoCA configuration than the other setups, although the measurement technique used did not enable differentiation between intra- and para-valvular leakage. However, it may be conjected that this additional leakage occurred as a result of the lack of CAs in the NoCA setup, which provide outflow for backflowing fluid and pressure during diastole in the 3 physiological setups. Instead, the lack of CA outlet for the flow during diastole results in additional leakage around and/or through the TAV. As the previous TAV experiments described and discussed in Chapter 5 were only concerned with the systolic portion of the cycle, direct comparison of the energy losses associated with the closed valve during diastole cannot be made, but the additional energy loss of 5.53 mJ in the NoCA setup is not thought to make a critical difference to the flow dynamics of the configuration, representing < 7 % of the total energy loss during the cycle.

PIV analysis of the downstream flow from the TAV in the NoCA setup, as illustrated in Figure 6-8, shows similar flow patterns to those observed for the TA1 configuration from the previous investigation in Chapter 6, the aligned TAV within native leaflets, presented in Figure 6-13 for convenience.

A summary of the fluid flow within the sinus for the different configurations is provided in Figure 6-14 . The forward flow extends to the commissural side wall during systole, with a small vortex sometimes observed above the native leaflet cusp here, whilst there is a larger and stronger vortex above the sinus side cusp, associated with a wider return flow next to the root wall that prevents the central jet from fully extending to the lumen. These flow patterns are also observed for the LCA, RCA, and NCA setups, although the sinus side vortex of the NCA flow is larger and further downstream than in the other physiological cross-sections. Systolic coronary flow may draw this vortex closer to the sinus, implied by closest position of this vortex to the sinus at mid systole in the LCA setup which has the highest CA flow, which then appears to increase flow into the sinus region as a whole. On the contrary, in the NCA setup, the backflow along the sinus side wall appears to be diverted away from the sinus and back along the cusp of the native and TAV leaflets by this vortex, reducing flow into the sinus. A small vortex, possibly generated by this return flow passing the relatively static flow of the sinus as theorised by Yap *et al.*[102], is observed at the upper most point of the sinus from late systole until late diastole, providing

some washout of the upper sinus but not significantly influencing the flow of the lower sinus during this period, which remains below 0.012 m/s. The varying position of this sinus side vortex across the setups also explains the disparity between the STJ velocity profiles between X = +5.0 and +12.5 mm as shown in Figure 6-7, with the position of the vortex determining whether the flow across the STJ is primarily downstream or more lateral.

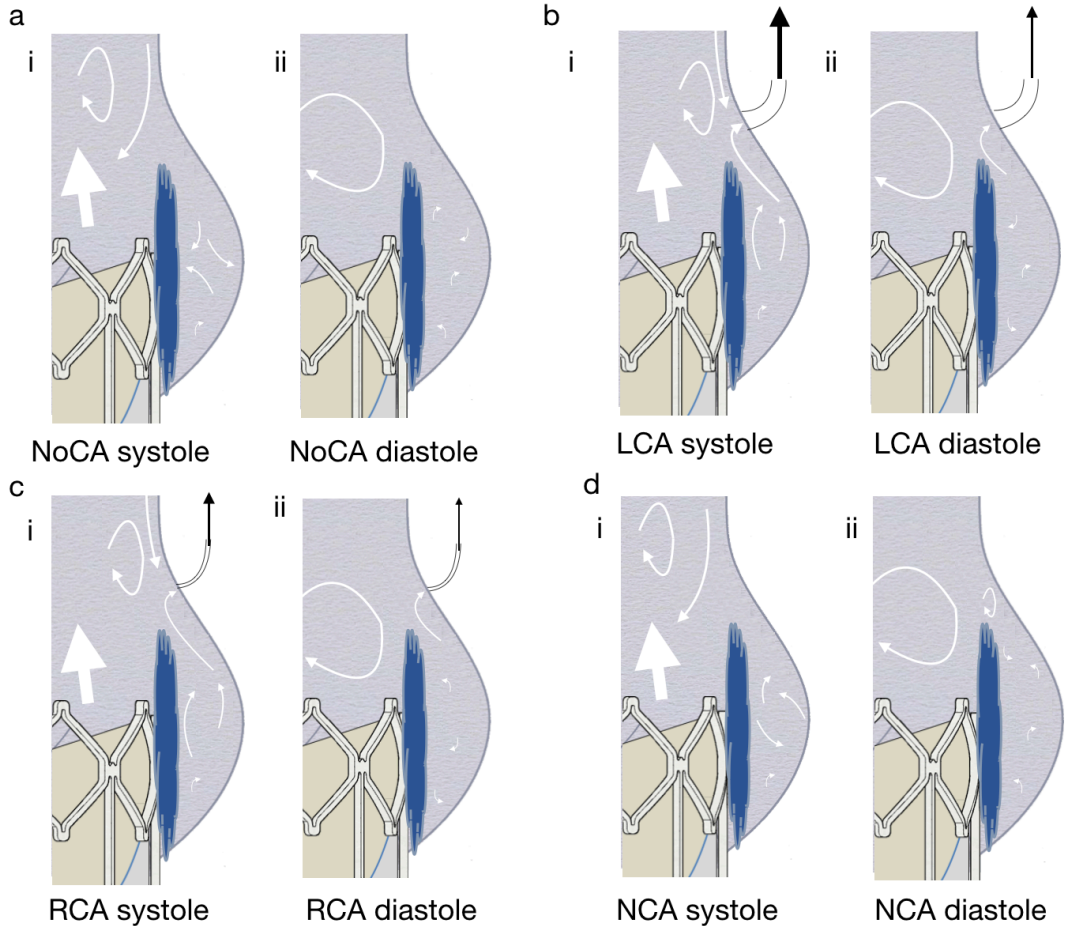

Figure 6-14: Summary of sinus fluid flow for the (a) NoCA, (b) LCA, (c) RCA, and (d) NCA configurations in (i) systole and (ii) diastole. The systolic vortex at the STJ is drawn towards the sinus due to the CA flow in the LCA and RCA configurations, alongside increased flow into the sinus. Flow in the upper sinus of the LCA and, to a lesser extent, the RCA is directed towards the ostium, but it much slower and without a clear direction for the NoCA and NCA sinuses, with the exception of a small vortex close to the STJ in the upper NCA sinus. Flow at the base of the sinus is very slow without a clearly defined direction of flow for all configurations in both systole and diastole.

Sinus flow is indicated to be much slower than that reported in previous *in vitro* investigations[72] of the aortic root region following surgical implantation of an aortic valve prosthesis, as indicated in Figure 6-15, most likely due to the presence of the native leaflets around the TAV. This reduced sinus velocity is in agreement with previous investigations of the region that omitted the CAs but included the native leaflets in the model, which report that the flow speed of

blood within the native sinus (and towards the basal annulus of the root in relation to the permanently held open native leaflet cusps) remains below 0.1 m/s throughout the entire cardiac cycle[213]. The LCA configuration results in flow in the upper sinus that remains above 0.05 m/s for the majority of each cycle, associated with a notable reduction in persistent stagnation, and accordingly a lower risk of thrombosis[83,92]. The RCA upper sinus flow is slower, and dips beneath this threshold during diastole, but the NoCA and NCA setups are much lower throughout diastole, never rising above 0.03 m/s, indicating a significantly elevated risk of thrombosis compared to the two coronary sinuses, especially the LCA, and measured at similar magnitudes to that measured for the lower sinus, already indicated by the literature to be of high thrombotic risk due to flow stagnation[83,269].

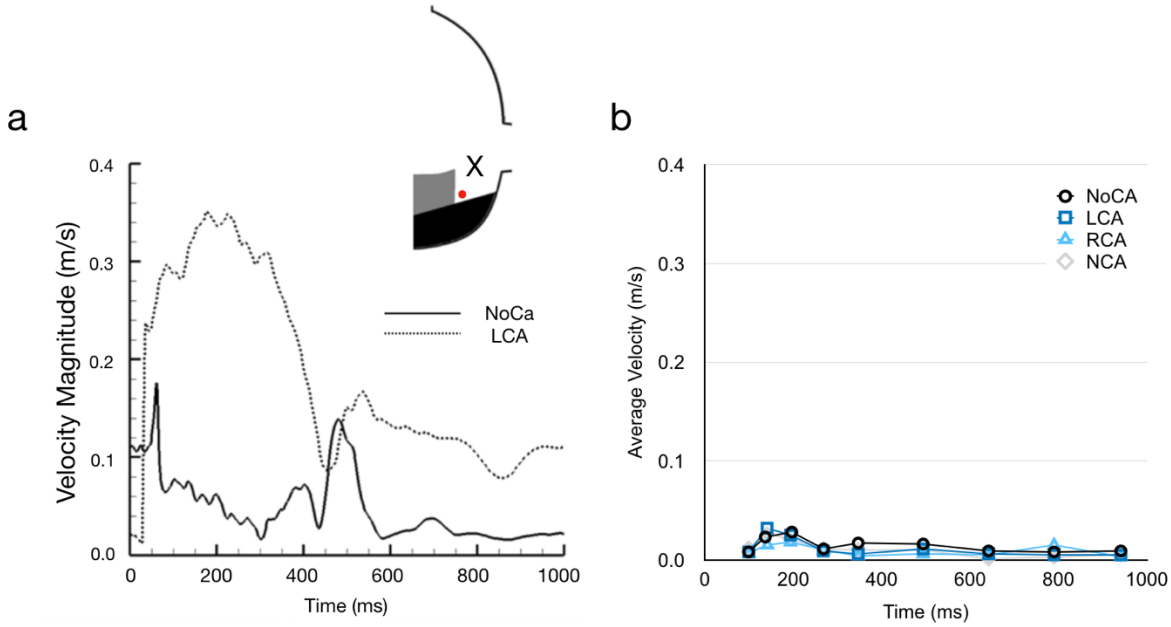

Figure 6-15: Comparison of lower sinus flow between (a) surgical aortic valve root[72] and (b) post-TAV implantation. The velocity data for (a) is taken from a single co-ordinate from the cross-section, indicated by the red dot labelled 'X' in the figure, whereas the data for (b) is averaged over the full lower half of the visible sinus.

The native leaflet, permanently displaced into an open configuration, fills much of the volume of the sinus, reducing the likelihood of vortical generation within the SoV. The extent of native leaflet presence is bound to be variable from patient to patient, as the extent and location of calcification across the leaflets is not uniform[270], causing a multitude of native leaflet shapes around the implanted TAV. Accordingly, the modelling of the native leaflets with a simple vinyl wrap from the investigation in Chapter 5, resulting in a thin walled cylinder

surrounding the TAV, can be considered to be a relatively mild and/or uniform calcification of the native leaflets, whilst the thicker silicone leaflets of the model presented in this chapter represent a more severe calcification. As a result, more of the mock native leaflet occupies the thickest part of the sinus cross-section, which is where a systolic vortex is present in the velocity fields acquired from configuration TA1 from Chapter 6, the equivalent setup of NoCA. A future study could involve varying the degree of sinus penetration by the native leaflets, possibly related to the thickness and/or calcification of the native leaflets, and establishing the relationship between this reduction of sinus volume and the sinus flow speed through the cardiac cycle, already indicated by this research to be substantially reduced from the physiological or post-surgical-intervention environment[20,72].

Possibly as a result of this increased native leaflet intrusion into the native sinus, the flow at the base of the sinuses is not significantly affected by the presence or otherwise of CA flow. Fluid velocity remains very slow throughout the modelled cardiac cycle, with only a small increase during peak systole, yet still remaining below 0.04 m/s for all setups, indicating a very stagnant region of flow and, as blood flow speeds lower than 0.05 m/s are associated with a drastic increase in the likelihood of thrombosis, an elevated risk of blood clots[83,92], which could cause local interference of leaflet function and/or downstream pathologies such as stroke. The minimal flow also indicates reduced wall shear stress along the lumen of the root in this region, reducing the alignment of endothelial cells and increasing the likelihood of inflammation[83], which in turn raises the risk of the exposure of subendothelial tissue to the blood. Virchow's triad of factors, made up of hypercoagulability, interruptions to the blood flow (such as blood flow stasis), and phenomena associated with the surfaces within and around the blood flow (such as exposure of the subendothelial layer of the lumen), indicate the main contributors to thrombosis[83,269]. The presence of two of these factors in the Valsalva sinuses post-TAV implantation, particularly towards the basal annulus region and especially in the non-coronary sinus, indicates an elevated potential for a highly thrombotic environment following non-surgical replacement of the aortic valve. These flow dynamics could therefore be strongly associated with

the reported raised incidence of sub-clinical leaflet thrombosis, stroke, and silent ischemic attacks following TAV implantation[192,207].

6.4.1 Limitations

The interpretation of these results requires consideration of the limitations present in the setup of the investigation. The idealisation of the root and native aortic valve geometry for the silicone models is not reflective of all physiologies, with anatomical variability and irregular calcification distribution alongside the potential for asymmetrical and non-standard TAV deployments contributing to alterations to the fluid dynamics presented here[12,186]. In particular, modelling and analysing the variation of the CA position may reveal further information on the post-TAVI environment, e.g. a lower CA, with the ostium situated closer to the basal annulus, may experience a reduced CA flow but may also influence the flow at the base of the sinus more, resulting in less sinus flow stagnation. Rigid root walls were used, precluding the modelling of aortic compliance, however the extensive application of TAVs within the elderly community[189], with lower compliance aortic roots[267], makes the conclusions of this study representative of a major proportion of the patient population. Imposing different haemodynamic cycles, with variations to the CO and/or the mean aortic pressure could reveal alterations to the CA flow during the cardiac cycle, leading to variations in the influence of the flow to the CA upon the sinus flow. The Newtonian blood analogue used will result in altered fluid dynamics in comparison to the shear thinning properties of blood, particularly in the low shear regions within the native sinuses focused on in this report, where the raised viscosity of a non-Newtonian fluid in low shear would reduce the velocity of the fluid in comparison to the Newtonian fluid used in this investigation. Finally, the 2D PIV analysis technique used cannot measure any out-of-plane dynamics, although it is expected that the plane investigated contains the most relevant flow structures of the region.

6.5 Concluding Remarks

Mock coronary arteries were included in a model of the aortic root, and a commonly implanted TAV device was positioned within. The resultant flowrate through these coronary arteries was found to be within the net cycle flow and maximum flow speed of the coronary arteries compared to previous *in vitro* and

in vivo reports[72,111]. The fluid dynamics within the upper sinus of an aortic root post-TAV implantation are affected by the presence of CA, with the mean velocity of the upper LCA sinus, 0.057 m/s, approximately twice that of the upper NCA or NoCA sinuses, 0.029 and 0.032 m/s respectively. Flow towards the LCA or RCA raises the flow speed in the associated chamber region closest to the STJ throughout the cardiac cycle, and non-modelling of these anatomical features during *in vitro* testing[102,271] could lead to under estimation of the flow within the upper sinus for the LCA and RCA, halving the flow velocity. CA flow also appears to affect the position of the sinus side vortex during late systole, with the increased flow to the LCA drawing this vortex towards the sinus. This increased fluid velocity suggests increased washout of the coronary sinuses, which could help lower the risk of thrombosis and endothelium damage. Therefore it can be stated that flow into the coronary arteries has an effect upon the fluid dynamics of the aortic root after TAV implantation.

Flow at the base of the sinus was relatively unaffected, remaining slow throughout the cycle and at elevated risk of thrombosis and endothelium damage, whilst global haemodynamic performance indicators were unaffected by the presence or otherwise of CAs.

7 Conclusions and Recommendations for Future Work

7.1 The Present Contribution

The major objective of this research was to establish the changes in the fluid dynamics of the aortic root due to the implantation of a TAV device. The increasing prevalence of treatment of aortic stenosis and other incurable aortic valve deficiencies with these novel prosthetics means a full understanding of the flow changes post-procedure is vital, especially when considered alongside the reported raised incidence of stroke and silent ischemic events after TAV implantation. These pathologies are strongly associated with (and often caused by) blood thrombosis, indicated by Virchow's triad to be strongly influenced by 3 broad categories of factors: interrupted blood flow (such as stagnation or turbulence), hypercoagulability (due to changes to the biological constitution of blood), and contact with non-standard surfaces (such as exposed sub-endothelium or foreign materials)[84].

In order to characterise and evaluate the flow of the post-TAV implantation aortic root region, the local flow patterns within both healthy and surgically treated aortic roots were first determined, enabling the differences between TAV and its alternatives to be ascertained.

The fluid flow patterns of the healthy native aortic valve and root were captured via *in vitro* analysis. Several configurations, representing the healthy condition as well as 5 distinct post-surgical treatment environments (an 'ideal' bioprosthetic sizing and positioning; the inclusion of a vascular graft that occludes the sinuses; a sub-annular implantation; an undersized bioprosthetic; a mechanical aortic valve implantation), were modelled and fixed inside a pulse duplicator, and physiological flow and pressure was imposed. Global haemodynamic performance parameters were calculated from pressure and flow transducers, enabling valve function to be compared across the configurations. Simultaneously, PIV images were acquired at several pre-defined instants within the mock systolic flow, enabling velocity fields of a cross-section of the aortic root to be generated, from which properties such as the RSS, vorticity, and turbulence could be quantified or elucidated. These local

fluid flow patterns could then be used to explain differences in the global haemodynamic performance data, as well as reveal characteristics of each configuration's flow that would not be possible by pressure/flow analysis alone. The same pulse duplicator and PIV techniques were then employed to investigate the fluid flow of an aortic root after TAV implantation, enabling comparison of the contour maps to that of the healthy, native root, and characterisation of the resultant flow. As the native- and TAV-commissural alignment is essentially random following prosthesis implantation, the fluid dynamics of the TAV were captured at both perfect commissural alignment and maximum non-alignment, to establish whether valve performance or other more discrete flow properties were affected. As many previous *in vitro* studies have not modelled the native leaflets during their procedure, the effect of including and omitting these anatomical features was also represented.

Finally, mock coronary arteries were designed and incorporated into the TAV analysis setup. The TAV was inserted into a mock aortic valve constructed from silicone, and the flowrate through the CAs was measured and compared to reported *in vivo* values. Each of the physiological sinuses, the LCA, the RCA, and the NCA sinus, was investigated using the pulse duplicator and PIV rig, in addition to a setup with all of these coronary arteries clamped off, representing both a configuration from the TAV alignment study and multiple reports from the literature, which have not included any representation of the CAs.

7.2 Main Findings of the Investigation

Investigation of the role of the valve-root system upon the functional mode and hydrodynamic performance of the left side of the heart revealed that significant alteration to the valve position or the geometric proportions of the aortic valve and/or root caused changes to the downstream fluid dynamics of the region. Common post-surgical environments resulted in a 32 – 42 % decrease in the EOA and a 64 – 110 % increase in the systolic transvalvular pressure loss. These global haemodynamic performance indicators were accompanied by a 10 – 40 % narrowing of the central jet flow and peak systole, increasing blood velocities as high as 3.0 m/s in contrast to the upper physiological limit of 1.7 m/s[55,98], and elevating the chance of RBC damage, a possible factor in the pathological incidence of calcification in bioprosthetics. These configurations

are also representative of common *in vitro* setups, providing reasoning for the non-consensus within the community in regard to the systolic fluid dynamics of the aortic region, as described in Section 2.1.3.2.1, in particular Figure 2-8, whereby some research claims the initial vortices persists within the SoV throughout systole and aid with valve closure[18–21], whilst other work states that these first vortices migrate away and are replaced by a second set of vortices, often with the opposite rotation[32–35]. The position and containment of the initial vortices generated by the forward flow though the aortic valve, indicated to remain within the SoV throughout systole once generated in the healthy, native condition, varies across the different root-valve configurations of the experiment described in Chapter 4, leading to increased impingement of the central flow, generation of secondary counter-vortices, and alterations to the closing characteristics of the valve.

Implantation of a TAV within the aortic district results in changes to the flow dynamics of the region in comparison to the healthy native environment. The central flow is narrowed and displaced away from the sinus side root wall, and the sinus flow is significantly diminished, especially at the base of the sinus, heightening the risk of thrombosis due to flow stagnation, and providing an explanation for the increased levels of sub-clinical thrombosis and thrombosis related pathologies, such as stroke and silent ischemic events, that have been reported following TAV procedures[13–16]. If the TAV is rotated from an ideal commissure-upon-commissure alignment, this sinus flow is further reduced, and flow patterns in the vicinity of the native commissures become altered from the flow patterns observed in the healthy, physiological condition modelled in Chapter 4, becoming more oscillatory, raising concerns of lumen pathologies. However, the haemodynamic performance indicators, such as EOA and ΔP, of the valve are unaffected, most likely due to the presence of the native leaflets, which form a pseudo-cylindrical structure extending around and beyond the outflow of the TAV. Omitting a model of these native leaflets from an *in vitro* investigation of TAVs may lead to substantially different flow features within the mock root, including significant, non-physiological sensitivity to the rotational alignment of the bioprosthesis, suggesting that representing the native valve is essential in producing accurate haemodynamics, and an explicit requirement for

their presence should be including in the regulations for preclinical testing of TAVs.

Flow in the upper sinuses of the post-TAV implantation region is affected by the extent of flow to the CA, with diastolic flow in the upper NCA sinus (i.e. a sinus with no CA flow) 43 % lower than in the upper LCA sinus and 22 % lower than in the upper RCA sinus, indicating sinus flow could be under-estimated in studies omitting modelling of CA flow. The systolic vortical patterns observed in the central root are also affected by this coronary flow, which draws the associated vortex around the level of the STJ closer towards the chamber, possibly contributing to the increased washout of the CA sinuses. However, this coronary flow does not affect the flow in the lower sinuses, which remains extremely slow throughout the cycle in all 3 of the physiological sinuses, indicating risk of thrombosis and susceptibility of the endothelium to inflammation and damage, thus fulfilling two of the categories of Verchow's triad[84], and providing more explanation for the increased levels of thrombotic-associated pathologies following TAV implantation[13–16].

7.3 Recommendations for Future Work

The work presented in this thesis has provided information on the fluid dynamics of the aortic root, especially within the sinuses of Valsalva, before and after the implantation of a TAV bioprosthesis. Further work could build upon this work, whether by providing measurements that could not be taken using the *in vitro* methodologies employed here, or by further developing the bench top models.

Numerical models have been used to simulate the aortic region in previous reports in the literature, and, once validated, can yield information about the dynamics of the volume that are difficult or impossible to derive from *in vitro* or *in vivo* studies of the equivalent anatomy. For example, wall shear stress is particularly difficult to estimate using PIV, as the cross-correlation method used to derive the velocity vectors over a given cross-section results in biasing estimation of these values near walls, due to high velocity gradients and lower concentration of particles[272]. Computational simulation would enable accurate calculation of the wall shear stress, providing information on low or highly oscillating regions of the aortic lumen, associated with early stage

atherogenesis and plaque localisation[93,273]. Numerical models could also enable 3D analysis of the root, rather than being limited to the pseudo-2D laser sheet of the presented PIV technique, and alterations to the fluid and root properties, such as modelling the non-Newtonian response of blood to shear and the inclusion of various levels of compliance in the root wall, could be more easily incorporated into the simulation. Work towards this goal has been undertaken via the validation of a fluid-structure interaction model with the experimental data of the physiological configuration from Chapter 4 of this thesis, wherein a numerical model was designed to simulate as closely as possible the configuration from the PIV study, and velocity maps of the equivalent cross-section of the two investigations were compared[250]. Once validated, this computational construct was modified, introducing wall compliance, matching the viscosity of the blood at high shear, and removing the prosthesis frame from the simulation, and rerun. The removal of the prosthetic frame appeared to cause substantially altered systolic positioning of the active leaflets, as they moved further into the sinus chamber without the polymer scaffold inhibiting them.

Continuing with the idea of removing the presence of a non-physiological frame from a model of the physiological environment, the combined silicone root and valve, used in Chapter 6 to represent the native root and valve and described in Sections 3.4.1.4 and 3.5.2, is currently being developed to more closely represent the healthy native anatomy, and reproduce the associated haemodynamics. In TRIZ parlance, the unresolved contradiction of silicone leaflets that are too thick and/or stiff to reproduce the dynamics of the healthy aortic leaflets, as indicated by the PIV results presented in Figure 7-1, but simultaneously not durable enough to withstand the rigours of testing at physiological pressure and flow within the pulse duplicator requires an inventive solution. Novel blood analogue solutions, incorporating polyacrylamide, xanthan gum, dimethylsulfoxide, hyaluronic acid, and/or sucrose, have been indicated to more closely match the shear thinning properties of blood, as well as matching the RI (± 0.03) of the silicone used to model the aortic root[274]. If these chemicals cause no significant change to the mechanical characteristics of the active leaflets and are suitable for PIV analysis, use of one or more these solutions could provide more accurate fluid dynamic responses for data acquisition.

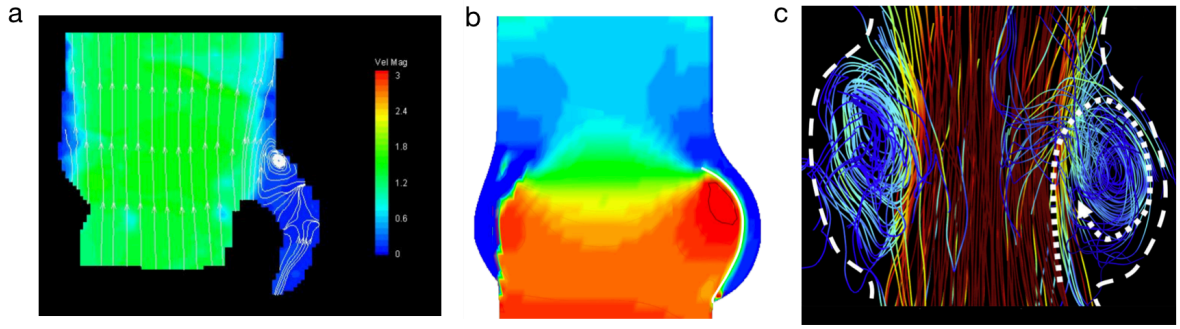

Figure 7-1: Cross-sectional images of native aortic district (a) PIV derived velocity field of a cross-section of the root at peak systole at an imposed cardiac output of 5 lpm at 100 mmHg mean aortic pressure. In comparison with (b) the computational cross-section[250], and (c) 4D-flow MRI in vivo *image, the* in vitro *leaflet does not extend as far into the sinus, is positioned too low, and does not reproduce the same vortical patterns.*

Study of the degree of sinus penetration into the sinus chambers by the native leaflets following TAV implantation, which may vary due to the degree of non-uniform leaflet calcification[270], could elucidate the extent of the effect this has upon the sinus flow speeds. A threshold of sinus penetration could then potentially be associated with increased flow stagnation and subsequent elevated risk of thrombosis, leading to improved therapeutic advice concerning anti-coagulation medication. Reversing this information pathway, the recording of TAV rotational alignment with their host native commissures in correlation with the cause of death of the patient could lend weight to the suggestion of increased thrombosis resulting from misalignment, or reveal other associated pathologies, which could then be specifically investigated within an *in vitro* experiment.

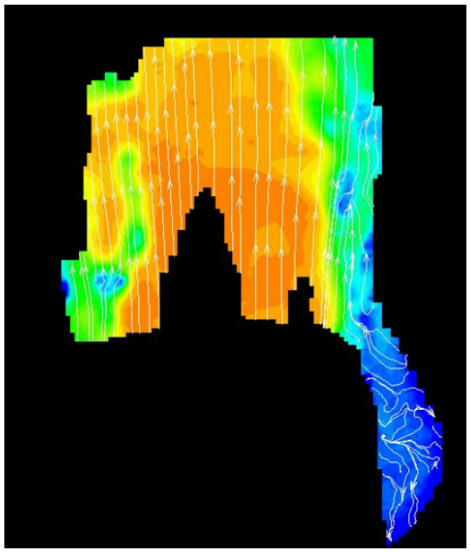

Figure 7-2: PIV velocity field of a CoreValve TAV device. Considerable artefacts resulting from the nitinol wire frame downstream of the valve are evident in the central

jet flow, and reflection from these metallic struts also reduces the quality of the data acquisition from the sinus region

As the TAV device investigated in this thesis was the Edwards SAPIEN XT prosthesis, it would be beneficial to also study a device representative of the other major TAV type used, the Medtronic CoreValve, previously described in Section 2.3.3.1.2. Preliminary PIV analysis of this technology has been hindered by the increased amount of metal struts and pericardial tissue incorporated into the design, which have caused increased out of plane reflection of the laser sheet, leading to central jet flow artefacts and reducing the quality of the data for the sinus region, as indicated in Figure 7-2, despite efforts such as dyeing the leaflet tissue black and coating the frame with a matt finish. Once these issues are resolved, comparison of the CoreValve data with the Edwards SAPIEN XT data presented in this thesis could provide improved therapeutic advice based on the prosthesis chosen for each patient, and inform future device design. Alternative methods of PIV analysis, such as time-resolved streak vectors or dye injection[72,243,275], could further elucidate the flow dynamics of the region, especially the paths and residence time of RBCs. Finally, the duration of the study of the effects of the chemicals investigated in the appendices could be extended, providing information on the storage or longer-term testing (i.e. more than 24-hours) of devices partially or fully made up of GA-fixed pericardium tissue, particularly glycerol, which, as discussed in Section 9.1.4, was indicated to affect the low stretch modulus of the pericardial tissue, albeit to an acceptable degree for the scope of these experiments. Exposure for extended periods of time (e.g. 6 months) to these testing fluids may eventually cause significant stiffening or loosening of the tissue, leading to substantially altered hydrodynamic responses. Additionally, the increased translucency observed after storage in 100 % glycerol may have beneficial uses, as long as the mechanical characteristics of the tissue are not significantly altered. The ability to see through the valve tissue during operation in the pulse duplicator could lead to PIV elucidation of the fluid velocity at the very centre of the valve during peak flow.

8 References

1. Nkomo VT, Gardin JM, Skelton TN, Gottdiener JS, Scott CG, Enriquez-Sarano M. Burden of valvular heart diseases: a population-based study. *Lancet*. 2006;368:1005–1011.
2. Waite L. Biofluid Mechanics in Cardiovascular Systems. McGraw-Hill; 2006.
3. Dweck MR, Boon NA, Newby DE. Calcific Aortic Stenosis: A Disease of the Valve and the Myocardium. *J Am Coll Cardiol*. 2012;60:1854–1863.
4. Otto CM, Lind BK, Kitzman DW, Gersh BJ, Siscovick DS. Association of aortic valve sclerosis with cardiovascular mortality and morbidity in the elderly. *N Engl J Med*. 1999;341:142–7.
5. Lindroos M, Kupari M, Heikkilä J, Tilvis R. Prevalence of aortic valve abnormalities in the elderly: An echocardiographic study of a random population sample. *J Am Coll Cardiol*. 1993;21:1220–1225.
6. Díez JG. Transcatheter aortic valve implantation (TAVI): the hype and the hope. *Tex Heart Inst J* [Internet]. 2013;40:298–301.
7. Padala M, Keeling WB, Guyton R a, Thourani VH. Innovations in therapies for heart valve disease. *Circ J*. 2011;75:1028–1041.
8. Sotiropoulos F, Le TB, Gilmanov A. Fluid Mechanics of Heart Valves and Their Replacements. *Annu Rev Fluid Mech*. 2016;48:259–283.
9. Head SJ, Çelik M, Kappetein AP. Mechanical versus bioprosthetic aortic valve replacement. *Eur Heart J*. 2017;38:2183–2191.
10. Horne A, Reineck E a., Hasan RK, Resar JR, Chacko M. Transcatheter aortic valve replacement: Historical perspectives, current evidence, and future directions. *Am Heart J* [Internet]. 2014;168:414–423.
11. Pollak PM, Mack MJ, Holmes DR. Quality, economics, and national guidelines for transcatheter aortic valve replacement. *Prog Cardiovasc Dis* [Internet]. 2014;56:610–618.
12. Padala M, Sarin EL, Willis P, Babaliaros V, Block P, Guyton RA, Thourani VH. An Engineering Review of Transcatheter Aortic Valve Technologies. *Cardiovasc Eng Technol*. 2010;1:77–87.
13. Rodes-Cabau J, Dumont E, Boone RH, Larose E, Bagur R, Gurvitch R, Bedard F, Doyle D, De Larochelliere R, Jayasuria C, Villeneuve J,

Marrero A, Cote M, Pibarot P, Webb JG. Cerebral embolism following transcatheter aortic valve implantation: Comparison of transfemoral and transapical approaches. *J Am Coll Cardiol*. 2011;57:18–28.

14. Kahlert P, Knipp SC, Schlamann M, Thielmann M, Al-Rashid F, Weber M, Johansson U, Wendt D, Jakob HG, Forsting M, Sack S, Erbel R, Eggebrecht H. Silent and apparent cerebral ischemia after percutaneous transfemoral aortic valve implantation: A diffusion-weighted magnetic resonance imaging study. *Circulation*. 2010;121:870–878.
15. Astarci P, Glineur D, Kefer J, D'Hoore W, Renkin J, Vanoverschelde JL, El Khoury G, Grandin C. Magnetic resonance imaging evaluation of cerebral embolization during percutaneous aortic valve implantation: Comparison of transfemoral and trans-apical approaches using Edwards Sapiens valve. *Eur J Cardio-thoracic Surg*. 2011;40:475–479.
16. Schaff H V. Transcatheter Aortic-Valve Implantation — At What Price ? *N Engl J Med*. 2011;364:2256–2258.
17. Lowe GDO. Virchow's Triad Revisited : Abnormal Flow. *Pathophysiol Haemost Thromb*. 2003;33:455–457.
18. Bellhouse BJ, Bellhouse FH. Mechanismn of Closure of the Aortic Valve. *Nature*. 1968;217:86–87.
19. Ming L, Zhen-huang K. Study of the Closing Mechanism of Natural Heart Valves. *Appl Math Mech*. 1986;7:955–964.
20. Peacock JA. An in vitro study of the onset of turbulence in the sinus of Valsalva. *Circ Res*. 1990;67:448–460.
21. Lim WL, Chew YT, Chew TC, Low HT. Pulsatile flow studies of a porcine bioprosthetic aortic valve in vitro: PIV measurements and shear-induced blood damage. *J Biomech*. 2001;34:1417–1427.
22. Yang GZ, Mohiaddin RH, Kilner PJ, Firmin DN. Vortical Flow Feature Recognition : A Topological Study of In Vivo Flow Patterns Using MR Velocity Mapping. *J Comput Assist Tomogr*. 1998;22:577–586.
23. Escobar Kvitting JP, Ebbers T, Wigström L, Engvall J, Olin CL, Bolger AF. Flow patterns in the aortic root and the aorta studied with time-resolved, 3-dimensional, phase-contrast magnetic resonance imaging: Implications for aortic valve-sparing surgery. *J Thorac Cardiovasc Surg*. 2004;127:1602–1607.

24. Markl M, Draney MT, Miller DC, Levin JM, Williamson EE, Pelc NJ, Liang DH, Herfkens RJ. Time-resolved three-dimensional magnetic resonance velocity mapping of aortic flow in healthy volunteers and patients after valve-sparing aortic root replacement. *J Thorac Cardiovasc Surg*. 2005;130:456–463.
25. Ranga A, Bouchot O, Mongrain R, Ugolini P, Cartier R. Computational simulations of the aortic valve validated by imaging data: evaluation of valve-sparing techniques. *Interact Cardiovasc Thorac Surg*. 2006;5:373–378.
26. Markl M, Kilner PJ, Ebbers T. Comprehensive 4D velocity mapping of the heart and great vessels by cardiovascular magnetic resonance. *J Cardiovasc Magn Reson* [Internet]. 2011;13:7–28.
27. Swanson WM, Clark RE. Aortic valve leaflet motion during systole. Numerical-graphical determination. *Circ Res*. 1973;32:42–48.
28. De Hart J. Numerical Analysis of a Three-Leaflet Aortic Valve Prosthesis Numerical Analysis of a Three-Leaflet Aortic Valve Prosthesis. 1997;
29. De Hart J, Peters GWM, Schreurs PJG, Baaijens FPT. A three-dimensional computational analysis of fluid-structure interaction in the aortic valve. *J Biomech*. 2003;36:103–112.
30. Korakianitis T, Shi Y. Numerical simulation of cardiovascular dynamics with healthy and diseased heart valves. *J Biomech*. 2006;39:1964–1982.
31. Katayama S, Umetani N, Sugiura S, Hisada T. The sinus of Valsalva relieves abnormal stress on aortic valve leaflets by facilitating smooth closure. *J Thorac Cardiovasc Surg* [Internet]. 2008;136:1528-1535.e1.
32. Leo HL, Dasi LP, Carberry J, Simon H a., Yoganathan AP. Fluid dynamic assessment of three polymeric heart valves using particle image velocimetry. *Ann Biomed Eng*. 2006;34:936–952.
33. Dasi LP, Simon H a., Sucosky P, Yoganathan AP. Fluid mechanics of artificial heart valves. *Clin Exp Pharmacol Physiol*. 2009;36:225–237.
34. Saikrishnan N, Yap C-H, Milligan NC, Vasilyev N V., Yoganathan AP. In Vitro Characterization of Bicuspid Aortic Valve Hemodynamics Using Particle Image Velocimetry. *Ann Biomed Eng*. 2012;40:1760–1775.
35. Ducci A, Tzamtzis S, Mullen MJ, Burriesci G. Hemodynamics in the Valsalva sinuses after transcatheter aortic valve implantation (TAVI). *J*

Heart Valve Dis. 2013;22:688–696.

36. Chandran KB, Rittgers SE, Yoganathan AP. Biofluid Mechanics - The Human Circulation. Second. CRC Press, Inc.; 2012.
37. Caro CG, Pedley TJ, Schroter RC, Seed WA. The Mechanics of Circulation. 2nd ed. Cambridge; 2012.
38. Hall J, Guyton A. Textbook of Medical Physiology. 11th ed. Philadelphia: Elsevier Saunders; 2006.
39. Krug JW, Rose G, Clifford GD, Oster J. ECG-based gating in ultra high field cardiovascular magnetic resonance using an independent component analysis approach. *J Cardiovasc Magn Reson*. 2013;15:1–13.
40. Rubenstein DA, Yin W, Frame MD. Biofluid mechanics. Elsevier; 2012.
41. Sutton JP, Ho SY, Anderson RH. The forgotten interleaflet triangles: A review of the surgical anatomy of the aortic valve. *Ann Thorac Surg*. 1995;59:419–427.
42. Yacoub MH, Kilner PJ, Birks EJ, Misfeld M. The aortic outflow and root: a tale of dynamism and crosstalk. *Ann Thorac Surg*. 1999;68:S37–S43.
43. Underwood MJ, Khoury G El, Deronck D, Glineur D, Dion R. The aortic root : structure , function , and surgical reconstruction. *Heart*. 2000;83:376–380.
44. Tamburino C, Ussia GP. Percutaneous Treatment of Left Side Cardiac Valves [Internet]. Springer; 2010.
45. Thubrikar MJ, Piepgrass WC, Shaner TW, Nolan SP. The design of the normal aortic valve. *Am Physiol Soc*. 1981;H795–H801.
46. Davis AE, Lewandowski AJ, Holloway CJ, Ntusi N a B, Banerjee R, Nethononda R, Pitcher A, Francis JM, Myerson SG, Leeson P, Donovan T, Neubauer S, Rider OJ. Observational study of regional aortic size referenced to body size: production of a cardiovascular magnetic resonance nomogram. *J Cardiovasc Magn Reson* [Internet]. 2014;16:9–17.
47. Vriz O, Aboyans V, D'Andrea A, Ferrara F, Acri E, Limongelli G, Della Corte A, Driussi C, Bettio M, Pluchinotta FR, Citro R, Russo MG, Isselbacher E, Bossone E. Normal Values of Aortic Root Dimensions in Healthy Adults. *Am J Cardiol* [Internet]. 2014;114:921–927.
48. Gripari P. Multimodality imaging assessment of the anatomy of the aortic

valve apparatus in TAVI patients. Implications for prosthesis sizing and paravalvular regurgitation. 2014;

49. Zalkind D, Kim M, Salcedo EE. A Framework for the Systematic Characterization of the Aortic Valve Complex by Real-Time Three Dimensional Echocardiography : Implications for Transcatheter Aortic Valve Replacement. In: Squeri A, editor. Hot Topics in Echocardiography. InTech; 2013. p. 119–138.
50. Silver MA, Roberts WC. Detailed anatomy of the normally functioning aortic valve in hearts of normal and increased weight. *Am J Cardiol*. 1985;55:454–461.
51. Piazza N, de Jaegere P, Schultz C, Becker AE, Serruys PW, Anderson RH. Anatomy of the aortic valvar complex and its implications for transcatheter implantation of the aortic valve. *Circ Cardiovasc Interv*. 2008;1:74–81.
52. Misfeld M, Sievers H-H. Heart valve macro- and microstructure. *Philos Trans R Soc B Biol Sci*. 2007;362:1421–1436.
53. Ho SY. Structure and anatomy of the aortic root. *Eur J Echocardiogr*. 2009;10:3–10.
54. Vesely I, Lozon a. Natural preload of aortic valve leaflet components during glutaraldehyde fixation: Effects on tissue mechanics. *J Biomech*. 1993;26:121–131.
55. Sacks MS, David Merryman W, Schmidt DE. On the biomechanics of heart valve function. *J Biomech*. 2009;42:1804–1824.
56. Stella JA, Liao J, Sacks MS. Time-dependent biaxial mechanical behavior of the aortic heart valve leaflet. *J Biomech*. 2007;40:3169–3177.
57. Schoen FJ. Mechanisms of Function and Disease of Natural and Replacement Heart Valves. *Annu Rev Pathol Mech Dis* [Internet]. 2012;7:161–183.
58. Paranya G, Vineberg S, Dvorin E, Kaushal S, Roth SJ, Rabkin E, Schoen FJ, Bischoff J. Aortic valve endothelial cells undergo transforming growth factor-beta-mediated and non-transforming growth factor-beta-mediated transdifferentiation in vitro. *Am J Pathol*. 2001;159:1335–43.
59. Keele KD. Leonardo da Vinci as Physiologist. *Postgrad Med J*. 1952;521–528.

60. Lim WL, Chew YT, Chew TC, Low HT. Steady flow velocity field and turbulent stress mappings downstream of a porcine bioprosthetic aortic valve in vitro. *Ann Biomed Eng*. 1997;25:86–95.
61. Higashidate M, Tamiya K, Beppu T, Imai Y. Regulation of the aortic valve opening: In vivo dynamic measurement of aortic valve orifice area. *J Thorac Cardiovasc Surg*. 1995;110:496–503.
62. Leyh RG, Schmidtke C, Sievers H, Yacoub MH. Opening and Closing Characteristics of the Aortic Valve. *Circulation*. 1999;100:2153–2161.
63. Baumgartner H, Hung J, Bermejo J, Chambers JB, Evangelista A, Griffin BP, Iung B, Otto CM, Pellikka PA, Quinones M, Maran G. Echocardiographic assessment of valve stenosis : EAE / ASE recommendations for clinical practice. *Eur J Echocardiogr*. 2008;1–25.
64. Reid K. The anatomy of the sinus of Valsalva. *Thorax*. 1970;25:79–85.
65. Reul H, Vahlbruch A, Giersiepen M, Schmitz-Rode T, Hirtz V, Effert S. The Geometry of the Aortic Root in Health , at Valve Disease and after Valve Replacement. *J Biomech*. 1990;23:181–191.
66. Leyh RG, Schmidtke C, Sievers HH, Yacoub MH. Opening and closing characteristics of the aortic valve after different types of valve-preserving surgery. *Circulation*. 1999;100:2153–2160.
67. Bellhouse BJ, Talbot L. Fluid mechanics of the aortic valve. *J Fluid Mech*. 1969;35:721–735.
68. Pisani G, Scaffa R, Ieropoli O, Dell'Amico EM, Maselli D, Morbiducci U, De Paulis R. Role of the sinuses of Valsalva on the opening of the aortic valve. *J Thorac Cardiovasc Surg* [Internet]. 2013;145:999–1003.
69. Peskin CS. the Fluid Dynamics of Computational Methods. *Ann Rev Fluid Mech*. 1982;14:235–259.
70. Knight J, Kurtcuoglu V, Muffy K, Marshall W, Stolzmann P, Desbiolles L, Seifert B, Poulikakos D, Alkadhi H. Ex vivo and in vivo coronary ostial locations in humans. *Surg Radiol Anat*. 2009;31:597–604.
71. Ben-Dor I, Malik R, Minha S, Goldstein S a., Wang Z, Magalhaes M a., Weissman G, Okubagzi PG, Torguson R, Lindsay J, Satler LF, Pichard AD, Waksman R. Coronary Blood Flow in Patients With Severe Aortic Stenosis Before and After Transcatheter Aortic Valve Implantation. *Am J Cardiol*. 2014;114:1264–1268.

72. Moore BL, Dasi LP. Coronary Flow Impacts Aortic Leaflet Mechanics and Aortic Sinus Hemodynamics. *Ann Biomed Eng*. 2015;43:2231–2241.
73. Stock S, Scharfschwerdt M, Meyer-Saraei R, Richardt D, Charitos EI, Sievers HH, Hanke T. In vitro coronary flow after transcatheter aortic valve-in-valve implantation: A comparison of 2 valves. *J Thorac Cardiovasc Surg* [Internet]. 2016;153:255–263.
74. Parimala Sirikonda SS. Measurement and location of coronary ostia. *Int J Biol Med Res* [Internet]. 2012;3:2489–2496.
75. Burriesci G, Marincola FC, Zervides C. Design of a novel polymeric heart valve. *J Med Eng Technol*. 2010;34:7–22.
76. Gorlin R, Gorlin SG. Hydraulic Formula for Calculation of the Area of the Stenotic Mitral Valve, Other Cardiac Valves, and Central Circulatory Shunts. I. *Am Heart J*. 1951;41:1–29.
77. Akins CW, Travis B, Yoganathan AP. Energy loss for evaluating heart valve performance. *J Thorac Cardiovasc Surg* [Internet]. 2008;136:820–833.
78. Saikrishnan N, Gupta S, Yoganathan AP. Hemodynamics of the Boston Scientific LotusTM Valve: An In Vitro Study. *Cardiovasc Eng Technol*. 2013;4:427–439.
79. Amindari A, Saltik L, Kirkkopru K, Yacoub M, Yalcin HC. Assessment of calcified aortic valve leaflet deformations and blood flow dynamics using fluid-structure interaction modeling. *Informatics Med Unlocked*. 2017;9:191–199.
80. Rahmani B, Tzamtzis S, Sheridan R, Mullen MJ, Yap J, Seifalian AM, Burriesci G. In Vitro Hydrodynamic Assessment of a New Transcatheter Heart Valve Concept (the TRISKELE). *J Cardiovasc Transl Res*. 2017;10:104–115.
81. Pop GAM, Duncker DJ, Gardien M, Versluis P, Hasan D, Slager CJ. The cinical significance of whole blood viscosity in (cardio) vascular medicine. *Netherlands Hear J*. 2002;10:512–516.
82. Baskurt OK, Meiselman HJ. Blood Rheology and Hemodynamics. *Semin Thromb Hemost*. 2003;29:435–450.
83. Wootton DM, Ku DN. Fluid Mechanics of Vascular Systems, Diseases, and Thrombosis. *Annu Rev Biomed Eng*. 1999;1:299–329.

84. Litvinov RI, Weisel JW. Role of red blood cells in haemostasis and thrombosis. *ISBT Sci Ser* [Internet]. 2017;12:176–183.
85. Hope MD, Sedlic T, Dyverfeldt P. Cardiothoracic magnetic resonance flow imaging. *J Thorac Imaging*. 2013;28:217–30.
86. Bluestein D, Chandran KB, Manning K. B. Towards Non-thrombogenic Performance of Blood Recirculation Devices. *Ann Biomed Eng*. 2010;38:1236–1256.
87. Morbiducci U, Ponzini R, Nobili M, Massai D, Montevecchi FM, Bluestein D, Redaelli A. Blood damage safety of prosthetic heart valves. Shear-induced platelet activation and local flow dynamics: A fluid-structure interaction approach. *J Biomech*. 2009;42:1952–1960.
88. Corbett SC, Ajdari A, Coskun AU, N-Hashemi H. In vitro and computational thrombosis on artificial surfaces with shear stress. *Artif Organs*. 2010;34:561–569.
89. Leverett LB, Hellums JD, Alfrey CP, Lynch EC. Red Blood Cell Damage by Shear Stress. *Biophys J*. 1972;12:257–273.
90. Yen JH, Chen SF, Chern MK, Lu PC. The effect of turbulent viscous shear stress on red blood cell hemolysis. *J Artif Organs*. 2014;17:178–185.
91. Heemskerk JWM, Bevers EM, Lindhout T. Platelet activation and blood coagulation. *Thromb Haemost*. 2002;88:186–193.
92. Corbett SC, Ajdari A, Coskun AU, Nayeb-Hashemi H. Effect of pulsatile blood flow on thrombosis potential with a step wall transition. *ASAIO J*. 2010;56:290–295.
93. Malek AM, Alper SL, Izumo S. Hemodynamic Shear Stress and Its Role in Atherosclerosis. *J Am Med Assoc* [Internet]. 1999;282:2035–42.
94. Makkar RR, Fontana G, Jilaihawi H, Chakravarty T, Kofoed KF, De Backer O, Asch FM, Ruiz CE, Olsen NT, Trento A, Friedman J, Berman D, Cheng W, Kashif M, Jelnin V, Kliger CA, Guo H, Pichard AD, Weissman NJ, Kapadia S, Manasse E, Bhatt DL, Leon MB, Søndergaard L. Possible Subclinical Leaflet Thrombosis in Bioprosthetic Aortic Valves. *N Engl J Med*. 2015;373:2015–2024.
95. Bellhouse BJ, Bellhouse FH, Reid KG. Fluid mechanics of the aortic root with application to coronary flow. *Nature*. 1968;219:1059–1061.

96. Van Steenhoven AA, Van Dongen MEH. Model studies of the closing behaviour of the aortic valve. *J Fluid Mech*. 1978;90:21–32.
97. Ducci A, Pirisi F, Tzamtzis S, Burriesci G. Transcatheter aortic valves produce unphysiological flows which may contribute to thromboembolic events: An in-vitro study. *J Biomech*. 2016;49:4080–4089.
98. Balachandran K, Sucosky P, Yoganathan AP. Hemodynamics and mechanobiology of aortic valve inflammation and calcification. *Int J Inflam* [Internet]. 2011;2011:263870.
99. Fortini S, Espa S, Querzoli G, Cenedese A. Turbulence investigation in a laboratory model of the ascending aorta. *J Turbul*. 2015;16:208–224.
100. Sacks MS, Yoganathan AP. Heart valve function: a biomechanical perspective. *Philos Trans R Soc B Biol Sci*. 2007;362:1369–1391.
101. Barker AJ, Markl M. Editorial The role of hemodynamics in bicuspid aortic valve disease. *Eur J Cardio-thoracic Surg*. 2011;39:805–806.
102. Yap CH, Saikrishnan N, Tamilselvan G, Yoganathan AP. Experimental measurement of dynamic fluid shear stress on the aortic surface of the aortic valve leaflet. *Biomech Model Mechanobiol*. 2012;11:171–182.
103. Fukui T, Orinishi K. Influence of Vortices in the Sinus of Valsalva on Local Wall Shear Stress Distribution. *Int J Life Sci Med Res*. 2013;3:94–102.
104. Dumont K. Experimental and numerical modeling of heart valve dynamics. 2005;
105. Nobari S, Mongrain R, Gaillard E, Leask R, Cartier R. Therapeutic vascular compliance change may cause significant variation in coronary perfusion: a numerical study. *Comput Math Methods Med* [Internet]. 2012;2012:791686.
106. Maleki H. Structural and Fluid-Structure Interaction Analysis of Stenotic Aortic Valves : Application to Percutaneous Aortic Valve Replacement. 2010;
107. Toninato R, Salmon J, Susin FM, Ducci A, Burriesci G. Physiological vortices in the sinuses of Valsalva: an in vitro approach for bio-prosthetic valves. *J Biomech*. 2016;49:2635–2643.
108. Sakamoto S, Takahashi S, Coskun AU, Papafaklis MI, Takahashi A, Saito S, Stone PH, Feldman CL. Relation of distribution of coronary blood flow volume to coronary artery dominance. *Am J Cardiol*. 2013;111:1420–

1424.

109. Benchimol A, Stegall HF, Gartlan JL. New Method to Measure Phasic Coronary Blood Velocity in Man. *Am Heart J*. 1971;81:93–101.
110. Ganz W, Tamura K, Marcus HS, Donoso R, Yoshida S, Swan HJC. Measurement of Coronary Sinus Blood Flow by Continuous Thermodilution in Man. *Circulation*. 1971;44:181–195.
111. Spiller P, Schmiel FK, Pölitz B, Block M, Fermor U, Hackbarth W, Jehle J, Körfer R, Pannek H. Measurement of systolic and diastolic flow rates in the coronary artery system by x-ray densitometry. *Circulation*. 1983;68:337–347.
112. Hundley WG, Lange RA, Clarke GD, Meshack BM, Payne J, Landau C, McColl R, Sayad DE, Willett DL, Willard JE, Hillis LD, Peshock RM. Assessment of coronary arterial flow and flow reserve in humans with magnetic resonance imaging. *Circulation* [Internet]. 1996;93:1502–8.
113. Johnston BM, Johnston PR, Corney S, Kilpatrick D. Non-Newtonian blood flow in human right coronary arteries: Steady state simulations. *J Biomech*. 2004;37:709–720.
114. Johnson K, Sharma P, Oshinski J. Coronary artery flow measurement using navigator echo gated phase contrast magnetic resonance velocity mapping at 3.0 T. *J Biomech*. 2008;41:595–602.
115. Soulis J V., Fytanidis DK, Seralidou K V., Giannoglou GD. Wall shear stress oscillation and its gradient in the normal left coronary artery tree bifurcations. *Hippokratia*. 2014;18:12–16.
116. De Paulis R, Tomai F, Bertoldo F, Ghini AS, Scaffa R, Nardi P, Chiariello L. Coronary flow characteristics after a Bentall procedure with or without sinuses of Valsalva. *Eur J Cardio-thoracic Surg*. 2004;26:66–72.
117. Zeng D, Ding Z, Friedman MH, Ross Ethier C. Effects of cardiac motion on right coronary artery hemodynamics. *Ann Biomed Eng*. 2003;31:420–429.
118. Jung J, Hassanein A, Lyczkowski RW. Hemodynamic computation using multiphase flow dynamics in a right coronary artery. *Ann Biomed Eng*. 2006;34:393–407.
119. Jung J, Lyczkowski RW, Panchal CB, Hassanein A. Multiphase hemodynamic simulation of pulsatile flow in a coronary artery. *J Biomech*.

2006;39:2064–2073.

120. Freeman R V., Otto CM. Spectrum of calcific aortic valve disease: Pathogenesis, disease progression, and treatment strategies. *Circulation*. 2005;111:3316–3326.
121. Yap CH, Kim H-S, Balachandran K, Weiler M, Haj-Ali R, Yoganathan AP. Dynamic deformation characteristics of porcine aortic valve leaflet under normal and hypertensive conditions. *Am J …*. 2010;395–405.
122. Sugimoto H, Sacks MS. Effects of Leaflet Stiffness on In Vitro Dynamic Bioprosthetic Heart Valve Leaflet Shape. *Cardiovasc Eng Technol*. 2013;4:2–15.
123. Auricchio F, Conti M, Morganti S, Reali A. Simulation of transcatheter aortic valve implantation: a patient-specific finite element approach. *Comput Methods Biomech Biomed Engin* [Internet]. 2014;17:1347–1357.
124. Cohn D, Younes H, Milgarter E, Uretzky G. Mechanical behaviour of isolated pericardium: species, isotropy, strain rate and collagenase effect on pericardial tissue. *Clin Mater*. 1987;2:115–124.
125. Hasan A, Ragaert K, Swieszkowski W, Selimović Š, Paul A, Camci-Unal G, Mofrad MRK, Khademhosseini A. Biomechanical properties of native and tissue engineered heart valve constructs. *J Biomech*. 2014;47:1949–1963.
126. Thubrikar MJ. The Aortic Valve. CRC Press, Inc.; 1990.
127. Becker AE. Surgical and Pathological Anatomy of the Aortic Valve and Root. *Oper Tech Card Thorac Surg*. 1996;1:3–14.
128. Saikrishnan N, Kumar G, Sawaya FJ, Lerakis S, Yoganathan AP. Accurate assessment of aortic stenosis: A review of diagnostic modalities and hemodynamics. *Circulation*. 2014;129:244–253.
129. Bäck M, Gasser TC, Michel JB, Caligiuri G. Biomechanical factors in the biology of aortic wall and aortic valve diseases. *Cardiovasc Res*. 2013;99:232–241.
130. Rajamannan NM, Evans FJ, Aikawa E, Grande-Allen KJ, Demer LL, Heistad DD, Simmons CA, Masters KS, Mathieu P, O'Brien KD, Schoen FJ, Towler DA, Yoganathan AP, Otto CM. Calcific Aortic Valve Disease: Not Simply a Degenerative Process: A Review and Agenda for Research From the National Heart and Lung and Blood Institute Aortic Stenosis

Working Group * Executive Summary: Calcific Aortic Valve Disease - 2011 Update. *Circulation*. 2011;124:1783–1791.

131. Otto CM. Calcification of bicuspid aortic valves. *Heart*. 2002;88:321–322.
132. Ge L, Sotiropoulos F. Direction and Magnitude of Blood Flow Shear Stresses on the Leaflets of Aortic Valves: Is There a Link With Valve Calcification? *J Biomech Eng*. 2009;132:014505.
133. Abbas AE, Franey LM, Goldstein J, Lester S. Aortic valve stenosis: To the gradient and beyond - The mismatch between area and gradient severity. *J Interv Cardiol*. 2013;26:183–194.
134. Pandian NG, Ramamurthi A, Applebaum S. Role of Echocardiography in Aortic Stenosis. *Prog Cardiovasc Dis*. 2014;57:47–54.
135. Blais C, Burwash IG, Mundigler G, Dumesnil JG, Loho N, Rader F, Baumgartner H, Beanlands RS, Chayer B, Kadem L, Garcia D, Durand LG, Pibarot P. Projected valve area at normal flow rate improves the assessment of stenosis severity in patients with low-flow, low-gradient aortic stenosis: The multicenter TOPAS (Truly or Pseudo-Severe Aortic Stenosis) study. *Circulation*. 2006;113:711–721.
136. Thaden JJ, Nkomo VT, Enriquez-Sarano M. The Global Burden of Aortic Stenosis. *Prog Cardiovasc Dis* [Internet]. 2014;56:565–571.
137. Ostadfar A. Biofluid Mechanics - Principles and Applications. 1st ed. Academic Press; 2016.
138. Yoganathan AP. Fluid mechanics of aortic stenosis. *Eur Heart J*. 1988;9:13–17.
139. Garcia D, Camici PG, Durand LG, Rajappan K, Gaillard E, Rimoldi OE, Pibarot P. Impairment of coronary flow reserve in aortic stenosis. *J Appl Physiol* [Internet]. 2009;106:113.
140. Yoganathan AP, He Z, Casey Jones S. Fluid mechanics of heart valves. *Annu Rev Biomed Eng*. 2004;6:331–362.
141. Nataf P, Lansac E. Dilation of the thoracic aorta: medical and surgical management. *Heart*. 2006;92:1345–1352.
142. Son M, Chang S-A, Kwak J, Lim H, Park S-J, Choi J-O, Lee S-C, Park S, Kim D-K, Oh JK. Comparative measurement of aortic root by transthoracic echocardiography in normal Korean population based on two different guidelines. *Cardiovasc Ultrasound* [Internet]. 2013;11:28–35.

143. Cozijnsen L, Braam RL, Waalewijn RA, Schepens MAAM, Loeys BL, Van Oosterhout MFM, Barge-Schaapveld DQCM, Mulder BJM. What is new in dilatation of the ascending aorta?: Review of current literature and practical advice for the cardiologist. *Circulation*. 2011;123:924–928.
144. Wilton E, Jahangiri M. Post-stenotic aortic dilatation. *J Cardiothorac Surg*. 2006;1:7.
145. Querzoli G, Fortini S, Espa S, Costantini M, Sorgini F. Fluid dynamics of aortic root dilation in Marfan syndrome. *J Biomech*. 2014;47:3120–3128.
146. Grande-Allen KJ, Cochran RP, Reinhall PG, Kunzelman KS. Re-creation of sinuses is important for sparing the aortic valve: a finite element study. *J Thorac Cardiovasc Surg*. 2000;119:753–763.
147. Holman BL, Adams DF, Jewitt D, Eldh P, Idoine J, Cohn PF, Gorlin R, Adelstein SJ. Measuring Regional Myocardial Blood Flow with 133Xe and the Anger Camera. *Nucl Med*. 1974;112:99–107.
148. Borazjani I, Ge L, Sotiropoulos F. High-Resolution Fluid-Structure Interaction Simulations of Flow Throiugh a Bi-Leaflet Mechanical Heart Valve in an Anatomic Aorta. *Ann Biomed Eng*. 2010;February:326–344.
149. Butany J, Ahluwalia MS, Fayet C, Munroe C, Blit P, Ahn C. Hufnagel valve - The first prosthetic mechanical valve. *Cardiovasc Pathol*. 2002;11:351–353.
150. Aslam AK, Aslam AF, Vasavada BC, Khan I a. Prosthetic heart valves: types and echocardiographic evaluation. *Int J Cardiol*. 2007;122:99–110.
151. Mohammadi H, Mequanint K. Prosthetic aortic heart valves: Modeling and design. *Med Eng Phys*. 2011;33:131–147.
152. Baudet EM, Puel V, McBride JT, Grimaud J-P, Roques F, Clerc F, Roques X, Laborde N. Surgery for Acquired Heart Disease: Long-term Results of Valve Replacement with the St. Jude Medical Prosthesis. *J Thorac Cardiovasc Surg*. 1995;109:858–870.
153. van Geldorp MWA, Eric Jamieson WR, Kappetein AP, Ye J, Fradet GJ, Eijkemans MJC, Grunkemeier GL, Bogers AJJC, Takkenberg JJM. Patient outcome after aortic valve replacement with a mechanical or biological prosthesis: Weighing lifetime anticoagulant-related event risk against reoperation risk. *J Thorac Cardiovasc Surg*. 2009;137:881–886.
154. Vahanian A, Alfieri O, Andreotti F, Antunes MJ, Bar??n-Esquivias G,

Baumgartner H, Borger MA, Carrel TP, De Bonis M, Evangelista A, Falk V, Iung B, Lancellotti P, Pierard L, Price S, Sch??fers HJ, Schuler G, Stepinska J, Swedberg K, Takkenberg J, Von Oppell UO, Windecker S, Zamorano JL, Zembala M, Bax JJ, Ceconi C, Dean V, Deaton C, Fagard R, Funck-Brentano C, Hasdai D, Hoes A, Kirchhof P, Knuuti J, Kolh P, McDonagh T, Moulin C, Popescu BA, Reiner ??eljko, Sechtem U, Sirnes PA, Tendera M, Torbicki A, Von Segesser L, Badano LP, Bunc M, Claeys MJ, Drinkovic N, Filippatos G, Habib G, Pieter Kappetein A, Kassab R, Lip GYH, Moat N, Nickenig G, Otto CM, Pepper J, Piazza N, Pieper PG, Rosenhek R, Shuka N, Schwammenthal E, Schwitter J, Mas PT, Trindade PT, Walther T. Guidelines on the management of valvular heart disease (version 2012). *Eur Heart J*. 2012;33:2451–2496.

155. Leo H-L, Simon H a, Dasi LP, Yoganathan AP. Effect of hinge gap width on the microflow structures in 27-mm bileaflet mechanical heart valves. *J Heart Valve Dis*. 2006;15:800–8.
156. Dasi LP, Ge L, Simon AH, Sotiropoulos F, Yoganathan PA. Vorticity dynamics of a bileaflet mechanical heart valve in an axisymmetric aorta. *Phys Fluids*. 2007;19.
157. Johansen P. Mechanical heart valve cavitation. *Expert Rev Med Devices*. 2004;1:95–104.
158. Daebritz SH, Sachweh JS, Hermanns B, Fausten B, Franke A, Groetzner J, Klosterhalfen B, Mesmer BJ. Introduction of a Flexible Polymeric Heart Valve Prosthesis With Special Design for Mitral Position. *Circulation*. 2003;108:134II--139.
159. Ghanbari H, Viatge H, Kidane AG, Burriesci G, Tavakoli M, Seifalian AM. Polymeric heart valves: new materials, emerging hopes. *Trends Biotechnol*. 2009;27:359–367.
160. Dahm M, Husmann M, Mayer E. Relevance of immunologic reactions failure of bioprosthetic heart valves for tissue. *Ann Thorac Surg*. 1995;60:S348--52.
161. Kobayashi J. Stentless aortic valve replacement: An update. *Vasc Health Risk Manag*. 2011;7:345–351.
162. Ott DA, Coelho AT, Cooley DA, Reul GJ. Ionescu-Shiley pericardial xenograft valve: Hemodynamic evaluation and early clinical follow-up of

326 patients. *Cardiovasc Dis*. 1980;7:137–148.

163. Schoen FJ, Fernandez J, Gonzalez-Lavin L, Cernaianu a. Causes of failure and pathologic findings in surgically removed Ionescu-Shiley standard bovine pericardial heart valve bioprostheses: emphasis on progressive structural deterioration. *Circulation*. 1987;76:618–627.
164. Fiore A, Cooley DA, Grande AM, Vigan M, Angelini P. Unusual 25-year durability of an Ionescu-Shiley pericardial bioprosthesis. *Ann Thorac Surg*. 2011;91:e52–e53.
165. Singhal P, Luk A, Butany J. Bioprosthetic Heart Valves: Impact of Implantation on Biomaterials. *ISRN Biomater*. 2013;2013:1–14.
166. Capelli C, Corsini C, Biscarini D, Ruffini F, Migliavacca F, Kocher A, Laufer G, Taylor AM, Schievano S, Andreas M, Burriesci G, Rath C. Pledget-Armed Sutures Affect the Haemodynamic Performance of Biologic Aortic Valve Substitutes: A Preliminary Experimental and Computational Study. *Cardiovasc Eng Technol*. 2017;8:17–29.
167. Hatoum H, Moore BL, Maureira P, Dollery J, Crestanello JA, Dasi LP. Aortic sinus flow stasis likely in valve-in-valve transcatheter aortic valve implantation. *J Thorac Cardiovasc Surg* [Internet]. 2017;154:32-43.e1.
168. Bourantas C V., Serruys PW. Evolution of transcatheter aortic valve replacement. *Circ Res*. 2014;114:1037–1051.
169. Cribier A, Eltchaninoff H, Bash A, Borenstein N, Tron C, Bauer F, Derumeaux G, Anselme F, Laborde F, Leon MB. Percutaneous transcatheter implantation of an aortic valve prosthesis for calcific aortic stenosis: First human case description. *Circulation*. 2002;106:3006–3008.
170. Zareian R, Tseng J-C, Fraser R, Meganck J, Kilduff M, Sarraf M, Dvir D, Kheradvar A. Effect of stent crimping on calcification of transcatheter aortic valves. *Interact Cardiovasc Thorac Surg*. 2019;1–10.
171. Vahidkhah K, Javani S, Abbasi M, Azadani PN, Tandar A, Dvir D, Azadani AN. Blood Stasis on Transcatheter Valve Leaflets and Implications for Valve-in-Valve Leaflet Thrombosis. *Ann Thorac Surg* [Internet]. 2017;104:751–759.
172. Webb JG, Wood DA. Current status of transcatheter aortic valve replacement. *J Am Coll Cardiol* [Internet]. 2012;60:483–492.
173. Walther T, Kempfert J. Transapical vs transfemoral aortic valve

implantation: Which approach for which patient, from a surgeon's standpoint. *Ann Cardiothorac Surg*. 2012;1:216–219.

174. Rodes-Cabau J, Webb JG, Cheung A, Ye J, Dumont E, Feindel CM, Osten M, Natarajan MK, Velianou JL, Martucci G, DeVarennes B, Chisholm R, Peterson MD, Lichtenstein S V., Nietlispach F, Doyle D, DeLarochelliere R, Teoh K, Chu V, Dancea A, Lachapelle K, Cheema A, Latter D, Horlick E. Transcatheter Aortic Valve Implantation for the Treatment of Severe Symptomatic Aortic Stenosis in Patients at Very High or Prohibitive Surgical Risk. Acute and Late Outcomes of the Multicenter Canadian Experience. *J Am Coll Cardiol*. 2010;55:1080–1090.
175. FDA Expands CoreValve TAVR Valve Use for Intermediate Risk Patients. *Diagnostic Interv Cardiol*. 2017;
176. Leon MB, Gada H, Fontana GP. Challenges and Future Opportunities for Transcatheter Aortic Valve Therapy. *Prog Cardiovasc Dis* [Internet]. 2014;56:635–645.
177. Xuan Y, Krishnan K, Ye J, Dvir D, Guccione JM, Ge L, Tseng EE. Stent and Leaflet Stresses in 29-mm Second-Generation Balloon-Expandable Transcatheter Aortic Valve. *Ann Thorac Surg* [Internet]. 2017;104:773–781.
178. Litzler P-Y, Cribier A, Zajarias A, Comte D, Eltchaninoff H, Tron C, Haas-Hubscher C, Bessou J-P. Surgical aortic valve replacement after percutaneous aortic valve implantation: what have we learned? *J Thorac Cardiovasc Surg*. 2008;136:697–701.
179. Ludman PF, Moat N, De Belder MA, Blackman DJ, Duncan A, Banya W, MacCarthy PA, Cunningham D, Wendler O, Marlee D, Hildick-Smith D, Young CP, Kovac J, Uren NG, Spyt T, Trivedi U, Howell J, Gray H, National Institute for Cardiovascular Outcomes Research. Transcatheter aortic valve implantation in the United Kingdom: Temporal trends, predictors of outcome, and 6-year follow-up: A report from the UK transcatheter aortic valve implantation (TAVI) registry, 2007 to 2012. *Circulation*. 2015;131:1181–1190.
180. D'Errigo P, Barbanti M, Ranucci M, Onorati F, Covello RD, Rosato S, Tamburino C, Santini F, Santoro G, Seccareccia F. Transcatheter aortic

valve implantation versus surgical aortic valve replacement for severe aortic stenosis: Results from an intermediate risk propensity-matched population of the Italian OBSERVANT study. *Int J Cardiol* [Internet]. 2013;167:1945–1952.

181. Clavel MA, Webb JG, Pibarot P, Altwegg L, Dumont E, Thompson C, De Larochellière R, Doyle D, Masson JB, Bergeron S, Bertrand OF, Rodés-Cabau J. Comparison of the Hemodynamic Performance of Percutaneous and Surgical Bioprostheses for the Treatment of Severe Aortic Stenosis. *J Am Coll Cardiol*. 2009;53:1883–1891.
182. Kuetting M, Sedaghat A, Utzenrath M, Sinning JM, Schmitz C, Roggenkamp J, Werner N, Schmitz-Rode T, Steinseifer U. In vitro assessment of the influence of aortic annulus ovality on the hydrodynamic performance of self-expanding transcatheter heart valve prostheses. *J Biomech* [Internet]. 2014;47:957–965.
183. Tang GHL, Lansman SL, Cohen M, Spielvogel D, Cuomo L, Ahmad H, Dutta T. Transcatheter Aortic Valve Replacement: Current Developments, Ongoing Issues, Future Outlook. *Cardiol Rev*. 2013;21:2944–2948.
184. Stuhle S, Wendt D, Houl G, Wendt H, Schlamann M, Thielmann M, Jakob H, Kowalczyk W. In-vitro investigation of the hemodynamics of the Edwards Sapien transcatheter heart valve. *J Hear Valve Dis*. 2011;20:53–63.
185. Groves EM, Falahatpisheh A, Su JL, Kheradvar A. The Effects of Positioning of Transcatheter Aortic Valve on Fluid Dynamics of the Aortic Root. *ASAIO J*. 2014;60:545–552.
186. Gunning PS, Saikrishnan N, Mcnamara LM, Yoganathan AP. An in vitro evaluation of the impact of eccentric deployment on transcatheter aortic valve hemodynamics. *Ann Biomed Eng*. 2014;42:1195–1206.
187. Tseng EE, Wisneski A, Azadani AN, Ge L. Engineering perspective on transcatheter aortic valve implantation. *Interv Cardiol* [Internet]. 2013;5:53–70.
188. Azadani AN, Jaussaud N, Matthews PB, Ge L, Guy TS, Chuter T a M, Tseng EE. Energy loss due to paravalvular leak with transcatheter aortic valve implantation. *Ann Thorac Surg*. 2009;88:1857–1863.
189. Vahl TP, Kodali SK, Leon MB. Transcatheter Aortic Valve Replacement

2016 - A Modern-Day “Through the Looking-Glass” Adventure. *J Am Coll Cardiol* [Internet]. 2016;67:1472–1487.

190. Fishbein GA, Schoen FJ, Fishbein MC. Transcatheter aortic valve implantation: Status and challenges. *Cardiovasc Pathol* [Internet]. 2014;23:65–70.
191. Midha PA, Raghav V, Okafor I, Yoganathan AP. The Effect of Valve-in-Valve Implantation Height on Sinus Flow. *Ann Biomed Eng*. 2017;45:405–412.
192. Chakravarty T, Søndergaard L, Friedman J, De Backer O, Berman D, Kofoed KF, Jilaihawi H, Shiota T, Abramowitz Y, Jørgensen TH, Rami T, Israr S, Fontana G, de Knegt M, Fuchs A, Lyden P, Trento A, Bhatt DL, Leon MB, Makkar RR, Ramzy D, Cheng W, Siegel RJ, Thomson LM, Mangat G, Hariri B, Sawaya FJ, Iversen HK. Subclinical leaflet thrombosis in surgical and transcatheter bioprosthetic aortic valves: an observational study. *Lancet*. 2017;389:2383–2392.
193. Kopanidis A, Pantos I, Alexopoulos N, Theodorakakos A, Efstathopoulos E, Katritsis D. Aortic flow patterns after simulated implantation of transcatheter aortic valves. *Hell J Cardiol*. 2015;56:418–428.
194. Young E, Chen JF, Dong O, Gao S, Massiello A, Fukamachi K. Transcatheter heart valve with variable geometric configuration: In vitro evaluation. *Artif Organs*. 2011;35:1151–1159.
195. Schultz CJ, Weustink A, Piazza N, Otten A, Mollet N, Krestin G, van Geuns RJ, de Feyter P, Serruys PWJ, de Jaegere P. Geometry and Degree of Apposition of the CoreValve ReValving System With Multislice Computed Tomography After Implantation in Patients With Aortic Stenosis. *J Am Coll Cardiol*. 2009;54:911–918.
196. Midha PA, Raghav V, Condado JF, Okafor IU, Lerakis S, Thourani VH, Babaliaros V, Yoganathan AP. Valve Type, Size, and Deployment Location Affect Hemodynamics in an In Vitro Valve-in-Valve Model. *JACC Cardiovasc Interv*. 2016;9:1618–1628.
197. Grube E, Buellesfeld L, Mueller R, Sauren B, Zickmann B, Nair D, Beucher H, Felderhoff T, Iversen S, Gerckens U. Progress and current status of percutaneous aortic valve replacement: results of three device generations of the CoreValve Revalving system. *Circ Cardiovasc Interv*.

2008;1:167–175.

198. Rubín JM, Avanzas P, Del Valle R, Renilla A, Ríos E, Calvo D, Lozano I, Anguera I, Díaz-Molina B, Cequier A, De La Tassa CM. Atrioventricular conduction disturbance characterization in transcatheter aortic valve implantation with the corevalve prosthesis. *Circ Cardiovasc Interv*. 2011;4:280–286.
199. van der Boon RM, Nuis R-J, Van Mieghem NM, Jordaens L, Rodés-Cabau J, van Domburg RT, Serruys PW, Anderson RH, de Jaegere PPT. New conduction abnormalities after TAVI--frequency and causes. *Nat Rev Cardiol*. 2012;9:454–63.
200. Lenders GD, Collas V, Hernandez JM, Legrand V, Danenberg HD, den Heijer P, Rodrigus IE, Paelinck BP, Vrints CJ, Bosmans JM. Depth of valve implantation, conduction disturbances and pacemaker implantation with CoreValve and CoreValve Accutrak system for Transcatheter Aortic Valve Implantation, a multi-center study. *Int J Cardiol* [Internet]. 2014;176:771–775.
201. Ducci A, Tzamtzis S, Mullen MJ, Burriesci G. Phase-resolved velocity measurements in the Valsalva sinus downstream of a Transcatheter Aortic Valve. In: 16th Int Symp on Applications of Laser Techniques to Fluid Mechanics. 2012. p. 9-12 July.
202. Saikrishnan N, Yoganathan A. Transcatheter Valve Implantation Can Alter the Fluid Flow Fields in the Aortic Sinuses and Ascending Aorta: an in Vitro Study. *J Am Coll Cardiol* [Internet]. 2013;61:E1957.
203. Kumar G, Raghav V, Lerakis S, Yoganathan AP. High Transcatheter Valve Replacement May Reduce Washout in the Aortic Sinuses: an In-Vitro Study. *J Heart Valve Dis* [Internet]. 2015;24:22–9.
204. Kapadia S, Tuzcu EM, Svensson LG. Anatomy and Flow Characteristics of Neosinus: Important Consideration for Thrombosis of Transcatheter Aortic Valves. *Circulation*. 2017;136:1610–1612.
205. Córdoba-Soriano JG, Puri R, Amat-Santos I, Ribeiro HB, Abdul-Jawad Altisent O, del Trigo M, Paradis JM, Dumont E, Urena M, Rodés-Cabau J. Valve thrombosis following transcatheter aortic valve implantation: a systematic review. *Rev Esp Cardiol (Engl Ed)*. 2015;68:198–204.
206. De Marchena E, Mesa J, Pomenti S, Marin Y Kall C, Marincic X, Yahagi

K, Ladich E, Kutz R, Aga Y, Ragosta M, Chawla A, Ring ME, Virmani R. Thrombus formation following transcatheter aortic valve replacement. *JACC Cardiovasc Interv* [Internet]. 2015;8:728–739.

207. Trantalis G, Toutouzas K, Latsios G, Synetos A, Brili S, Logitsi D, Penesopoulou V, Tousoulis D. TAVR and Thrombosis. *JACC Cardiovasc Imaging*. 2017;10:86–87.
208. Sirois E, Wang Q, Sun W. Fluid Simulation of a Transcatheter Aortic Valve Deployment into a Patient-Specific Aortic Root. *Cardiovasc Eng Technol*. 2011;2:186–195.
209. Piazza N, Onuma Y, Jesserun E, Kint PP, Maugenest AM, Anderson RH, de Jaegere PPT, Serruys PW. Early and Persistent Intraventricular Conduction Abnormalities and Requirements for Pacemaking After Percutaneous Replacement of the Aortic Valve. *JACC Cardiovasc Interv*. 2008;1:310–316.
210. Lerakis S, Hayek SS, Douglas PS. Paravalvular aortic leak after transcatheter aortic valve replacement: Current knowledge. *Circulation*. 2013;127:397–407.
211. Davies WR, Thomas MR. European Experience and Perspectives on Transcatheter Aortic Valve Replacement. *Prog Cardiovasc Dis* [Internet]. 2014;56:625–634.
212. Azadani AN, Jaussaud N, Ge L, Chitsaz S, Chuter T a M, Tseng EE. Valve-in-valve hemodynamics of 20-mm transcatheter aortic valves in small bioprostheses. *Ann Thorac Surg*. 2011;92:548–555.
213. Midha PA, Raghav V, Sharma R, Condado JF, Okafor IU, Rami T, Kumar G, Thourani VH, Jilaihawi H, Babaliaros V, Makkar RR, Yoganathan AP. The Fluid Mechanics of Transcatheter Heart Valve Leaflet Thrombosis in the Neo-Sinus. *Circulation*. 2017;1598–1609.
214. Dvir D, Lavi I, Eltchaninoff H, Himbert D, Almagor Y, Descoutures F, Vahanian A, Tron C, Cribier A, Kornowski R. Multicenter evaluation of Edwards SAPIEN positioning during transcatheter aortic valve implantation with correlates for device movement during final deployment. *JACC Cardiovasc Interv* [Internet]. 2012;5:563–570.
215. Azadani AN, Jaussaud N, Matthews PB, Ge L, Chuter T a M, Tseng EE. Transcatheter aortic valves inadequately relieve stenosis in small

degenerated bioprostheses. *Interact Cardiovasc Thorac Surg*. 2010;11:70–77.

216. Midha PA, Raghav V, Condado JF, Arjunon S, Uceda DE, Lerakis S, Thourani VH, Babaliaros V, Yoganathan AP. How Can We Help a Patient with a Small Failing Bioprosthesis? An in Vitro Case Study. *JACC Cardiovasc Interv*. 2015;8:2026–2033.
217. Billiar KL, Sacks MS. Biaxial mechanical properties of the native and glutaraldehyde-treated aortic valve cusp: Part II--A structural constitutive model. *J Biomech Eng*. 2000;122:327–335.
218. Aguiari P, Fiorese M, Iop L, Gerosa G, Bagno A. Mechanical testing of pericardium for manufacturing prosthetic heart valves. *Interact Cardiovasc Thorac Surg*. 2016;22:72–84.
219. Lieber BB, Livescu V, Hopkins LN, Wakhloo AK. Particle image velocimetry assessment of stent design influence on intra-aneurysmal flow. *Ann Biomed Eng*. 2002;30:768–777.
220. Kadem L, Knapp Y, Pibarot P, Bertrand E, Garcia D, Durand LG, Rieu R. A new experimental method for the determination of the effective orifice area based on the acoustical source term. *Exp Fluids*. 2005;39:1051–1060.
221. Gorlin WB, Gorlin R. A Generalized Formulation of the Gorlin Formula for Calculating the Area of the Stenotic Mitral Valve and Other Stenotic Cardiac Valves. *JACC*. 1990;15:246–247.
222. BS EN ISO 5840-1:2015 Cardiovascular implants - cardiac valve prostheses. Part 1: General requirements. 2015.
223. Leefe SE, Gentle CR. Theoretical evaluation of energy loss methods in the analysis of prosthetic heart valves. *J Biomed Eng*. 1987;9:121–127.
224. Lim WL, Chew YT, Chew TC, Low HT. Particle image velocimetry in the investigation of flow past artificial heart valves. *Ann Biomed Eng*. 1994;22:307–18.
225. Raffel M, Willert CE, Wereley ST, Kompenhans J. Particle Image Velocimetry - A Practical Guide. 2nd ed. Springer; 2007.
226. Sun Z, Ni H, Chen H, Li S, Lu G, Yu J. Designing and optimizing a stirring system for a cold model of a lithium electrolysis cell based on CFD simulations and optical experiments. *RSC Adv*. 2015;5:84503–84516.

227. Budwig R. Refractive index matching methods for liquid flow investigations. *Exp Fluids*. 1994;17:350–355.
228. Willert CE, Gharib M. Digital particle image velocimetry. *Exp Fluids*. 1991;10:181–193.
229. Cabral B, Leedom LC. Imaging Vector Fields Using Line Integral Convolution. In: Computer Graphics (SIGGRAPH '93 Proceedings), The 20th Annual Conference. 1993. p. 263–270.
230. Pavie AJ, Nzomvuama AN, Bonnet N, Bors VH, Gandjbakhch I. Aortic valve replacement with the composite Labcor(TM) porcine bioprosthesis in the elderly. *J Cardiovasc Surg (Torino)*. 2001;42:317–22.
231. Schlomicher M, Taghiyev Z, Al-Jabery Y, Lukas Haldenwang P, Markthaler L, Moustafine V, Maria Laczkovics A, Thomas Strauch J, Bechtel M. Aortic Valve Replacement with the Labcor TLPB Supra Porcine Bioprosthesis: Intermediate Clinical and Echocardiographic Outcomes. *J Heart Valve Dis*. 2017;26:90–97.
232. Gutsche JT, Patel PA, Walsh EK, Sophocles A, Chern SYS, Jones DB, Anwaruddin S, Desai ND, Weiss SJ, Augoustides JGT. New frontiers in aortic therapy: Focus on current trials and devices in transcatheter aortic valve replacement. *J Cardiothorac Vasc Anesth* [Internet]. 2015;29:536–541.
233. Kalejs M, Segesser LK von. Rapid prototyping of compliant human aortic roots for assessment of valved stents. *Interact Cardiovasc Thorac Surg* [Internet]. 2009;8:182–186.
234. Grigioni M, Daniele C, Del Gaudio C, Morbiducci U, Balducci A, D'Avenio G, Barbaro V. Three-Dimensional Numeric Simulation of Flow Through an Aortic Bileaflet Valve in a Realistic Model of Aortic Root. *Am Soc Artif Intern Organs*. 2005;51:176–183.
235. BS EN ISO 5840-3:2013 Cardiovascular implants — Cardiac valve prostheses Part 3 : Heart valve substitutes implanted by transcatheter techniques. 2013.
236. Pulse Duplicator System User Manual. Victoria, British Columbia, Canada: ViVitro Labs Inc.; 2011.
237. Cho YI, Kensey KR. Effects of the Non-Newtonian Viscosity of Blood on Flows in a Diseased Arterial Vessel. Part 1: Steady Flows. *Biorheology*.

1991;28:241–262.
238. Johnston BM, Johnston PR, Corney S, Kilpatrick D. Non-Newtonian blood flow in human right coronary arteries: Transient simulations. *J Biomech*. 2006;39:1116–1128.
239. Yoganathan AP, Corcoran WH, Harrison EC, Carl JR. The Björk-Shiley aortic prosthesis: flow characteristics, thrombus formation and tissue overgrowth. *Circulation*. 1978;58:70–76.
240. Parker R, Randev R, Wain WH, Ross DN. Storage of heart valve allografts in glycerol with subsequent antibiotic sterilisation. *Thorax*. 1978;33:638–645.
241. Wright JTM. Hydrodynamic Evaluation of Tissue Valves. *Tissue Hear Valves*. 1979;29–87.
242. Pirisi F. Flow Characterisation Downstream of a Transcatheter Aortic Valve Implantation Device. 2014;
243. Balducci A, Grigioni M, Querzoli G, Romano GP, Daniele C, D'Avenio G, Barbaro V. PIV and PTV measurements downstream of an artificial heart valve. 2011.
244. Nygaard H, Giersiepen M, Hasenkam JM, Reul H, Paulsen PK, Rovsing PE, Westphal D. Shear Stress Distribution Downstream of two Aortic Bioprosthetic Valve in vitro. *Biomechanics*. 1992;25:429–440.
245. Robicsek F. Leonardo da Vinci and the sinuses of Valsalva. *Ann Thorac Surg* [Internet]. 1991;52:328–335.
246. van Steenhoven AA, Veenstra PC, Reneman RS. The Effect of some Hemodynamic Factors on the Behaviour of the Aortic Valve. *J Biomech*. 1982;15:941–950.
247. Moore B, Dasi LP. Spatiotemporal complexity of the aortic sinus vortex. *Exp Fluids*. 2014;55.
248. Leo HL, Simon H, Carberry J, Lee SC, Yoganathan AP. A comparison of flow field structures of two tri-leaflet polymeric heart valves. *Ann Biomed Eng*. 2005;33:429–443.
249. Head SJ, Çelik M, Kappetein AP. Mechanical versus bioprosthetic aortic valve replacement. *Eur Heart J*. 2017;38:2183–2191.
250. Tango AM, Salmonsmith J, Ducci A, Burriesci G. Validation and Extension of a Fluid-Structure Interaction Model of the Healthy Aortic

Valve. *Cardiovasc Eng Technol*. 2018;9:739–751.

251. Westaby S, Karp RB, Blackstone EH, Bishop SP. Adult human valve dimensions and their surgical significance. *Am J Cardiol*. 1984;53:552–556.
252. Spadaccio C, Nappi F, Al-Attar N, Sutherland FW, Acar C, Nenna A, Trombetta M, Chello M, Rainer A. Old Myths, New Concerns: the Long-Term Effects of Ascending Aorta Replacement with Dacron Grafts. Not All That Glitters Is Gold. *J Cardiovasc Transl Res*. 2016;9:334–342.
253. Lim WL, Chew YT, Chew TC, Low HT. Steady flow dynamics of prosthetic aortic heart valves. *J Biomech*. 1998;31:411–421.
254. Cavalcante JL, Lima JAC, Redheuil A, Al-Mallah MH. Aortic stiffness: Current understanding and future directions. *J Am Coll Cardiol*. 2011;57:1511–1522.
255. Sripathi VC, Kumar RK, Balakrishnan KR. Further Insights into Normal Aortic Valve Function: Role of a Compliant Aortic Root on Leaflet Opening and Valve Orifice Area. *Ann Thorac Surg*. 2004;77:844–851.
256. Schoenhoff FS, Loupatatzis C, Immer FF, Stoupis C, Carrel TP, Eckstein FS. The role of the sinuses of Valsalva in aortic root flow dynamics and aortic root surgery: evaluation by magnetic resonance imaging. *J Heart Valve Dis*. 2009;18:380–385.
257. Binder RK, Leipsic J, Wood D, Moore T, Toggweiler S, Willson A, Gurvitch R, Freeman M, Webb JG. Prediction of optimal deployment projection for transcatheter aortic valve replacement: Angiographic 3-dimensional reconstruction of the aortic root versus multidetector computed tomography. *Circ Cardiovasc Interv*. 2012;5:247–252.
258. Bleakley C, Monaghan MJ. The Pivotal Role of Imaging in TAVR Procedures. *Curr Cardiol Rep*. 2018;20.
259. Fuchs A, Kofoed KF, Yoon SH, Schaffner Y, Bieliauskas G, Thyregod HG, Makkar R, Søndergaard L, De Backer O, Bapat V. Commissural Alignment of Bioprosthetic Aortic Valve and Native Aortic Valve Following Surgical and Transcatheter Aortic Valve Replacement and its Impact on Valvular Function and Coronary Filling. *JACC Cardiovasc Interv*. 2018;11:1733–1743.
260. Pieter Kappetein A, Head SJ, Généreux P, Piazza N, Van Mieghem NM,

Blackstone EH, Brott TG, Cohen DJ, Cutlip DE, Van Es GA, Hahn RT, Kirtane AJ, Krucoff MW, Kodali S, Mack MJ, Mehran R, Rodés-Cabau J, Vranckx P, Webb JG, Windecker S, Serruys PW, Leon MB. Updated standardized endpoint definitions for transcatheter aortic valve implantation: The Valve Academic Research Consortium-2 consensus document. *EuroIntervention*. 2012;8:782–795.

261. Bieging ET, Frydrychowicz A, Wentland A, Landgraf BR, Johnson KM, Wieben O, François CJ. In vivo three-dimensional MR wall shear stress estimation in ascending aortic dilatation. *J Magn Reson Imaging*. 2011;33:589–597.
262. Dagum P, Green GR, Nistal FJ, Daughters GT, Timek T a, Foppiano LE, Bolger a F, Ingels NB, Miller DC. Deformational dynamics of the aortic root: modes and physiologic determinants. *Circulation*. 1999;100:II54-I62.
263. Ku DN, Giddens DP, Zarins CK, Glagov S. Pulsatile flow and atherosclerosis in the human carotid bifurcation. Positive correlation between plaque location and low oscillating shear stress. *Arterioscler Thromb Vasc Biol*. 1985;5:293–302.
264. Bailey J, Curzen N, Bressloff NW. The impact of imperfect frame deployment and rotational orientation on stress within the prosthetic leaflets during transcatheter aortic valve implantation. *J Biomech*. 2017;53:22–28.
265. Jones BYBM, Krishnaswamy A. New TAVR Devices : European Experience and Status of US Trials. *Card Interv Today*. 2016;10:47–52.
266. Sahasakul Y, Edwards WD, Naessens JM, Tajik AJ. Age-related changes in aortic and mitral valve thickness: Implications for two-dimensional echocardiography based on an autopsy study of 200 normal human hearts. *Am J Cardiol*. 1988;62:424–430.
267. Tanaka H, Dinenno FA, Monahan KD, Clevenger CM, DeSouza CA, Seals DR. Aging, Habitual Exercise, and Dynamic Arterial Compliance. *Circulation* [Internet]. 2000;102:1270–1275.
268. BS EN ISO 5840-2:2015 Cardiovascular implants - cardiac valve prostheses. Part 2: Surgically implanted heart valve substitutes. 2015;55p.
269. Turitto VT, Hall CL. Mechanical factors affecting hemostasis and

thrombosis. *Thromb Res*. 1998;92:25–31.

270. Sturla F, Ronzoni M, Vitali M, Dimasi A, Vismara R, Preston-Maher G, Burriesci G, Votta E, Redaelli A. Impact of different aortic valve calcification patterns on the outcome of transcatheter aortic valve implantation: A finite element study. *J Biomech*. 2016;49:2520–2530.
271. Chandra S, Rajamannan NM, Sucosky P. Computational assessment of bicuspid aortic valve wall-shear stress: Implications for calcific aortic valve disease. *Biomech Model Mechanobiol*. 2012;11:1085–1096.
272. Kähler CJ, Scharnowski S, Cierpka C. On the uncertainty of digital PIV and PTV near walls. *Exp Fluids*. 2012;52:1641–1656.
273. Kefayati S, Milner JS, Holdsworth DW, Poepping TL. In vitro shear stress measurements using particle image velocimetry in a family of carotid artery models: Effect of stenosis severity, plaque eccentricity, and ulceration. *PLoS One*. 2014;9.
274. Campo-Deaño L, Dullens RPA, Aarts DGAL, Pinho FT, Oliveira MSN. Viscoelasticity of blood and viscoelastic blood analogues for use in polydymethylsiloxane in vitro models of the circulatory system. *Biomicrofluidics*. 2013;7.
275. Balducci A, Grigioni M, Querzoli G, Romano GP, Daniele C, D'Avenio G, Barbaro V. Investigation of the flow field downstream of an artificial heart valve by means of PIV and PTV. *Exp Fluids*. 2004;36:204–213.
276. Carey RF, Herman BA. The effects of a glycerin-based blood analog on the testing of bioprosthetic heart valves. *J Biomech*. 1989;22:1185–1192.
277. Chandran KB, Khalighi B. A Note on the Blood Analog for In-Vitro Testing of Heart Valve Bioprostheses. *J Biomech Eng*. 1984;106:112–114.
278. Zigras TC. Biomechanics of human pericardium: a comparative study of fresh and fixed tissue. 2007;
279. Thiene G, Valente M. Calcification of Valve Bioprostheses: the Cardiac Surgeon's Nightmare. *J Cardiothorac Surg*. 1994;8.
280. Pettenazzo E, Deiwick M, Thiene G, Molin G, Glasmacher B, Martignago F, Bottio T, Reul H, Valente M. Dynamic in vitro calcification of bioprosthetic porcine valves: Evidence of apatite crystallization. *J Thorac Cardiovasc Surg*. 2001;121:500–509.
281. Mavrilas D, Missirlis Y. An approach to the optimization of preparation of

bioprosthetic heart valves. *J Biomech*. 1991;24:331–339.

282. Bozkurt S, Preston-Maher GL, Torii R, Burriesci G. Design, Analysis and Testing of a Novel Mitral Valve for Transcatheter Implantation. *Ann Biomed Eng*. 2017;
283. McGregor C, Byrne G, Rahmani B, Chisari E, Kyriakopoulou K, Burriesci G. Physical equivalency of wild type and galactose α 1,3 galactose free porcine pericardium; a new source material for bioprosthetic heart valves. *Acta Biomater*. 2016;41:204–209.
284. Robinson PS, Tranquillo RT. Planar biaxial behavior of fibrin-based tissue-engineered heart valve leaflets. *Tissue Eng Part A* [Internet]. 2009;15:2763–72.
285. BS ISO 37-2011 Rubber, vulcanized or thermoplastic — Determination of tensile stress-strain properties. 2011.
286. Sacks MS. Biaxial mechanical evaluation of planar biological materials. *J Elast*. 2000;61:199–246.
287. O'Leary SA, Doyle BJ, McGloughlin TM. The impact of long term freezing on the mechanical properties of porcine aortic tissue. *J Mech Behav Biomed Mater* [Internet]. 2014;37:165–173.
288. Sacks MS, Chuong CJ. Orthotropic mechanical properties of chemically treated bovine pericardium. *Ann Biomed Eng*. 1998;26:892–902.
289. Gauvin R, Marinov G, Mehri Y, Klein J, Li B, Larouche D, Guzman R, Zhang Z, Germain L, Guidoin R. A comparative study of bovine and porcine pericardium to highlight their potential advantages to manufacture percutaneous cardiovascular implants. *J Biomater Appl* [Internet]. 2013;28:552–565.
290. Lally C, Reid AJ, Prendergast PJ. Elastic behavior of porcine coronary artery tissue under uniaxial and equibiaxial tension. *Ann Biomed Eng*. 2004;32:1355–1364.
291. Miller KS, Edelstein L, Connizzo BK, Soslowsky LJ. Effect of Preconditioning and Stress Relaxation on Local Collagen Fiber Re-Alignment: Inhomogeneous Properties of Rat Supraspinatus Tendon. *J Biomech Eng* [Internet]. 2012;134:031007.

9 Appendices

9.1 Assessment of the Potential Influence of Testing Solution upon the Mechanical Properties of GA Fixed Tissue

9.1.1 Introduction

As of 2015, all FDA-approved TAVs were produced with either GA fixed bovine (such as the Edwards SAPIEN valves detailed in Section 0) or porcine pericardium, and the bioprosthetic surgical valves planned to be used during these investigations are constructed using GA-fixed porcine aortic valve leaflets, as outlined in Section 3.4.1.1. However, some research has indicated that glycerol, used to raise the viscosity level of the blood analogue used to a more physiological level during *in vitro* testing[21,102,239], may alter the mechanical properties of the leaflet tissue of bioprosthetic valves[240,241]. Wright suggested that a water-glycerol solution may cause stiffening of the tissue[241], whilst Parker *et al*. reported that soft tissue samples stored in glycerol "developed a patchy distribution of the collagen, which had a loose, disorganised arrangement when compared with the fresh control tissue", with a corresponding fall of up to 30 % in elastic properties[240]. Other reports refute these claims however, stating that hydrodynamic testing in glycerine based fluids for up to 80 days caused no trend of change in the valvular performance caused by absorption of the glycerine, although these reports were based on qualitative comparison of valve performance rather than mechanical characterisation of the tissue[276,277].

As the planned tests for this thesis involved exposing the GA fixed pericardium to different fluids made up of some combination of glycerol, saline, deionised water, and potassium iodide (KI) for periods of hours, it was decided to avoid using glycerol until it could be established that it did not significantly affect the mechanical properties of the tissue leaflets used. Although there have been no reports of potassium iodide or buffered phosphate saline mechanically affecting the tissue, it was also decided to investigate the effect of the fluids that contained no glycerol but were intended for use in these investigations.

GA fixation of soft tissue causes modifications, dependent upon the concentration of and exposure to the GA and the temperature during the fixation, but allows stabilisation of the tissue and reduces antigenicity, reducing rejection by the immune system of the patient[278], but also triggers structural damage to the extra cellular matrix and increases the risk of tissue calcification[279,280], reducing the performance of the valve if the pericardium based on that tissue. Mechanical characterisation of pericardial tissue does not yet currently have a univocal process, making inter-experimental comparison problematic[218]. Even with these restrictions in mind, native and GA fixed pericardial tissue shows qualitatively similar stress-strain responses[218].
The mechanical properties of heart valve tissue are most commonly ascertained using uniaxial testing[125], and the J-curve is a commonly used description of the stress-strain relationship of pericardium[124,218,281], presented in Figure 9-1(a), where the various parts of the curve may be split into regions where specific physiological functions dictate the characteristics of the mechanical response[125]. The tissue has a relatively large region characterised by a large strain response to low stresses, corresponding to the crimped collagen fibres straightening and the elastin fibres elongating, in an approximately linear fashion, defined by a low stretch modulus (E_L)[125,281]. Once the collagen fibres start to become uncrimped, any further extension of the tissue requires the stretching of these collagen fibres, which are much stiffer than the elastin fibres, and so the strain response to stress decreases, and enters a non-linear transition phase as the collagen fibres transition from straightening to stretching, marked on Figure 9-1(a) by ε_L. With continued extension of the tissue, the stress-strain relationship enters a third phase at a strain of ε_H. Like the first phase, this region is again approximately linear, but with a much-reduced strain response to additional stress, defined by a high stretch modulus (E_H), as now all the collagen fibres are fully straightened and aligned. Further stretching of the sample results in the tissue entering the rupture phase, a second non-linear phase as shown in Figure 9-1(a), as the elastin and collagen fibres break.

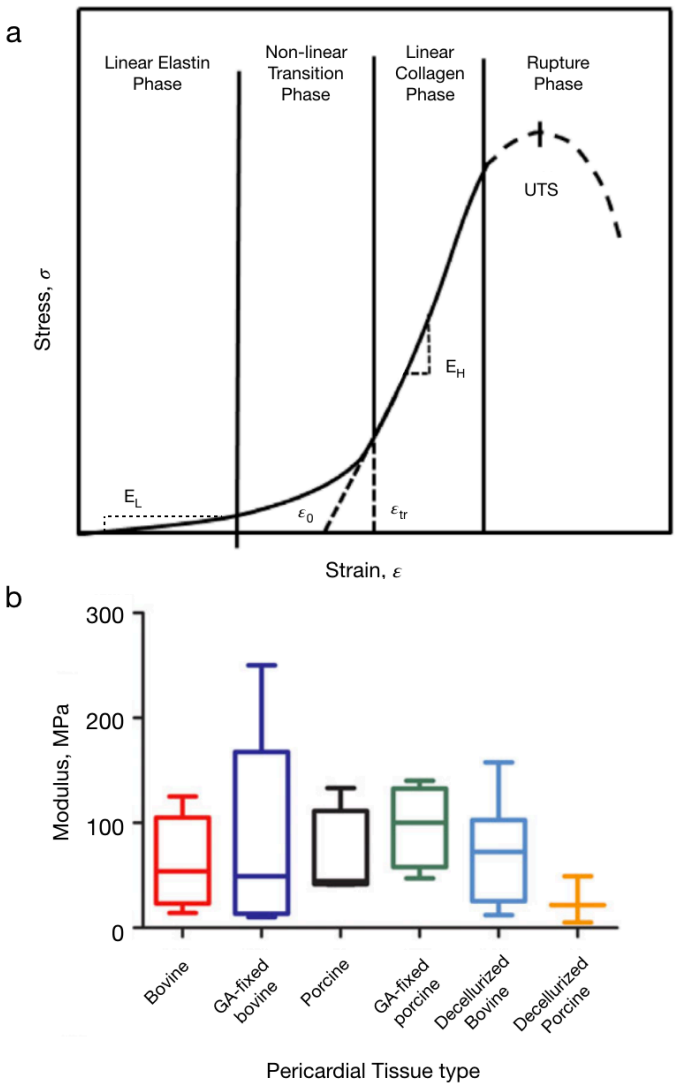

Figure 9-1: Mechanical Characteristics of Bovine and Porcine Pericardial Tissue: (a) J-curve stress-strain relationship of pericardial tissue, adapted from Hasan et al. *2014*[125]*; (b) Range of stress-strain moduli reported in the literature, adapted from Aguiari et al 2016*[218]

Previous uniaxial tests in the literature report a wide range of high stretch moduli for the GA fixed pericardial tissue, with bovine E_H in the range of 15 to 150 MPa (and outlying values of up to 250 MPa reported) and porcine E_H varying from 60 to 130 MPa (with outlying values as low as 47 MPa and as high as 150 MPa)[218], with these ranges illustrated in Figure 9-1 for clarity. This is due to inconsistencies in the test methods and large variabilities in the material properties, related to the phenotype, age, and sex of the animal, as well as the location, fibre orientation, and testing temperature of the sample.

Uniaxial testing of GA fixed bovine and porcine pericardial tissue was undertaken, with the force-displacement readings recorded during each cycle, which were then converted into stress and strain values. These measurements

were then repeated after the tissue was exposed for 24 hours, representing the maximum duration of a PIV testing setup and hence the maximum exposure of tissue to a particular testing fluid, to one of the various fluids being investigated, and then the investigation was repeated for the same tissue sample for the remaining solutions. Concurrently, samples taken from the same original sheet of GA fixed pericardium as the sample being uniaxially tested were periodically examined for shrinkage or expansion over a 150-hour time span.

9.1.2 Methods

9.1.2.1 Tissue

In order to investigate whether the stiffness of the bioprosthetic tissue of the valves would be altered by exposure to the working fluids described in Section 3.6, samples of equivalent bovine and porcine tissue were required.

For the bovine tissue[282], heart lung blocks were collected, and chilled on ice prior to pericardium removal. The pericardial sacs were dissected from the heart, cleaned of excess fat and parietal pericardium, thoroughly rinsed in sterile saline (20 mM HEPES-Saline (pH 7.4) containing 13 mM $MgCl_2$-H_2O), and fixed in a 0.5% solution of GA for 48 hours. They were then removed from the 0.5% GA solution, and stored at 4 °C in a 0.2% GA solution, ready for thickness mapping and uniaxial tensile testing.

The porcine tissue procedure[283] was the same as for the bovine pericardium, except the fixation solution was 0.6% GA, matching the fixation of the Labcor TLPB valves[230], and the fixation period was 24 hours .

9.1.2.2 Fluids

9.1.2.2.1 Phosphate Buffered Saline

The saline used in the investigations was Phosphate Buffered Saline (PBS, Fisher Bioreagents BP2438-20), containing 0.137M NaCl, 0.0027M KCl, and 0.0119M phosphates. PBS is a Newtonian fluid, used both to store bioprosthetic heart valves[213] and as a medium to contain biological soft tissue during uniaxial testing[284], and adheres to the ISO 5840-2:2015 requirements for the testing fluid of cardiac valve prostheses[268]. At a temperature of 25 °C, the PBS has a dynamic viscosity, η_s, of 0.001 Pa.s, as measured by a viscometer (Viscolite 700, Hydramotion, UK), and a density, ρ_S, of 1.01 g/cm^3.

9.1.2.2.2 Viscosity Matched Testing Fluid

A solution of 40 % glycerol and 60 % saline (by weight), used during pulse duplicator testing in order to match the viscosity of blood at high shear[97,104,220], labelled as the η solution. Although is a Newtonian fluid, in contrast to the non-Newtonian nature of blood, the shear-thinning effects are less pronounced in the relatively large diameter vessels of the aortic root [237], and so many tests use a fluid reproducing the viscosity of blood for a given shear[97,104,220]. As blood at 37 °C exits the aortic valve, it reaches shears of > 100 s^{-1}, tending towards a dynamic viscosity of 0.0035 – 0.004 Pa.s[81]. The η solution used in this investigation has a dynamic viscosity, η_η, of 0.004 Pa.s, and a density, ρ_η, of 1.11 g/cm^3.

9.1.2.2.3 Refractive Index and Viscosity Matched Testing Fluid

A solution of 15.2 % KI, 36.2 % glycerol, and 48.5 % deionised and filtered water, used during PIV investigations to both raise the RI and match the viscosity to that of blood at high shear (η-RI solution)[97]. As the RIs of glycerol and PBS are 1.47 and 1.33 respectively, a mixture of 50% glycerol and 50 % saline[242] would be required to match the RI of the resultant fluid to that of Med-6015, a typical silicone used in PIV studies[107,250] with a RI of 1.40, and thus avoid image distortion due to RI mismatch. This would result in a dynamic viscosity of 0.007 Pa.s, indicating a much more viscous fluid than that observed in large blood vessels at high shear[81]. The high RI of 1.67 for KI in its crystalline form, alongside its high solubility in water at 25 °C, minimal risk for human health, and affordability, makes it an ideal chemical to be used alongside to raise the RI of the analogue fluid whilst keeping the dynamic viscosity similar to that of blood at high shear[242]. The presence of ions in the resultant solution, due to the inclusion of KI, removes the requirement of using PBS to provide ions to be detected and measured by the electro-magnetic flowmeter of the pulse duplicators commonly used in heart valve assessment[97,104,220], and so it was preferred to use deionised and filtered water instead of PBS. The η-RI solution used in this investigation has a dynamic viscosity, $\eta_{\eta R}$, of 0.004 Pa.s, and a density, $\rho_{\eta R}$, of 1.29 g/cm^3.

9.1.2.3 Shrinkage and Expansion of Tissue

An alteration to the mechanical characteristics of the tissue could be caused by an increase or decrease in the stiffness of the tissue, but it could also be caused by shrinkage or expansion of the tissue. In order to establish whether the various fluids the GA fixed pericardial tissue was being tested in caused the samples to shrink or expand, image analysis of a sample before and after exposure to the fluid was taken out.

A sample of bovine or porcine pericardial tissue was taken from the each sheet of GA fixed tissue as used in the uniaxial testing described in Section 9.1.2.4, with each shrinkage/expansion sample consisting of one of the end Sections of a type 4 test sample as recommended by ISO 37-2011[285], illustrated in Figure 9-2(a). Each tissue sample had the thickness at its centre measured and was then placed between two glass slides, with sufficient corresponding testing fluid to completely surround the sample within the slides, and photographed alongside a reference distance of 10 mm from a height of 200 mm above the top surface of the slides, as described in Figure 9-2(b). This enabled calculation of the sample width, L_s (m), via acquisition of the pixel length of the sample width using image analysis software (ImageJ, National Institutes of Health, Maryland, USA), as illustrated in Figure 9-2(c), and conversion into length in metres by inputting into:

$$L_s = \left(\frac{L_{sp} * 0.01\ m}{L_{rp}} \right) \tag{9-1}$$

where L_{sp} is the sample width in pixels, L_{rp} is the image length of the reference distance in pixels, and 0.01 m is the chosen reference distance.

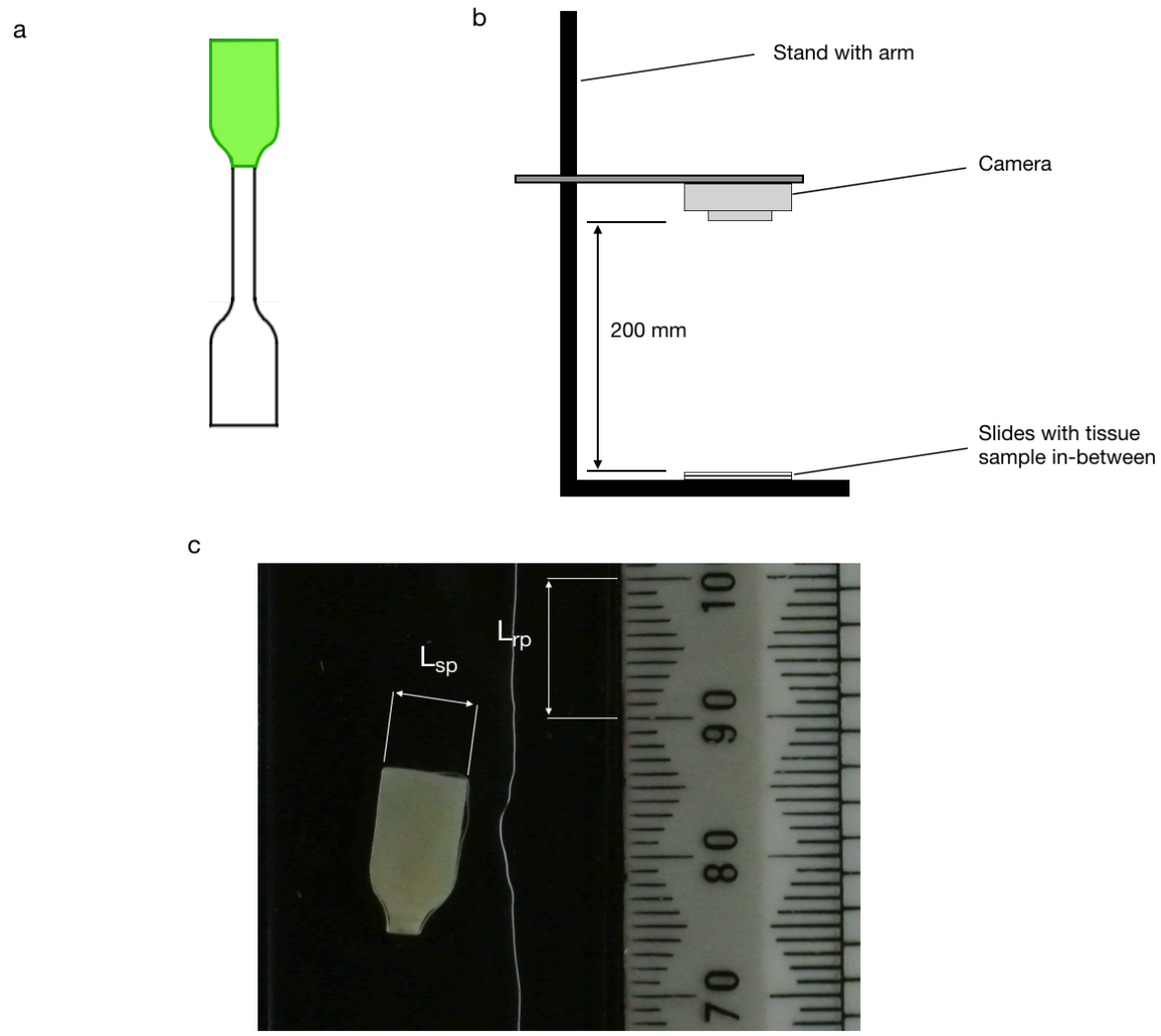

Figure 9-2: Shrinkage/Expansion test: (a) shape of tissue sample, taken from the head of the dumbbell cut-outs from the uniaxial testing; (b) a tissue sample held between two slides alongside reference measurements for image acquisition and analysis; (c) schematic of photo acquisition setup.

After this, each sample was immersed in 300 ml of the corresponding testing fluid contained within a plastic box, and kept at a room temperature of 25 °C. Further photos were taken after 25, 50 and 150 hours. These photos were then analysed using the same method as described above, to ascertain the width of each sample at each time point, to see whether any shrinkage or expansion of the GA fixed pericardium had occurred. The change in width of each sample, ΔL (%), was defined as:

$$\Delta L = \left(\frac{L_t - L_{t0}}{L_{t0}}\right) * 100 \quad (9\text{-}2)$$

where L_t was the sample width after immersion in a fluid after t hours (m) and L_{t0} was the initial sample width before immersion (m). After the final immersion period, the thickness of tissue was again taken from the centre of each sample. The following 5 fluids were investigated:

- PBS, described in Section 9.1.2.2.1, and used as a control in this investigation
- The η solution described in Section 9.1.2.2.2
- A solution of 43.5 % KI and 56.5 % deionised and filtered water (by weight), used during PIV investigations in order to raise the RI of the fluid to reduce optical distortion of the acquired image pairs for cross correlation[107,250] (RI solution)
- The η-RI solution described in Section 9.1.2.2.3
- Pure glycerol, to further investigate the effects of glycerol in the absence of water, due to previous reports of glycerol potentially affecting the properties of pericardial tissue[240,241].

9.1.2.4 Uniaxial Testing

9.1.2.4.1 Uniaxial Testing Rig

The uniaxial testing rig (BT1-FR5.0TN, Zwick Roell Group, Ulm, Germany) consisted of two grips, with coapting face surfaces of 30 x 45 mm, arranged vertically, holding either end of a tissue sample being tested, as shown in Figure 9-3(a). The upper grip was servo controlled and attached to a 0.5 kN loading cell (KAP-TC, Zwick Roell Group, Ulm, Germany), measuring the force applied to the tissue through the grip. An open liquid container was positioned around the sample and grips, submersing the sample in a user chosen solution throughout the testing procedure. The temperature of this solution was monitored and controlled by a low temperature thermostat (E300 Ecoline, Lauda Brinkmann, New Jersey, USA), with resolution 0.05 °C. This fluid could be drained and refilled with the sample still loaded between the grips, enabling testing of multiple fluids without altering the sample's fixation. Upon starting the test, the upper grip moved away from the lower grip at a rate defined from the attached software (TestXpert II, Zwick Roell Group, Ulm, Germany), and the force exerted on and the displacement of the upper grip were recorded at sampling rate of 10 Hz.

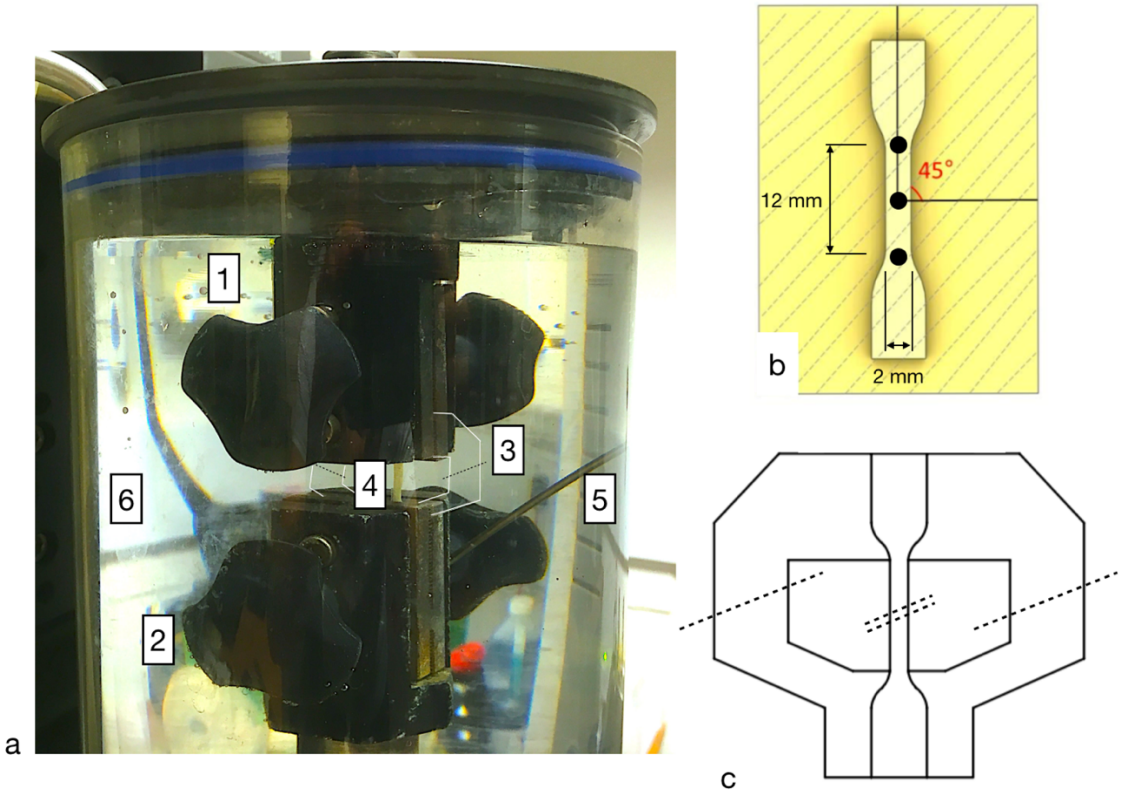

Figure 9-3: Tensile testing of tissue: (a) Uniaxial testing rig:

1 – Upper clamp; 2 – Lower clamp; 3 – Acetate loader (highlighted in white, snipped along dashed lines); 4 – Tissue sample; 5 – Thermostat; 6 – Fluid reservoir; (b) critical dimensions and fibre alignment of dumbbell shape tissue samples. Thickness measurements are taken at each location marked by •; (c) acetate sample loader – the central double dashed line is cut before the sample is placed on top of the acetate, whilst the single dashed outside lines are cut once both uniaxial rig clamps have been tightened onto the ends of the sample.

9.1.2.4.2 Tissue Samples

The pericardial tissue being investigated was cut by a punch into a dumbbell-shape with a central section of 12 mm length and 2 mm width, in accordance with type 4 test sample dimensions as recommended by ISO 37-2011[285], illustrated in Figure 9-3(b). Samples were cut so that the extracellular matrix fibres were running close to a 45 ° angle across the tissue for each sample, in order to represent both parallel and perpendicular fibre alignments. Samples were chosen with fibre distribution and orientation as uniform as possible, in order to obtain more uniform stress and strain distributions[217,286]. The thickness of each sample was measured at three locations, as indicated in Figure 9-3(b), with a thickness gauge (Mitutuyo 543-402BS, Sakado, Japan) with resolution

0.01 mm, and then averaged to produce an average cross-sectional area for each sample.

9.1.2.4.3 Uniaxial Testing Procedure

In order to overcome the limitations associated with the large variabilities of tissue properties, 7 samples of GA-foxed bovine tissue and 7 samples of GA-fixed porcine tissue were tested before and after 24 hours of immersion in one of the test fluids, to assess variations to the mechanical properties, and this was repeated for each of the test fluids. The fluid reservoir of the uniaxial rig was filled with the first of the fluids under investigation, which were tested in the following order:

1. PBS
2. η solution
3. η-RI solution

The tissue samples were tested individually and loaded onto the uniaxial tensile rig via the use of an acetate loading template, displayed in Figure 9-3(c). The central sprue of the template was cut in half before the wet tissue sample was placed on top of the template, positioned so that the central portion of the dumbbell aligned with the central portion of the template. With the wet tissue adhered to the acetate and the uniaxial grips set 12.0 mm apart, the assembly was clamped into the rig, so that the central portion of the dumbbell was between the two grips. The fluid container was filled so that it covered the tissue sample, releasing the tissue from the acetate and, as the density of the fluid is close to that of the tissue, reducing the pre-stressing of the samples by gravity. The outside sprues of the acetate template were then cut, resulting in the configuration shown in Figure 9-3(a) where only the tissue sample is connected between the two grips. Once the temperature of the fluid bath had stabilised at the designated level, the force sensors were zeroed. A pre-load, F_p (N), was applied, mitigating any differences caused by slight variations in the loading procedure[286], applying a stress of 50 kPa across the tissue. F_p was determined by applying the equation:

$$F_p = 50{,}000\ Pa * A_{cs} \tag{9-3}$$

where A_{cs} is the cross-sectional area (m^2) of the central portion of the unloaded dumbbell for each tissue sample. With the pre-load applied to the tissue, the force sensors were zeroed again, and the displacement was set as zero. The uniaxial testing schedule is illustrated in Figure 9-4.

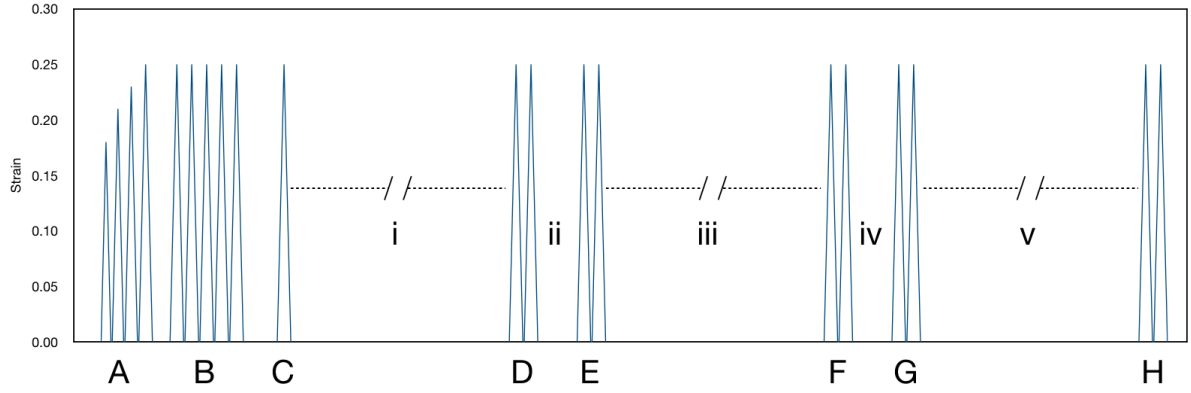

Figure 9-4: Strain magnitude and timing of uniaxial tests. After filling the fluid reservoir with PBS and loading the tissue, each sample was gradually brought to testing strain (A), and then cycled at testing strain until the stress at testing strain was constant (B) and 10 cycles of stress-strain data were acquired (C). The sample was then left submerged in PBS for 24 hours (i), after which the sample was conditioned with 10 cycles at testing strain, and then had 10 cycles of stress-stain data acquired (D). The reservoir was then drained of PBS and refilled with the η solution (40 % glycerol and 60 % PBS) (ii), the sample was conditioned, and another 10 cycles of stress-strain data were acquired (E). The sample was left in the η solution for 24 hours (iii), followed by sample conditioning and data acquisition (F). The reservoir was drained of the η solution and refilled with the η-RI solution (glycerol, KI, and deionised water) (iv), followed by tissue conditioning and data acquisition (G). The sample was left submerged in the η-RI solution for 24 hours (v), after which the tissue was again conditioned followed by 10 cycles of stress-strain data acquisition (H).

Testing strain was determined as 0.25, equivalent to a 3 mm extension of the 12 mm length of the tissue dumbbell within the two grips, chosen because the maximum physiological strain of leaflet tissue is reported as 0.25[287], and this level of strain is sufficient to assess both the low stretch modulus (E_L) and high stretch modulus (E_H) of the tissue[288], at a strain rate of 0.008 /s[288]. Each sample was gradually brought to this testing strain of 0.25 over 4 x 10 cycles, with each block of 10 cycles peaking at a maximum strain of 0.18, 0.21, 0.23 and 0.25 respectively. In order to ensure uniformity of the tissue's strain response to the applied force, the tissue was repeatedly cycled up to the testing strain of 0.25, until the force necessary to produce this maximum strain was constant (± 0.5%) for 10 cycles. Ten cycles up to this strain were run, and the force and displacement throughout each cycle was acquired and recorded. The sample was then left in the clamps submersed in PBS for a 24-hour period. The force

sensors were not zeroed at this point, in order to indicate whether a shrinkage or expansion of the tissue had taken place during the 24-hour time span, indicated by a positive or negative force respectively at a strain of zero. The tissue samples were pre-conditioned for 10 cycles at testing strain before data acquisition of 10 cycles. The reservoir was then drained of saline and refilled with the next fluid, the η solution of 40 % glycerol and 60 % saline, with the sample still in place between the grips throughout the fluid change. This was followed by a re-zeroing of the force sensors, necessary due to the change in fluid density altering the buoyant forces acting upon the top grip. Another 10 cycles of pre-conditioning at testing strain were carried out, followed by the 10 cycles of data acquisition, followed by a 24-hour period of tissue exposure, then data acquisition as for the saline. This process was then repeated one last time for the η-RI solution of KI, glycerol, and deionised water.

9.1.2.4.4 Identification of Elastin and Collagen Regions

Due to the viscoelastic properties of pericardium, resulting in hysteresis and significant relaxation during strain cycles[218], the tissue has a different force-displacement response during loading than unloading. To maintain uniformity and enable comparison between data sets, only the loading cycles of the tissue were analysed. The sampling of the data acquisition led to measurements being recorded at slightly different displacements from cycle to cycle, so it was decided to take one sample cycle (the tenth in each block of cycles) rather than an average of the 10 cycles.

The stress acting upon the sample can be calculated from the force measurements in several different ways. The nominal stress can be determined by basing the calculation upon the original cross-sectional area of the sample, whilst the true stress is calculated from the cross-sectional area of the sample at the moment of analysis, so that as the sample becomes elongated, the cross-sectional area will decrease. Cauchy stress, a common form of true stress, is a symmetric tensor defined by the forces acting on an element of infinitesimal area in the deformed body, with the force components and the normal to the area having fixed directions in space. Fixing these directions to be defined along the material's direction throughout the deformation, e.g. due twisting or bending of the sample, results in Second Piola-Kirchhoff stress. However, use

of the current tissue cross-sectional area required estimation of the Poisson ratio and lateral contraction of the samples during testing, so removing these factors from the calculation of the relative stress of each measurement would increase the precision of the result[54]. Although Engineering Stress may underestimate the true stress content of the sample, it is an appropriate quantity for comparing tissue properties within a test group[54], and has been used for many previous soft tissue uniaxial tests[278,284,289,290]. Accordingly, the force applied to the sample, F_t (N), was used to calculate the nominal tensile engineering stress, σ_t (MPa) across the centre of the sample as follows:

$$\sigma_t = \frac{F_t}{A_{cs} * 10^6} \tag{9-4}$$

Several different types of strain can be measured from the testing. Similarly to the stress definitions, the Engineering (or Nominal) Strain is based upon the original length of the sample at the start of testing, the True Strain is based upon the current length of the sample undergoing a given stress defined according to fixed directions in space, and the Lagrange-Green strain, useful for geometrically non-linear cases, contains derivatives of the sample displacements with respect to the original configuration. In line with the selection of Engineering Stress in this investigation, Engineering Strain, ε, was used, defined as the ratio between the elongated length, L (m), and the original length, L_0 (m), and calculated by:

$$\varepsilon = \frac{L - L_0}{L_0} \tag{9-5}$$

In order to relate these results to the J-curve description identified in numerous investigations as reported by Aguiari et al[218], identification of the elastin phase (with a corresponding low stress-strain modulus, E_L), the non-linear transition phase (starting at a lower strain of ε_L and ending at a higher strain of ε_H), and the collagen phase (with high stress-strain modulus, E_H), as shown in Figure 9-1(a), was necessary. The crossover point of the elastin phase to the transition

phase was identified as when the change in the modulus, T_M, increases to 0.02, as shown in Figure 9-5, with T_M calculated according to

$$T_M = \frac{\sigma_n - \sigma_{n-1}}{\sigma_n} \tag{9-6}$$

where σ_n is the stress (MPa) at the nth sample of the cycle and σ_{n-1} is the stress (MPa) of the sample before. A linear line of best fit was applied to the stress-strain results before this sample, and the gradient of this line was equal to the E_L (in MPa). The strain at this lower transition point was recorded as the 'elastin transition strain', ε_L. The collagen region was identified in a similar manner to the elastin region, with the region defined when T_M decreases to 0.02 after the transition region, illustrated in Figure 9-5. Once again, a linear line of best fit was applied to the stress-strain results within this region, and the gradient of this line was equal to the E_H (in MPa). The strain at this upper transition point was recorded as the collagen transition strain, ε_H.

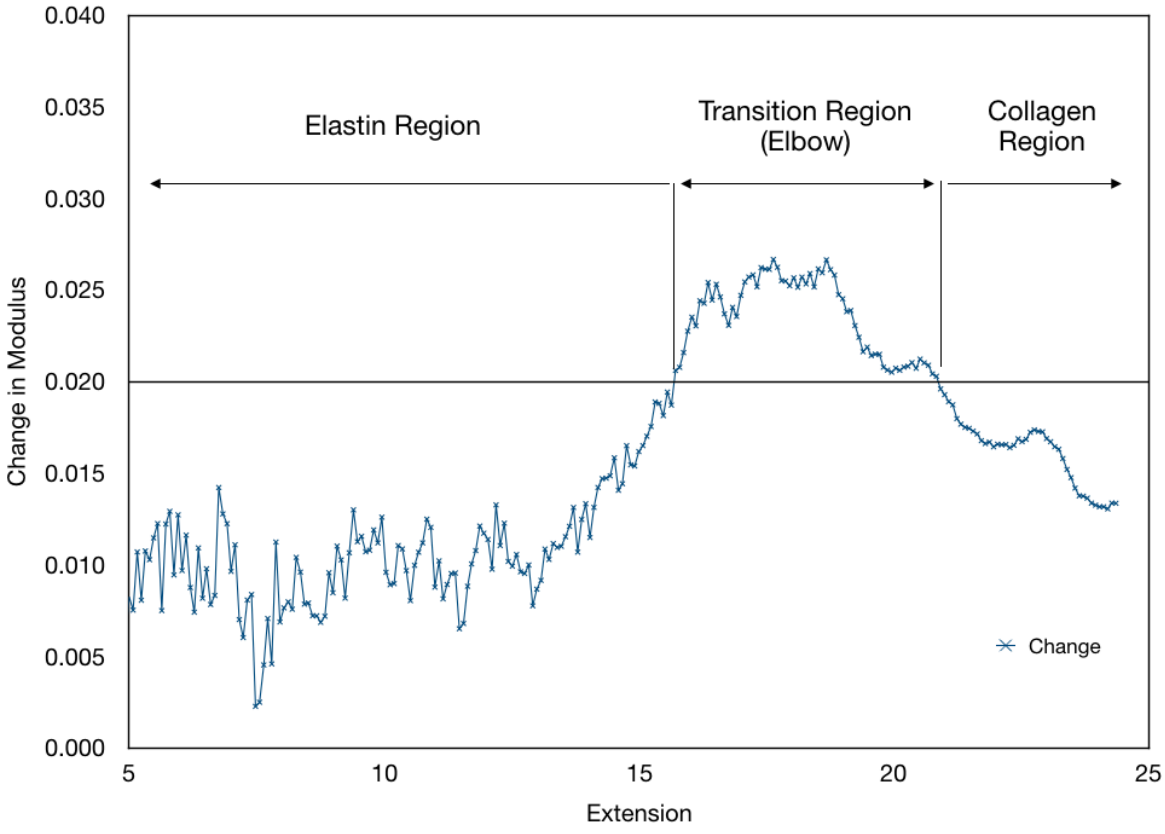

Figure 9-5: Identification of Low and High Stretch Regions of soft tissue stress-strain response.

9.1.3 Results

9.1.3.1 Shrink/Expansion results

The average change in width of the tissue samples for each fluid type after 25, 50 and 150 hours is presented in Table 9-1, with the distribution for each fluid after 150 hours shown in box and whisker charts for both bovine and porcine pericardium in Figure 9-10. The thickness of the bovine pericardium across all samples was measured as 0.31 ± 0.13 mm, whilst the porcine pericardium was measured as 0.11 ± 0.06 mm. No change in thickness after immersion exceeded ± 0.02 mm, with no observable trend of increase or decrease in thickness. No change in width exceeded 1 % for any of the fluids or tissue types, but the 100 % glycerol resulted in an expansion between 0.28 and 0.63 % for both GA fixed bovine and porcine pericardium.

Fluid	*Time in solution (hours)*	*Mean change in width (%)*	
		Porcine	Bovine
Buffered Saline	25	-0.12	+0.07
	50	-0.22	-0.33
	150	+0.13	+0.11
40 % Glycerol	25	-0.14	-0.07
	50	-0.09	-0.06
	150	-0.90	-0.01
RI Solution	25	-0.44	-0.02
	50	-0.16	-0.07
	150	-0.09	-0.12
RI and η Solution	25	-0.26	-0.04
	50	-0.38	-0.09
	150	-0.12	-0.07
100 % Glycerol	25	+0.28	+0.63
	50	+0.32	+0.57
	150	+0.42	+0.43

Table 9-1: Change in size of tissue samples after exposure to different testing fluids

Observationally, it was noticed that the 100 % glycerol solution also resulted in the pericardial tissue becoming more translucent than before the fluid exposure, as presented in Figure 9-6.

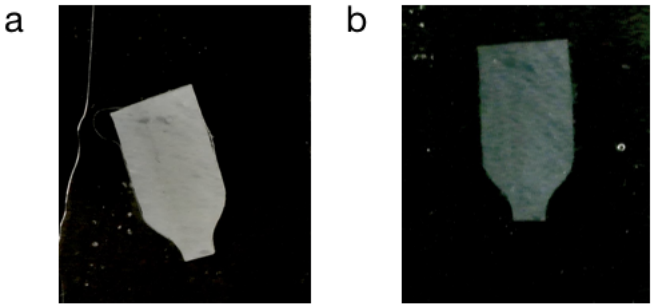

Figure 9-6: Pre- (a) and Post- (b) 150-hour exposure of GA fixed porcine pericardium to pure glycerol.

9.1.3.2 Uniaxial Results

The average thickness of the uniaxial GA fixed bovine samples was 0.29 ± 0.07 mm, with an initial - i.e. after pre-conditioning but at the start of exposure to the buffered saline - E_L of 1.93 ± 5.69 MPa with an average R^2 value of 0.941 ± 0.057 for the line of best fit, and an initial E_H of 76.40 ± 28.67 MPa (R^2 value of 0.993 ± 0.008). The average transition phase between the LSM and HSM for the bovine tissue samples occupied a strain period of 0.0717 ± 0.0337. A plot of the stress-strain during a typical loading cycle of a tissue sample is presented in Figure 9-7.

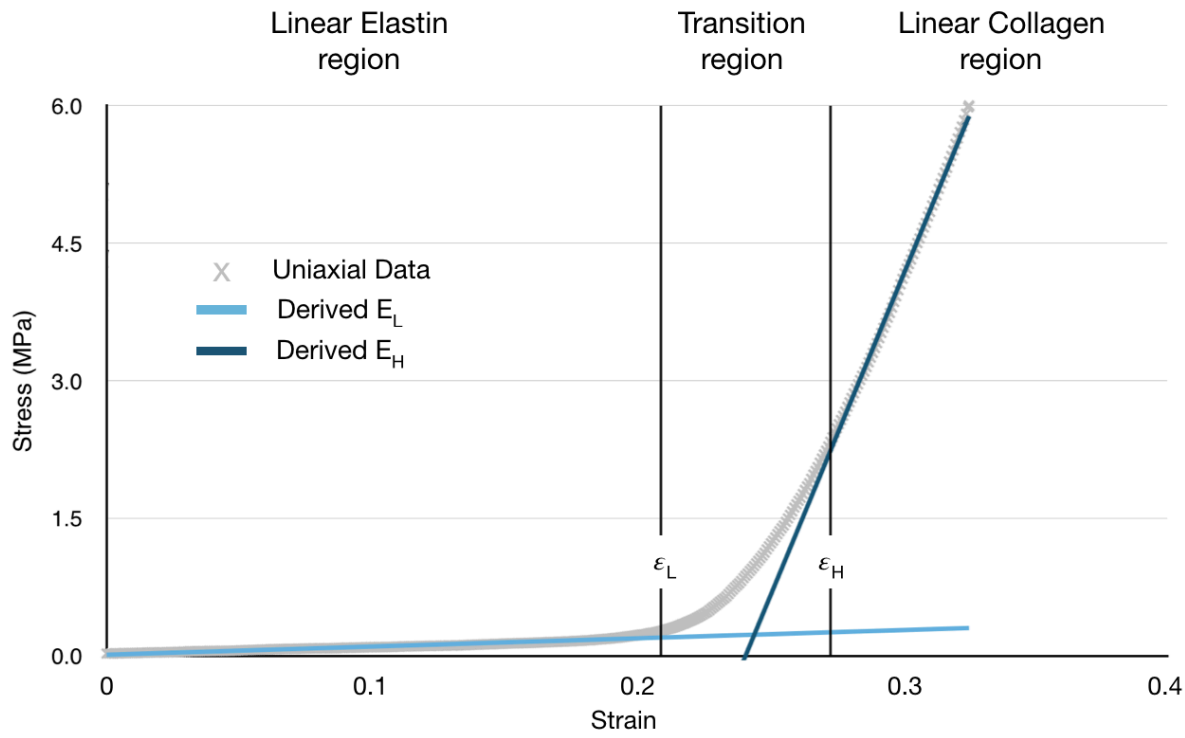

Figure 9-7: Stress-strain data from uniaxial test. Data taken from loading cycle of GA Fixed Bovine Pericardium submersed in buffered saline for 0 hours. The transition points from linear elastin to transition and from transition to linear collagen are derived in terms of strain from data analysis as detailed in Section 9.1.2.4.4, and then a line of best fit is applied to each set of data within the two linear region, the gradient of which is equal to the modulus of the tissue in that region

The GA fixed porcine samples were thinner, with an average thickness of 0.12 ± 0.02 mm. E_L after initial precondition was 2.24 ± 0.76 MPa (R^2 value of 0.940 ± 0.076) whilst E_H was 81.37 ± 19.46 MPa (R^2 value of 0.996 ± 0.036). The average transition phase between the LSM and HSM occupied a strain range of 0.0876 ± 0.0374.

The mean values and changes to E_L, E_H, ε_L and ε_H after the samples were submerged in the three solutions are presented in Table 9-2, and box and whisker plots of these changes, showing the statistical variation across the 7 samples tested for each tissue type, is illustrated in Figure 9-8 and Figure 9-9 for the bovine and procine results respectively.

The E_L of the tissue samples had the greatest relative variation of the 4 measured parameters after exposure to the fluids, decreasing by up to 0.293 MPa (12.89 %) after 24 hours exposure to the glycerol, KI, and water solution, and by up to 0.105 MPa (9.19 %) in the buffered saline, showing a trend of decreasing E_L for both bovine and porcine GA fixed pericardium. However, both tissue types appeared to stiffen after exposure to the 40 % Glycerol solution, especially the porcine pericardium, which displayed an average change in

modulus of 0.145 MPa, a 6.52 % increase. None of the average transition strains between the linear elastin region and the transition phase changed by more than 3.9 % after solution exposure. For the collagen region, no E_H changed by more than 1.337 MPa (1.56 %) across all the tests, and the ε_H remained within a strain of 0.0011 (a change of 0.93 %).

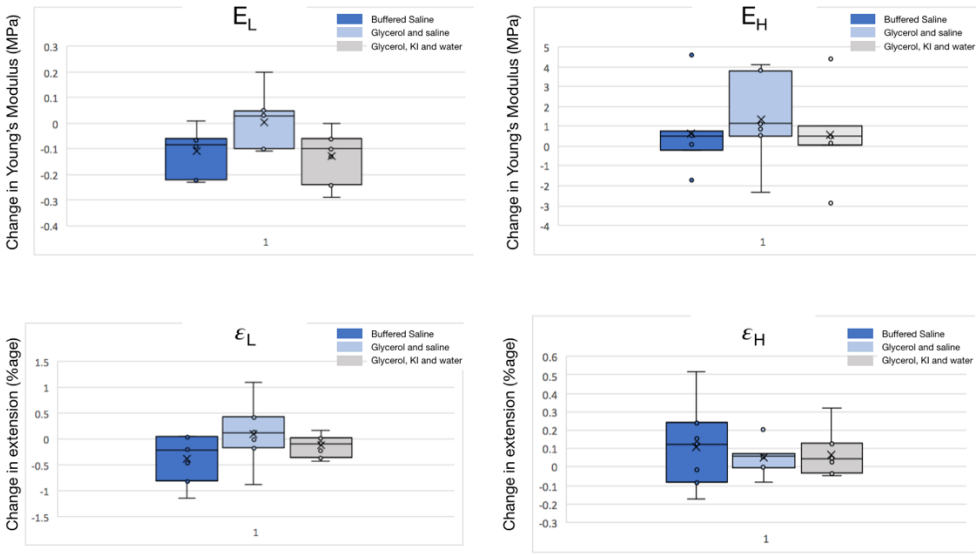

Figure 9-8: Changes in stiffness of GA Fixed Bovine Pericardium. Box and whisker charts for the change in size of tissue samples after 24 hours exposure in the various testing fluids. For each fluid, the mean value is represented by an 'X', the median value by the central line, the box plot is bounded by the upper and lower quartiles, and the extremes of the whiskers are bound by the inter-quartile range from the median value.

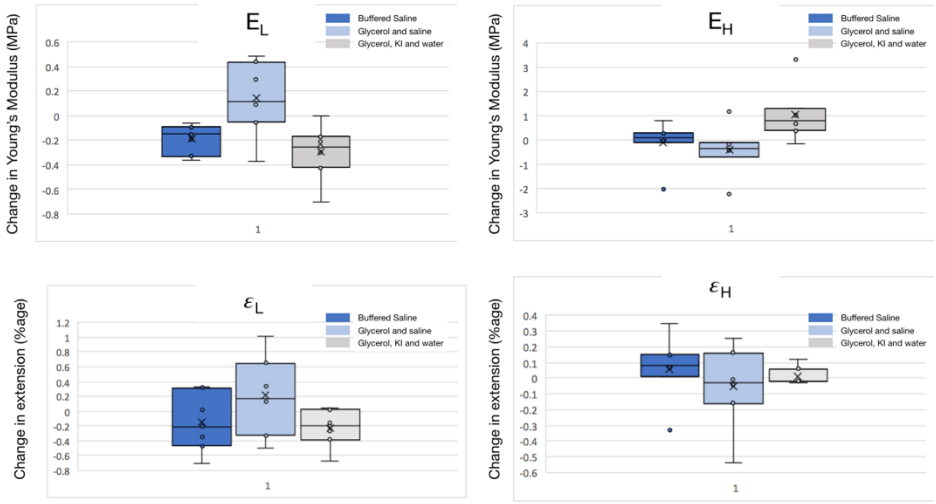

Figure 9-9: Changes in stiffness of GA Fixed Porcine Pericardium. Box and whisker charts for the change in size of tissue samples after 24 hours exposure in the various testing fluids. For each fluid, the mean value is represented by an 'X', the median value by the central line, the box plot is bounded by the upper and lower quartiles, and the extremes of the whiskers are bound by the inter-quartile range from the median value.

Property		*Buffered Saline*		*η*		*RI and η*	
		Bovine	Porcine	Bovine	Porcine	Bovine	Porcine
E_L *(MPa)*	0 hr	1.931	2.243	1.691	2.170	1.739	2.523
	24 hr	1.825	2.054	1.694	2.315	1.162	2.230
	ΔE_L	-0.105 (0.088)	-0.189 (0.115)	+0.004 (0.112)	+0.145 (0.299)	-0.126 (0.104)	-0.293 (0.221)
	% change	-9.19 %	-8.33 %	+1.64 %	+6.52 %	-8.60 %	-12.89 %
ε_L	0 hr	0.1247	0.1300	0.1248	0.1279	0.1237	0.1321
	24 hr	0.1209	0.1285	0.1259	0.1300	0.1224	0.1298
	$\Delta\varepsilon_L$	-0.0038 (0.0045)	-0.0015 (0.0040)	+0.0011 (0.0060)	+0.0021 (0.0052)	-0.0013 (0.0022)	-0.0023 (0.0025)
	% change	-3.88 %	-0.95 %	+2.63 %	+1.72 %	-1.86 %	-1.90 %
ε_H	0 hr	0.1964	0.2176	0.1983	0.2174	0.1987	0.2159
	24 hr	0.1975	0.2182	0.1988	0.2169	0.1994	0.2161
	$\Delta\varepsilon_H$	+0.0011 (0.0023)	+0.0006 (0.0020)	+0.0005 (0.0009)	-0.0005 (0.0025)	+0.0007 (0.0012)	+0.0001 (0.0006)
	% change	+0.93 %	+0.28 %	+0.49 %	-0.21 %	+0.33 %	+0.06 %
E_H *(MPa)*	0 hr	76.40	81.37	76.77	80.45	77.10	79.30
	24 hr	77.06	81.28	78.11	80.68	77.66	80.37
	ΔE_H	+0.65 (1.934)	-0.087 (0.901)	+1.34 (2.167)	+0.234 (0.106)	+0.557 (2.134)	+1.06 (1.112)
	% change	+0.89 %	-0.05 %	+1.56 %	+0.31 %	+0.85 %	+1.28 %

Table 9-2: Uniaxial testing results. Results for GA fixed bovine and porcine pericardium after 24 hours exposure to each of 3 solutions – buffered saline, 40 % glycerol (η), and glycerol/KI/deionised water (RI and η) - given as the absolute value before and after 24 hours' immersion in each fluid, the absolute value change (with standard deviation across all sample results), and the relative value change, expressed as a percentage.

9.1.4 Discussion

As no shrink/expansion test resulted in an average change of more than 0.9 % (and no individual sample had a change above 1.6 % for any time period) after 150 hours of submersion in the various solutions, as presented in Figure 9-10, it can be reasonably expected that any changes to the size of the tissue in the valve due to exposure to these solutions would not be large enough to cause significant changes to the functioning of the valves, such as a reduction in leaflet coaptation or increased stress on the stent attached to the leaflets.

However, it is interesting to note that the 100 % glycerol appeared to cause a slight swelling of the tissue in almost all cases, as well as causing the tissue to lose its opacity, as shown in Figure 9-6.

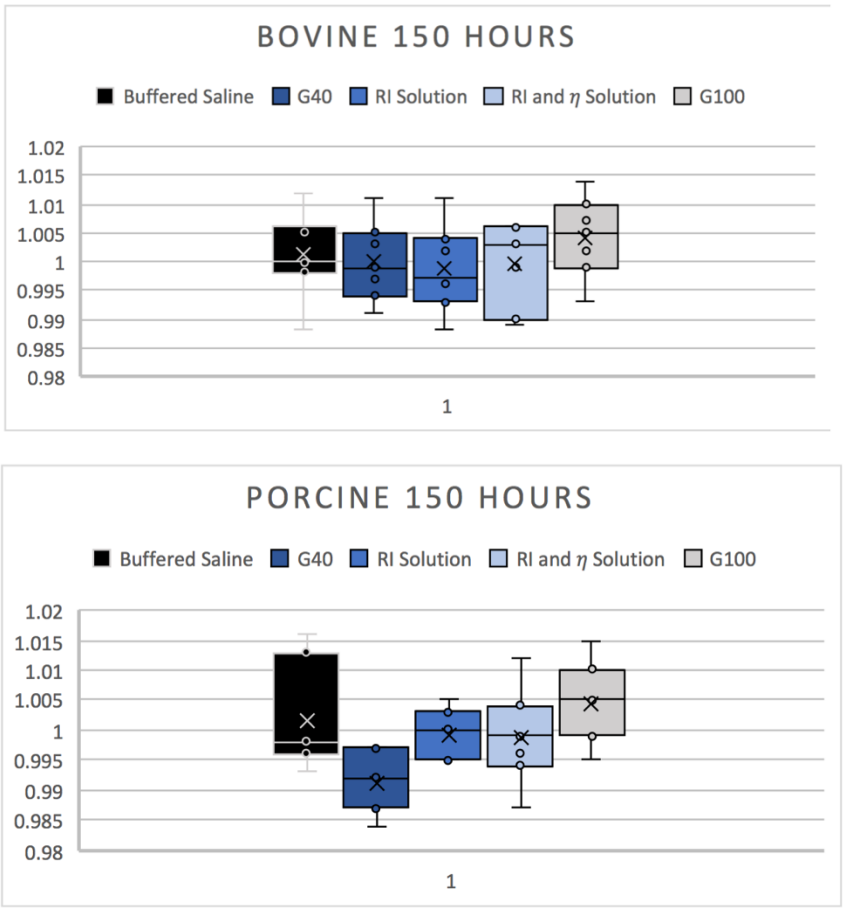

Figure 9-10: Box and whisker charts for the change in size of tissue samples after 150 hours exposure in the various testing fluids. For each fluid, the mean value is represented by an 'X', the median value by the central line, the box plot is bounded by the upper and lower quartiles, and the extremes of the whiskers are bound by the inter-quartile range from the median value.

The indications of the uniaxial experiments are that the effect of the fluids used during *in vitro* testing of bioprosthetic valves upon the stiffness of GA fixed porcine and bovine pericardial tissue is mainly confined to the elastin phase of deformation. Solutions of buffered phosphate saline, commonly used in the storage and testing of these devices, and a solution comprising glycerol, KI, and water, used to match the viscosity of the blood analogue used in testing to that of blood at high shear whilst also reducing PIV image artefacts via RI matching of the testing chamber and the fluid, both reduced the stiffness of the tissue by 8 – 13 % over a 24-hour period, a decrease in the modulus of the tissue of 0.1 – 0.3 MPa. This was observed for almost all of the samples to some degree as shown by the diagrams for E_L in Figure 9-8 and Figure 9-9, with just one of the

bovine samples showing an increase in stiffness of any magnitude. This reduction in stiffness could also be due to viscoelastic effects and microstructural reorganisation of collagen fibres away from the direction of the load[291].

Conversely, exposure of the tissues to a solution of 40% glycerol and 60 % buffered phosphate saline (by weight) indicated a stiffening of the samples on average, by 1.64 % (0.0035 MPa) for the bovine tissue and 6.52 % (0.145 MPa) for the porcine tissue. However, unlike the loosening effect observed for the other two solutions, consideration of the results for individual samples reveals that while most samples were stiffened after the exposure, others were loosened by up to 10.7 % for the bovine tissue and 15.0 % for the porcine tissue, making the overall average values obtained less compelling.

The maximum average change of high stress tissue stiffness, described by E_H, of 1.56 % across the different fluids is not sufficient to cause any major deviations in the response of the tissue to the flows during the *in vitro* experiments undertaken during the research for this thesis. Similarly, the change to the beginning or end to strain range of the transition phase (ε_L and ε_H respectively) of the tissue after 24-hour exposure to the various fluids did not exceed 3.9 %. In addition, these three parameters delivered both positive and negative changes to the recorded values at the start of testing for both tissue types and all fluids, suggesting that any effect caused by the solutions was within experimental variability, making conclusive statements about mechanical characteristic alteration unwise. Instead, it can be said that any changes to the 3 parameters discussed here, E_L, ε_L and ε_H, as a result of up to 24-hours exposure to the testing fluids to be used in the ensuing experiments would not result in functional differences to the response of the pericardial tissue between the start and end of testing.

Although these findings indicate that the mechanical characteristics of the GA fixed pericardial tissue is altered within low stress environments after exposure to the common testing fluids presented, the changes within the expected lifetime of the tests planned for this thesis keep the E_L well within the expected range encountered both during this test and in the literature[218]. Due to the variability of the mechanical properties of both GA fixed- and native- pericardial tissue, a change of 0.3 MPa within a range of 1.93 ± 5.96 MPa or 2.24 ± 0.76

MPa (the measured range of E_L for bovine and porcine GA fixed pericardium in this experiment) will not significantly alter the mechanical response of the tissue in comparison to another piece of tissue. In other words, the tissue will still respond to low stresses after 24-hours submersed in one of the testing fluids in a similar way to another piece of tissue that has not been exposed.
However, the consistent stiffening of the porcine and bovine GA fixed pericardium after exposure to glycerol, alongside the slight expansion and translucent effect caused by the 100 % glycerol solution in the shrink/expansion test, indicates that glycerol does alter the mechanical characteristics of GA fixed bovine and porcine pericardial tissue over time, as previously indicated in the literature[240,241], even if it does not do so to a valve-function altering extent during the lifetime of these experiments. Further investigation of the long-term effect of glycerol upon GA fixed pericardial tissue could elucidate further detail on the alterations, and storage of bioprosthetic valves with GA fixed pericardial leaflets in glycerol is to be avoided until the effects of the chemical can be clarified.

9.1.4.1 Limitations

The results presented in this chapter are based on some assumptions and limitations that need to be addressed in order to ensure that the conclusions above are taken in the correct context. Firstly, in order to simplify the analysis, the cross-sections of the tissue samples were assumed to be a uniform rectangular shape, with 2 sides equal to the average thickness of each sample and 2 sides equal to 2.0 mm, the intended width of the central strip of the dumbbell. However, these values may not be uniform along the strip of tissue, and furthermore this cross-section will be altered in accordance to Poisson's ratio as the sample is extended and unloaded. Stress concentrations at the grip edges will have been reduced by use of a dumbbell shaped tissue sample[290], but it is not expected that their effect was completely eliminated from the experiment. In addition, although the tissue samples were cut with an attempt to broadly keep the fibre alignment at 45 ° through the sample, this was not completely achievable due to the variation of fibre alignment in every sheet of GA fixed pericardial tissue.

However, as the intent of this experiment was to observe relative mechanical differences to the tissue samples before and after exposure to the various testing fluids investigated, these limitations do not fundamentally affect the findings.

9.1.5 Concluding Remarks

In this chapter, GA fixed bovine and porcine pericardial tissue, used in both surgical and transcatheter bioprosthetic heart valves, was uniaxially tested before and after 24-hour exposure to 3 solutions used during *in vitro* testing, in order to determine whether these fluids would affect the mechanical characteristics of the tissue leaflets during the testing procedure, making comparison between a setup used at the start of testing and a setup used at the end of testing problematic. It was concluded that the high stretch modulus and transition phase of both tissues are negligibly affected by all of the fluids during a testing time period, and that the low stretch modulus may be altered, but, if so, the mechanical properties of the tissue at low stress remain representative of the tissue type, and should not functionally change the fluid dynamics resulting from the bioprosthetic valve. It was also concluded that the tissue would not undergo significant shrinkage or expansion during the benchtop studies of the valves.

Accordingly, it was decided that these three solutions, buffered phosphate saline, 40 % glycerol/ 60 % buffered saline, and a combination of KI, glycerol, and deionised and filtered water, could be used during *in vitro* experiments where the required testing procedure did not require the valves to be submersed in the testing fluid for a period of more than 24 hours. As none of the subsequent investigations are expected to require the bioprosthetic valves to be in the pulse duplicator for more than 24 hours in total, it can be confirmed that Glycerol and Potassium Iodide, chemicals used to alter the properties of fluids used during *in vitro* tests upon heart valves, do not significantly alter the stiffness of the porcine or bovine pericardial tissue of the valves during the lifetime of the test.

As the experiments for Chapter 4, Physiological Vortices in the Sinuses of Valsalva, had already necessarily commenced before the investigation described in this chapter could be concluded, due to the time constraints of the

PhD programme, the use of glycerol, previously indicated by the literature to have an effect upon the GA fixed pericardial tissue, was omitted, meaning the blood analogue did not have a dynamics viscosity similar to that of blood at high shear. Accordingly, the blood analogue used consisted of deionised water and KI in a 100:77 ratio by weight, in order to raise the RI of the fluid to reduce image distortions due to the non-orthogonal interface of silicone mock aortic root and blood analogue. However, the benchtop experiments of Chapters 5 and 6 did incorporate the findings of this chapter, and the fluid used in these experiments could match both the RI of the silicone mock aortic root and the viscosity of blood at high shear.

9.2 Additional PIV images from Physiological Vortices in the Sinuses of Valsalva

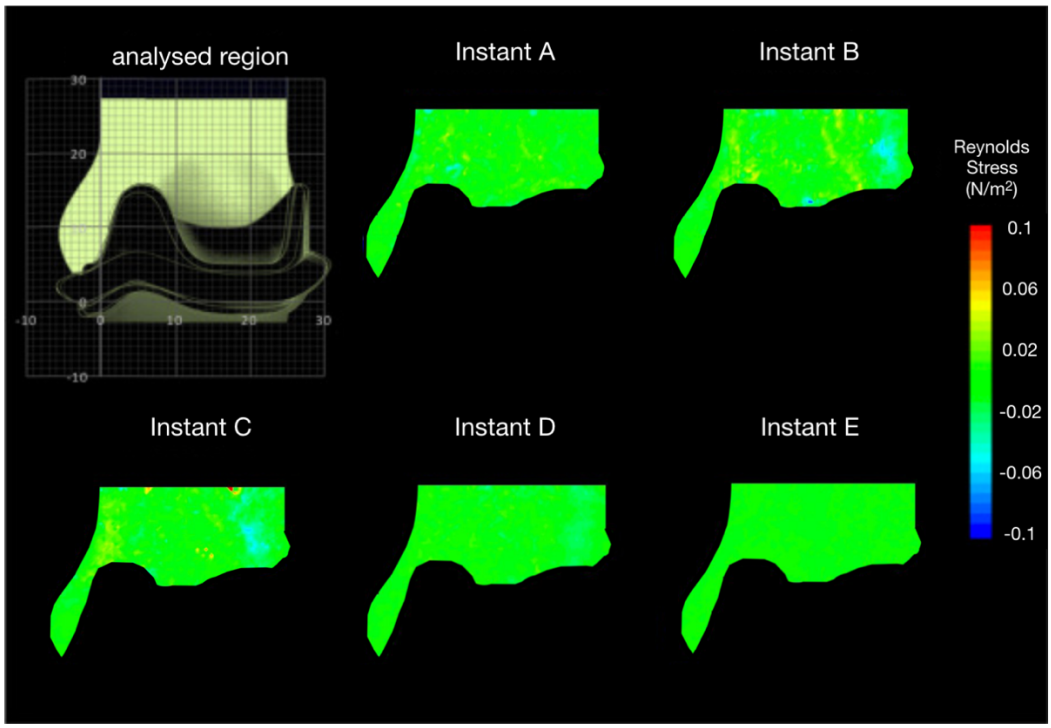

Figure 9-11: RSS contour maps for the physiological root configuration.

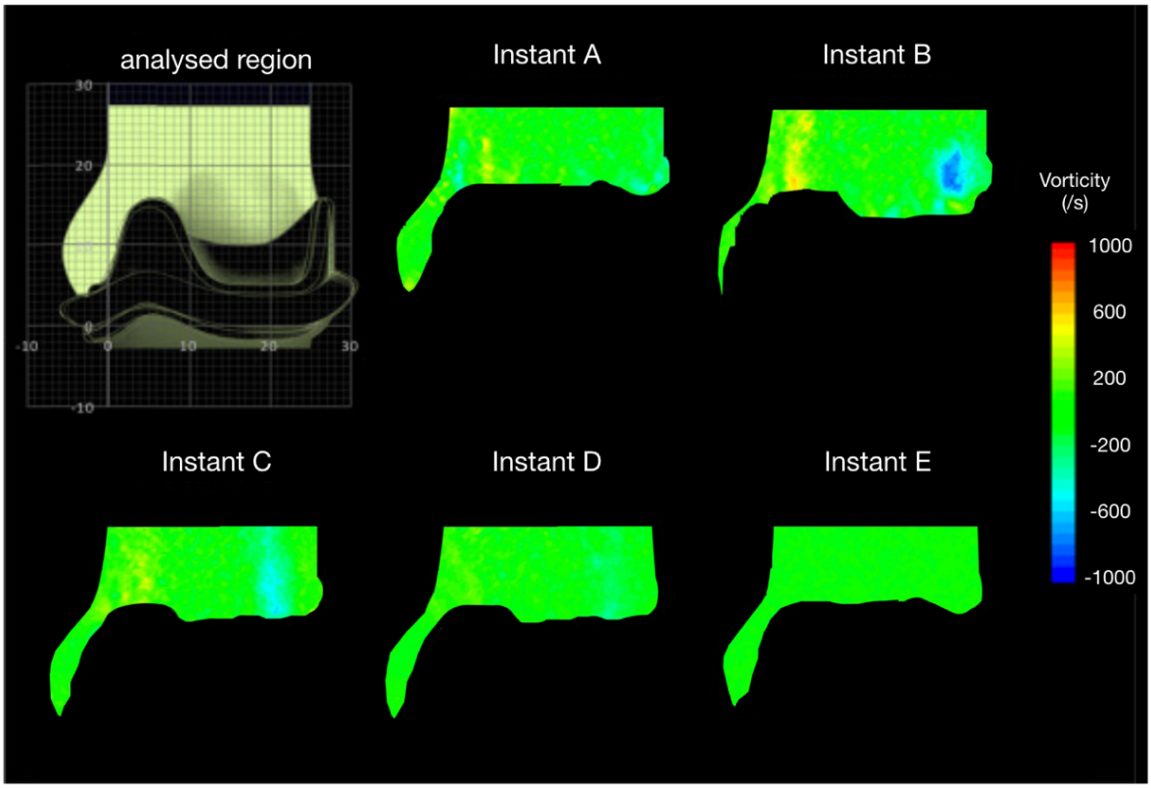

Figure 9-12: Vorticity contour maps for the physiological root configuration.

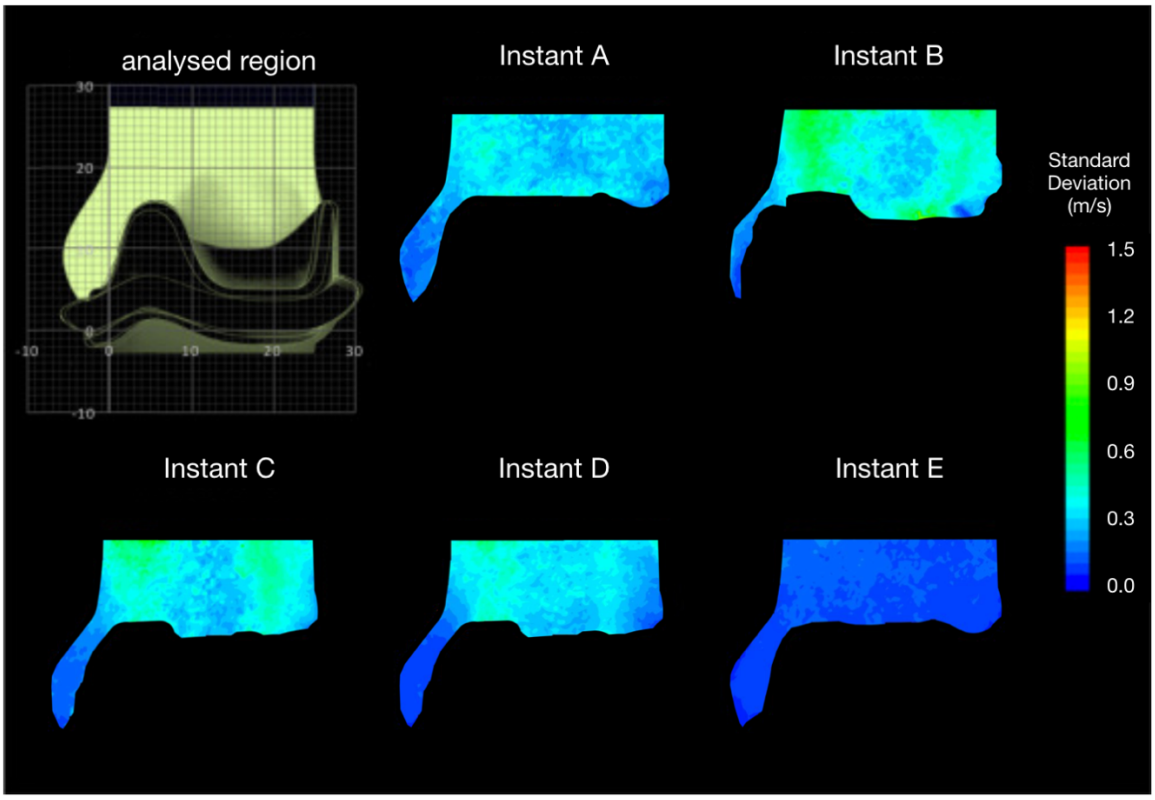

Figure 9-13: Standard Deviation contour maps for the physiological root configuration.

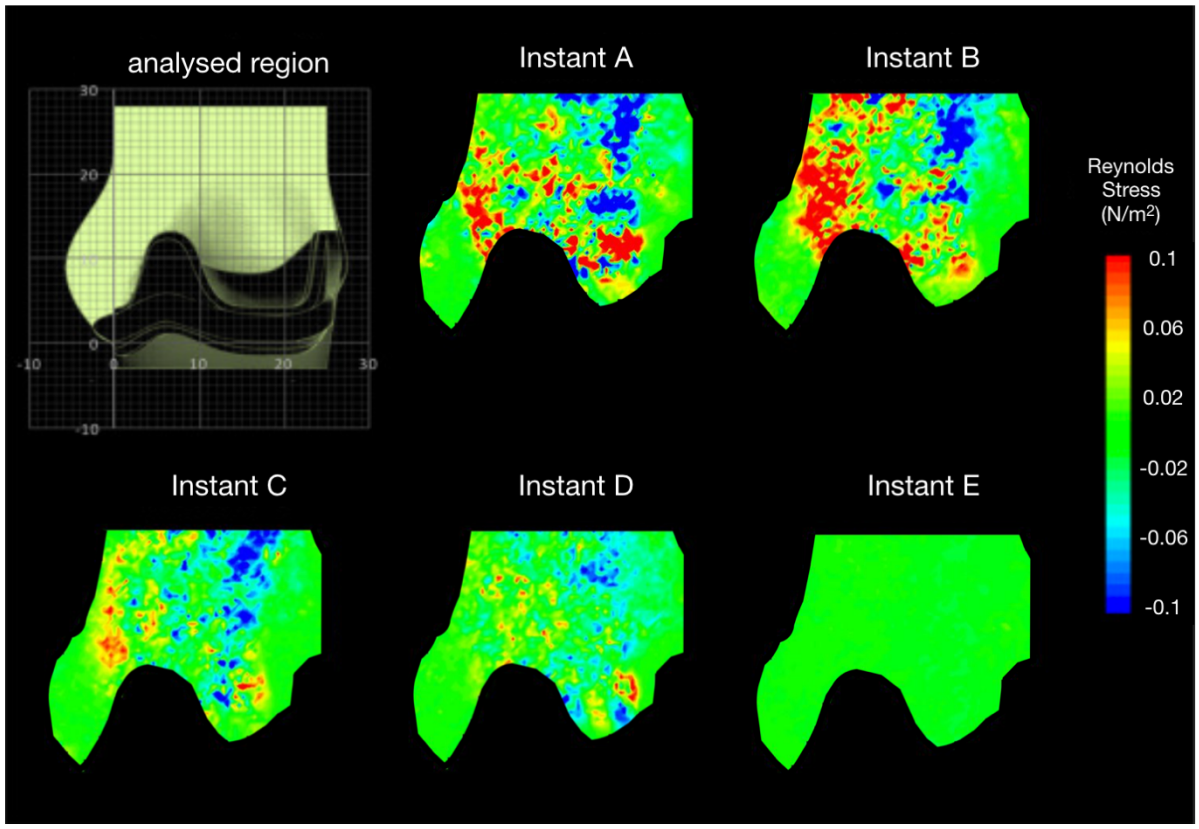

Figure 9-14: RSS contour maps for the optimal surgical root configuration.

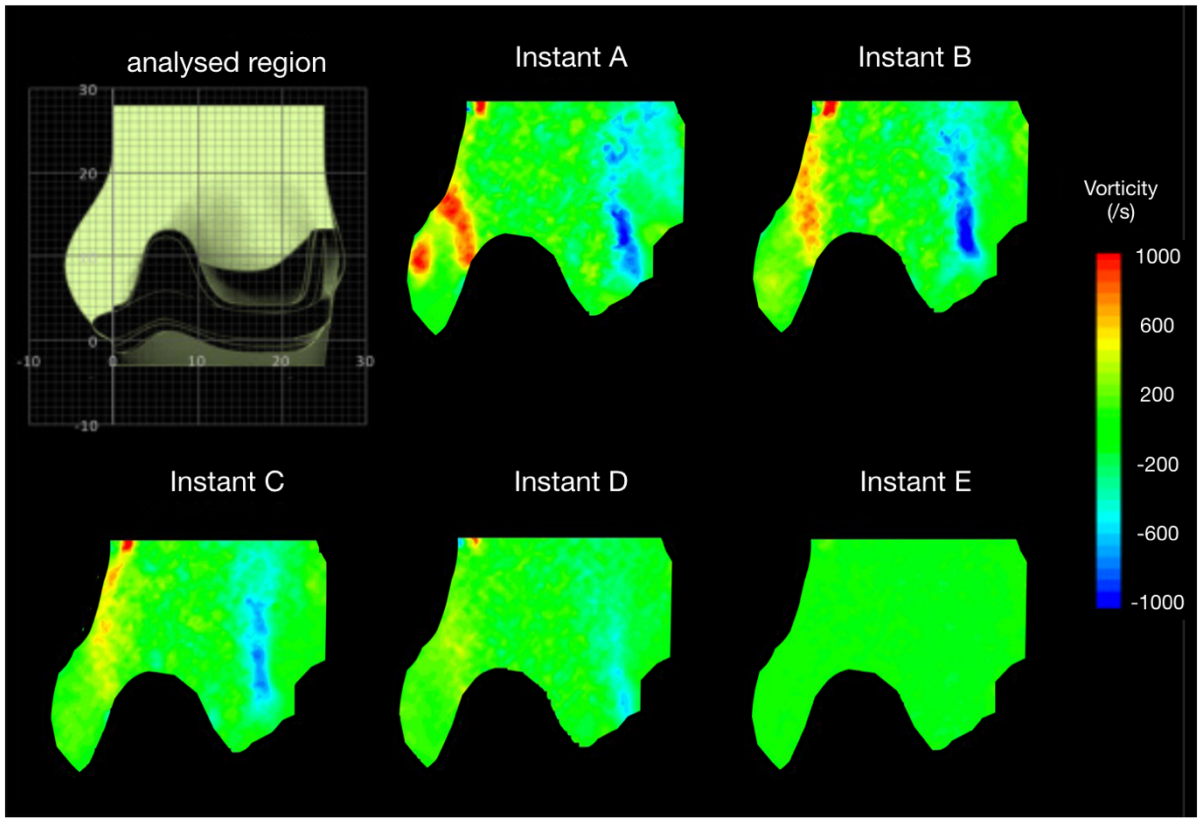

Figure 9-15: Vorticity contour maps for the optimal surgical root configuration.

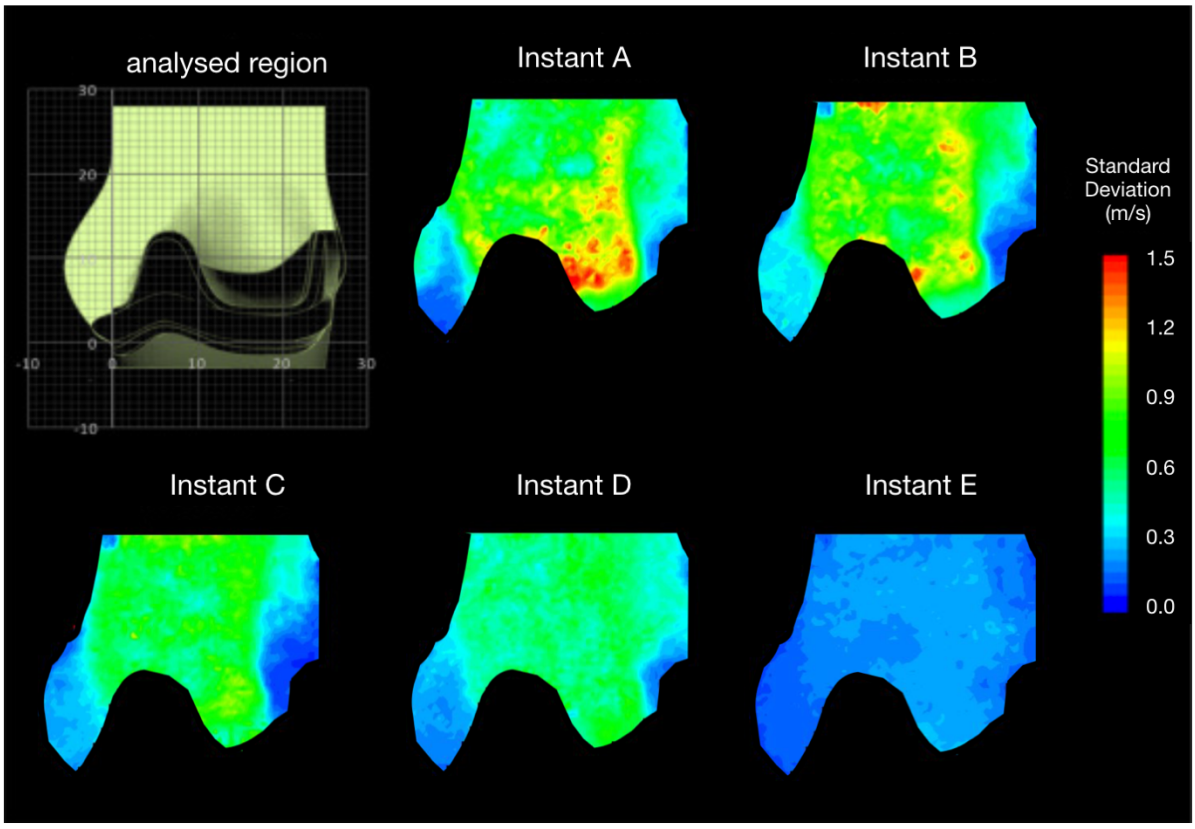

Figure 9-16: Standard Deviation contour maps for the optimal surgical root configuration.

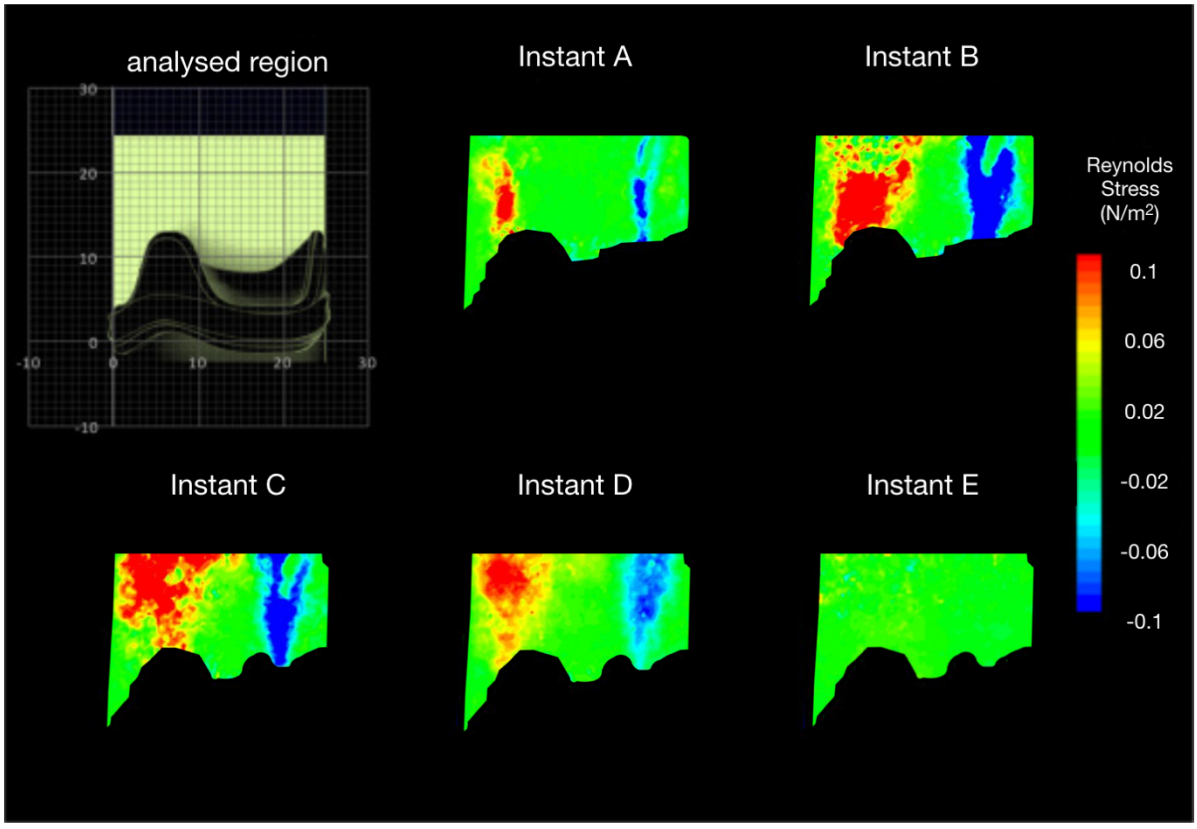

Figure 9-17: RSS contour maps for the sinusless root configuration.

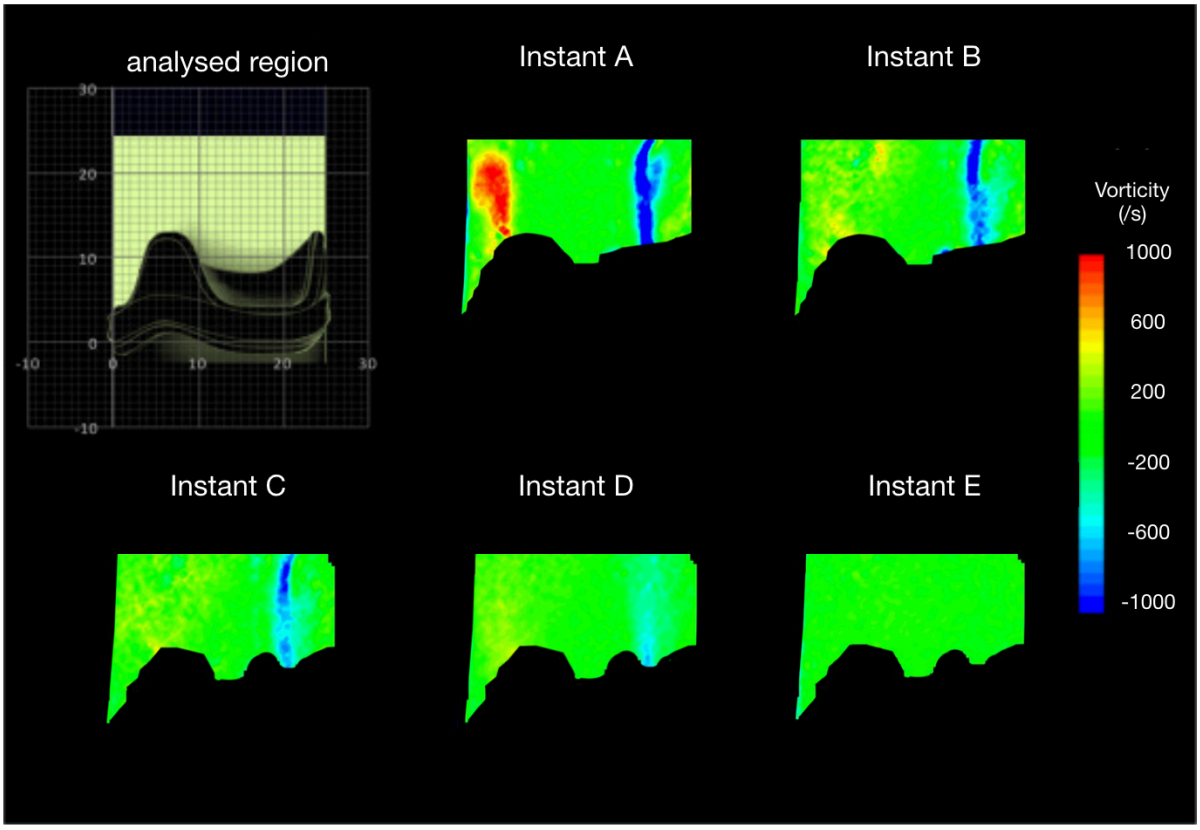

Figure 9-18: Vorticity contour maps for the sinusless root configuration.

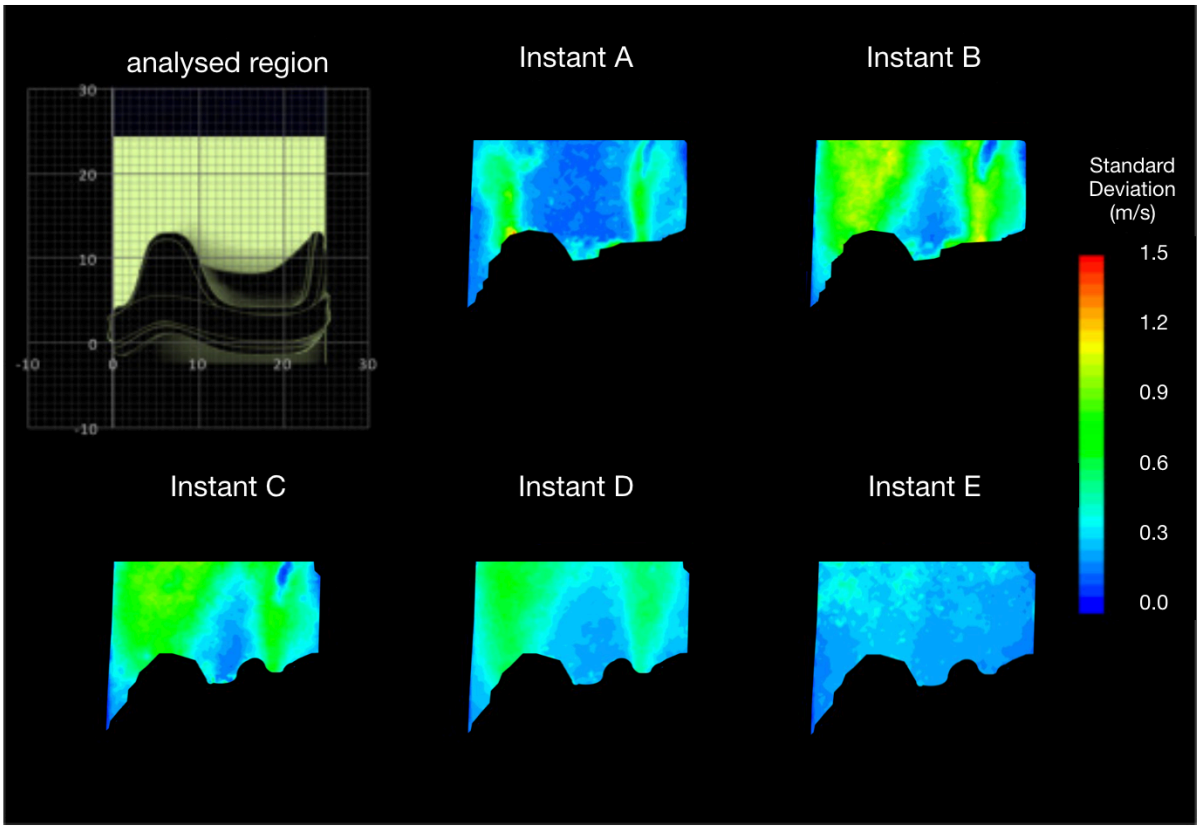

Figure 9-19: Standard Deviation contour maps for the sinusless root configuration.

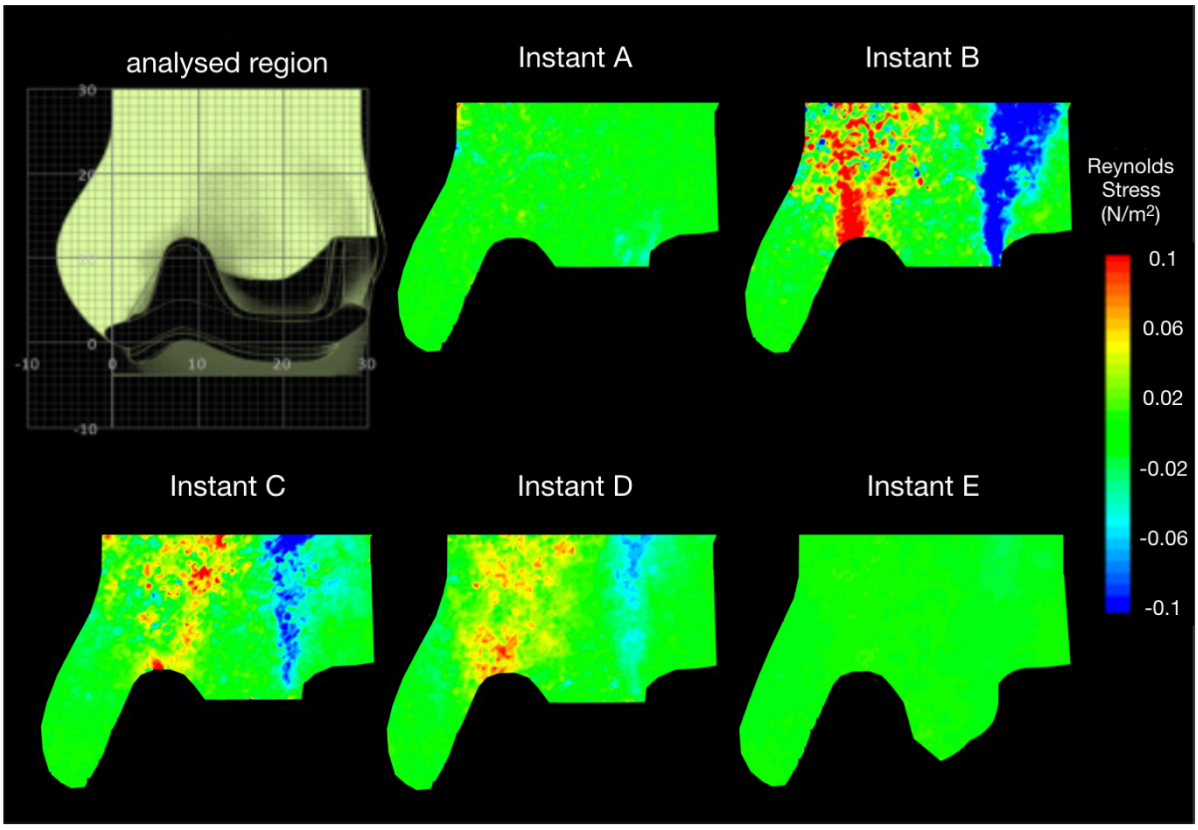

Figure 9-20: RSS contour maps for the oversized/dilated root configuration.

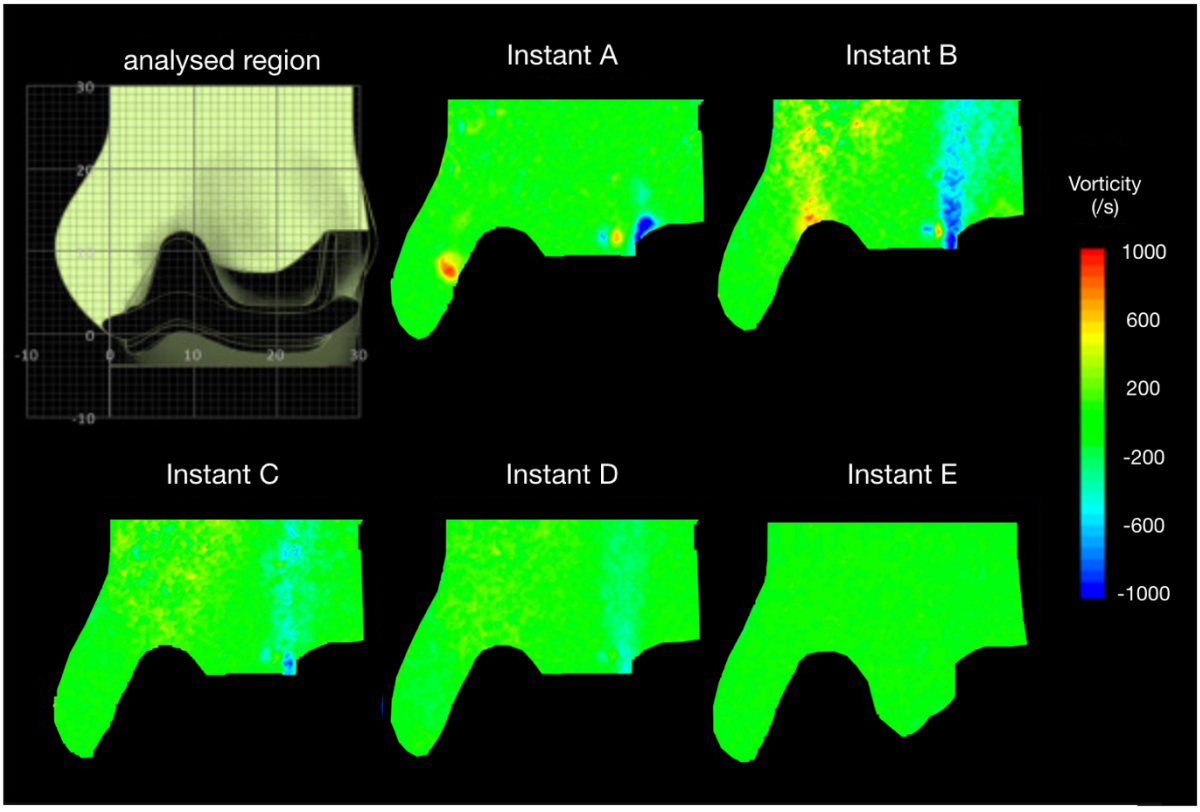

Figure 9-21: Vorticity contour maps for the oversized/dilated root configuration.

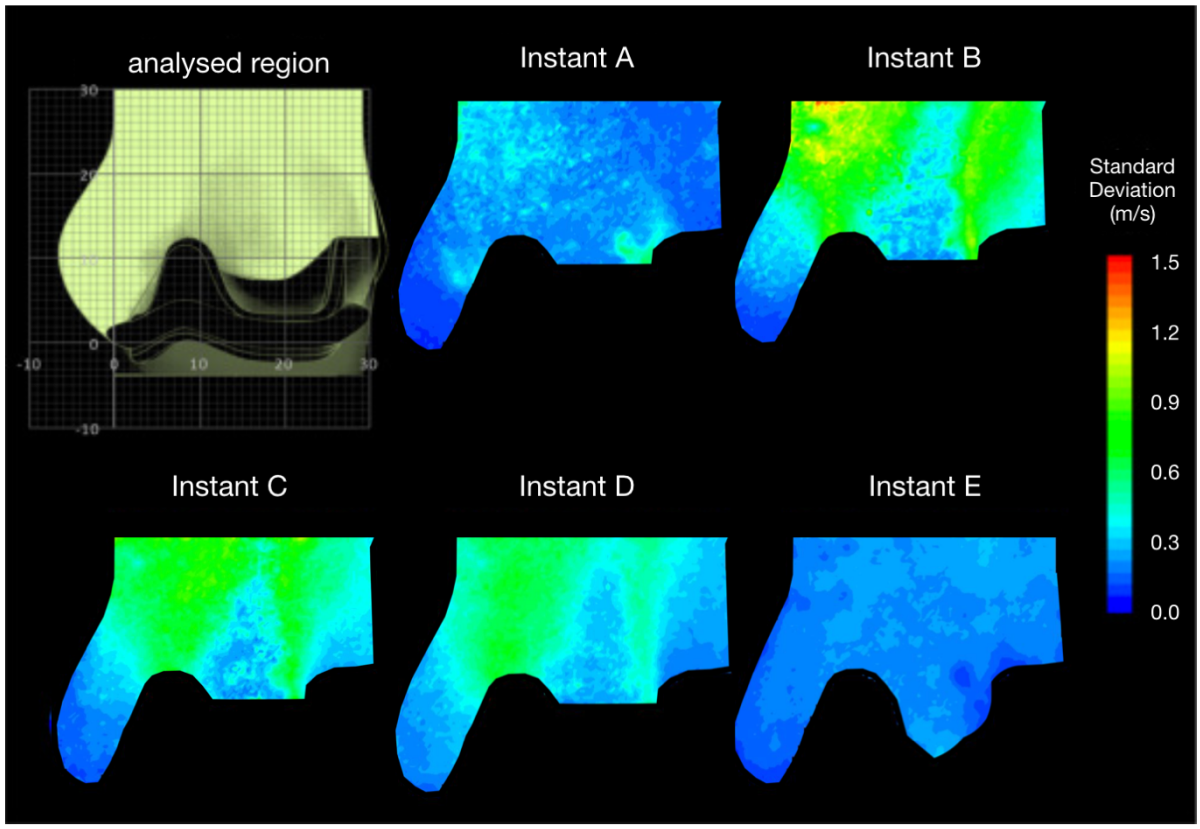

Figure 9-22: Standard Deviation contour maps for the oversized/dilated root configuration.

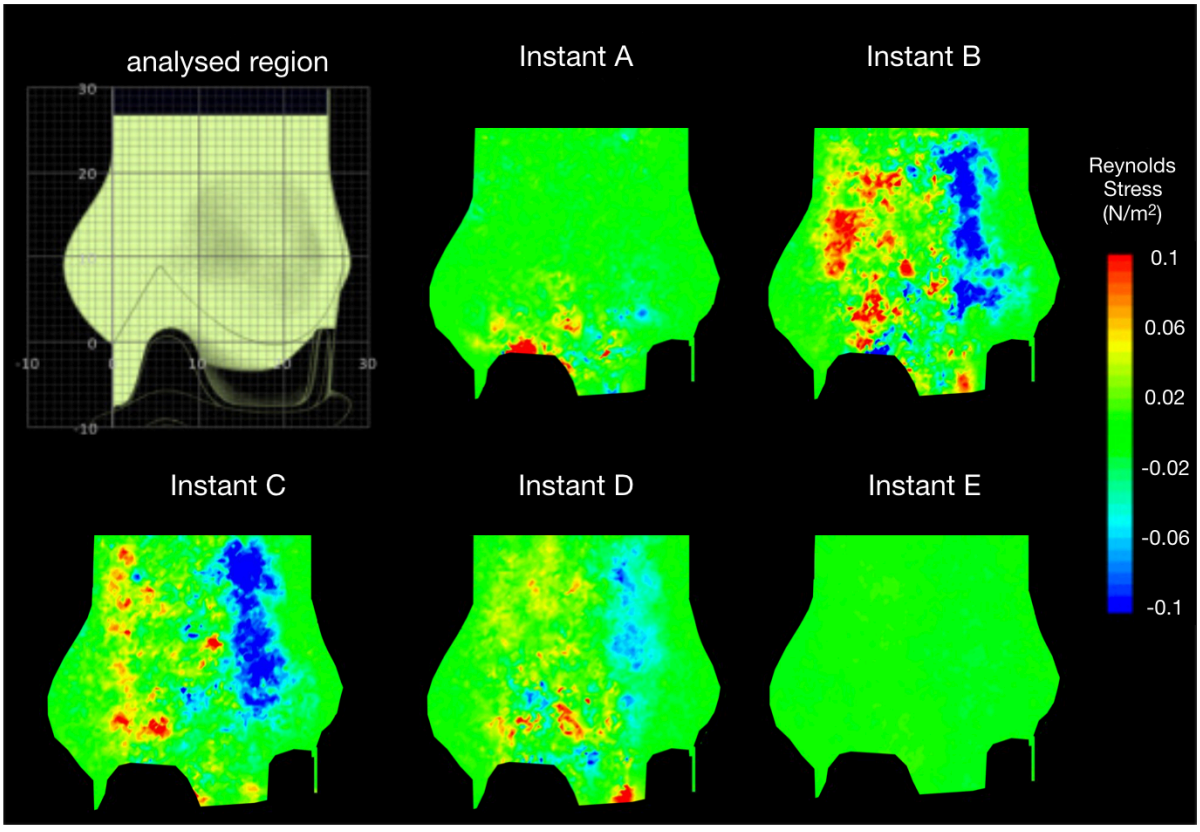

Figure 9-23: RSS contour maps for the sub-annular root configuration.

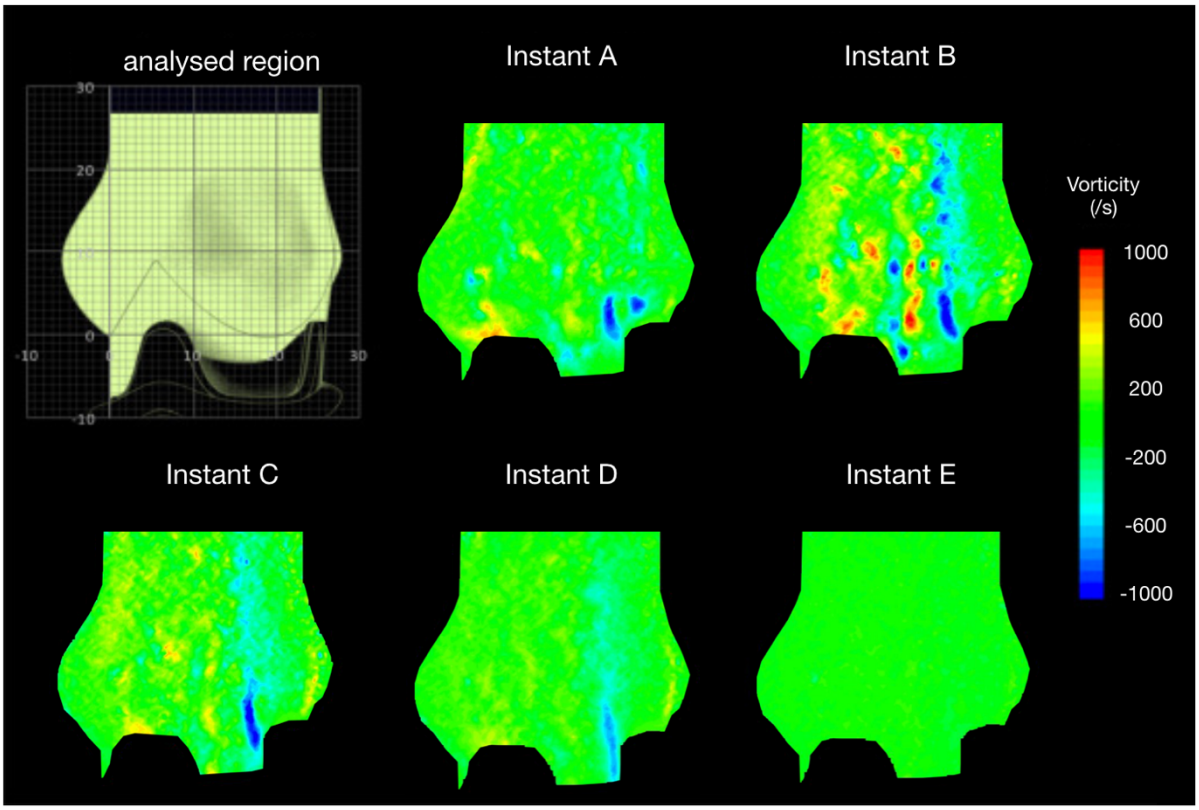

Figure 9-24: Vorticity contour maps for the sub-annular root configuration.

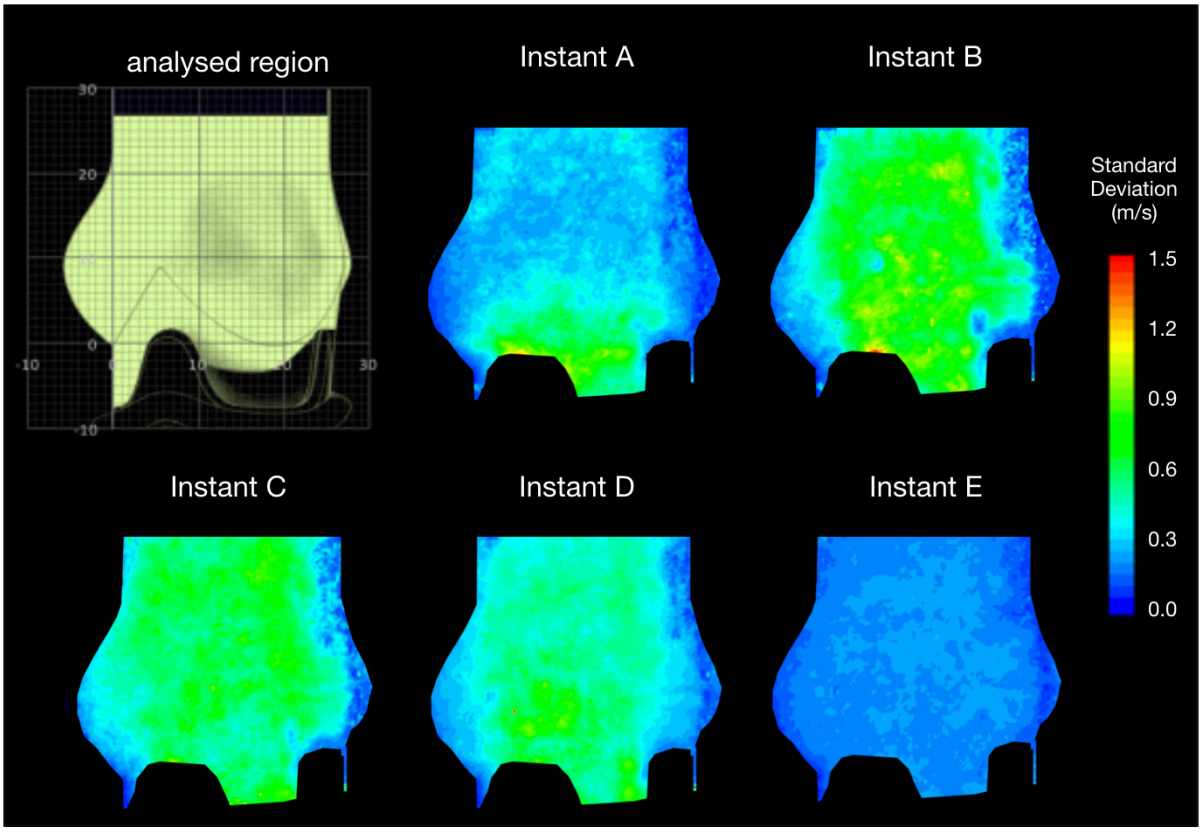

Figure 9-25: Standard Deviation contour maps for the sub-annular root configuration.

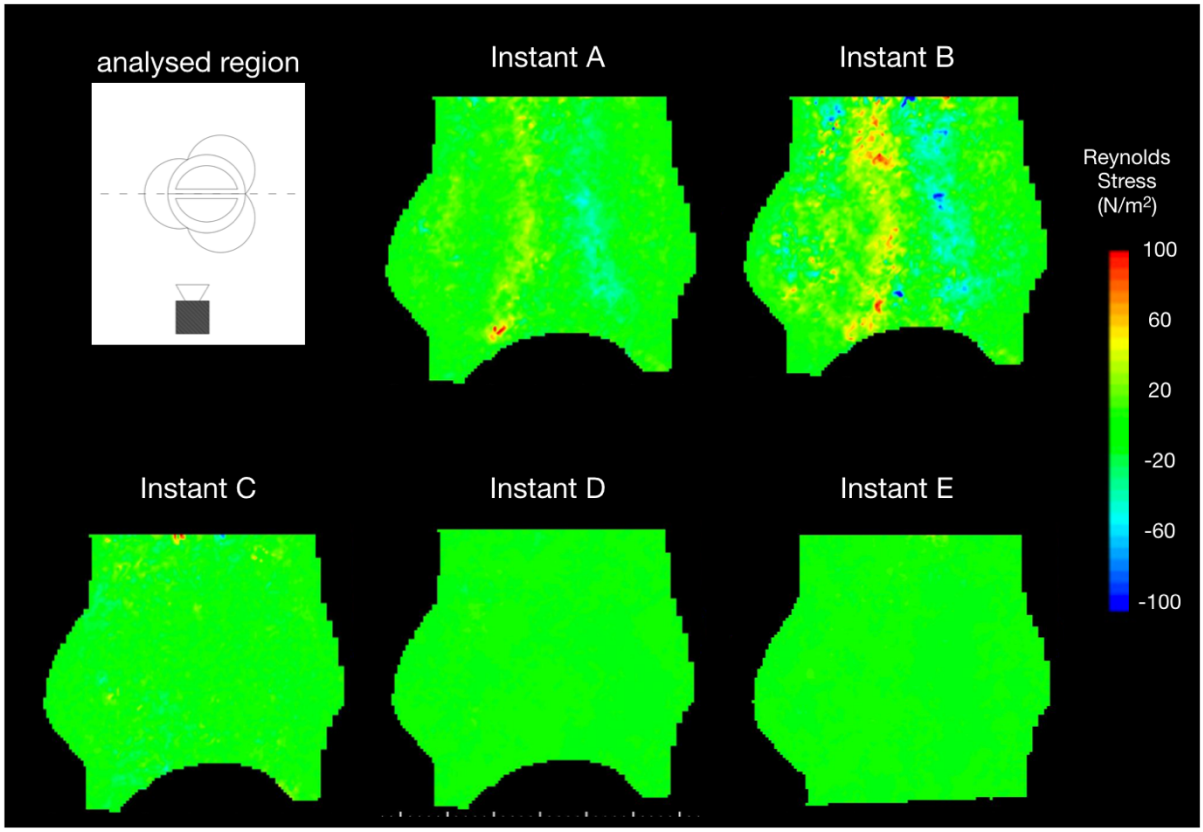

Figure 9-26: RSS contour maps for the mechanical root configuration.

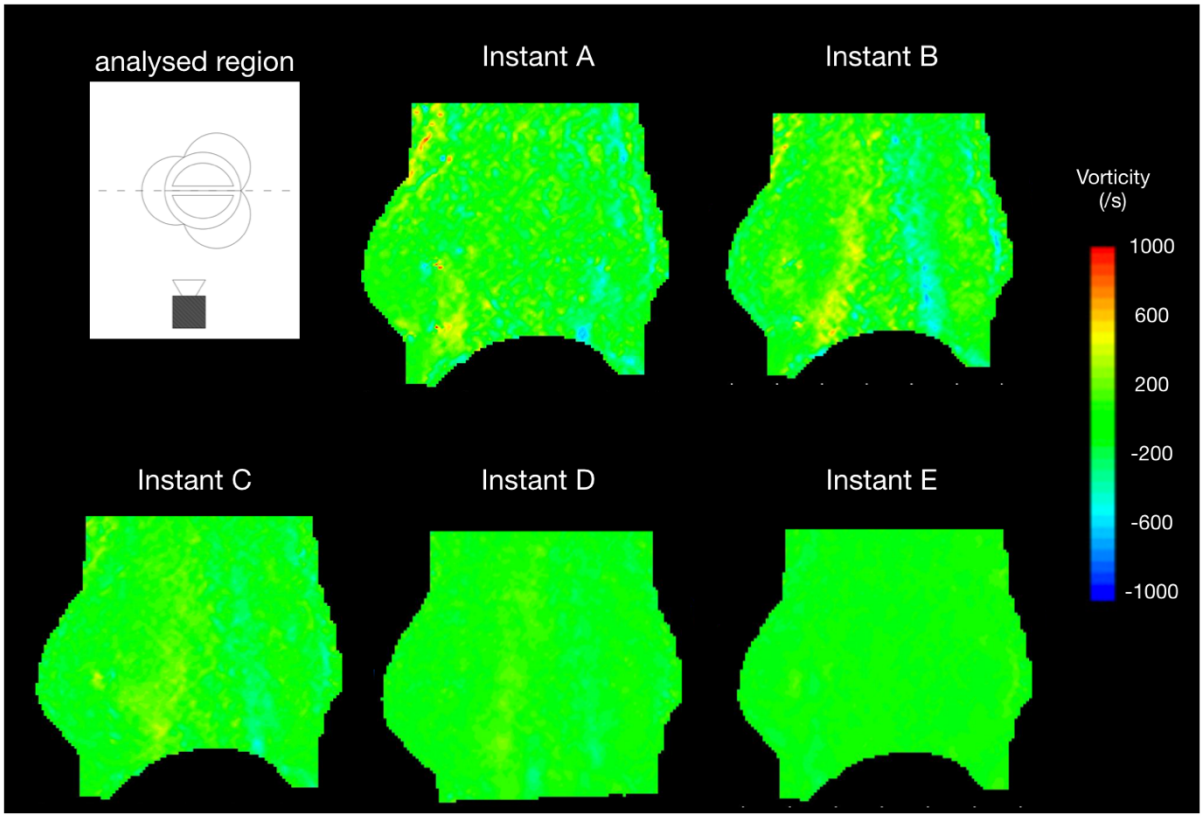

Figure 9-27: Vorticity contour maps for the mechanical root configuration.

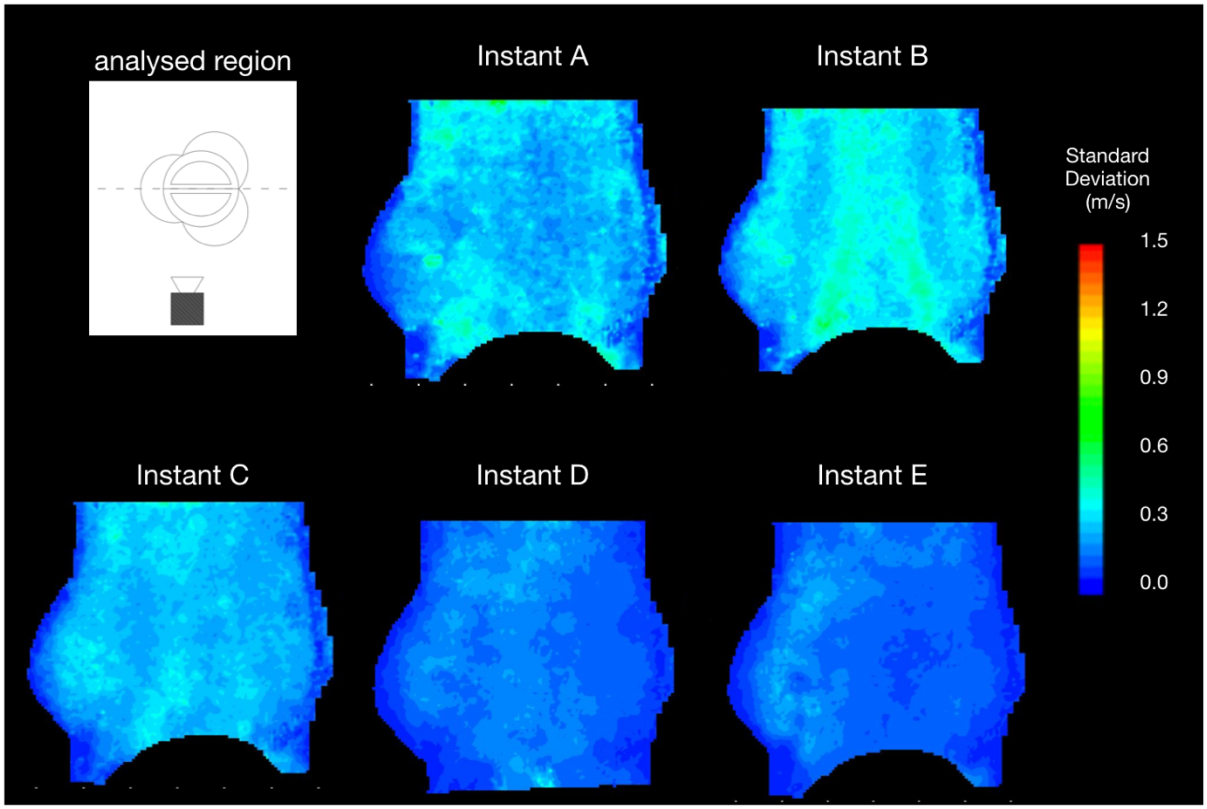

Figure 9-28: Standard Deviation contour maps for the mechanical root configuration.

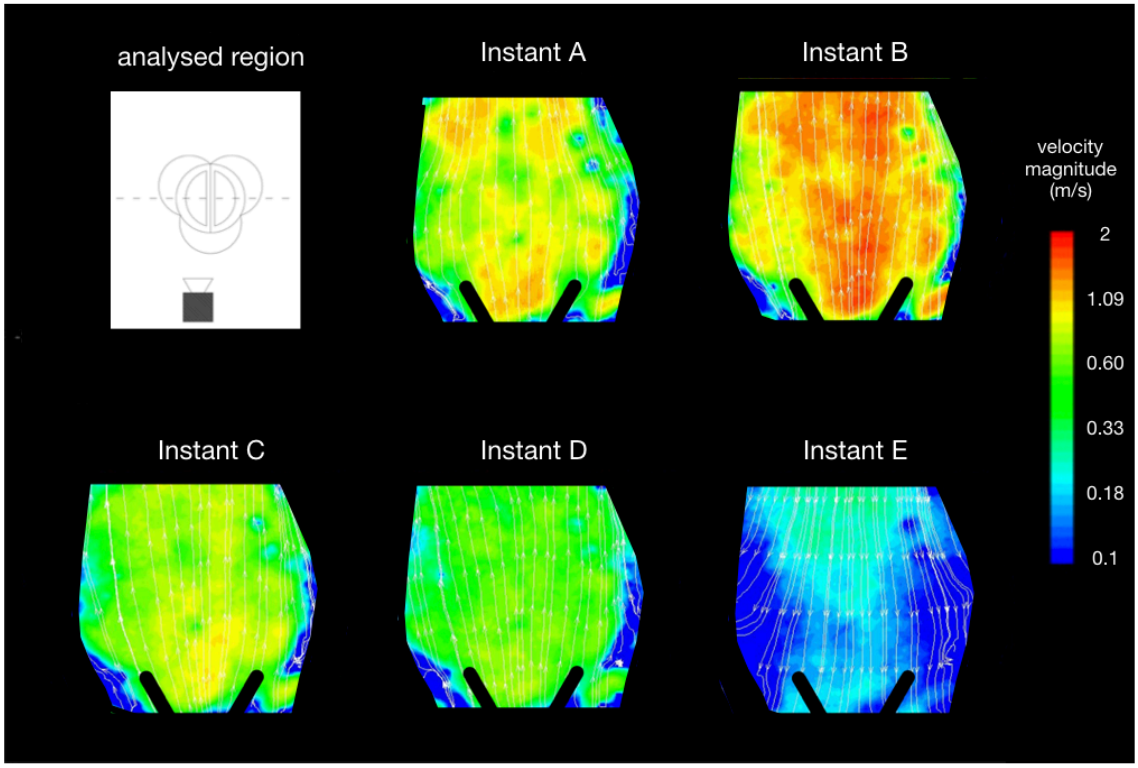

Figure 9-29: Velocity contour maps for the mechanical valve configuration, with the PIV laser sheet over the cross-section of the root and valve where the valve is at 90 ° rotation to that of the orientation shown in Figure 4-16.

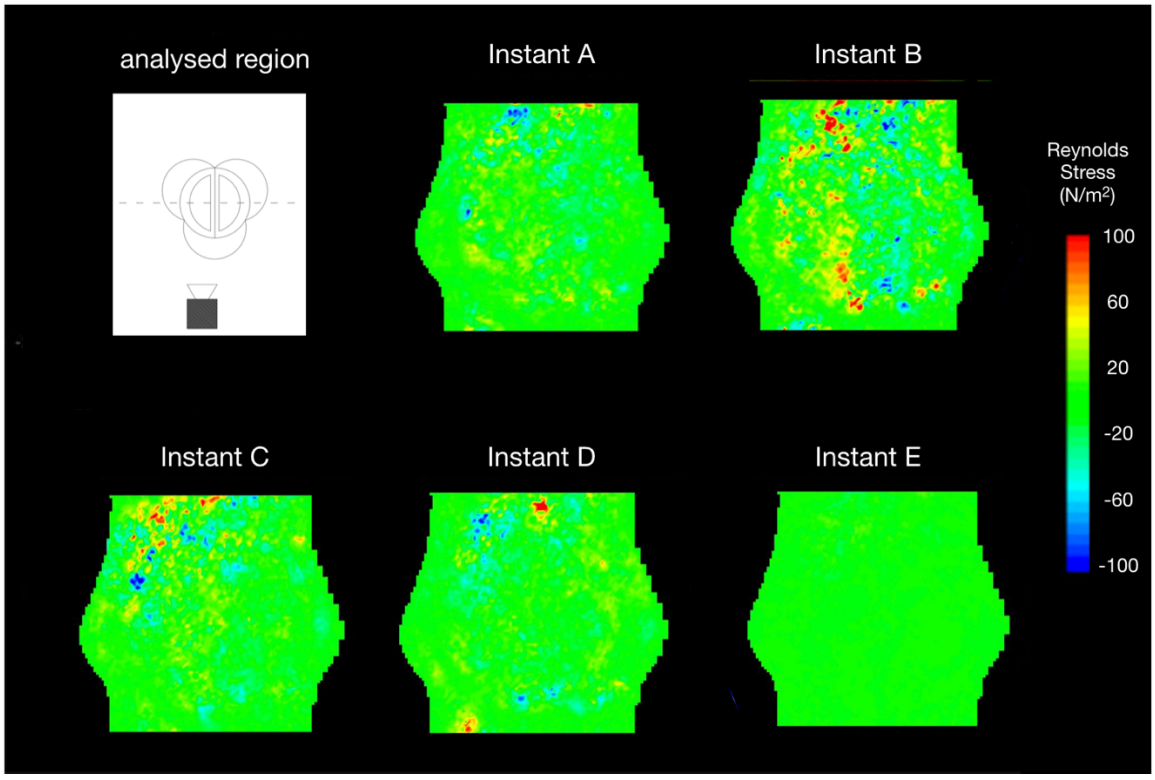

Figure 9-30: RSS contour maps for the mechanical valve configuration, with the PIV laser sheet over the cross-section of the root and valve where the valve is at 90 ° rotation to that of the orientation shown in Figure 4-16.

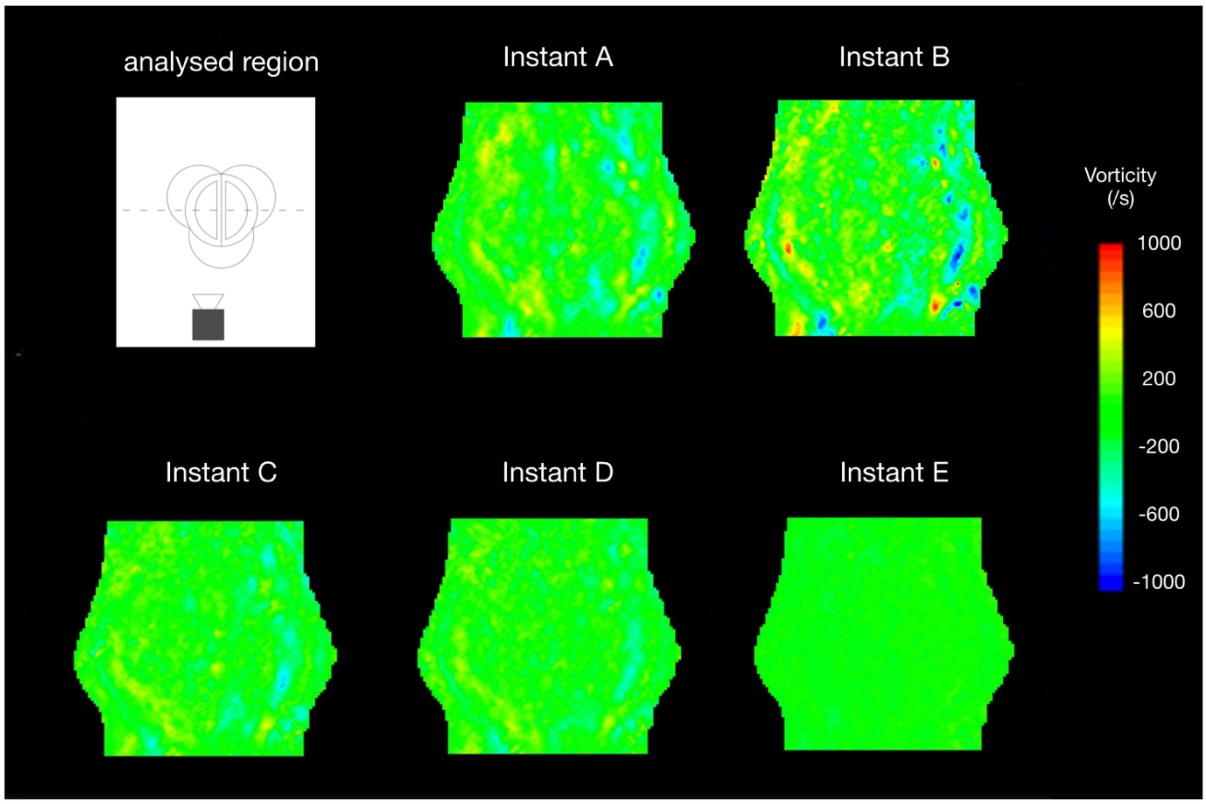

Figure 9-31: Vorticity contour maps for the mechanical valve configuration, with the PIV laser sheet over the cross-section of the root and valve where the valve is at 90 ° rotation to that of the orientation shown in Figure 4-16.

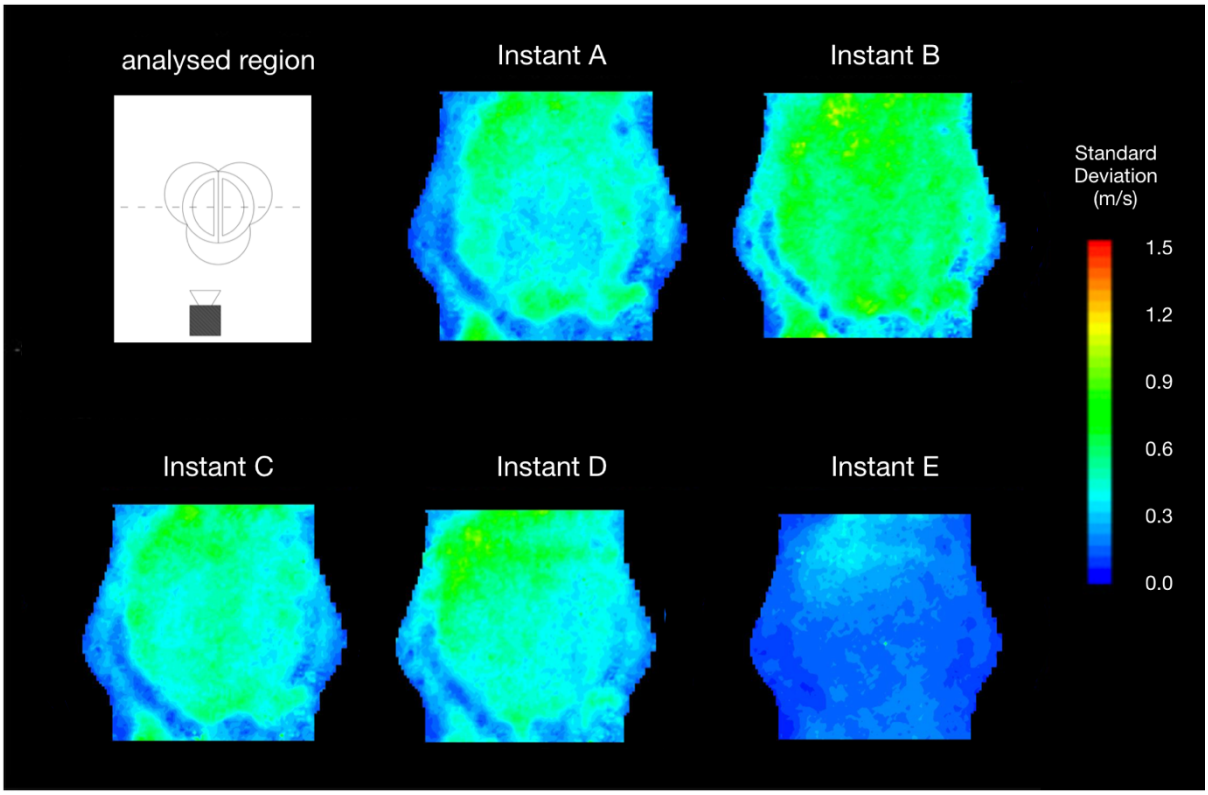

Figure 9-32: Standard Deviation contour maps for the mechanical valve configuration, with the PIV laser sheet over the cross-section of the root and valve where the valve is at 90 ° rotation to that of the orientation shown in Figure 4-16.

9.3 Additional PIV images from Does Transcatheter Aortic Valve Alignment Matter?

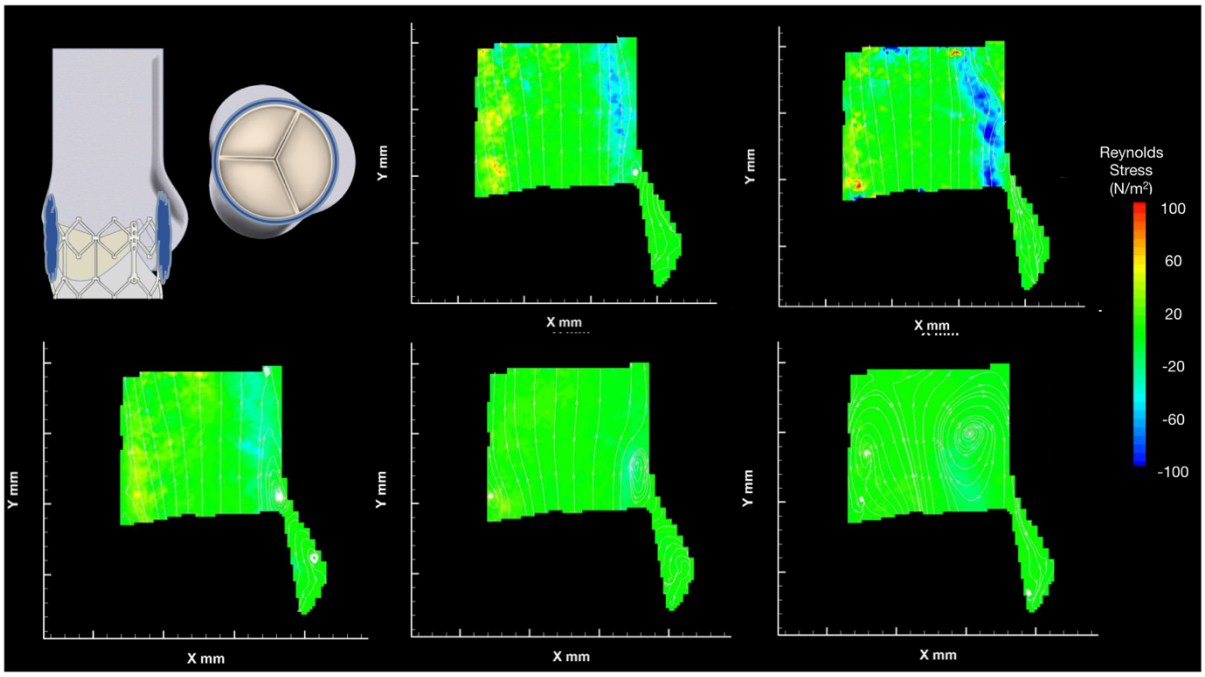

Figure 9-33: RSS contour maps for the TA1 configuration.

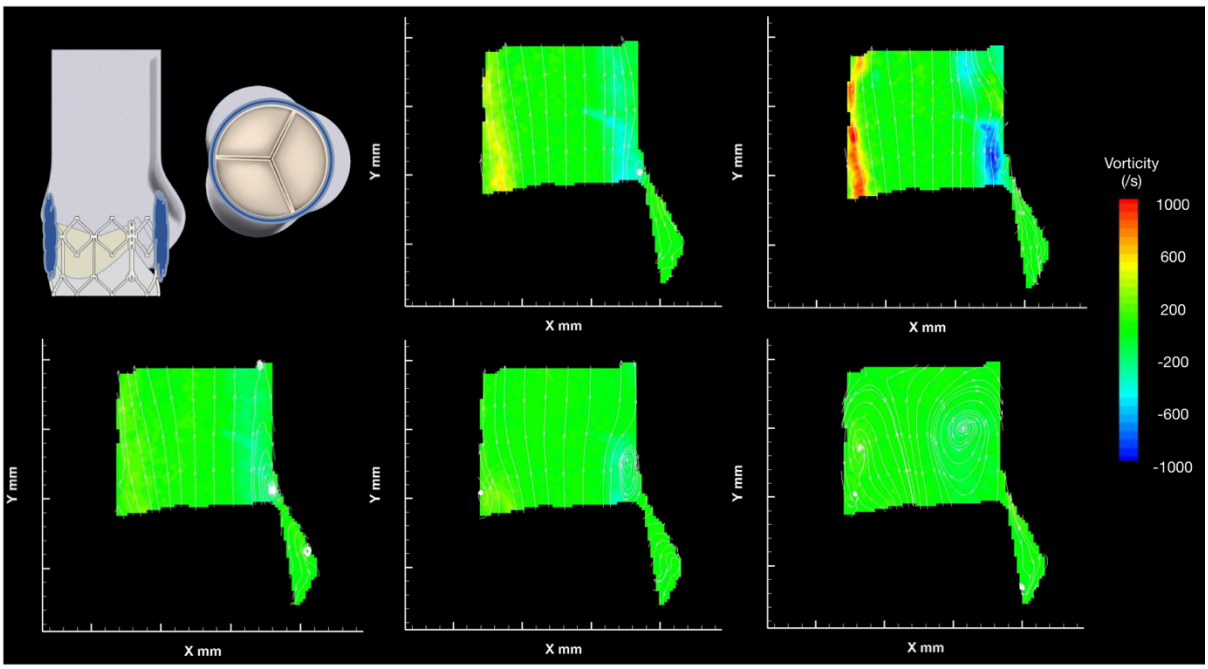

Figure 9-34: Vorticity contour maps for the TA1 configuration.

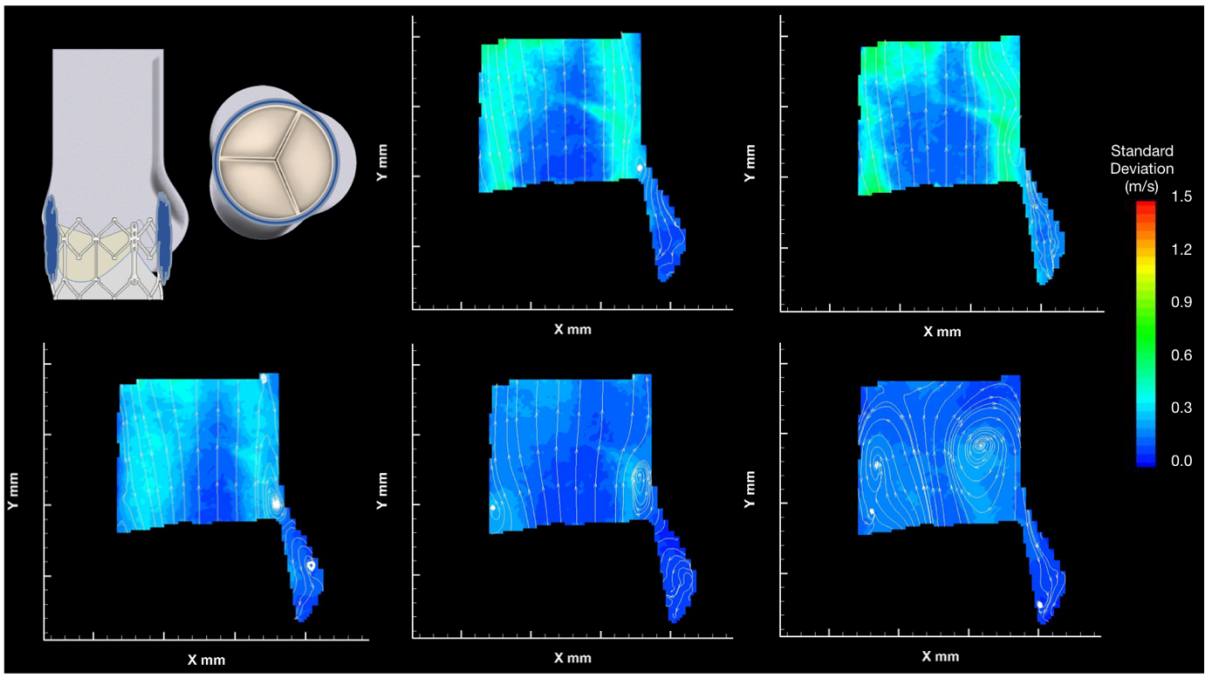

Figure 9-35: Standard Deviation contour maps for the TA1 configuration.

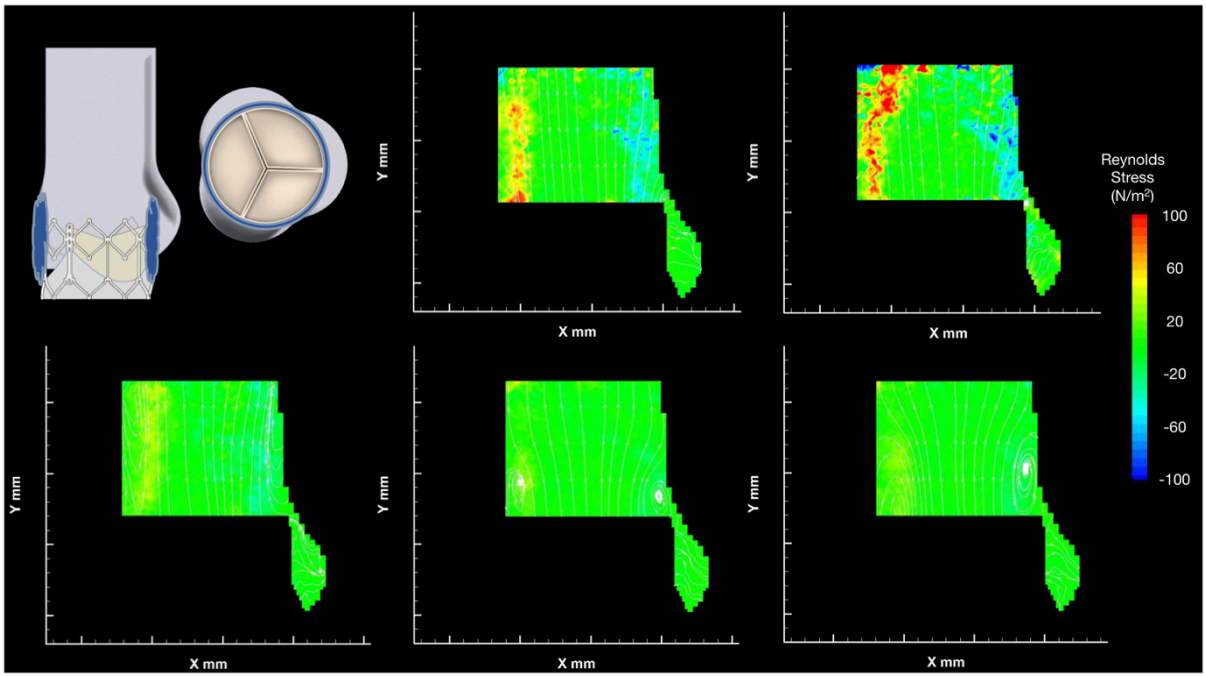

Figure 9-36: RSS contour maps for the TA2 configuration.

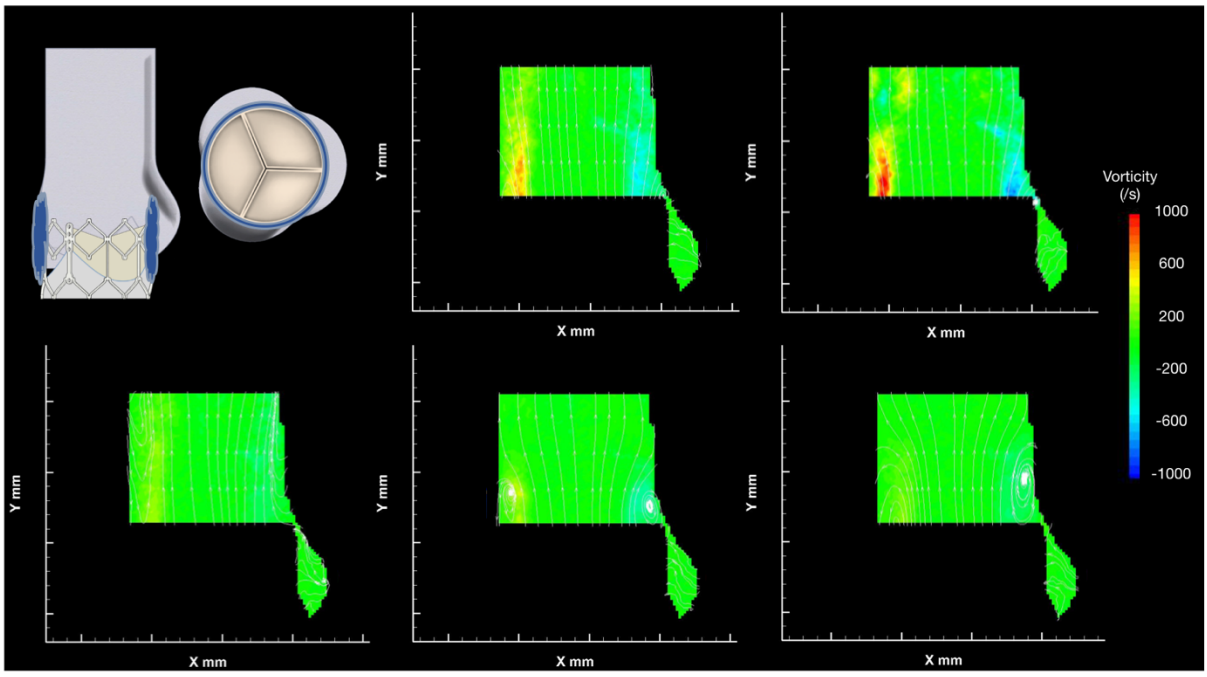

Figure 9-37: Vorticity contour maps for the TA2 configuration.

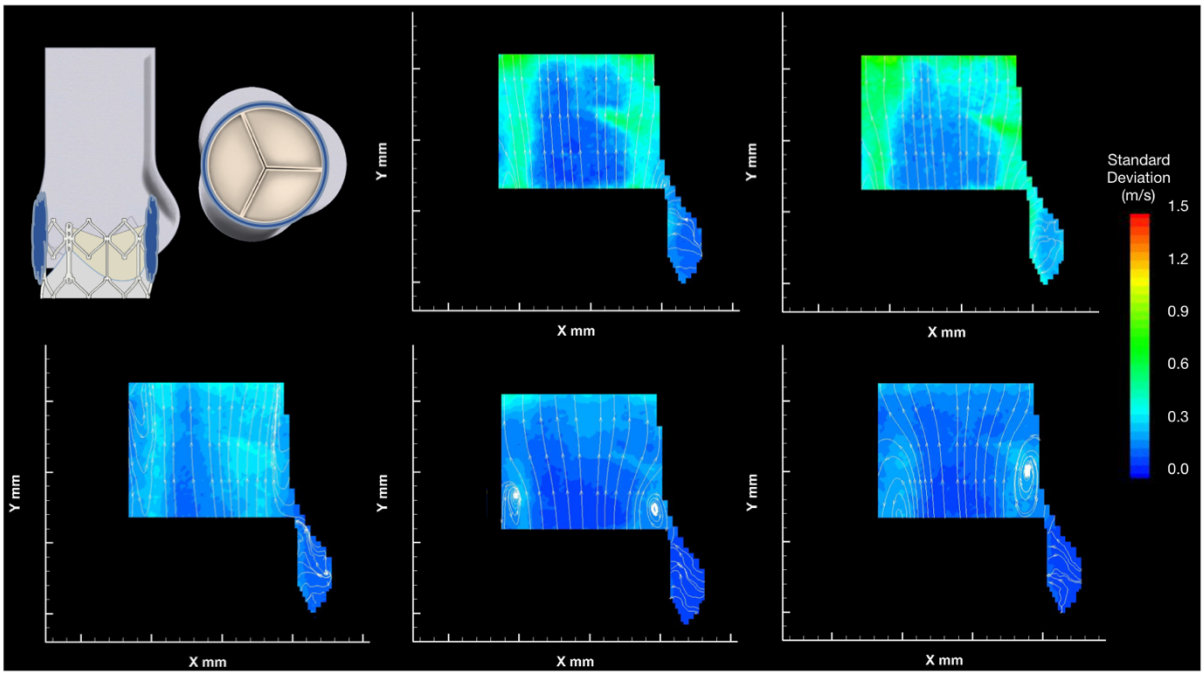

Figure 9-38: Standard Deviation contour maps for the TA2 configuration.

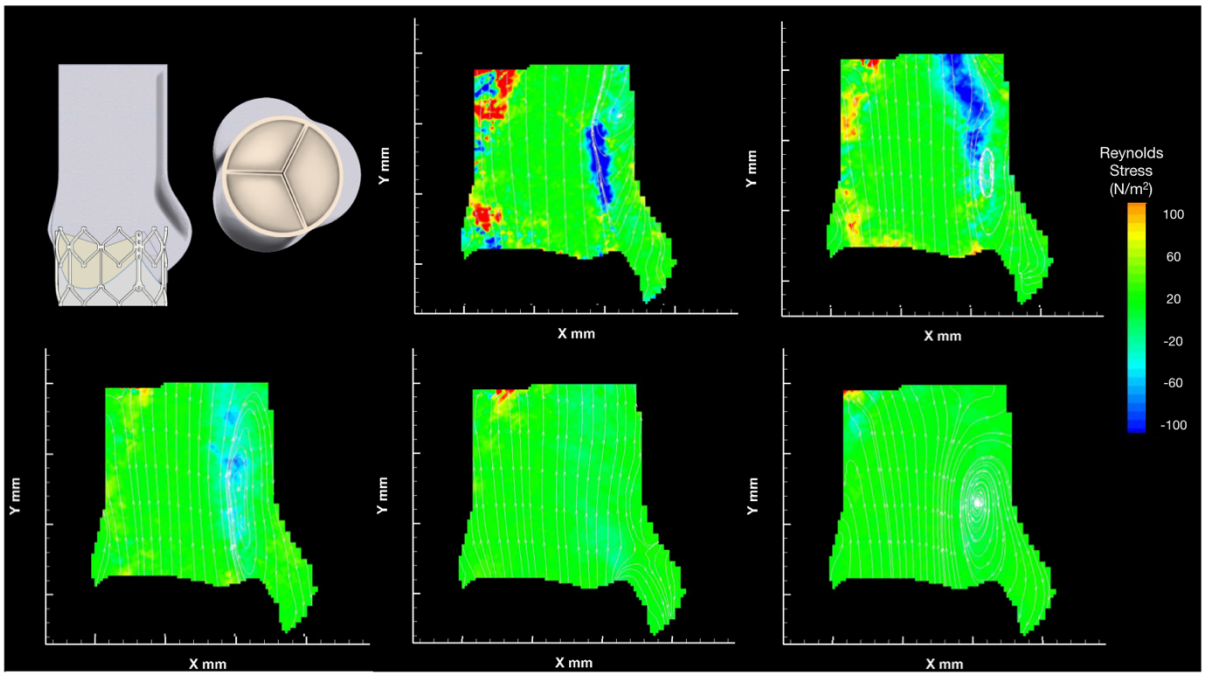

Figure 9-39: RSS contour maps for the TA3 configuration.

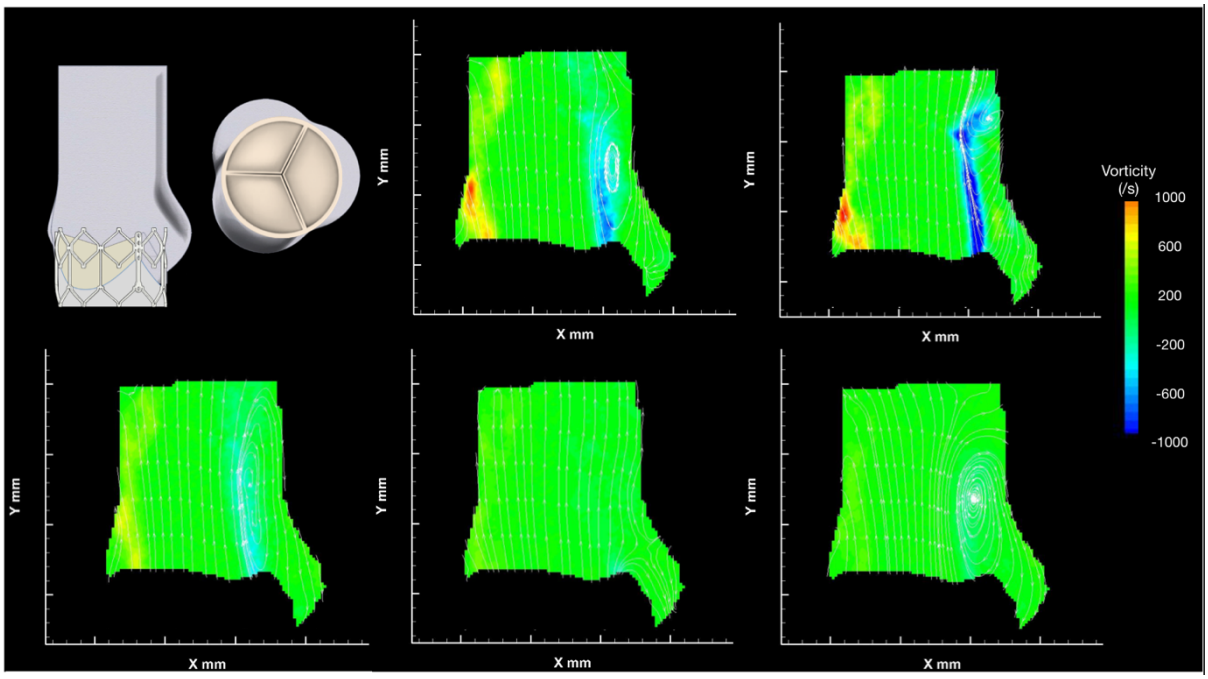

Figure 9-40: Vorticity contour maps for the TA3 configuration.

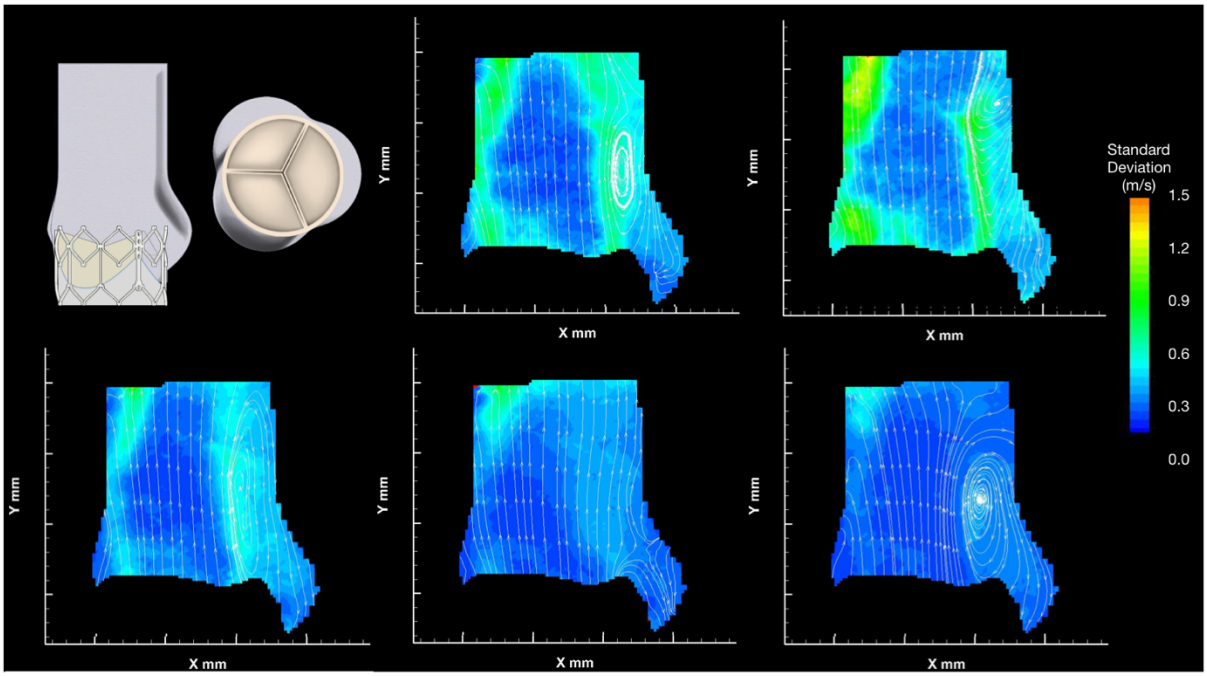

Figure 9-41: Standard Deviation contour maps for the TA3 configuration.

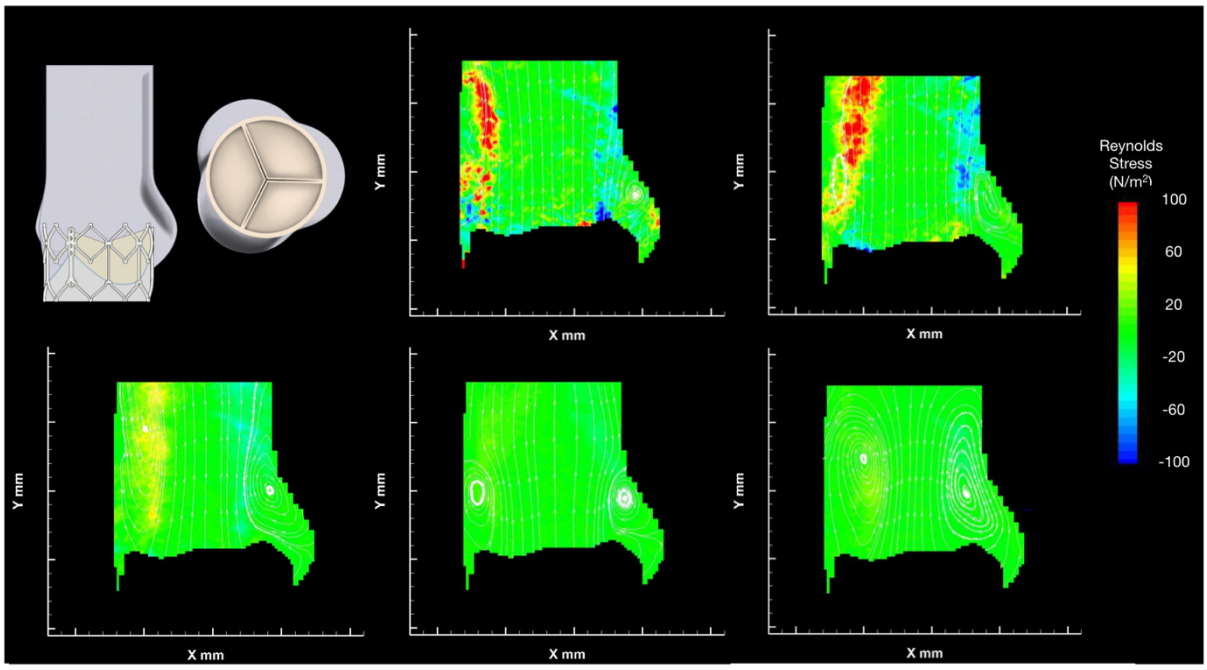

Figure 9-42: RSS contour maps for the TA4 configuration.

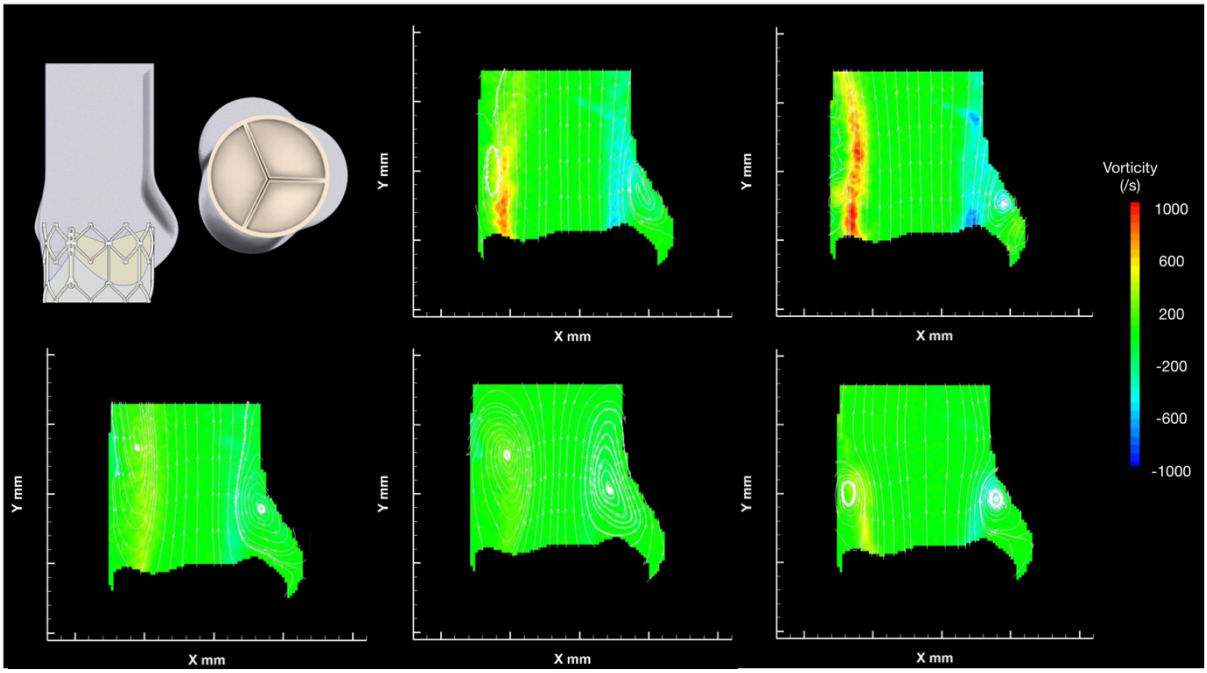

Figure 9-43: Vorticity contour maps for the TA4 configuration.

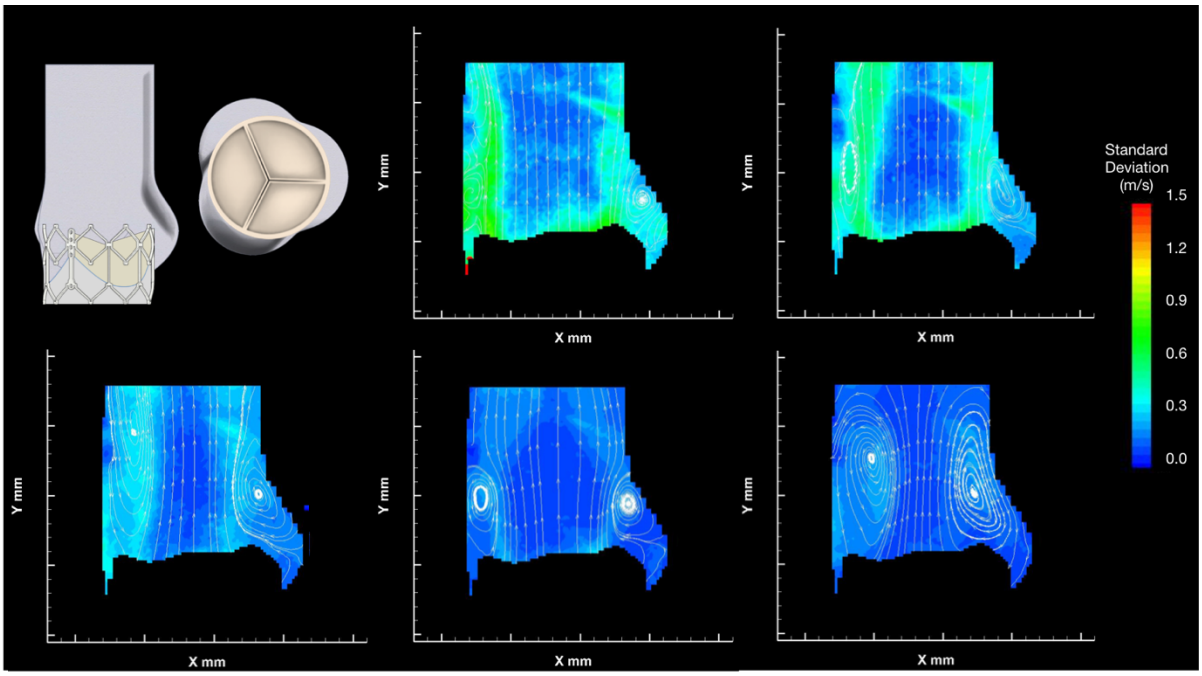

Figure 9-44: Standard Deviation contour maps for the TA4 configuration.

9.4 Additional PIV images from The Effect of Coronary Arteries upon Post-TAVI Flow

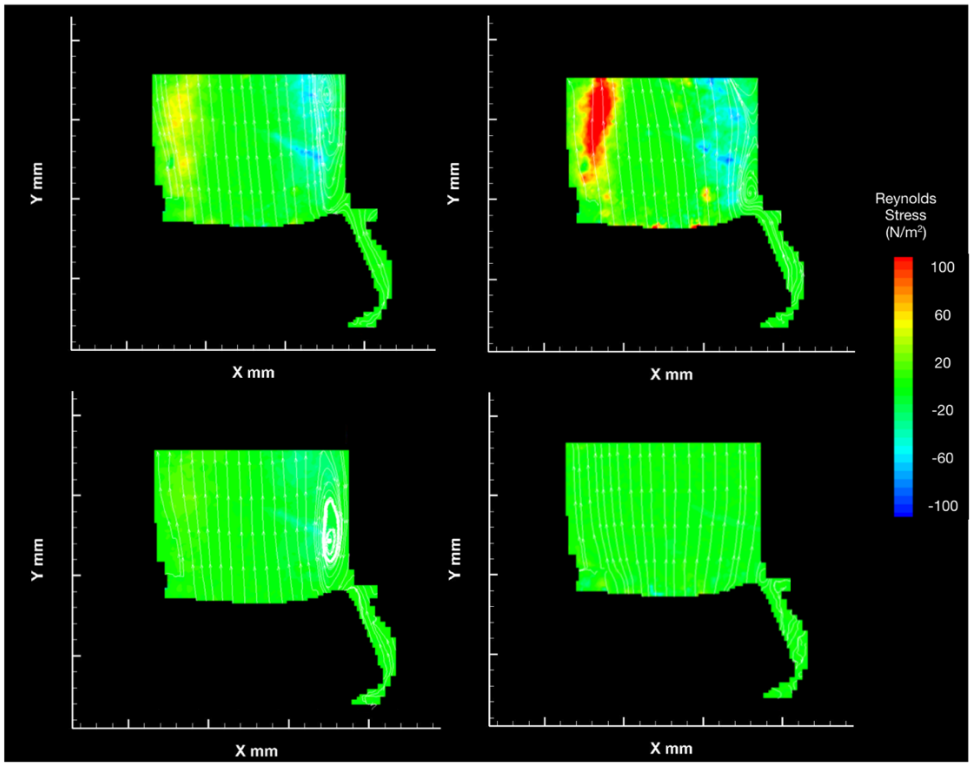

Figure 9-45: RSS contour maps for the NoCA configuration.

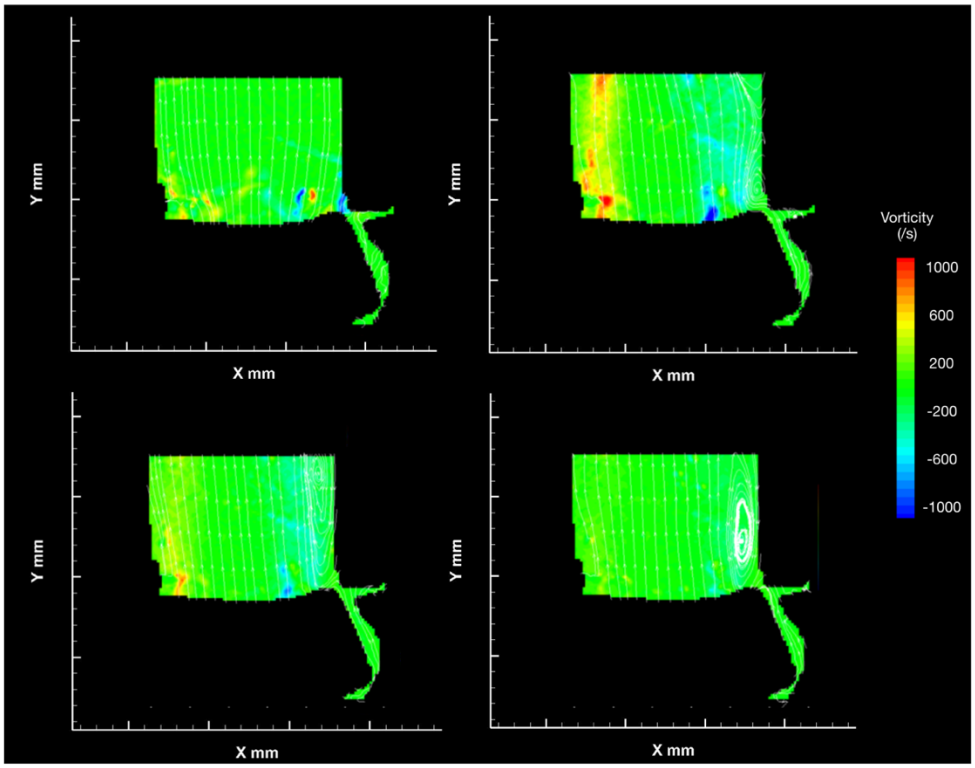

Figure 9-46: Vorticity contour maps for the NoCA configuration.

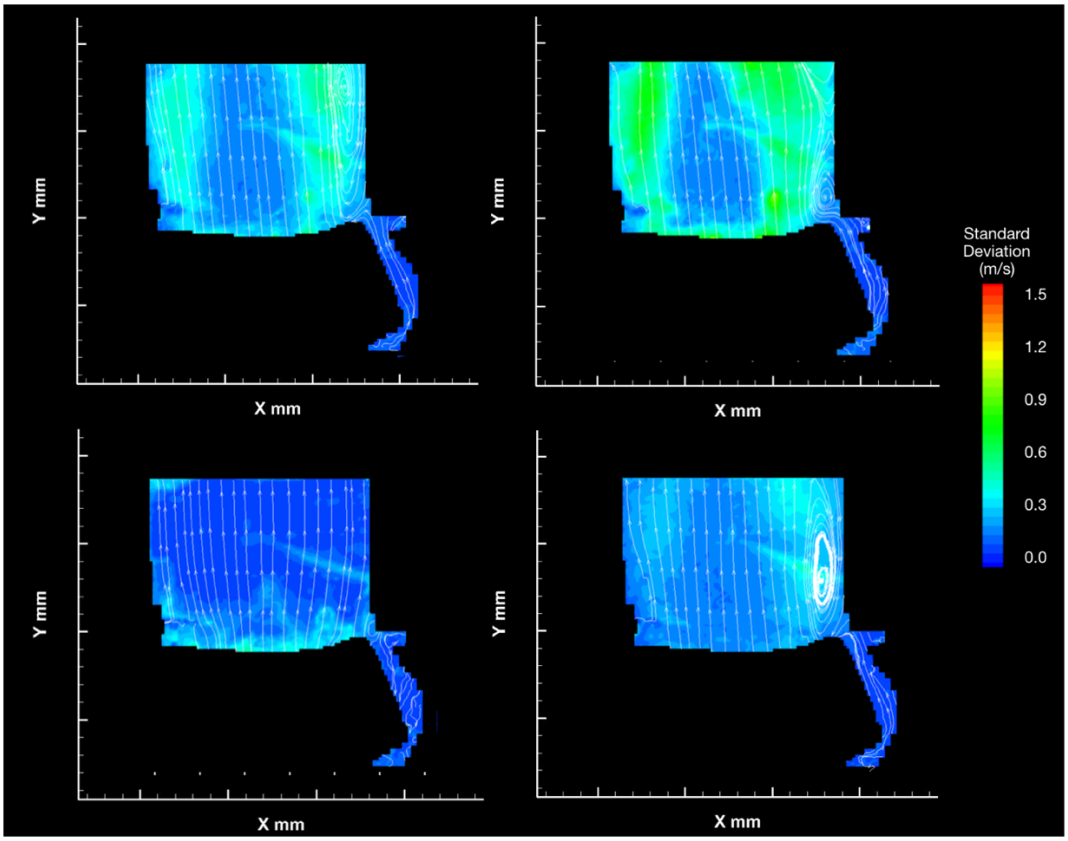

Figure 9-47: Standard Deviation contour maps for the NoCA configuration.

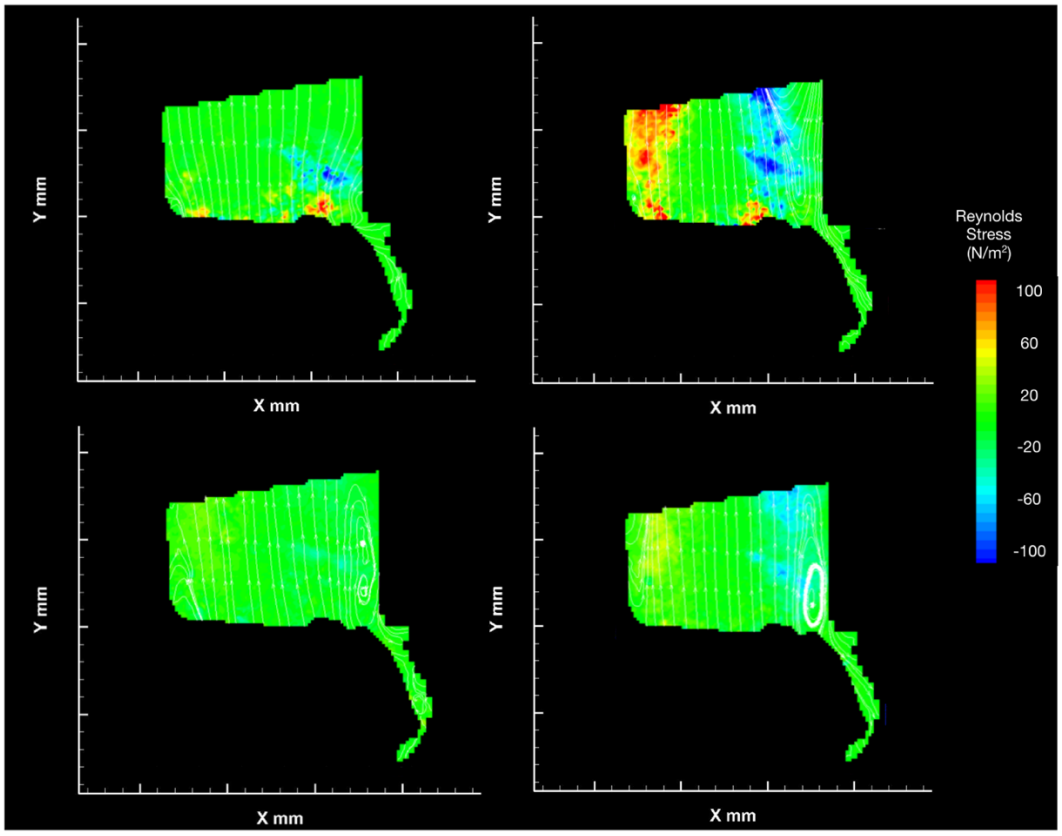

Figure 9-48: RSS contour maps for the LCA configuration.

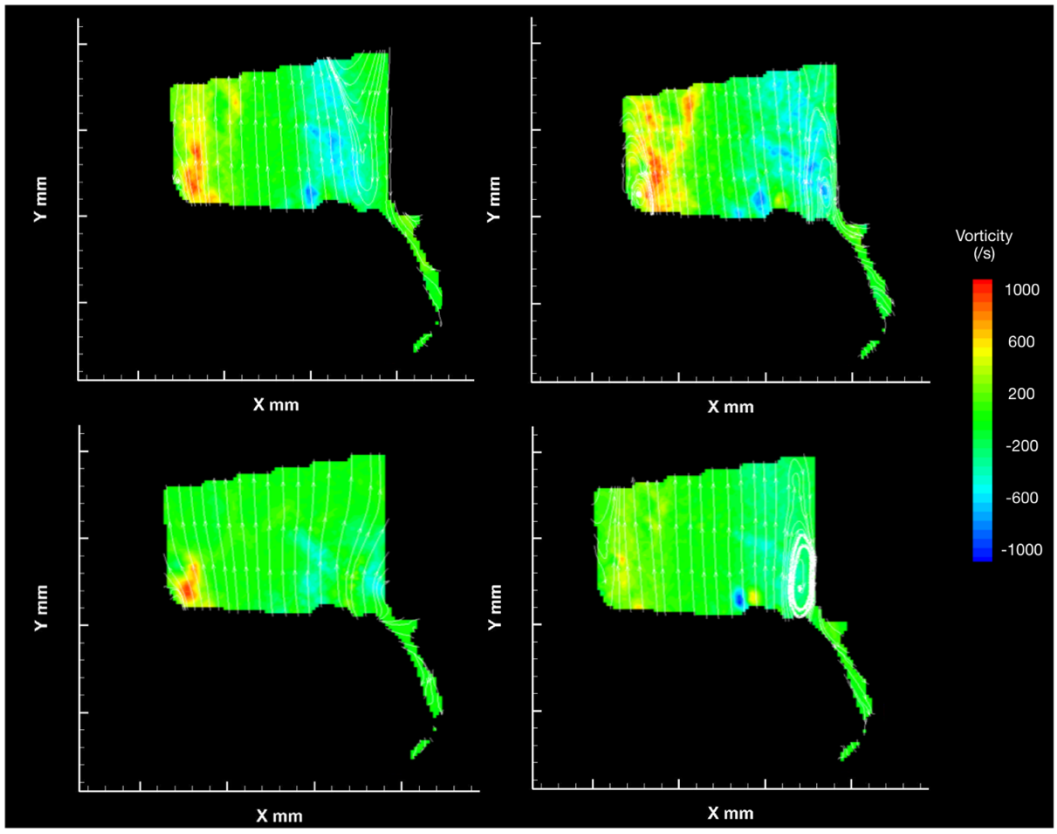

Figure 9-49: Vorticity contour maps for the LCA configuration.

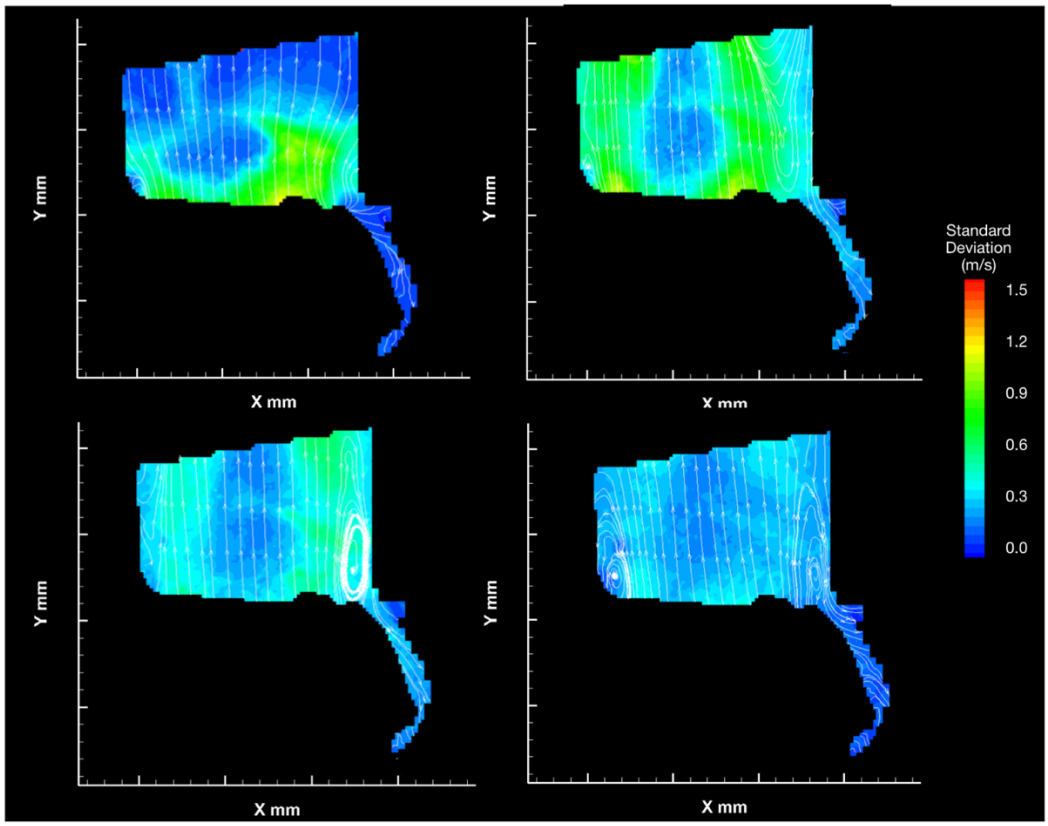

Figure 9-50: Standard Deviation contour maps for the LCA configuration.

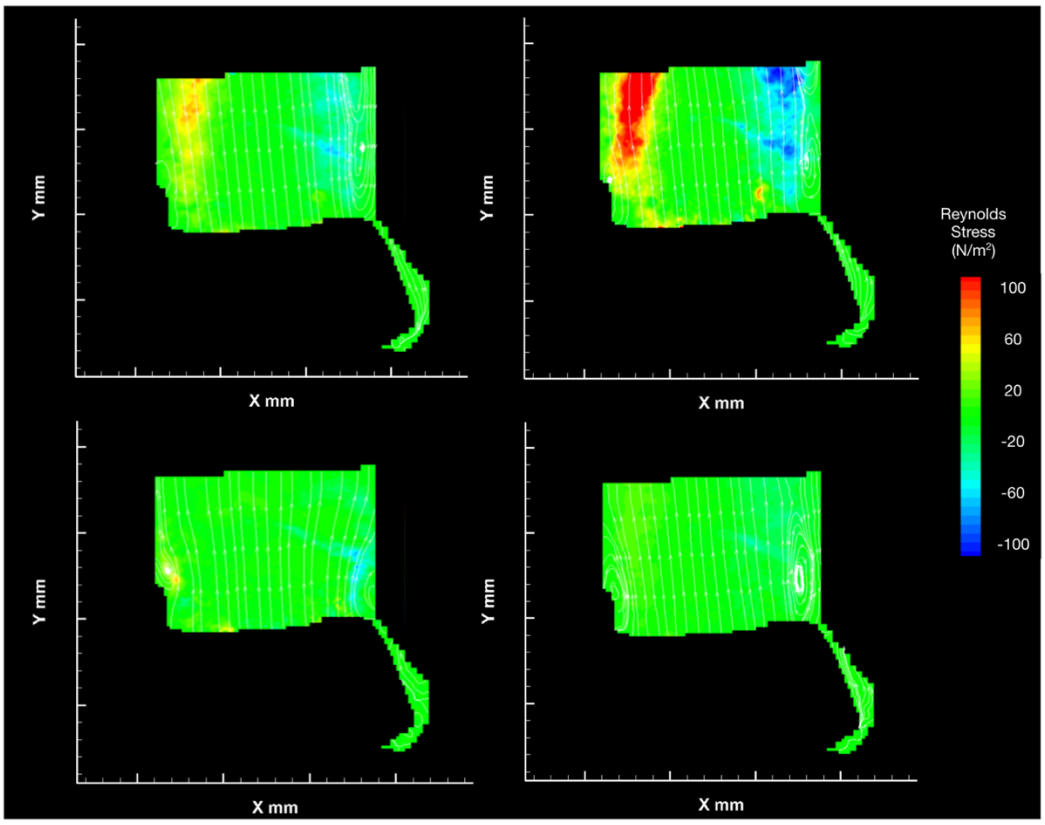

Figure 9-51: RSS contour maps for the RCA configuration.

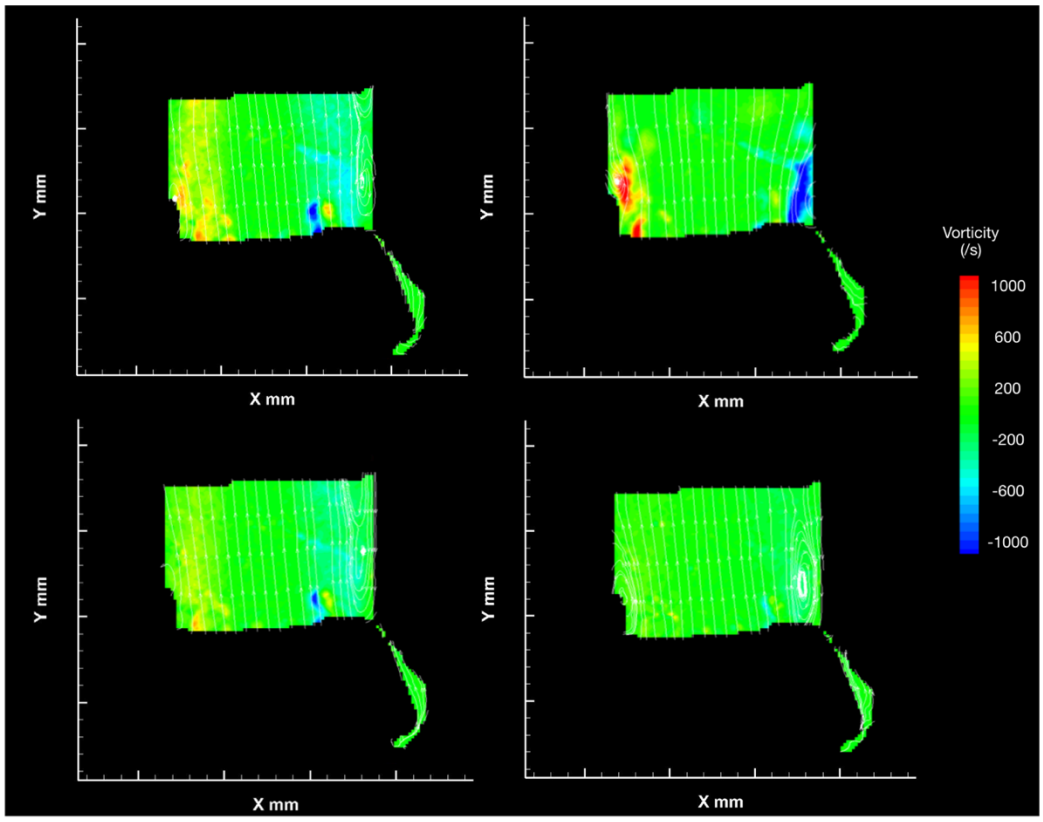

Figure 9-52: Vorticity contour maps for the RCA configuration.

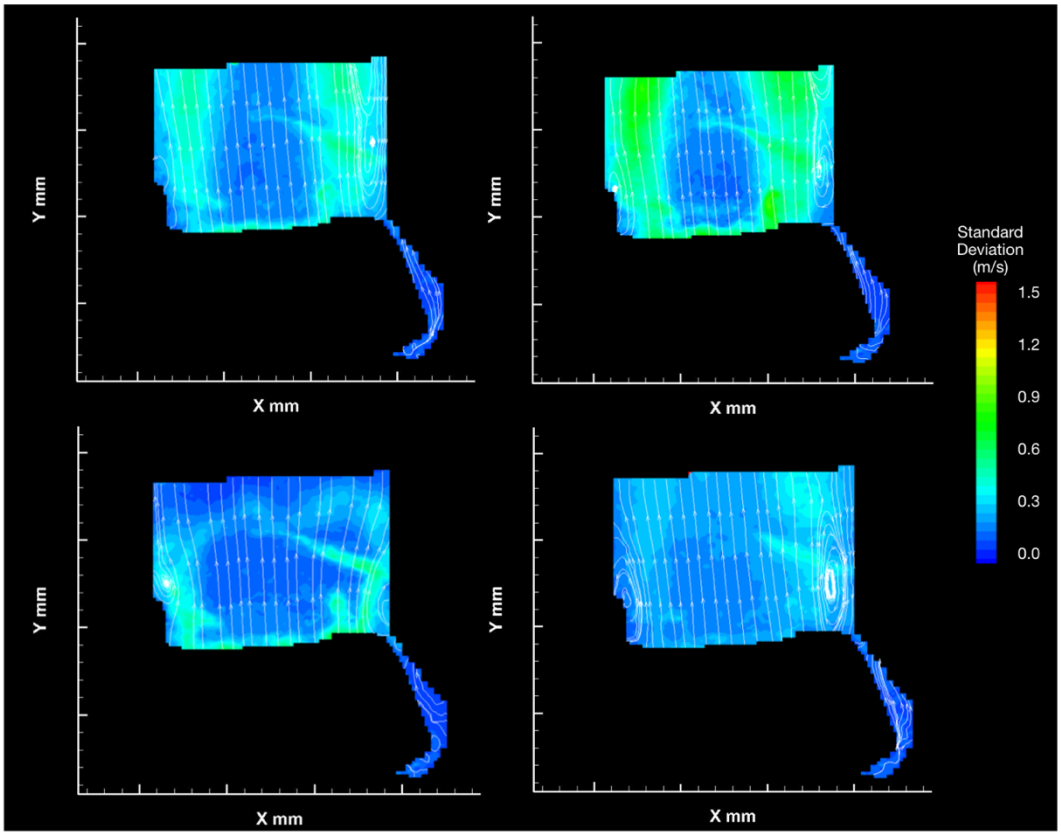

Figure 9-53: Standard Deviation contour maps for the RCA configuration.

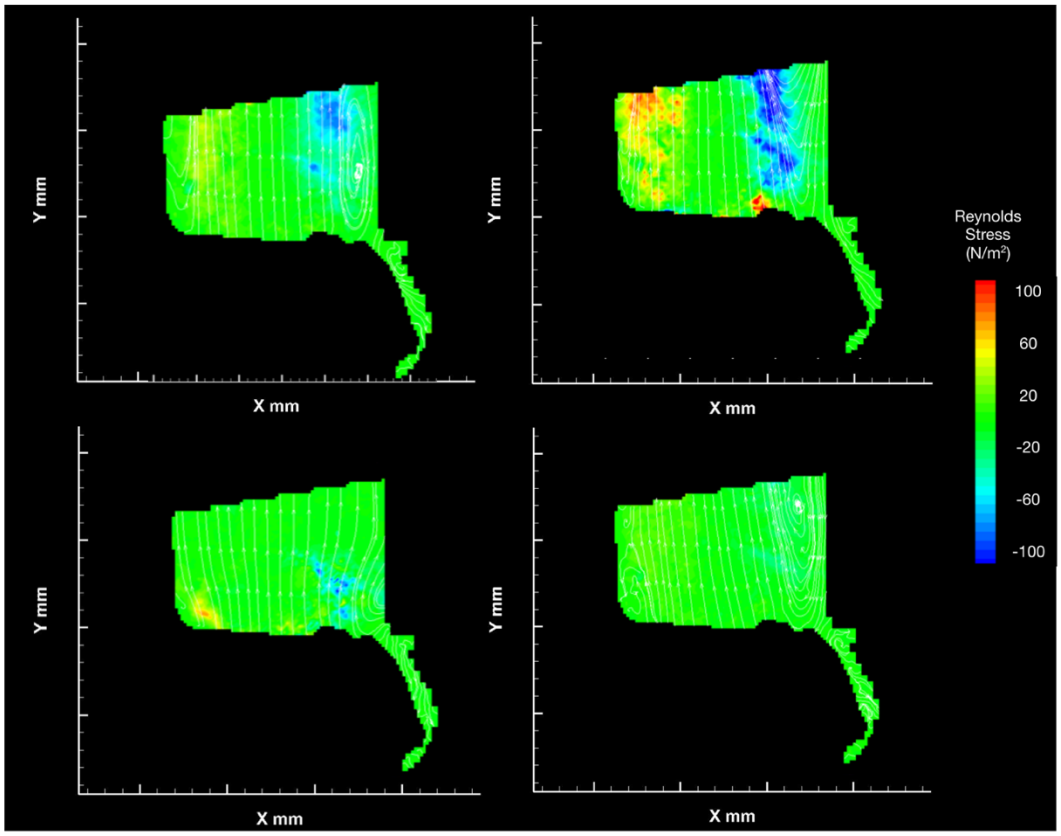

Figure 9-54: RSS contour maps for the NCA configuration.

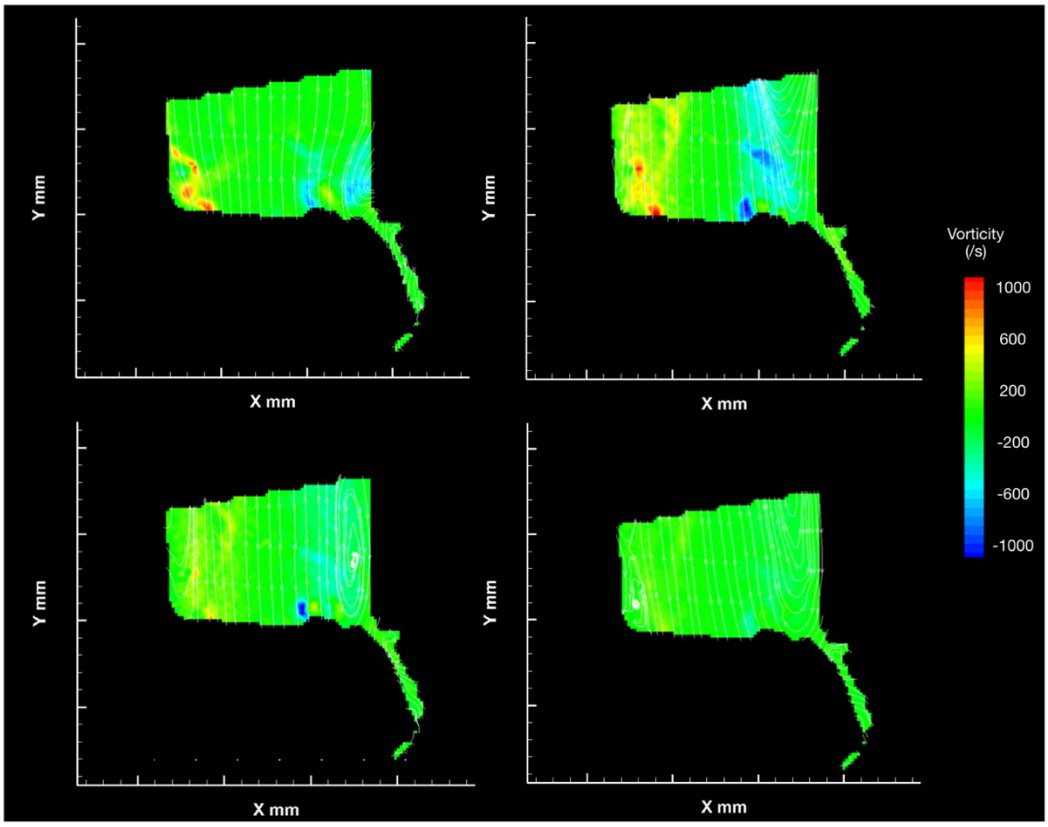

Figure 9-55: Vorticity contour maps for the NCA configuration.

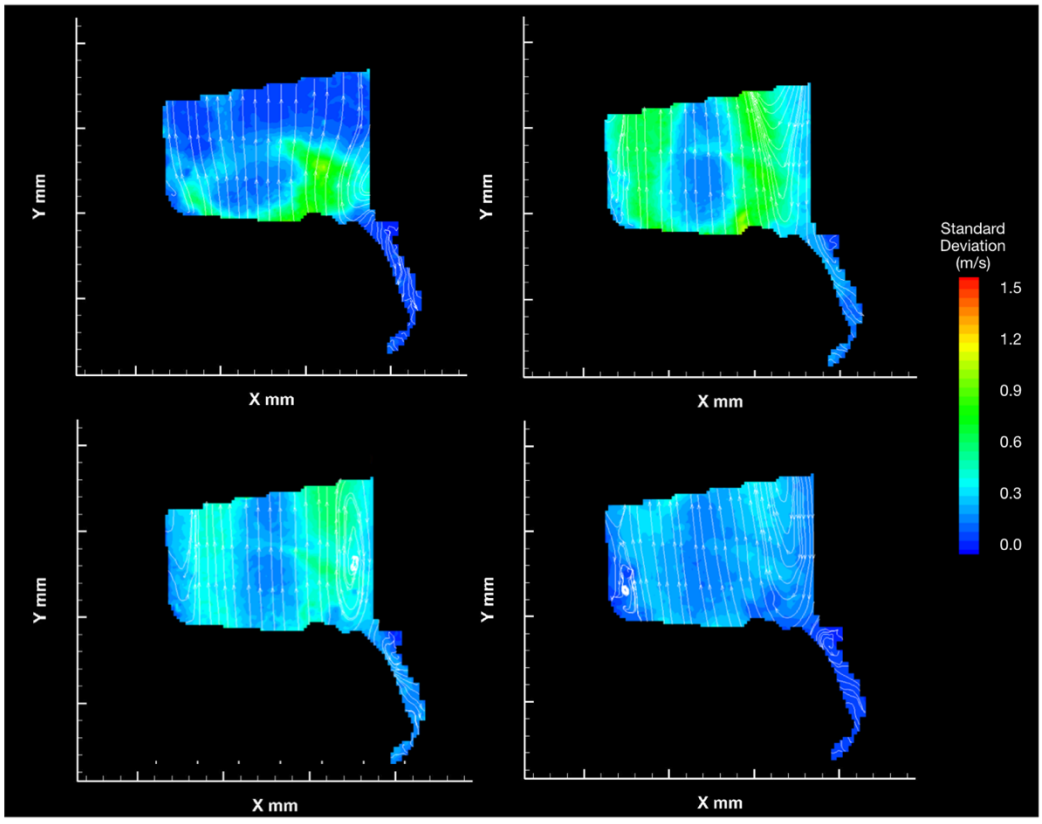

Figure 9-56: Standard Deviation contour maps for the NCA configuration.